2018

A field and laboratory study on the dynamic response of the Eddystone lighthouse to wave loading

Banfi, Davide

A field and laboratory study on the dynamic response of the Eddystone lighthouse to wave loading

Davide Banfi

School of Engineering

Plymouth University

Thesis submitted for the degree of

Doctor of Philosophy

September 2017

Acknowledgements

FIRST and foremost, I would like to express all my gratitude to my Director of Studies, Prof. Alison Raby, who gave me the opportunity to work on this PhD project. I am really grateful to her advice, patience and constant guidance, which played a decisive role in both the development of this project and the improvement of the work quality.

I would like to express also my gratitude to Emeritus Professor Geoffrey Bullock for the stimulating thoughts and encouragement, but also for questions that incented me to widen my research from various perspectives. His valuable suggestions have contributed to my personal and professional growth.

My sincere thanks also goes to Prof. David Simmonds and Prof. Yaqub Rafiq for the scientific suggestions, encouraging comments and sincere support provided during these studies.

My gratitude to Prof. Deborah Greaves and Prof. Gregorio Iglesias and, in general, to all the members of the COAST Research Group, who provided me with the valuable opportunity of having access to the state-of-the art research facilities of the COAST Laboratory of Plymouth University.

Thanks to Prof. Mario Calabrese, Prof. Mariano Buccino and Prof. Diego Vicinanza, who introduced me in the research environment of coastal engineering. In particular, I am infinitely grateful to Prof. Mariano Buccino who infused me with the passion for this topic.

My appreciation to all my friends, especially to Oreste and Antonio for their sincere support. I would also convey my gratitude to Carlos, Javier, Federico, Rob and Teng, with whom I shared not only endless hours of amusement and entertainment, but also the day-to-day work.

Thanks to Angela for giving me serenity and unconditional support, fundamental aspects to complete this project.

Last but not least, my warmest gratitude goes to my mother, my father and my sister, who always supported and encouraged me in all my decisions. This thesis is dedicated to them.

Authors declaration

THIS work is the result of my own investigation. At no time during the registration for the degree of Doctor of Philosophy has the author been registered for any other University award. Work submitted for this research degree at Plymouth University has not formed part of any other degree either at Plymouth University or at another establishment.

Five papers have been accepted for publication in refereed conference and journal papers. Other papers are in preparation and part of the work was presented at the ICE Conference in Liverpool (September 2017).

Word count for the main body of this thesis: **46171**

Signed: _____

Date: _____

Journal and conference papers:

Banfi, D., Raby, A., Simmonds, D., Rafiq, Y., & Bullock, G. N. (2017). *Wave impacts on the Eddystone lighthouse: a field and laboratory investigation.* ICE Coasts, Marine Structures and Breakwaters Conference. Liverpool, UK.

Banfi, D., Raby, A., & Simmonds, D. (2017). *Characterisation of breaking waves on the Eddystone lighthouse: a laboratory investigation on wave pressure.* Coastal Engineering Proceedings, 1(35), 15.

Trinh, Q., Raby, A., Banfi, D., Corrado, M., Chiaia, B., Rafiq, Y., & Cali, F. (2016).

Modelling the Eddystone lighthouse response to wave loading. Engineering Structures, 125, 566-578.

Raby, A., Bullock, G. N., Banfi, D., Rafiq, Y., & Cali, F. (2015). *Wave loading on rock lighthouses.* In Proceedings of the Institution of Civil Engineers-Maritime Engineering., 1-14.

Raby, A., Banfi, D., & Simmonds, D. (2015). *Wave impacts on rock lighthouses.* Coastal Structures & Solutions to Coastal Disasters Joint Conference, Boston, Massachusetts, USA.

Abstract

BECAUSE little was known about how the masonry lighthouses constructed during the 19^{th} century at exposed locations around the British Isles were responding to wave action, the dynamic response of the Eddystone lighthouse under wave impacts was investigated. Like other so called 'rock lighthouses', the Eddystone lighthouse was built on top of a steep reef at a site that is fully submerged at most states of the tide. Consequently, the structure is exposed to loading by unbroken, breaking and broken waves. When the breaking occurs, wave loading leads to complex phenomena that cannot be described theoretically due to the unknown mixture of air and water involved during the wave-structure interaction. In addition, breaking waves are generally distinguished from unbroken and broken wave due to the fact that they cause impulsive loads. As a consequence, the load effects on the structural response require a dynamic analysis. In this investigation the dynamic response of the Eddystone lighthouse is investigated both in the field and by means of a small-scale model mounted in a laboratory wave channel. In particular, field data obtained by the use of geophones, cameras and a wave buoy are presented together with wave loading information obtained during the laboratory tests under controlled conditions.

More than 3000 structural events were recorded during the exceptional sequence of winter storms that hit the South-West of England in 2013/2014. The geophone signals, which provide the structural response in terms of velocity data, are differentiated and integrated in order to obtain accelerations and displacements respectively. Dynamic responses show different behaviours and higher structural frequencies, which are related to more impulsive loads, tend to exhibit a predominant sharp peak in velocity time histories. As a consequence, the structural responses have been classified into four types depending on differences of ratio peaks in the time histories and spectra. Field video images indicate that higher structural frequencies are usually associated

with loads caused by plunging waves that break on or just in front of the structure. However, higher structural velocities and accelerations do not necessarily lead to the largest displacements of around a tenth of mm. Thus, while the impulsive nature of the structural response depends on the type of wave impact, the magnitude of the structural deflections is strongly affected by both elevation of the wave force on the structure and impact duration, as suggested by structural numerical simulations and laboratory tests respectively. The latter demonstrate how the limited water depth strongly affects the wave loading. In particular, only small plunging waves are able to break on or near the structure and larger waves that break further away can impose a greater overall impulse due to the longer duration of the load. As a consequence of the depth limited conditions, broken waves can generate significant deflections in the case of the Eddystone lighthouse. However, maximum accelerations of about 0.1g are related to larger plunging waves that are still able to hit the lighthouse with a plunging jet.

When compared to the Iribarren number, the dimensionless irregular momentum flux proposed by Hughes is found to be a better indicator concerning the occurrence of the structural response types. This is explained by the fact that the Iribarren number does not to take into account the effects of the wide tidal range at the Eddystone reef, which has a strong influence on the location of the breaking point with respect to the lighthouse.

Finally, maximum run up were not able to rise up to the top of the lighthouse model during the laboratory tests, despite this having been observed in the field. As a consequence, the particular configuration of the Eddystone reef and the wind could have a considerable bearing and exceptional values of the run up, greater than 40 m, cannot be excluded in the field.

Contents

List of Figures

List of Tables

Chapter 1

Introduction

1.1 Background

WAVE-STRUCTURE interactions due to breaking waves involve highly complex processes that cannot yet be described theoretically. This is caused by the intrinsic random nature of wave pressure due to the unknown mixture of water-air involved during the breaking (Bullock et al., 2001). Thus, while the aeration effects further add to the difficulty in predicting the underlying processes, non-breaking waves are well understood and their forces are considered as a quasi-static load in structural analyses. Conversely, breaking waves can generate highly impulsive loads, i.e. extreme load peaks with short impact durations. In particular, more violent impacts caused by plunging waves will correspond to shorter load durations. The effect of these impulsive loads on rigid coastal structures still represents an open issue and shock loads have often been ignored despite their magnitude. As a consequence, plunging waves are seldom included in the design practice of rigid coastal structures and dynamic analysis is rare. However, past failures of vertical breakwaters in the UK, Japan and Italy (Oumeraci, 1994) suggest the need to include plunging waves in the loading assessment, and to conduct dynamic analysis when designing rigid coastal structures (Cuomo, 2005).

Typically, engineers identify the design conditions (hydraulic and structural) in order to avoid the occurrence of plunging waves simplifying, thus, the design process. To this end, an extensive design guideline was drawn within the framework of the PROVERBS (Probabilistic design tools for Vertical Breakwaters) research project that represents the most recent and significant European effort towards the understanding and as-

sessment of wave forces on seawalls. However, some coastal structures can inevitably be exposed to breaking waves, as is the case with the so called 'rock lighthouses'. Commonly, these structures are erected on the top of a steep reef and in limited water depths. As a consequence of these environmental conditions, waves are strongly affected by surf-zone transformations and plunging waves can frequently occur (Goda, 2010).

There are about 20 masonry lighthouses constructed at exposed locations around the British Isles and most of these date back to the 19^{th} century. Little is known about how these historic structures respond to wave action. When, as typically happens along the North European coasts, a large tidal excursion and severe environmental conditions concur, some of these rock lighthouses can be subjected to extreme wave forces. On the other hand, climate change[1] is further increasing the general concern about effects of sea level rise on the reliability of these structures. The present PhD project, funded by the School of Marine and Science Engineering of Plymouth University, investigates a particular rock lighthouse exposed to breaking waves: the Eddystone lighthouse. This structure marks a perilous reef of the same name that lies in the English Channel some 21 km offshore from Plymouth, UK.

Over the centuries, countless shipwrecks occurred due to the rock outcrops of the Eddystone Reef before the building of the first tower that was completed 1698. This lighthouse, designed by Henry Winstanley, was one of the first in the world to be built on a small group of rocks in the open sea. In November 1703, a great storm hit the south-west of England and the stone-clad wooden structure of Winstanley was swept away. Subsequently, three further lighthouses have stood at that location, each larger and more sturdy than their predecessors.

[1] The UK planning policy statement 25 (Planning Portal, 2010) predicts a sea level rise, of 0.786 m by 2095, and increasing of extreme wave heights, to +10% by 2055, in the south-west of UK.

1.2 Motivation

Although the safety of navigation has increased with the development of radar and satellite based navigation technologies, the General Lighthouse Authorities (GLAs)[2] recognise the need to retain rock lighthouses as physical aids to navigation. The longevity of these heritage structures cannot be taken for granted and the current Eddystone lighthouse is a magnificent granite structure of incalculable cultural importance. James Douglass designed the present tower that was completed in 1882 after four years of works. This tower, for which Douglass was knighted, is a marvel of ingenuity given the hostile environment at the site.

Some of the historical anecdotes testify to the severe environmental conditions at the Eddystone, which is characterised by a three-fingered reef with a wave climate affected by a complex tidal range that can exceed 5 m. The historical anecdotes have been collected in Raby et al. (2015) and some of them are here reported in order to illustrate how difficult was the construction of the lighthouses, which were subjected to constant building delays due to the inability to land on the reef even during calm summer weather.

Winstanley (1699), who built the first tower, is quoted by Majdalany (1959) as saying that "...though the weather should seem to be most calm in other places, yet here it would mount and fly more than two hundred foot ($\sim$ 60 m)...". Smeaton, who designed the third lighthouse, made the observation that "on a perfectly calm day, with the water for half a mile around seemingly as smooth as glass, a scarcely perceptible ground swell could send an unexpected wave billowing over the rock, even though its peak was at the time nine feet ($\sim$ 2.7 m) above water level" (Majdalany, 1959). Smeaton made further interesting observations that during periods of "comparatively innocuous swell" waves could be sent up to a height of around 10 m or so as they broke at low tide on the western end of the reef, although at high tide the same was not witnessed

[2]GLAs consists of three agencies that cover different geographical regions: Trinity House (England, Wales, Channel Islands and Gibraltar), Northern Lighthouse Board (Scotland and the Isle of Man) and Commissioners of Irish Lights (Ireland).

even though the swell was much greater (Majdalany, 1959).

As illustrated by Raby et al. (2015), Majdalany (1959) recounts many tales concerning the behaviour of the early Eddystone Lighthouses. For example, Winstanley's structure was said to rock so much that crockery could be shaken from the table and the lighthouse keepers made seasick. Rudyard's tower, the second wood tower that was destroyed during a fire, was also said to vibrate enough not only to shake utensils off surfaces but also to rock men out of their bunks. The principal keeper's log indicates that even Smeaton's tower, the third structure on the Eddystone, could have a noticeable response to wave impacts. The report for a particularly violent storm states that it caused "considerable motion of the cylinder glasses fixed in the lamps" and describes how the tower appeared to "jump as if resting on an elastic body". The masonry lighthouse designed by Smeaton was replaced mainly because the gneiss rock on which it stood had been eroded. James Douglass (Douglass, 1878) also drew attention to the fact that storm waves could rise up the Smeaton's tower "considerably above the summit of the lantern, thus frequently eclipsing the light and altering its distinctive character"; an impressive feat given that the focal plane of the light was 72 ft ($\sim$ 23 m) above high water level. Furthermore, when the upward jet of water hit the projecting cornice just below the lantern it "lifted the portion of the building above this level". Thus, given the historical value of the Douglass' tower and the hostile environment condition at the Eddystone, the GLAs decided to monitor the lighthouse with the collaboration of Plymouth University in order to evaluate the reliability of the structure under wave loading.

1.3 Research approach

The central goal of the present investigation is to understand the effects of wave loading on the Eddystone lighthouse.

Typically, wave loading investigations due to breaking waves have been based on either field or laboratory measurements. The major advantage of field measurements over laboratory tests is the fact that measurements are not affected by laboratory ef-

fects and, possibly, small-scale distortions (Bullock et al., 2003; Cuomo et al., 2010a; Blenkinsopp & Chaplin, 2011; Bredmose et al., 2015).

Previous field investigations have generally used:

- pressure transducers to obtain local load measurements;
- electronic gauges to obtain wave run-up information;
- bottom-mounted pressure transducers or wave buoys to measure wave surface elevations.

For the present study some technical/practical constraints prohibited the use of these conventional instruments. In the first instance, the attachment of any device to the outside of the masonry structure would have been complicated from the perspective of both the historical value of the lighthouse and the hostile wave climate. In addition, the use of pressure transducers, which have been usually used to evaluate laboratory scale effects and to quantify pressures in the field (Blackmore & Hewson, 1984; Bullock et al., 2001), would not have provided an accurate estimation of the overall force and, as indicated by the large-scale experiments of Hofland et al. (2011), neither a clear indication of the impacting wave on the structure. This is due to the fact that breaking wave pressure is highly localised in the space (Bullock et al., 2007).

As a consequence of the above considerations, a novel research approach was devised for the present case of study Raby et al. (2015). The novel approach consisted of investigating the effects of wave loading by directly analysing the dynamic response of the tower. To this end, geophones and cameras were installed on the Eddystone lighthouse in July 2013. The instrumentation was designed and developed by the following team from Plymouth University: Mr Tony Tapp, Mr Peter Ganderton, Dr Alison Raby, Professor Geoffrey Bullock and Dr David Simmonds.

This approach had several advantages. In the first instance, the geophone system was both powered by batteries (i.e. electronically autonomous) and remote-controlled,

overcoming thus other two constraints of the site: limited energy supply and inability to frequently access to the instrumentation. In addition, when compared to local pressure measurements, geophone data have the advantage of reflecting the overall effects of the impacting wave on the structure. However, it should be noted that the dynamic response of the structure depends on both the wave pulse excitation and its line of action. As a consequence, it is reasonable to expect that the geophone signals are not strictly an indicator of the wave impulse, but they may tend to be gained depending on the application point of the wave load.

The hostile wave climate would also have produced several difficulties for any measurement of the wave surface in the proximity of the reef. Thus, the remote-controlled video cameras were used to record the wave conditions around the structure. Wave data were obtained from statistical offshore data recorded by the E1 Buoy operated by the Western Channel Observatory (WCO)[3]. The E1 buoy is located some 15 km south-west of the lighthouse. Water level data along the coast at Plymouth were obtained from the British Oceanographic Data Centre (BODC)[4].

1.4 Aims and obectives

This PhD project, which started in October 2013, investigates the field data set acquired during the UK winter storms 2013-2014. Analysis and interpretation of the data, obtained from the pre-existing field instruments installed in July 2013, was aided by a complementary physical modelling investigation devised during the present PhD project to shed further light on the field results. Laboratory tests at small scale were carried out in the COAST Laboratory of Plymouth University in September 2015.

The aim of the research is to assess the dynamic behaviour of the Eddystone lighthouse under wave loading. More specifically the objectives of this research are:

[3]WCO is an oceanographic time-series and marine biodiversity reference site in the Western English Channel.

[4]BODC is a national facility for preserving and distributing oceanographic and marine data.

- to understand the dynamic response of the Eddystone lighthouse, by examining the geophone signals;
- to provide a qualitative description of the wave characteristics of the various impacts on the lighthouse;
- to evaluate the effects of offshore wave data and instantaneous water levels on the dynamic responses of the lighthouse.

1.5 Thesis outline

This thesis consists of seven further chapters as follows: (2) Literature review, (3) Field instrumentation and physical modelling, (4) Data acquisition and processing, (5) Structural response of the Eddystone lighthouse, (6) Wave loading at small scale, (7) Laboratory test and interpretation of field data, and (8) Conclusions and recommendations. The chapters are described in more detail below.

Literature review. A literature review regarding wave loading is presented. In particular, the effects of breaking waves on pressure time history, force and impulse are described through the breaker classifications used in the coastal literature. In addition, the effects of wave loading on structural responses are presented and how the breakers are considered in dynamic analysis is illustrated. Finally, a review of the main coastal processes are provided, and the wave parameters typically used for their description.

Field instrumentation and physical modelling. The scene of the present investigation is set with a detailed description of both the Eddystone lighthouse and the reef. Furthermore, a finite element model which has been developed for a structural analysis of the lighthouse is described. Both field instrumentation and the hydraulic data set are described. The design of the physical modelling is illustrated. In particular, the description of two different models, used to analyse pressure and overall force by means of a load cells system, are described. Finally, the design of the test program is explained.

Data acquisition and processing. This chapter illustrates the data acquired from

both field instrumentation and laboratory tests. Then, the chapter explains how the data sets are processed in order to maximise the available information.

Structural response of the Eddystone lighthouse. The results are presented and discussed. There are four steps: (I) analysis and classification of the dynamic responses, (II) qualitative field description of the wave impacts causing the structural responses, (III) general considerations and observations on the field data set, (IV) dependence of the structural data set on the hydraulic data.

Wave loading at small scale. Results from the small-scale tests are presented. In particular, the wave loading characteristics, obtained under controlled conditions, are described.

Wave impacts on the Eddystone lighthouse and assessment procedures. Further interpretations of the field data are presented on the basis of the insights obtained from the laboratory tests. In addition, practical advice, which can be applied for the particular case of study of the Eddystone lighthouse, are suggested.

Conclusions and recommendations. The most important conclusions of this research are drawn together. In addition, possible future research directions are indicated.

Chapter 2

Literature review

FEW studies have focused on the dynamic response of coastal structures under breaking waves (Kirkgöz, 1990; Loraux, 2013; Manjula et al., 2014). Much more attention has been given to the analysis of wave loading by means of experimental tests. However, relatively little research has been conducted on the action of waves on structures like rock lighthouses. Some physical 3D tests have been conducted in order to investigate cylindrical structures (tripod and slender or composite cylinders) located on the top of particular submerged shoals (Goda, 1973; Kyte & Tørum, 1996; Hanssen & Tørum, 1999), but they merely provided predictive formulae to quantify the wave load.

Characterisation of load time histories has received more attention for coastal defence structures (Chan & Melville, 1988; Oumeraci et al., 1993; Hattori et al., 1994; Hull & Müller, 2002; Bullock et al., 2007) and slender cylinders (Tanimoto et al., 1986; Zhou et al., 1991; Chaplin et al., 1992; Chan et al., 1995; Chaplin et al., 1997). The latter have attracted further interest in the last decades following the development of offshore energy structures e.g. wind turbine monopiles (Wienke & Oumeraci, 2005; De Vos et al., 2007; Andersen et al., 2011).

Most of the previous investigations were carried out with physical tests in 2D. Although the complex bathymetry of the Eddystone lighthouse moves far away from 2D conditions, it is generally accepted that load histories on vertical structures, or 'near' vertical, tend to be affected by breaker shapes (Oumeraci et al., 1993). Therefore, the effects of wave impacts on the structural response of rock lighthouses may be, as a

first approach, analysed on the basis of the wave load histories recorded by physical investigations on rigid structures like vertical walls or cylinders.

This chapter provides a review of the description of wave load time histories, observations obtained from investigations on the structural response and hydraulic parameters typically used in coastal engineering.

2.1 Breaker classification on plane walls

The modest pulsating loads due to non-breaking waves can easily be predicted. The wave pressure is mainly given by the gravitational contribution of the wave. Therefore, the hydrostatic order of the maximum pressure head is about the incident wave height (H)[1] in the vicinity of the mean water level (i.e. $p/\rho gH = 1$, where ρ is the water density and g the gravitational acceleration). The pressure is in temporal phase with the wave, therefore the pressure rises from 0 to the peak value in a temporal duration of about 0.25 times the wave period (T)[2]. As a consequence, the time history generally varies very slowly with respect to the natural period of the oscillation of the structure; so the force can be applied statically without taking into account the dynamic characteristics of the structure.

Impulsive wave load is distinct from that of non-breaking waves in the superposition of an additional, transient force of short duration (which can be less than 0.01 times the wave period T). From the physical point of view the total force can be considered to be an overlapping of two forces, quasi-static and dynamic, with different nature of time histories. The quasi-static force varies according to the water surface elevation. When the impact force occurs, the total force shows a large increase in the load (Fig. 2.1). As mentioned earlier, the peak pressures due to breaking waves are difficult to predict, in part because the nature of the load time histories tends to be affected by the amount of trapped or entrained air and indirectly by the breaking shape at the structure.

[1] H is the distance between the maximum (crest) and minimum (trough) of the surface elevation.
[2] T is the time that the wave takes for one complete oscillation.

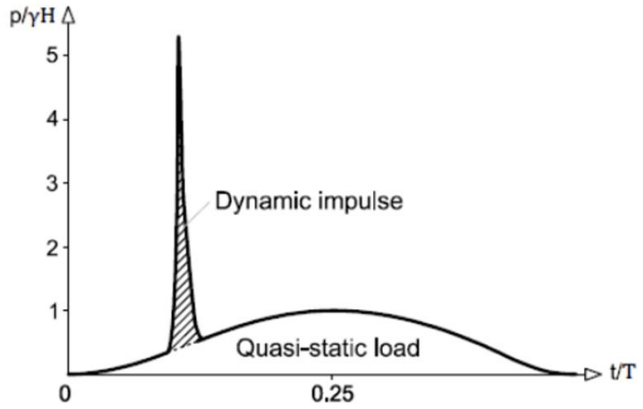

Figure 2.1: Simplified sketch of an impulsive pressure time history.

For vertical or 'near' vertical walls, a breaker-type classification is provided through the identification and discussion of four main breaker types obtained in 2D situations. Chan & Melville (1988) were some of the first to suggest that both the magnitude and the temporal distribution of the impact pressure, i.e. the resulting impact forces histories, are primarily determined by the position of the breaking point with respect to the location of the structure front and consequently by the breaker shape. Subsequently, several regular wave tests have been performed in order to provide more details on the breaker-type classification provided by Oumeraci et al. (1993) (Hattori et al., 1994; Hull & Müller, 2002). Although there are different definitions of breaker types, the breaker classification first proposed by Oumeraci et al. (1993) is used here:

1. Upward-deflected
2. Small air pocket
3. Large air pocket
4. Turbulent bore

This classification represents the four typical pressure events in a continuous series of breaker shapes which are given by a continuous increase in the breaking distances; i.e. from the upward-deflected breaker to the turbulent bore. The breaking distance

(x) is the distance between the structure and the location of the breaking wave height (H_b). The breaking takes place when the velocity of the water particle in the wave crest exceeds the wave celerity; as a consequence of breaking spray/turbulence is generated and the wave starts to dissipate energy.

Actually, upward-deflected is generally called flip-through in agreement with its first description given by Cooker & Peregrine (1990). This is a particular impulsive breaker that is subjected to a rapid reversal of the curvature of the crest, in proximity of the wall, with high vertical accelerations (Cooker & Peregrine, 1992). The ideal flip-through does not actually break or trap air between the wave surface and the plane surface of the structure. For this reason this breaker is unlikely to be observed in the field. Therefore, it will not be analysed in the following sub-sections which, instead, will be focus on the other three breakers.

2.1.1 Plunging with small air pocket

Breaking shape

The wave approaches the wall without breaking and then the wave front starts to overturn just in the proximity of the structure. Consequently, a relatively thin breaker tongue strikes the wall and a small air cushion, located above the still water level, is visible between the wave crest and the wall surface (Oumeraci et al., 1993). Moreover, when the wave becomes rapidly steeper and it starts to overturn, the wave front tends to be vertical (Hattori et al., 1994). However, the occurrence of a perfect parallel wave surface with the structure cannot be observed, since a small air pocket is always enclosed (Hull & Müller, 2002). After the impact, the entrapped air suddenly appears as small isolated bubbles in the surrounding water and as spray in the upward sloshing jet (Oumeraci et al., 1993).

Breaking distance and wave kinematics

The breaking distance (x) of this breaker is defined within a very narrow window and

it occurs at relatively short distance from the wall. Oumeraci et al. (1993) provide the lower and the upper limit respectively as 0.2 and 0.4 times the breaking wave height (H_b). At the breaking point, the horizontal water velocity is similar to the vertical one (Oumeraci et al., 1993). An interesting aspect, observed with Particle Image Velocimetry (PIV)[3] analysis, is that all particles at the wave front 'aim' at one point on the sea wall (Oumeraci et al., 1995a; Hull & Müller, 2002).

Pressure time history

This breaker is characterised by a very sharp single peak pressure, i.e. an impulsive pressure with very high magnitude and short duration (Oumeraci et al., 1993; Hattori et al., 1994). After this dynamic peak, the pressure signal persists due to the quasi-static component given by the wave surface. This quasi-static part of the signal is overlaid with oscillations of relatively high frequencies and small amplitude. The characteristics of these oscillations indicate the nature and the size of the entrapped air. The higher the frequency of these oscillations, the smaller the air cushion (Oumeraci et al., 1993).

2.1.2 Plunging with large air pocket

Breaking shape

The wave crest curls over the front face as it advances. It reaches the wall just before collapsing, so that it strikes the wall with a large air cushion of air and air-water mixture. This cushion, centred approximately on the still water level, is then highly compressed by the following impinging water mass, resulting in a violent upward ejection of spray and water (Oumeraci et al., 1993). Because the plunging is well-developed, a clear jet is projected from the crest of the wave, at high velocity, the tip of which is approximate in free fall (Hattori et al., 1994). Hull & Müller (2002) confirm that the air pocket consists of an entrapped air volume as well as small bubbles.

[3]PIV is an optical method of flow visualization. The fluid is seeded with small tracer particles. Due to appropriate illumination, it is possible to follow the motion of the seeding particles in order to calculate the velocity field (speed and direction) of the flow.

Breaking distance and wave kinematics

The onset of breaking occurs at a relative breaking distance 2-3 times the breaking wave height (Oumeraci et al., 1993) the relative breaking distance is the ratio of the breaking distance over the breaking wave height, i.e. x/H_b. The horizontal water velocity is larger than the vertical one. This breaker is characterised by both larger absolute value of the horizontal velocity (Oumeraci et al., 1993), when compared to small air pocket, and larger amounts of hydrodynamic mass as well (Oumeraci et al., 1995a; Klammer et al., 1996).

Pressure time history

This breaker is characterised by dynamic pressure oscillations with high frequencies (Oumeraci et al., 1993; Hattori et al., 1994). The large air pocket generates a high impact pressure with very short duration and high frequency pressure oscillations immediately after the rapid pressure drop. The pressure oscillations represent cyclic compression and expansion of the layer of bubbly water (Hattori et al., 1994). In agreement with the definition of Lundgren (1969), Oumeraci et al. (1993) associate the first peak with the hammer shock caused by the impinging breaker tongue; whilst the high frequency oscillation, called compression shock, is caused by the subsequent compression of the large air pocket (Fig. 2.2).

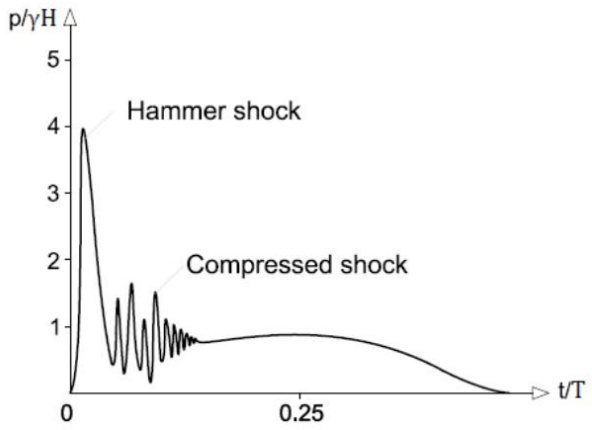

Figure 2.2: Simplified sketch of the aeration effect on an impulsive pressure time history. Hammer shock is due to impingement jet; compressed shock is due to the compressibility of the air.

Immediately after these irregular oscillations, a longer lasting quasi-static component occurs that is superimposed by a number of oscillations with much lower frequencies and larger amplitudes when compared to those observed in small air pocket case (Oumeraci et al., 1993).

2.1.3 Turbulent bore

Breaking shape

This is a broken wave with foamy front. The plunging is fully developed far from the structure (Hattori et al., 1994). Consequently, the jet strikes the water surface before impacting on the structure (Hull & Müller, 2002). The front and the top of the bore have a convex shape and are largely covered by an air-water turbulent mixture. The foam-covered bore front, with air entrained, first strikes the structure and is then compressed by the following impacting water mass. The preceding foamy mass is then deflected upwards to a large extent (Oumeraci et al., 1993).

Breaking distance and wave kinematics

The wave breaks away from the structure with a further increase in breaking distance. In agreement with Goda (1974), also Oumeraci et al. (1993) identify the range within a relative breaking distance of 4-5 times the breaking wave height. The vertical velocity is very small during the bore travel. The horizontal water velocity tends to be approximately uniformly distributed over the bore height (Oumeraci et al., 1993).

Pressure time history

The pressure distributions tend to vary relatively slowly and two similar peaks can usually be detected. The first phase corresponds to the impact of the foamy bore front that first hits the structure, followed by the water mass, which induces impact pressures in phase with the wave period (Oumeraci et al.; 1993). Then the pressure records display regular pressure oscillations with decreasing amplitude. These oscillations continue until air bubbles start to rise to the free surface (Hattori et al., 1994). Moreover, the

pressure traces generally contain a number of irregularities and peaks due to the impact of the air-water mixture (spray) and secondary small jets (Oumeraci et al.; 1993).

2.2 Aeration effects on wave loading characteristics

The amount and the distribution of entrapped air are mainly determined by breaker shape; this suggests that the breaker shape primarily determines not only the magnitude but also the distribution and the duration of the impact pressure (Oumeraci et al.; 1993). Although the investigations previously described (Oumeraci et al., 1993; Hattori et al., 1994; Hull & Müller, 2002) provide a qualitative description of the air, its effect on impact loads is significant, as perceived by Bagnold (1939) who was the first to indicate the important role of the air on the wave loading.

Bullock et al. (2007) performed detailed analysis on air and its effects on maximum peak pressure, pressure duration, spatial distribution and resulting overall force. The experiments were carried out in the large wave flume (GWK) of the Coastal Research Centre (FZK) in Hanover. Bullock et al. (2007) distinguished four types of impact on the structure depending on the different level of aeration under controlled conditions:

1. Slightly-breaking
2. Low aeration
3. High aeration
4. Broken

Slightly-breaking refers to a breaker condition between non-breaking waves and fully developed impacts characterised by a maximum quasi-hydrostatic pressure lower than $2.5\rho gH$. Usually this pressure value represents a threshold to distinguish loads in impact and non-impact cases. Extreme pressures can result in dimensionless values $p/\rho gH$ larger than 50 – note that the pressure (p) over the specific water weight ($\gamma = \rho g$) and incident wave height (H), i.e. the dimensionless pressure $p/\gamma H$, is usually

used as an indicator of the wave pressure impulsivity. Low and high-aeration conditions are those from are plunging waves impacting on the structure. Low-aeration are defined when the volumetric air fraction is less than about 5%. Although entrapment of air pockets were too small to detect individually, they produce a pressure time history with a single sharp peak as described by Oumeraci et al. (1993) for small air pocket. High-aeration impacts are characterised by a minimum volumetric air fraction of about 10% and they exhibit damped oscillations after the first pressure peak, similar to the large air pocket breaker described by Oumeraci et al. (1993). Broken impacts are equivalent to the breaker type previously described as turbulent bore.

2.2.1 Highest pressure peak

Typically broken waves with turbulent bores exhibit much smaller impact pressure when compared with plunging impacts. This is reasonable since those waves break far away from the structure and most energy is dissipated before reaching the structure (Goda, 1974; Oumeraci et al., 1993; Hull & Müller, 2002; Bullock et al., 2007).

Whilst the compressibility of the trapped or entrained air is often thought to dampen the shock pressure due to a cushion effect (Oumeraci et al., 1993; Hattori et al., 1994; Peregrine, 1994; Peregrine & Thais, 1996), researchers have so far given a somewhat contradictory picture about the question of which wave shape is responsible for the maximum pressure between plunging with small and large air pocket (Hull & Müller, 2002).

Kirkgöz (1982) found that a breaking wave with a front face parallel to the wall, without air entrapped at the instant of impact, produced the greatest shock pressures. Previous description suggests that this breaker should be close to the flip-through, although several investigations show that this impulsive breaker type has a lower maximum pressure when compared to plunging impacts (small or large air pockets). In fact Richert (1968), Partenscky (1988), Oumeraci et al. (1993) and Hattori et al. (1994) observed the most severe impulsive pressures when breaking waves hit the wall with a shape

somewhere between these two distinct forms: with trapped small air bubbles or a very thin lens shaped air pocket. However, Oumeraci et al. (1995a) and Hull & Müller (2002) have then found that the plunging with large air pocket resulted in the highest peak pressures. For Bullock et al. (2007) the possibility that high-aeration impacts are able to generate the most extreme pressures cannot be excluded. Further, both types of impact (low and high aeration) can generate pressures of a similar magnitude.

Bredmose et al. (2009, 2015), who completed the in-depth aeration investigation started by Bullock et al. (2007), modelled the air effects both analytically and numerically. Numerical simulations indicated that the maximum pressure is related to a breaker with entrapment of a small pocket of air (Bredmose et al., 2015).

However, maximum impact pressures are strongly affected by wave conditions (Bredmose et al., 2009) and the breaker shape at the wall depends on multiple parameters such as incident wave, slope, water depth, structure configuration, etc. Thus, it is reasonable to expect that small differences in setup could affect the breaker type responsible for the maximum dimensional load (p). Indeed, previous considerations concerning the highest load peaks were not found for High Mound Composite Breakwaters (HMCBs), which are characterised by large and steep mounds that cause a limited water depth at the toe of the vertical superstructure.

High Mound Composite Breakwater

Rubble breakwaters and vertical walls are the two most common coastal defence structures used in Europe. The former tend to dissipate the wave energy by breaking waves on the structure and they are usually located in the surf-zone i.e. where breaking occurs. Due to their trapezoidal configuration, they are economically disadvantageous in deeper waters and in these situations vertical walls (i.e. monolithic caissons) are typically adopted. However, it is good practice to dissipate the wave energy by reflecting the wave (non-breaking condition) when vertical walls are used. This is due to the difficulty in providing maintenance for these monolithic structures. As a consequence, the

water depth at the toe of the caisson is usually greater than 1.5 times the design wave height (Sainflou, 1928), note that the breaking tends to occur when the wave height reaches approximately the value of the water depth. The monolithic caissons can be located on the top of rubble mound foundations. These can have several purposes, e.g. to avoid excessively high caissons or to break the wave (reducing the water depth), as usually done in the Japanese design practice due to the fact that vertical walls are also constructed in the surf zone.

High Mound Composite Breakwaters have been more recently investigated by Muttray et al. (1998). A high mound breakwater consists of a rubble foundation which is larger than the foundation of a caisson breakwater but smaller than a traditional rubble mound breakwater. A monolithic superstructure which is much smaller than a typical caisson is placed on top of this foundation (Muttray et al., 1998). The high mound breakwater concept is very old (Takahashi et al., 1994). The Alderney breakwater (in the English Channel), built in 1890, is an example for an early high mound breakwater (Muttray et al., 1998).

Muttray et al. (1998) identify the advantages of high mound breakwaters as follows:

- the volume of the rubble material is smaller than for a traditional rubble mound breakwater;
- all armour units are placed below still water level (i.e. under the impact area), therefore a smaller block weight is required than for a rubble mound breakwater;
- the superstructure is much smaller than a traditional caisson breakwater.

Since armour units, mound and superstructure are smaller than for traditional breakwaters the construction is easier and the costs are lower. However, stability problems may arise from larger waves that impact on a comparatively small superstructure. Consequently, the breakwater development has moved from the high mound towards low mound composite breakwaters (Muttray et al., 1998).

As mentioned earlier, for traditional vertical breakwaters the highest load peaks are given by breakers close to the limit between slightly-breaking and breaking wave, i.e. when the wave breaks at the structure. In contrast, for HMCBs the critical load is given by breakers close to the limit between breaking wave and broken, i.e. for larger waves with the breaking point far from the structure (Muttray et al., 1998). This is due to the limited water depth, which allows breaking at the superstructure only for small plunging waves. As a consequence, larger waves break farther from the superstructure for the breaking criteria. Thus, although extreme waves can dissipate more wave energy due to the larger breaking distances, they are characterised by much larger wave heights and periods and, so, by larger amounts of energy when compared to the small plunging waves. Consequently, larger waves hit the superstructure with larger amounts of energy generating the extreme load peaks.

2.2.2 Regular waves and intrinsic random nature of breaking pressures

Most of the previous laboratory investigations were conducted using regular waves at small-scale (Hattori et al., 1994; Hull & Müller, 2002) or large (Oumeraci et al., 1993; Bullock et al., 2007). Although load characteristics gradually vary with the transition in breaker shape (Oumeraci et al., 1993; Hattori et al., 1994; Hull & Müller, 2002), investigators indicate how breaking pressures are extremely variable; even for waves of the same regular train. This is essentially due to the intrinsic random nature of air-water mixture that takes place during the breaking process (Bullock et al., 2007). In addition, breaking pressures are also strongly affected by small changes in wave kinematics that are influenced by previous wave train history. Bullock et al. (2007) highlight how impact pressure can result in one order of magnitude difference at the same location under nominally identical waves. This is because the extreme impact pressures are not only highly localised in time, but also in space (Bullock et al., 2007). As a consequence, impact pressures are poorly described by design formulae based on wave characteristics.

The wide variation in peak pressure was first addressed by Bagnold (1939) who noted that the pressure rise impulse was far more repeatable. The consistency of wave pressure impulse has often been expressed as an exponential relationship between the maximum impact pressure (p_{max}) and the rise time (t_r), i.e. the time for the pressure to rise to p_{max}, of the form:

$$p_{max} = a\,(t_r)^b \tag{2.1}$$

where a and b are empirical coefficients that assume different values due to the different experimental setup (Weggel et al., 1970; Blackmore & Hewson, 1984; Kirkgöz, 1990; Witte, 1990; Hattori et al., 1994; Bullock et al., 2001; Cuomo et al., 2011). This relationship is robust because, as Bagnold noted, the pressure impulse is limited: if p_{max} is large, then t_r tends to be small and *vice versa*. Consequently, the pressure impulse appears to be a more consistent feature of impact loading that the pressure maxima (Walkden et al., 1996).

2.2.3 Impact duration and pressure impulsivity

Extreme pressures related to small air pocket/low-aeration are characterised by very short rise time. Although high-aeration level does not always reduce the dimensional peak pressure when compared to low-aeration (Bullock et al., 2007), it tends to increase both rise time and total duration (Oumeraci et al., 1993; Hattori et al., 1994; Hull & Müller, 2002; Bullock et al., 2007). Therefore, in contrast with the maximum peak pressures, the pressure impulsivity (i.e. ratio maximum peak/impact duration) tends to decrease with air pocket thickness (Hattori et al., 1994) or with aeration level (Bullock et al., 2007). As a consequence, pressure records tend to show sharper peaks with decreasing breaking distance (Chan & Melville, 1988; Oumeraci et al., 1993).

The numerical simulations of Bredmose et al. (2015) confirm that increasing the level of aeration reduces the maximum impact pressure for all the four impact types de-

scribed in Bullock et al. (2007). Consequently, the pressure impulsivity decreases as the aeration level increases.

2.2.4 Overall force and impulse

In the previous sub-sections the breaking wave effects on local pressure measurements have been described. However, structural deflections depend on the overall wave impulse that acts on the whole structure. Consequently, a full characterisation on wave loading requires the spatial and temporal distributions of the overall force to be taken into account.

Spatial distributions

Different descriptions have been presented about the location of maximum pressure because the spatial distribution is irregular and variable for impacting waves, even for regular waves. Both Hattori et al. (1994) and Oumeraci et al. (1993) found that maximum pressure tends to occur at still water level (SWL), whereas Kirkgöz (1982) and Allsop et al. (1996a) found that it occurred at a higher elevation. An explanation for changes in the elevation of maximum pressure has been provided by Hull & Müller (2002) who suggest that the location of maximum pressure shifts from a position above SWL for a flip-through impact, to SWL for a breaker which traps an air pocket, to below SWL for a broken wave. This is confirmed also by Bullock et al. (2007). They found a sharp triangular distribution of maximum peaks (non-instantaneous) slightly above SWL. For high-aeration levels the triangular distribution tends both to enlarge and to centralise closer to the SWL. Broken impacts result in smoother and extended distributions with extreme pressures around or just below SWL.

Although broken impacts have generally been dismissed in considering critical load conditions, Bullock et al. (2007) indicate that this type of loading could well be of engineering significance because impact pressure could have much longer durations and tend to act simultaneously over larger impact areas.

Force peak

Although Oumeraci et al. (1993) identified the maximum force peaks (obtained by pressure integration) for small air pockets, several investigations found that high-pressures are generated over larger spatial extentions for large air pocket or high aeration level (Hattori et al., 1994; Kirkgöz, 1995; Hull & Müller, 2002; Bullock et al., 2007); therefore, these could result in greater forces. The theoretical-numerical studies of Bredmose et al. (2009) indicate the possible increase of force and impulse by the entrapment of air due to the increase in the spatial and temporal extent of the impact zone, even though the presence of air may reduce the magnitude of the maximum pressure.

Force time history

Oumeraci et al. (1993) pointed out how small and large air pocket breakers result in different temporal distributions. In particular, plunging with small air pocket are characterised by a single peak in the force time history due to the fact that pressure peaks occur almost simultaneously over the whole interface. In contrast, plunging with large air pocket present two distinct dynamic phases due to the hammer and compressed shock. Initially, the impinging breaker tongue (hammer shock) induces the first peak on a small impact area at higher elevations; immediately after the compressed large air pocket (compression shock) causes the damped high frequency oscillations. These oscillations are developed immediately under the first impact zone and they act on a larger area with longer duration. Consequently, these two distinct phases can result in a double dynamic peak in overall force signals (Oumeraci et al., 1993).

The extreme impact pressure can also have very short duration equal to 0.001 times the wave period (T). In addition, as already said, they are highly localised in space. Thus, whilst the structure could be locally damaged (Bredmose et al., 2009), the effects of these extreme local pressures on the structural deflection should be evaluated by integrating pressures over the whole interface in order to obtain the overall force acting on the structure.

Impulse

Bullock et al. (2007) analysed both dimensional maximum instantaneous force and impulse against the *momentum flux* (which will be described in Section 2.5.2); where maximum instantaneous force is obtained by integrating pressure measurements, whilst impulses are obtained by forces integrated over the load duration. They found trends that tend to increase with increasing *momentum flux*. However, the trend tends to be masked by a random variability for maximum instantaneous force; the scatter is much reduced with impulses.

It should be noted that spatial integrations are usually calculated by linear interpolations of a limited number of measurement points. As said earlier, even supposedly identical waves produce different spatial pressure distributions. Consequently, overall forces obtained by spatial integration tend to reflect the intrinsic random behaviour of pressure measurements.

2.3 Breaking waves on slender cylinders and analogies with plane walls

Except for the previous investigations on plane walls by Chan & Melville (1988, 1989), vertical or 'near' vertical walls were usually erected on the top of steep slopes and/or berms. Therefore, the water depth was not constant along the wave flume. As a consequence, the different breaking shapes, which are related to the breaking distance, were obtained by varying the wave inputs (H and T). This procedure was necessary because the wave height at the breaking point is constrained by the water depth value. In contrast, many offshore studies on slender cylinders have been carried out by locating the cylinder on a horizontal bottom. This has allowed investigation of the wave loading in a systematic and well-controlled manner by means of focused wave groups. Focused wave group is based on the concept of generating an extreme wave, at a known position and time, through the superposition of small amplitude linear waves of different frequencies. For many experimental investigation on slender cylinders, the same focused wave group (i.e. the same H and T) was simulated repeatedly by chang-

ing the focus point (i.e. the point where the extreme wave should break) or the location of the cylinder within the breaking region (Zhou et al., 1991; Chan et al., 1995). As a consequence, the different breaking shapes were obtained by supposedly identical wave conditions (i.e. H and T). In addition, thanks to the relatively small masses of slender cylinders, these have been often connected to force gauges[4] in order to obtain directly the overall forces on the 3D cylinder (avoiding in this way the inaccuracy related to the integration process of a limited number of pressure measurements).

As mentioned earlier, several investigations have been performed analysing breaking waves on vertical and slender cylinders (Tanimoto et al., 1986; Zhou et al., 1991; Chaplin et al., 1992; Chan et al., 1995; Wienke & Oumeraci, 2005) and the results are in broad agreement with those observed for vertical wall. Zhou et al. (1991) and Chan et al. (1995) comment that their results on cylinders are similar to those obtained on vertical plane walls by Chan & Melville (1988, 1989). Chan et al. (1995) listed the following similarities: peak pressure levels, impact pressure time scales, oscillatory characteristics of pressure after the occurrence of the peak pressures, and the overall vertical and temporal distributions of impact pressures.

2.3.1 Load impulsivity and breaking distance

Zhou et al. (1991) and Chan et al. (1995) studied the impact process at different cylinder locations within the region of wave plunging (i.e. from slightly breaking to broken). They found that pressure time histories are strongly affected by the cylinder location and, in particular, that magnitude peaks decrease with increasing breaking distance. In addition, they pointed out that maximum pressure peaks can be obtained over a narrow range (0.1-0.2 times the wavelength L[5] from the structure) rather than at one critical location.

[4] The force system, given by the structure model and force gauges, has a natural oscillation frequency. This depends on both rigidity and mass of the system. In order to avoid resonance effects, which affect the force time history, the system must be as light and rigid as possible.

[5] L is the distance between two successive points in the wave that are characterized by the same phase of oscillation.

Similar findings were reported by Wienke & Oumeraci (2005), who carried out laboratory experiments in the large wave flume (GWK) of the Coastal Research Centre (FZK) in Hanover. They analysed the wave load acting on a slender cylinder on a horizontal bottom using plunging breakers generated with focused wave groups (wave packets). Wienke & Oumeraci (2005) indicate that the overall force, obtained using two strain gauges, decreases as the breaking distance increases. As a consequence, they suggest a classification of loading cases based on visual evaluation on the breaking distance. In addition, they provided a dynamic load formula in order to calculate the maximum impact force (Section 2.4.1), which occurs when the wave breaks just in front of the cylinder. As shown in Irschik (2012), who confirmed the results of Wienke & Oumeraci (2005), strain gauges measurements (overall forces) do not exhibit the typical scatter exhibited by pressures (local measures), but quite clear tendency are shown when maximum force peaks are plotted against the breaking distance.

2.3.2 Variability and oscillation of pressure due to air

Despite the high variability in the peak pressures, both pressure time histories and spatial distributions are found to vary systematically depending on the cylinder locations within the wave breaking region (Zhou et al., 1991; Chan et al., 1995). The high variability of impact pressure is attributed to the presence of air entrapment during the impact process and the randomness of the trapped air dynamics (Zhou et al., 1991). Both Zhou et al. (1991) and Chan et al. (1995) pointed out that pressure oscillations were evident at elevations within the impact zone where air was entrapped during impact. Similarly, Wienke & Oumeraci (2005) discuss the presence of the air cushion between the cylinder and wave front to justify the difference between measured and theoretical predicted pressure.

Confirming the findings from vertical walls, Zhou et al. (1991) show that the impact pressure is highly localised in both space and time. Furthermore, Chan et al. (1995) identify in the pressure impulse (i.e. $\int p\,dt$) a quantity which is much more repeatable,

even if the peak pressure varied by more than 100%.

2.3.3 Wave run-up

Although the current Eddystone lighthouse has a tapered shape, considerations on wave run-up may be, to a first approximation, obtained from wind turbine investigations on vertical cylinders. One of the important issues in the design of offshore wind turbines is the wave run-up. Wave run-up on structures occurs when an incident wave hits a partially immersed structure and it is defined as the vertical distance from the mean water level to the maximum upward rush of water on the structure. Wave run-up is an important design parameter in offshore wind turbines because it is necessary to identify the free board from the turbine in order to ensure the efficiency and the stability of the structure. Although this parameter could have a minor importance in terms of the structure stability for rock lighthouses, it may however cause local damage when the superstructure (lantern) is proud of the tower. Typically, laboratory investigations indicate that the wave run-up tends to increase with decreasing wave steepness. However, an upper limit was identified in 2D situations on plane walls, for which the maximum run-up is up to 4 times the wave height in proximity of the structure (De Waal & Van der Meer, 1992). Numerical investigation of Andersen et al. (2011) showed that the highest run-up on vertical cylinders is caused by longer waves with higher crest velocities. Physical tests on cylinders by Christensen et al. (2005) showed that the run-up for nearly breaking/unstable waves is much higher than those for fully broken waves. De Vos et al. (2007) measured the run-up also around the circumference of the cylinder and they pointed out that the maximum run-up was at 45° to the incoming wave direction. This result was attributed to the fact that the run-up tongue for very high waves was thinner at the front side of the cylinder than at an angle of 45°.

2.4 Design practice of coastal structures

Because relatively little is known about the mechanism of breaker-structure interaction, many coastal structures are designed, at least in part, on the basis of small scale hydraulic model tests. This introduces laboratory effects that are difficult to quantify. The problem is particularly acute when the wave impact involves trapped and entrained air due to the fact that air is much more compressible than water (Blenkinsopp & Chaplin, 2007a, 2007b; Bredmose et al., 2009).

Several investigations have suggested that both small-scale tests and lower water salinity would tend to decrease aeration levels (Bullock et al., 2001; Bullock et al., 2003; Cuomo et al., 2010a; Blenkinsopp & Chaplin, 2011; Stagonas et al., 2011). As a consequence of lower aeration, peak pressures (scaled according to Froude scaling) would tend to increase and impact durations to decrease (Bullock et al., 2001; Cuomo et al., 2010a). The numerical simulations (at scale 1) of Bredmose et al. (2015) indicate that the Froude scaling of laboratory freshwater impact pressures leads to the prediction of unrealistic large full-scale pressures. Thus, they suggest that pressures below those predicted by the Froude law must be due to increased aeration rather than pure scale effects and that, in the absence of aeration, pressure significantly above the Froude-scaling level are possible.

2.4.1 Quasi-static and dynamic wave loads

The assessment of wave loads is usually categorised in three main types of wave attack, namely: non-breaking waves, breaking waves (i.e. plunging impacts) and broken. Well-established and reliable quasi-static load methods are available to determine the hydraulic force exerted by both non-breaking and broken waves. In contrast, breaking waves generate impulsive (high frequency) loads that require dynamic analyses in order to evaluate their effects on the structure (Allsop et al., 1996a, 1996b; Vicinanza, 1997).

Plane walls

Loads due to non-breaking or broken waves can be applied statically because they are considered pulsating loads (Allsop et al., 1996a, 1996b). There are different methods to estimate quasi-static wave forces on vertical or near vertical walls. One of the first models to calculate the spatial pressure distribution for vertical walls was given by Sainflou (1928). This analytical formulation, which is based on linear wave theory, can be only applied for standing waves, i.e. when the wave is completely reflected and breaking does not occur. Goda (1974) gave a semi-empirical formula that is the most widely used for the design of vertical walls. Contrary to the model of Sainflou, that of Goda is valid for both non-breaking wave and broken waves. Goda's formula, which provides a maximum pressure value of about 2.2 times the design wave height, was calibrated with different prototype breakwaters in Japan; the agreement was remarkable. Goda explained the absence of impulsive phenomena due to several reasons. First the mild Japanese sea beds decrease the occurrence of plunging wave. Moreover Japan's design practice recommends high mound that increase the occurrence of breaking and low caissons that allow the overtopping of the severest impacts. The original formula of Goda has subsequently been modified with coefficients that take into account slightly more impulsive loading and a different geometric configuration of the caisson (Takahashi et al., 1994; Goda, 2010). Goda (2010) also considers wave impacts in some detail.

In contrast, breaking waves produce much more rapidly-varying loads that cannot be applied statically because the natural oscillation frequency of the structure may be close to the frequency of the dynamic load. Therefore, these loads are more complex since that they require the dynamic response of the structure to be taken into account. As highlighted in the previous sections, impulsive loads due to breaking waves are difficult to predict due to the intrinsic random nature of wave pressure. However, the response of the structure to wave pulse excitation requires the definition of simplified spatial and temporal load distributions. Several formulations have been proposed in

order to estimate the dynamic load. Allsop & Vicinanza (1996) provided a relationship to estimate the magnitude of the horizontal force depending on the design wave height. For practical reasons the impact force history is typically reduced to a triangle and both rise time and total duration can be calculated with the method given by Oumeraci & Kortenhaus (1997). They provide a relationship of the rise time that depends on the relative impact force peak, water depth, berm configuration and on the breaker type; whilst the relationship of the total duration depends on the time rise and on the peak period of the wave. Due to the fact that the impact impulse is more consistent than one based only on the force peak, the following relationship proposed by McConnell & Kortenhaus (1997) has been found to closely represent the variability of wave impacts:

$$\frac{Fmax}{Fs} = a \left(\frac{t_r}{T}\right)^{-b} \tag{2.2}$$

where $Fmax$ is the maximum impulsive force, Fs is the quasi-static force, t_r is the rise time, T is the wave period, a and b are empirical coefficients. This dynamic formula is easily applicable since reliable methods exist for the evaluation of quasi-static force by Goda (1974), Oumeraci et al. (2001) and Cuomo et al. (2010b). Then, for plane walls, the spatial distribution is usually applied according to the model proposed by Hull et al. (1998). They suggest a bi-trapezoidal distribution with maximum peak at SWL.

Offshore slender cylinder

In contrast with plane walls, the wave interaction between waves and a circular cylinder is a three dimensional phenomenon. However, in offshore studies some simplification may be adopted. The cylinder is considered as a slender structure whenever the radius R of the structure must be much smaller than the wavelength ($R/L < 0.1$). In this condition, the diffraction and reflection phenomena can be neglected and the structure is defined 'transparent' because the wave does not change its height during the passage (i.e. the incident wave is equal to the transmitted wave).

In offshore situations, the total force due to breaking waves on a slender cylinder is the superposition of the slowly varying force (quasi-static component), proportional to the change of the water surface elevation, and the additional impulsive force (dynamic component) of short duration due to the impact of the breaker front and/or the breaker tongue.

The quasi-static wave forces below the impact zone at the wave surface are calculated by using a Morison force formulation (Morison et al., 1950), for a vertical slender pile on a uniformly sloping bottom. The so-called Morison equation gives the total force on a fixed cylinder, being the sum of two components: the drag force and the inertial one. Two coefficients must be defined as a function of the *Keulegan-Carpenter number* ($Kc = u \cdot T/\mathrm{D}$, where u is the horizontal velocity of the water particle, T is the wave period and D is the diameter of the cylinder); one for the drag force and the other for the inertial component. Usually the inertial and the drag forces are assumed additive in intermediate water. For small value of Kc the inertial component dominates, i.e. in deep water and for smaller wave heights; while for large numbers (turbulence) only the drag forces are important, i.e. in shallow water and for larger wave heights.

Chaplin et al. (1992) performed an in-depth laboratory investigation on breaking waves on vertical cylinders. Their laboratory tests, which were conducted at three different scales in order to obtain results free from scale effects, showed that the Morison's equation is unsuitable in predicting the breaking wave force at higher elevation of the cylinder because the impulsive peak force is larger and occurs earlier. As a consequence, Chaplin et al. (1992) provide a breaking load relationship based on the drag force component of the Morison's equation. In particular, they calibrated the value of the drag coefficient on the basis of the horizontal velocity profile measured at the cylinder in order to estimate the maximum force peak. Chaplin et al. (1992) expressed the maximum force in terms of drag component rather than the inertial component because for design purposes the magnitude of the velocity of the flow in breaking waves can probably be predicted with slightly more confidence than its acceleration.

The first attempt to provide a formulation for impact forces on cylinders was made by Von Karman (1929), who derived his formulation from theoretical considerations. In particular, Von Karman compared the impact situation to a falling cylinder that hits a water surface in order to apply the momentum theorem. Today the time dependent force formula of Von Karman is given in the following form:

$$F(t) = \rho\ \pi\ \mathrm{R}\ \mathrm{V}^2\ \Delta z\ (1 - t \cdot \mathrm{V}/\mathrm{R}) \tag{2.3}$$

where ρ is the water density, R the radius of the cylinder, V the water velocity at the instant of the impact and Δz is the vertical extent of the impact – note that the constant value π is known as slamming coefficient (Cs). Von Karman considers that the impact force has its maximum value at $t = 0$, i.e. in the beginning of the impact. Then, the force linearly decreases and it becomes zero at t =R/V, i.e. until the cylinder is half submerged into the water (Fig. 2.3).

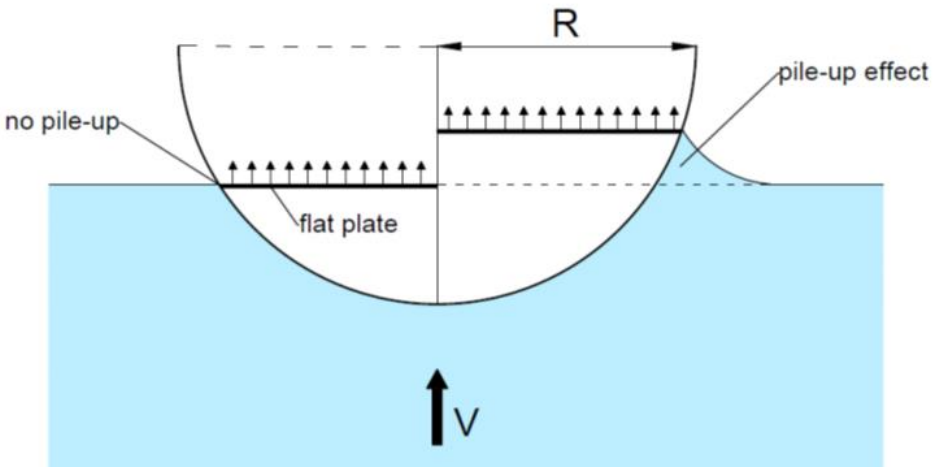

Figure 2.3: Left: no pile-up effect (Von Karman). Right: pile-up effect (Wagner).

Wagner (1932) grasped that the impact force are characterised by a large spike with very short duration due to the pile-up effect, which is a deformation of the water free surface. For this pile-up effect, the immersion of the cylinder occurs earlier. As a result, he believes that the duration of impact decreases and the maximum line force (flat

plate) increases (Fig. 2.3). Therefore, Wagner considered the maximum force at the beginning of the impact to be twice that of von Karman's value (i.e. setting $Cs = 2\pi$) and the impact time 0.43 times smaller. Consequently, the impulse of total force results 0.7 times the impulse calculated using Von Karman.

Several coastal investigations (Goda et al., 1966; Wiegel, 1982; Tanimoto et al., 1986; Wienke & Oumeraci, 2005) have modified the two theoretical relationships for coastal design problems by introducing an empirical coefficient (*curling factor* λ) in order to calibrate the extension of the impact area with the breaking wave height H_b. Starting from Wagner's formulae, Wienke & Oumeraci (2005) defined the impact height Δz equal to $\lambda\ \eta_b$, which represents the fraction (λ) of the maximum crest elevation ($\eta_b = 0.78 H_b$) over which the jet impingement acts (Fig. 2.4a). On the basis of strain gauge measurements, they estimated a curling factor $\lambda = 0.46$ for vertical cylinders. This value was determined at the severest impact condition, which occurs when the wave breaks immediately in front of the cylinder. As a consequence, it is assumed that the velocity V of the water jet hitting the cylinder reaches the value of the wave celerity c[6] at the breaking point; this assumption derives from the fact that when the velocity of the particle in the crest equals the celerity of the wave, the wave overturns and breaks. The impact force is then equally distributed along the vertical extent of the impact, i.e. $\lambda\ \eta_b$ (Fig. 2.4b). However, measurements obtained by Wienke & Oumeraci (2005) showed, after the maximum force peak, a strong oscillation (extended for approximately 2 seconds) due to resonance effects of the cylinder. Therefore, force measures were only used just to obtain the maximum load peak; measurements of the impact duration were determined by using pressure transducers located around the cylinder (in order to evaluate the time taken by the water jet to submerge the half section of the cylinder). Thus, Wienke & Oumeraci (2005) estimated an impact duration equal to 0.4 R/V and they provided a composite force time history obtained on the basis of a pressure time history.

[6]The wave celerity c is equal to L/T.

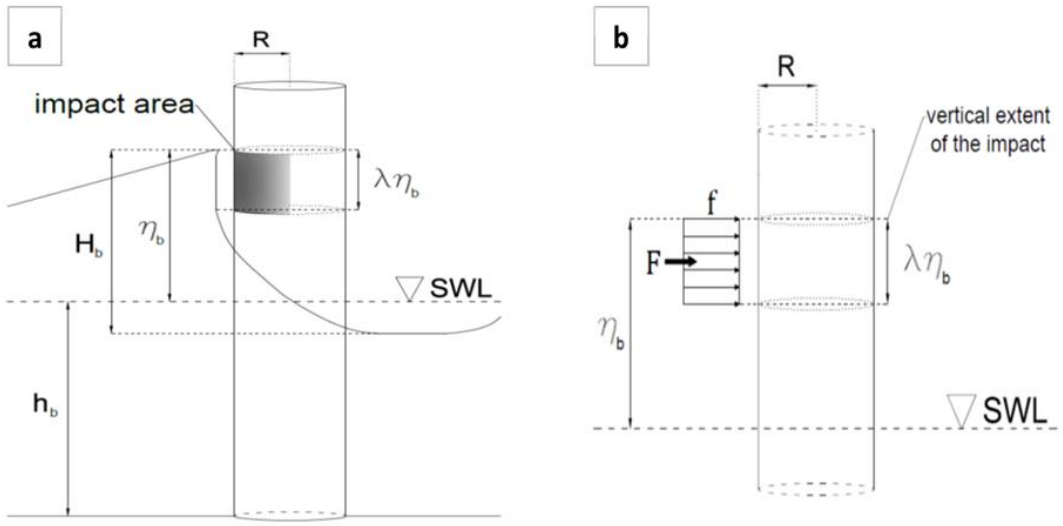

Figure 2.4: Load distribution on a slender cylinder proposed by Wienke and Oumeraci (2005): (a) elevation of the impact area and (b) uniform spatial distribution.

2.4.2 Breaker type prediction on coastal defence structures

Although the magnitudes of impact loads are not predictable, the breaker type can be predicted. One of the first design guides was given by Goda (1985). He described a number of rules to identify whether particular combinations of wave conditions, bottom slope, mound and vertical wall profiles cause a risk of impulsive wave condition. However, this qualitative procedure was built on the results of experimental tests conducted with regular wave trains. Instead, in nature waves travel in groups with different heights and periods, so that the first breaker of a group will be preceded by a non-breaking wave as suggested by field observations (Hull & Müller, 2002). A random sea-state includes typically 200-300 waves, generated by a rather stationary wind event (approximately 30-40 minutes). Because of the random nature of natural waves, a statistical description of the waves is normally used. In deep water, the individual wave heights of the random sea-state tend to be described by the Rayleigh-distribution. Several wave statistics ($H_{1/3}$, $H_{1/10}$, $H_{1/100}$, $H_{1/250}$) are calculated based on this distribution. They are defined with a ratio ($H_{1/n}$), which represents the mean of the waves included in the highest $1/n$ of the waves, related to the time-series of the sea state (time do-

main). Typically, the significant wave height ($H_s = H_{1/3}$) is the most used wave statistic to characterise the random sea state. Over the ratio $1/3$ and this included, the statistical wave periods tend to coincide with the significant wave period ($T_s = T_{1/3}$), i.e. $T_{1/3} \simeq T_{1/10} \simeq T_{1/100} \simeq T_{1/250}$. On the basis of the spectrum (frequency domain), the peak period (T_p) is often used in coastal structure studies because it represents the wave period with the highest energy. In the frequency domain, H_s is referred to as H_{m0}.

Based on data from a series of small-scale irregular wave tests completed at HR Wallingford, Allsop et al. (1996c) suggested a parameter map for prediction of the breaker type on vertical walls and composite breakwaters as a function of structure geometry (length and height of the berm) and wave conditions (wave height, wave period and water depth). The parameter map was further tested against a wide range of data within the PROVERBS (Probabilistic Design tools for Vertical Breakwaters) project including large scale model tests. Then, a modified version of the parameter map was proposed by Kortenhaus & Oumeraci (1998). The parameter map, which is an easy-to-use guidance for the type of wave loading to be expected on mild slope (<1:50) and for random sea-states, identifies the breaker types as quasi-standing, slightly-breaking, impact and broken (Fig. 2.5). These four possible loading cases were classified adopting a mix of probabilistic procedures and video observations. Impact type was defined on the base of the subjective definition proposed by Kortenhaus & Löffler (1998), i.e. when the force event causes a dynamic peak (F_{max}) 2.5 times higher than the hydrostatic one (F_s) (Fig. 2.5).

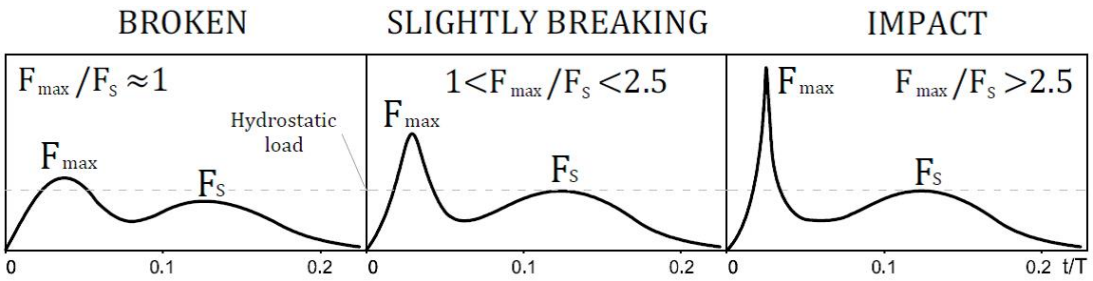

Figure 2.5: Load classification for the several breaker types of the parameter map.

When load cases result in quasi-standing, slightly-breaking or broken, the design forces can be applied statically because they are considered pulsating loads. In contrast, the impact type requires the dynamic analysis. The impact type includes flip-through, plunging with small air pocket and plunging with large air pocket.

The parameter map identifies impact type but it does not say how many of the waves approaching the structure will break at the wall (thus causing impulsive forces) and how many will not break at the wall (inducing non-impulsive Goda type forces). It is possible to calculate the probability of occurrence of both breaking and broken waves using the method suggested by Calabrese & Allsop (1997). The method is based on the idea that every wave with a higher wave height than the breaking wave height at the structure is already broken or will break as an impact breaker at the wall. The breaking wave height at the structure is calculated with the formula given by Calabrese (1997) based on extensive random wave tests and previous theoretical work (Oumeraci et al., 1993). The breaking formula of Calabrese (1997) depends on both wave parameters (wave height, period and water depth) and properties of the structure (berm and reflection coefficient). The breaking occurrence is regarded as a filter in the impact domain of the parameter map. For very low percentages of impacts (smaller than 1%) the problem can be reduced to the quasi-static problem and the Goda method can be used to calculate wave forces. In all the other cases the magnitude of the horizontal force can be calculated with the different methods previously described (Allsop & Vicinanza, 1996; McConnell & Kortenhaus, 1997; Oumeraci & Kortenhaus, 1997; Hull et al., 1998).

However, the parameter map is only valid for seabed slopes less than $1:50$. As a result, the parameter map is not useful for steep slopes, where rock lighthouses are built. According to Goda (2010), steep slopes increase the occurrence of plunging impacts and several investigations have already demonstrated that they tend also to increase the wave celerity (Wiegel, 1982; Tanimoto et al., 1986; Kyte & Tørum, 1996) and the wave force (Kirkgöz, 1995; Buccino et al., 2012). In addition, steeper slopes tend to cause an even more significant increase in wave height at breaking point and moreover

waves do not break until quite near to the shore (Allsop et al., 1998; Goda, 2010).

2.4.3 Structural response in dynamic analysis

Structural deflection is caused by an impulse[7] related to the wave i.e. it is depends on the combinations of both peak of the force and its time duration. The impulsivity[8] of the load is related to the way in which the load acts on the structure and, in particular, it is related to the rapidity of the load. The load is defined as impulsive when it has a short time duration or, to be more precise, when the load frequency is higher than the lowest natural frequency of the structure.

The dynamic response of a structure is strongly affected by the impulse duration of the dynamic force. This is easily verifiable through the frequency response of a simple system with a single degree of freedom. The same force magnitude produces different displacements for different impulse durations. In particular, the dynamic displacement increases with increasing impulse duration if compared to the static displacement given by the same force magnitude. Conversely, it decreases with decreasing impulse duration and it tends to zero for very short durations (Clough & Penzien, 1975).

Although for traditional coastal structures it is generally accepted that maximum wave loads are caused by impulsive impacts, the importance of impact duration and total impulse should not be understimated (Kirkgöz, 1990; Bullock et al., 2007). However, very few studies have considered the dynamic response of structures under breaking waves. This might be undertaken with accelerometers, which provide acceleration data, or with geophones, which provide velocity data. Such a structural response depends on both the characteristics of the structure (natural frequencies and geometrical configuration) and the external wave load (temporal and spatial variation of the force).

In this regard, Kirkgöz (1990) found that the longer-lasting low impact forces were more effective in producing the larger wall deflections. Manjula et al. (2014) used accelerom-

[7] The impulse is the product of the force for the time i.e. the integration of the force in the time.

[8] The ratio of the maximum force peak to the impact duration is usually used as an indicator of the impulsivity of the load.

eters in their laboratory tests in order to investigate the effect of breaking waves on the dynamic response of a slender cylinder. They found that maximum structural deflections were not related to the extreme force events, suggesting that the impulse should have more importance than the violence of the impact. For their part, Loraux (2013) and Chollet (2014) combined numerical modelling and geophone data obtained from the Jument lighthouse in France. These numerical investigations indicated that the structural response is strongly affected by the nature of the impulse. In fact, Loraux (2013) found that equivalent instantaneous forces (maximum value) caused different responses depending on the extent of the load duration. In particular, he demonstrated that impulses characterised by shorter impact durations resulted in higher structural acceleration but lower deflections when compared to those caused by longer impact durations. As a consequence, higher accelerations of the structure do not necessarily lead to the largest displacements. Also, the contribution of higher frequencies also increases when the impulse is quicker i.e. for higher impulsivity. Consequently, the frequency of the signal decreases as the load duration increases (Loraux, 2013).

2.5 Coastal processes and wave parameters

Waves are affected by transformations when they propagate from deep to shallow water. In first instance, the decrease in water depth (h) leads to a decrease of the wave length L and the variation of the offshore wave height H_o. Because wave data are typically collected from offshore buoys, it is necessary to propagate the wave from deep water to shallow water since the local local wave height $H_{(h)}$ is the main input variable in the design of depth-limited structures. The estimation of the local wave height is usually determined in the water depth at the seaward toe of the structure (h_s).

A few design methods (Goda, 1974, 1975; parameter map) adopt as inputs wave statistics determined offshore. The predicted outputs are directly calibrated through empirical investigations for a range of simple bed slopes or structure configurations. The best-known examples are methods developed by Goda (1974, 1975) to predict forces

and overtopping on vertical walls which use a single equivalent sea bed slope (α). Such methods assume that each approach bathymetry may be represented by a simple bed slope, and that the empirical prediction methods fully represent the effects of different wave transformations on the response of interest.

Usually the hydraulic variables are combined to form dimensionless wave parameters which helps reduce the number of independent variables. The following are the three basic dimensionless wave parameters:

- h/L: Relative water depth
- H/L: Wave steepness
- H/h: Relative wave height

Water depth conditions (deep, intermediate and shallow water) are categorised on the basis of the linear theory (Airy) by means of the relative water depth h/L.

2.5.1 Regular waves and wave transformations

Decrease of the wave length

As said above, the decrease of the depth implies the decrease of the wave length. The linear dispersion relationship relates the wave period T and the local wave length L, at the generic depth h, with the following expression:

$$L = L_o \tanh(kh) = \frac{gT^2}{2\pi} \tanh(kh) \tag{2.4}$$

where L_o represents the wave length in deepwater ($h/L > 0.5$) and k is the wave number ($2\pi/L$).

Breaking limit for wave steepness

The wave transformations involve several phenomena which are not present offshore.

In deep-intermediate water, the primary cause for wave breaking is that the wave steepness exceeds the fundamental limit given for individual waves by:

$$(H/L)_{max} = 0.142 \tag{2.5}$$

Wave propagation and coastal phenomena

During the wave propagation from deep to shallow water ($h/L < 0.05$), the main processes of interest in wave transformations may be divided into two groups. The first group includes processes of wave transformations up to, but not beyond, the point of breaking. These are refraction, diffraction and, above all, shoaling. These phenomena are essentially reversible and they do not involve significant loss of energy. In contrast, the second set of processes are those which occur from breaking onwards. The breaking process involves significant loss of energy and is not reversible. The decreasing depth as the wave moves shoreward causes wave height transformation (shoaling), whilst the topography configuration can generate effects that alter the direction and the characteristics of the wave (refraction, diffraction, reflection).

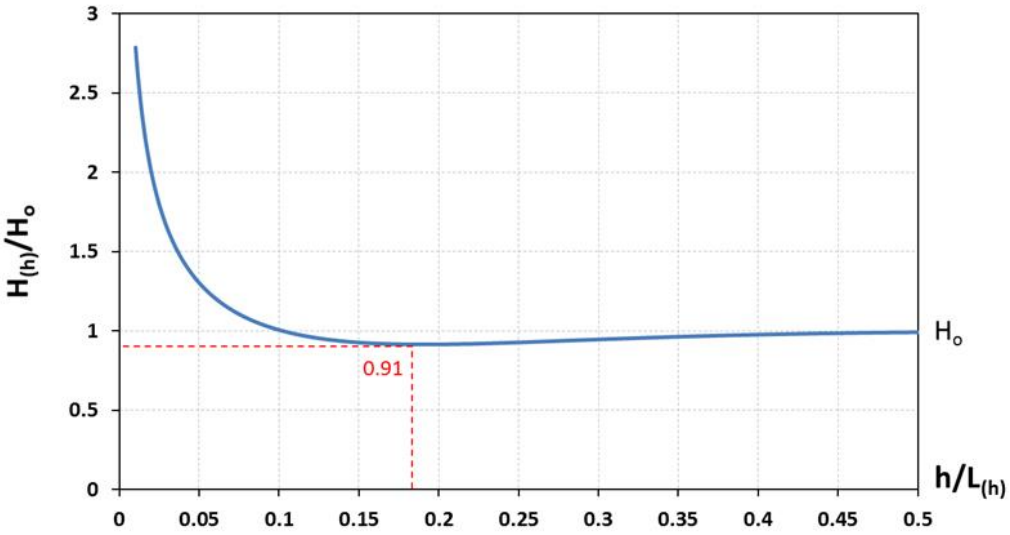

Figure 2.6: Shoaling curve: regular wave height variation that occurs during wave propagation (linear theory of Airy). Note the ratio H_h/H_o reaches a minimum value of 0.91.

When slopes are not very steep (lower than 1:10), wave shoaling is relatively slow, and the variation of the offshore regular wave height (H_o) is reasonably well understood and easily calculable with theoretical formulae (CEM, 2003), as shown in Figure 2.6; but steep bed slopes transform waves quickly and give more severe hydraulic and structure responses. Typically, slopes milder than 1:50 are indicative of shallow sand beach slopes; 1:30 and 20 are indicative of steeper sand beaches, whilst 1:10 and 1:7 are indicative of rock coasts and shingle beaches (Allsop et al., 1998).

Breaking limit for wave height

The wave height cannot tend to infinity, as implied in Figure 2.6, because the wave breaks in shallow water. For very shallow bed slopes, usually taken as flatter than 1:100, it is often assumed that a simple breaking limit to the individual wave height relative to local water depth may be given in shallow water as approximately:

$$(H_{max}/h) = 0.78 \tag{2.6}$$

In analysing laboratory regular data for slopes steeper than 1:100, breaking conditions do not exhibit any systematic dependence on wave height; but the breaking is strongly influenced by both wave steepness (H/L) and slope (α). In particular, waves of large steepness begin to break as they travel up a slope, before they attain further appreciable increase in wave height by shoaling and moreover they do not break until quite near to the shore (Weggel, 1972). Contrary, lower wave steepnesses (H/L) show more shoaling, reach a greater wave height (i.e. a greater breaking limit H_b/h_b) and break earlier. Moreover, the breaking limit of the relative wave height (H_b/h_b) increases with increasing bed slope (α).

The relative breaking distance ($d = x/H_b$) assumes a predominant role in terms of wave loading on the structure. Therefore, the breaking limit (H_b/h_b), when related to the slope (α) and to the value of the water depth at the toe of the structure (h_s), represents the main parameter that regulates the wave loading characteristics.

Breaker violence and wave kinematics

The wave steepness (H/L) and the relative water depth (h/L) have, however, a significant effect on wave loading. The wave steepness (H/L) is an index of breaker violence, which in combination with the slope of the seabed (α) determines the type of breaker (spilling, plunging, collapsing and surging) through the well-known *surf similarity parameter* or *Iribarren number* (Section 2.5.1).

The relative water depth (h/L) strongly affects the wave kinematics prior to breaking and, so, its influence on the dynamic response of a structure should not be neglected. It implicitly takes into account the effects of the wave period and is mainly used to distinguish the water depth conditions (deep water, intermediate and shallow water) and the celerity of the wave ($c = L/T$).

Wave-structure interactions and coastal relationships

The major advantage of laboratory experiments over field measurements is the control over wave characteristics in order to understand the influence of the various hydraulic variables (H, T and h) on the structures during the load process. Typically, coastal relationships use one or, at most, two of the three basic wave parameters (H/L, H/h and h/L). Two of the most used coastal relationships are the *Iribarren number* and *momentum flux*. The *Iribarren number* is indicative of wave steepness and it allows the estimation of the breaker type on uniform slope; whilst the *momentum flux* is more indicative of the wave kinematics, as suggested by Hughes (2004a).

2.5.2 *Iribarren number*

One coastal parameter of proven usefulness when describing wave processes on beaches and at coastal structures is the *Iribarren number*, also known as the *surf similarity parameter* (Battjes, 1974a). This parameter, which relates the wave steepness to the slope, was developed to describe the occurrence of regular wave breaking on beaches. Iversen (1952) proposed the first breaker classification (spilling, plunging and

surging) which was developed on three slope values (1:10, 1:20 and 1:50) and used a linear relationship of the deepwater wave steepness. Then Galvin (1968) extended the investigation on another sloping beach (1:5, 1:10 and 1:20) and he identified a fourth breaker shape (collapsing). Today the breaker classification is defined according to the *surf similarity parameter* proposed by Battjes (1974a). He calculated the deepwater wave steepness under square root similarly to Hunt & Ira (1959). Usually, two *surf similarity parameters* are defined:

$$\xi_o = \frac{\tan\alpha}{\sqrt{H_o/L_o}} \quad \text{or} \quad \xi_b = \frac{\tan\alpha}{\sqrt{H_b/L_o}} \tag{2.7}$$

where H_o is the wave height in deep water (before wave transformation due to shoaling), H_b is the value of the wave height at the break point in shallow water; whilst L_o is the offshore wave length and α is the slope of the seabed. As suggested by Battjes (1974a), the two parameters are called *Iribarren number* in honour of the first author who combined the wave steepness and the seabed slope (Iribarren Cavanilles & Casto Nogales, 1949).

The transition of the four breaker types is gradual and without distinct dividing lines. Table 2.1 shows the different ranges used to identify the four different breaking types on the basis of ξ.

Table 2.1: Approximate range of the breaker types

Breaker type	**Range** ξ_o	**Range** ξ_b
Spilling	$\xi_o < 0.5$	$\xi_b < 0.4$
Plunging	$0.5 < \xi_o < 3.3$	$0.4 < \xi_b < 2.2$
Collapsing-Surging	$\xi_o > 3.3$	$\xi_b > 2.2$

- **Spilling**: this is wave breaking that occurs for excessive steepness of the wave

(Fig. 2.7). The wave crest becomes unstable and cascades down producing a foamy water surface. It is a weak form of breaking in which the wave gradually dissipates its energy.

- **Plunging**: this is a violent breaker caused by a combination of a steep wave that moves on an inclined slope (Fig. 2.7). The wave is affected by the bottom that regulates the transformation of waves from deep to shallow water. In particular its length L decreases and its height H may increase, causing the wave steepness H/L to increase. In this way the crest curls over the shoreward face of the wave, resulting in a plunging jet with associated splashing.

- **Collapsing**: for this breaker the break point is on the slope (Fig. 2.7). In particular the crest remains unbroken while the lower part of the shoreward face steepness and then falls, producing an irregular turbulent water surface.

- **Surging**: this breaker tends to happen when the steepness of the wave is very gentle (Fig. 2.7). The crest remains unbroken and the front face of the wave advances up the slope with minor breaking.

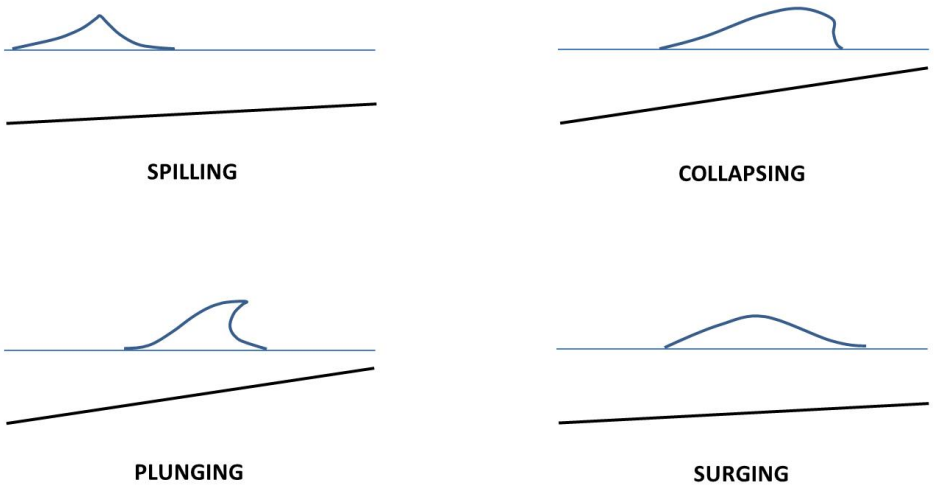

Figure 2.7: Wave shapes of the different breaker types on plane beaches.

Spilling and plunging are characterised by similar deepwater wave steepnesses (relatively high), but different slopes. When the slope is mild, the shoaling is slow and consequently the wave breaks softly as a spilling breaker. In contrast, a violent plunging wave is only generated in presence of steeper slopes. Collapsing is a particular breaker, which breaks on the slope, given by the combination of large waves approaching a steep beach. Finally, surging breakers are gentle waves which tend to be totally reflected (standing waves) if the slope is completely vertical (walls).

Furthermore, Figure 2.8 highlights how the combination of the wave steepness (alternatively formulated as H_b/gT^2) with the slope, and hence indirectly the Iribarren number, regulates the wave transformation and in particular the relative wave height limit at breaking point (H_b/h_b).The relative wave height at breaking, or breaker depth index, increases with slope and milder wave steepness.

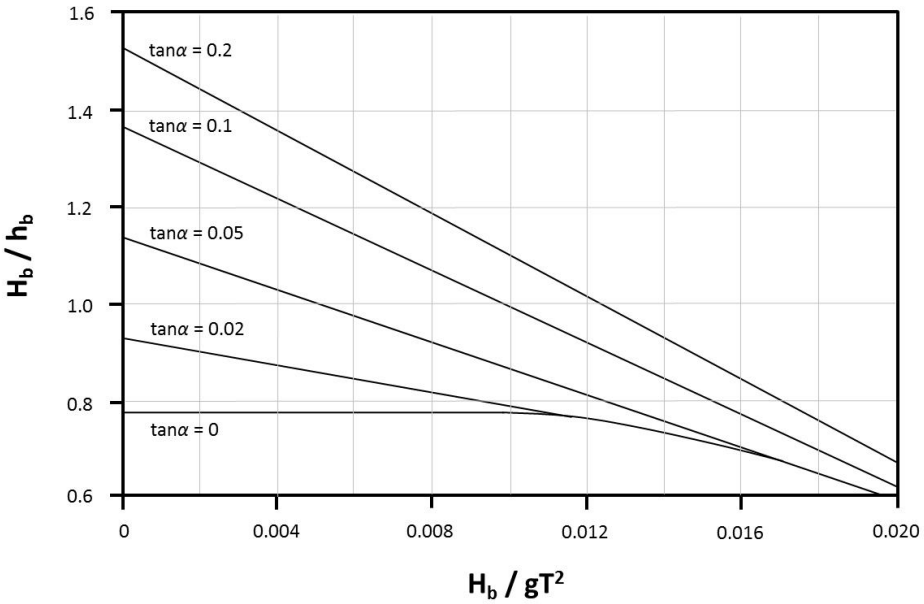

Figure 2.8: Breaker depth index as a function of wave steepness H_b/gT^2 (Weggel, 1972).

Criteria based on the *Iribarren number* have not proved successful in the identification of different breaker shapes on vertical walls, where the presence of a berm reduces

suddenly the water depth and the breaking can be accelerated or delayed due to the high reflection of the vertical walls (Oumeraci et al., 1993). Similarly, the *Iribarren number* was found unsuitable for the description of breaker types on submerged reefs, where the water level over the crest affects the breaking waves (Blenkinsopp & Chaplin, 2008).

Recapping, the *Iribarren number* describes:

- the breaker type;
- the wave steepness and hence the violence of the wave;
- the wave transformation and the breaker depth index (H_b/h_b).

2.5.3 *Momentum flux*

Hughes (2004a) suggests that the *Iribarren number* may be not the best parameter to describe flow kinematics because local water depth is not included. Thus, while different combinations of H/h and h/L yield the same value of deepwater wave steepness, the wave kinematics will be different. Consequently, Hughes (2004a) considers the *momentum flux* as the property of progressive waves which most closely relates to force loads on coastal structures. For this reason, he describes the wave momentum flux as a "compelling wave property" for characterising waves in the near shore region, and potentially, for relating waves to response of coastal structures due to wave loading.

The instantaneous flux of horizontal momentum (m_f) across a unit area of a vertical plane oriented parallel to the wave crests is given by:

$$m_f(x,z,t) = p_d + \rho u^2 \tag{2.8}$$

where p_d is the instantaneous wave dynamic pressure at a specified elevation; u is the

instantaneous horizontal water velocity at the same elevation and ρ the water density.

For wave loading on structures, it is logical to consider the maximum depth-integrated wave momentum flux that occurs during the passage of waves, i.e., the maximum of

$$m_{f,int}(x,t) = \int_{-h}^{\eta(x)} (p_d + \rho u^2)\, dz \tag{2.9}$$

that occurs at the wave crest when $\eta(x) = a$. The wave surface (η) is measured with respect to the mean water level ($z = 0$) and the amplitude of the wave (a) coincides to $H/2$ for a linear wave. Using linear (Airy) wave theory and with appropriate substitutions, it is possible to obtain the following nondimensional maximum depth integrated (from the bottom up to still water level) wave momentum flux.

$$M_f = \left(\frac{m_{f,int}}{\rho g h^2}\right) = \frac{1}{2}\frac{H}{h}\frac{\tanh kh}{kh} + \frac{1}{8}\left(\frac{H}{h}\right)^2\left[1 + \frac{2kh}{\sinh 2kh}\right] \tag{2.10}$$

For convenience, Equation 2.10 will be referred to as simply the "*momentum flux*".

As is shown in Equation 2.10, the momentum flux depends on two of the three basic wave parameters: relative wave height (H/h) and relative water depth (h/L) through kh ($kh = 2\pi h/L$). Then the wavelength L is expressed through the wave period T, at the generic depth h, with Equation 2.4.

As may be seen in Figure 2.9, the momentum flux increases with increasing relative wave height H/h and/or with decreasing relative water depth h/L. Equivalently, it means that the momentum flux can increase if:

- H increases;
- T increases;
- h decreases.

Consequently, due to the fact that the *momentum flux* is related to H and T but inversely

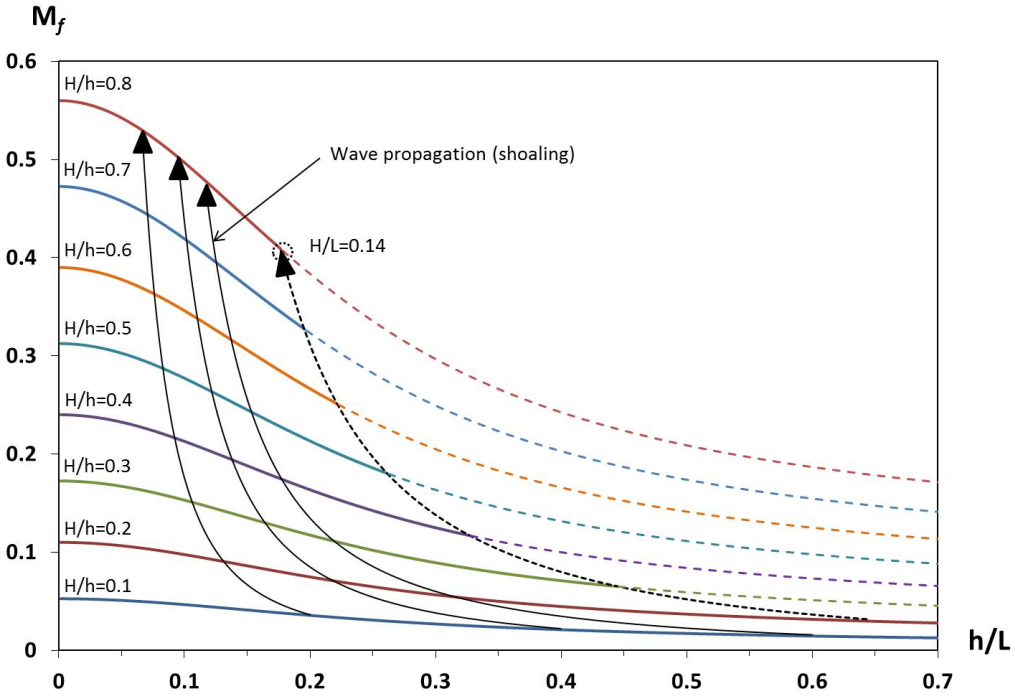

Figure 2.9: Wave momentum flux parameter versus relative water depth (linear wave theory according to Airy).

related to h, it may be considered as a breaking distance indicator. In particular, once the depth section is fixed (where h is determined) the breaking point moves seawards (i.e. in deeper waters) with increasing *momentum flux*. However, the previous affirmation is strictly true in ideal conditions i.e. assuming depths that decrease uniformly to the shore and excluding secondary phenomena (reflection, refraction, diffraction, breaking). These phenomena, which can be caused by wave-structure interactions or 3D effects, could accelerate or delay the breaking. Black curves in Figure 2.9 show how the *momentum flux* varies due to the shoaling phenomenon that occurs during the wave propagation. As may be observed, the *momentum flux* increases when waves move from deeper to shallower waters. The dashed black line (Fig. 2.9) is the wave propagation curve related to an extreme wave steepness limit reaching the following value $H/L = (H/h) \cdot (h/L) = 0.14$.

Equation 2.10 indicates that the momentum flux relationship is given by the sum of two components. The first factor is the gravitational term (related to pressure component

p_d), whilst the second factor is the kinematic term of the momentum flux (related to the velocity component ρu^2). The gravitational component dominates the kinematic one (Fig. 2.10). Moreover, the gravitational component tends to be predominant for lower values of the relative wave height. As may been observed in Figure 2.10, when $H/h < 0.4$, in shallow water ($h/L < 0.05$), the kinematic component is lower than $1/4$ of the gravitational component. Therefore, the contribution of the kinematic component tends to increase with increasing of H/h and hence with increasing of M_f.

Similarly, the wave celerity increases with increasing of the wave period T and hence with increasing of M_f. Furthermore, an increase in the wave height H and/or wave period T, results in an increase of M_f, and implies an increase in the mass of water involved.

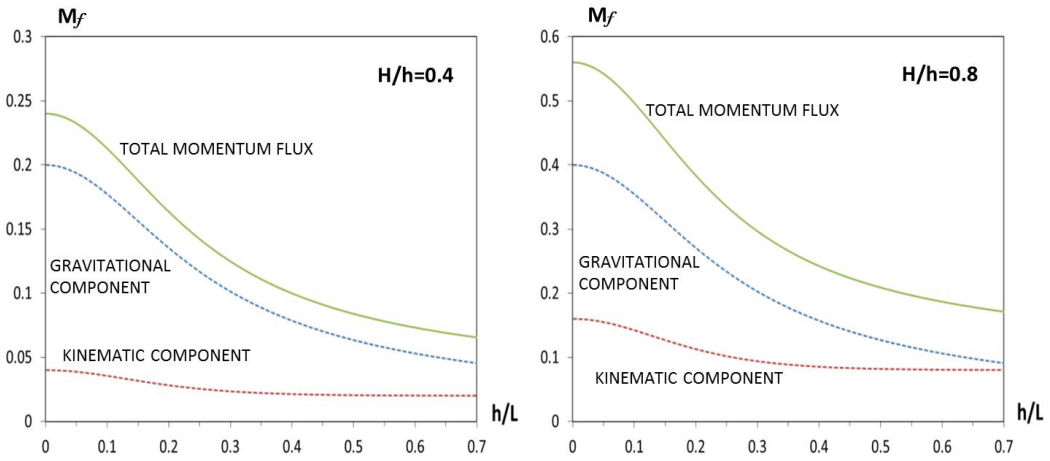

Figure 2.10: Gravitational and kinematic components of the momentum flux for $H/h = 0.4$ (left) and $H/h = 0.8$ (right).

Recapping an increasing of the *momentum flux* tends to increase:

- the breaking distance;
- the kinematic contribution;
- the amount of water mass involved.

2.5.4 Coastal parameters in irregular wave conditions

All coastal processes described above occur also in irregular wave conditions. However, the identification of clear wave limits is more complicated in part due to the fact that a random sea state encompasses a wide range of different waves.

Usually, irregular breaking limits are provided on the basis of the significant breaking wave height ($H_{s,b}$) (Ostendorf & Madsen, 1979; Owen, 1980; Singamsetti & Wind, 1980; SPM, 1984; Goda, 1974, 2010; Hansen, 1990; Kamphuis, 1991; Allsop et al., 1998). Goda (1974, 1975) developed two different prediction methods estimating both significant ($H_{s,b}$) and maximum ($H_{1/250,b}$) breaking wave conditions.

Incident wave acting on the structure

In real situations, the structural response of a rigid structure is not only affected by the local wave height $H_{(h)}$, but it is caused by an incident wave that depends on many variables, e.g.:

- Hydraulic
  - Wave height
  - Wave period
  - Water depth at the toe of the structure
  - Water current
- Bathymetric
  - Slope
  - Topography configuration
- Structural
  - Freebord and ratio structure width/wave length

- Berm
- Natural frequency

The presence of the berm, which is usually at the base of vertical walls, modifies the wave transformation of the incident wave close to the structure and, moreover, it can also cause breaking. The incident wave is also affected by reflection which tends to increase for highly reflective structures (vertical and no overtopping) and not wide structures (structure width/wave length > 0.1).

The effects of random sea states on wave-structure interactions have been often analysed by means of experimental tests. Although the coastal relationships were originally defined using regular wave parameters, both the *Iribarren number* (De Waal & Van der Meer, 1992; Van der Meer, 1988; Muttray et al., 1998) and the *momentum flux* (Hughes, 2004b; Melby & Hughes, 2004) have demonstrated useful application under fully random conditions. The following sections will explain how thsee relationships are usually used in random sea-state investigations.

Iribarren number for irregular waves

Several random wave investigations have adopted the *Iribarren number* for beach processes. The regular wave variables were substituted with mean and significant values of wave height and wavelength, both calculated in deepwater (Battjes, 1971; Holman, 1986; Mase, 1989; Mayer & Kriebel, 1994). In particular, Mase (1989) compared his laboratory results, obtained from four different slopes ($1:5$, $1:10$, $1:20$ and $1:30$), with several field investigations of random wave run up on natural beaches (Huntley et al., 1977; Guza & Thornton, 1982; Holman, 1986).

Although appropriate physical justifications are not always provided, the *Iribarren number* has often been identified as a good predictor parameter in several design applications for which it is necessary to describe irregular waves. In particular approaches are provided for the hydraulic design, including run up, overtopping, wave reflection

(Battjes, 1974b; Ahrens, 1981; Seelig, 1983; Allsop & Hettiarachchi, 1988; De Waal & Van der Meer, 1992; Van der Meer & Janssen, 1995; Muttray et al., 1998), and for the structural design of rubble breakwaters (Van der Meer, 1988). Statistical wave parameters are substituted into the empirical relationship showed in Equation 2.7 and several formulations are provided. Typically, it is possible to find the two following formulations:

$$\xi_{o,m} = \frac{\tan\alpha}{\sqrt{H_s/L_{o,m}}} \quad \text{or} \quad \xi_{o,p} = \frac{\tan\alpha}{\sqrt{H_s/L_{o,p}}} \tag{2.11}$$

where the deepwater wave length $L_{o,m}$ is calculated using the mean wave period T_m, whilst the deepwater wave length $L_{o,p}$ is calculated using the peak period T_p. In design applications α represents the slope geometry of the structure. Then the wave height is generally calculated with the significant wave height H_s. In design applications, where it is necessary to define an accurate design value, the significant wave height is calculated at the toe of the structure for allowing a generalisation of the relationship for any seabed. Therefore, the designer must define the effects of the wave transformation avoiding under/over-design. Consequently, the wave steepness H_s/L_o, defined also as s_o, is a fictitious wave steepness because it is the ratio between a statistical wave height at the structure and the representative deepwater wavelength. Generally, the structure design is performed on the basis of the peak period.

Momentum flux of Hughes for irregular waves

Linear wave theory neglects the effects of non-sinusoidal forms typical of nonlinear shallow water waves. This omission becomes more accentuated as the wave approaches its limiting relative wave height (H/h). Therefore, Hughes (2004a) suggests the following empirical equation, derived from regular waves and applying Fourier approximation wave theory, in order to estimate the dimensionless maximum wave momentum flux for irregular waves.

$$M_F = A_o \left(\frac{h}{g{T_p}^2} \right)^{-A_1} \tag{2.12}$$

where

$$A_o = 0.64 \left(\frac{H_{s,o}}{h} \right)^{2.02} \quad \text{and} \quad A_1 = 0.18 \left(\frac{H_{s,o}}{h} \right)^{-0.39} \tag{2.13}$$

Hughes (2004a) suggests that the above relationships are a reasonably representative estimation of the maximum wave momentum flux for an irregular wave train. He identifies *momentum flux* as a good descriptor for nearshore processes. In particular he believes that the wave momentum flux parameter should provide a better characterization of the wave-structure interactions and lead to better response correlations. However, it should be noted that, whenever the *momentum flux* is strictly used to quantify wave forces, the breaking dissipates energy but not *momentum flux*. The change in *momentum flux* is caused by a force. The force can be applied by a structure, the sea bed, an increase in the mean water level or some combination of all three. Therefore, if *momentum flux* is used in order to quantify wave forces, these may be estimated only before the occurrence of breaking.

The irregular wave formulation has been used to describe wave run up on slopes (Hughes, 2004b) and to produce a new expression for rubble-mound armor layer stability under breaking waves (Melby & Hughes, 2004).

Chapter 3

Field instrumentation and physical modelling

THIS chapter includes the description of the field site and the structural characteristics of the current Eddystone lighthouse designed by Douglass. Field instrumentation and the acquisition of hydraulic data (statistical offshore wave data and instantaneous water level) are also described. Furthermore, the design of the physical modelling is illustrated.

3.1 Eddystone lighthouse and field measurements

As mentioned in Chapter 1, geophones and cameras were installed on the Eddystone lighthouse in July 2013. The lighthouse is situated on the Eddystone Reef, which in the English Channel some 23 km offshore from Plymouth (South-West of England) (Fig. 3.1).

3.1.1 The field test site

The outcrops of the Eddystone Reef are the pinnacle of a much larger granite rock mass (Fig. 3.2a). This rises steeply from the seabed to almost the level of the highest astronomical tides in a depth of around 42-50 m.

At low tides, the lighthouse is virtually protected by surface-piercing rocks, with the exception of a small sector (Fig. 3.2b), centred approximately in the South-West direction ($194°$-$244°$). This sector is of great importance, since it coincides with the prevailing

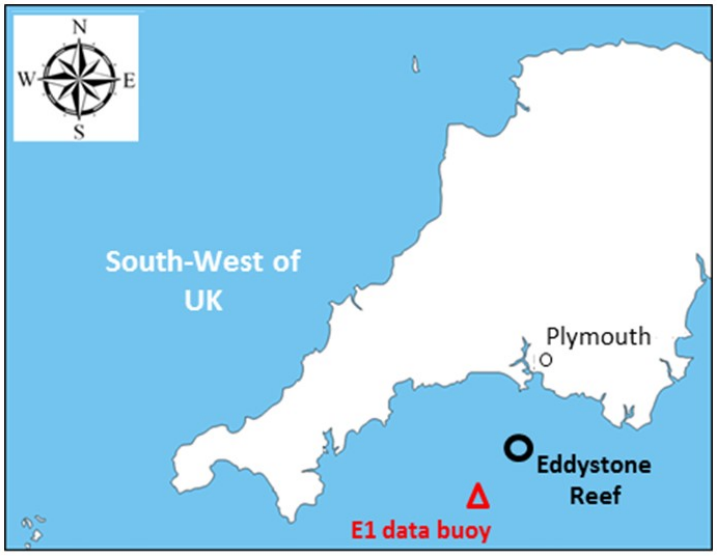

Figure 3.1: Location of the Eddystone Reef and of the E1 data buoy.

wind direction and the longest fetches from the Atlantic Ocean.

The Hydrographic Department 1984, as cited by the British Geological Survey (BGS)[1] in 1996, has data that shows the prevailing winds are from a South-West direction and are at their worst in winter when small depressions move quickly eastwards, causing the strength of the wind to vary but not its direction.

At highest astronomical tides the entire reef is completely submerged, except for the rock on the West side where the stump of Smeaton's tower is located (Fig. 3.2a). Smeaton's lighthouse, which was the third lighthouse at the site, was almost completely dismantled and rebuilt, as a memorial to its brilliant designer, on the mainland of Plymouth.

Bathymetric survey and processing data with SURFER 3D

The historical design drawings of the Eddystone lighthouse permitted the identification of the geographical exposure of the rocky outcrops that surrounds the tower at approximately lowest astronomical tide condition. However, the drawings do not give accurate

[1] BGS (1996) collected information on the physical environment of the coastal region, including the Eddystone Rocks, from historic and other archive resources.

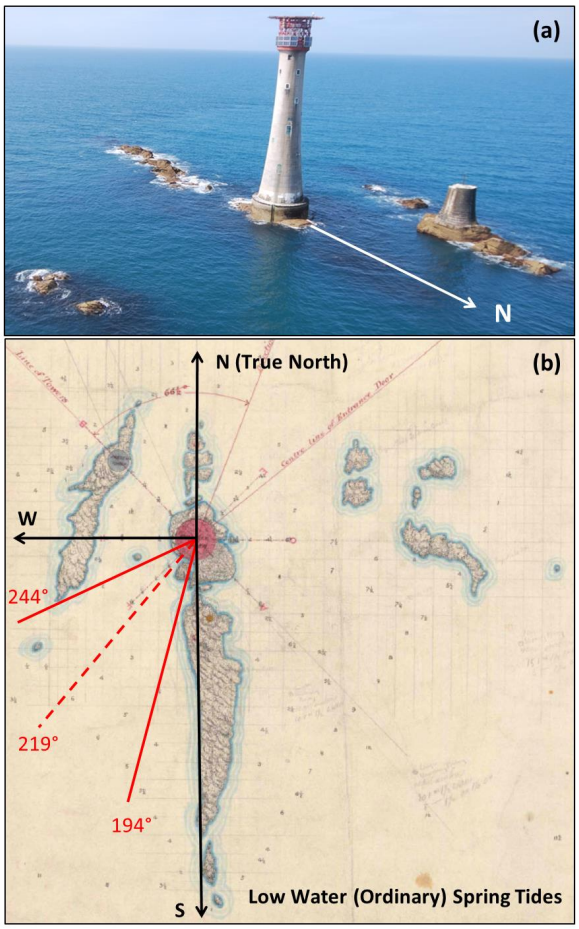

Figure 3.2: Eddystone Reef: (a) photograph of the current Eddystone lighthouse designed by Douglass and Smeaton's stump; (b) historic plane map showing the rock outcrops (reproduced by kind permission of Trinity House).

information about the configuration of the reef under the water. For the location of the Eddystone Reef, public access bathymetry data is available from Admiralty Charts at 1:7500 (Leisure Folio 5602.6 C Eddystone Rocks), which permitted to determine average values of the seabed. A bathymetric data set, acquired during a hydrography survey (McAuley, 2013), allowed a more accurate local characterization of the reef. This was measured using multibeam sonar coupled to an inertial unit (for motion reference) and GPS system (for position).

Within the present PhD project, the field data set was then processed with SURFER (3D map) in order to obtain a three-dimensional representation of the reef (Fig. 3.3).

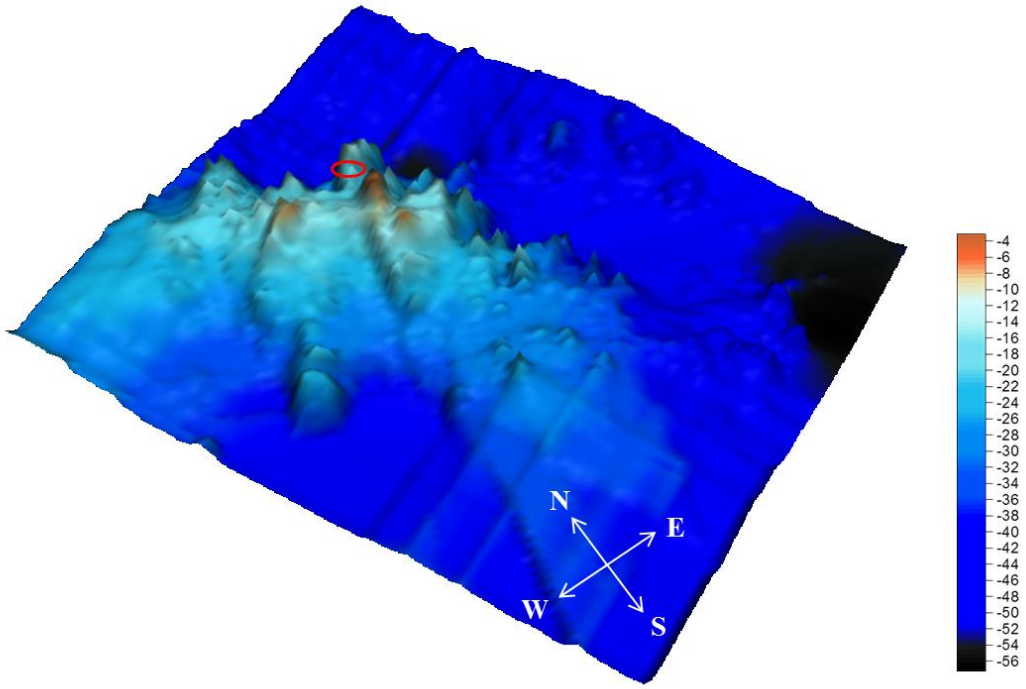

Figure 3.3: Bathymetry of the Eddystone reef (depths in m).

In agreement with the description provided by BGS (1996), the reef rises vertically on the eastern side; whilst the sea bottom rises more gradually on the western side. In addition, the latter appears much smoother with the absence of sharp peaks which are visible on the eastern side.

The visible brown peaks are in close proximity to two larger rocks (on South and West sides) visible in Figure 3.3. The bathymetric survey did not collect data in the surrounding area of the dry rocks, though the red circle gives an idea of the location of the current lighthouse (Fig. 3.3). This is situated on the rock to South, which is completely submerged at highest astronomical tide. The stump of Smeaton's tower is situated on the rock to West, a small amount of which is slightly above the water level at the highest astronomical tide. These two rocks tend to enclose an underwater channel, with lateral walls that rise rapidly; in addition they tend to assume a bottleneck shape. The rock to the South rises up to the lighthouse, while the 'vertical' rock to the West is farther from

the structure. Concerning the dry rock to the South (Fig. 3.3), this is actually located on the top of a submerged step that is oriented from the South to the West direction. In the middle of this channel (SW), which corresponds to the direction of the longest Atlantic fetches and the prevailing wind direction, the seabed appears relatively gradual and regular.

It is reasonable to expect that the wave climate at the Eddystone Reef is greatly affected by both the local tidal system and the presence of the rocks, as already pointed out by Majdalany (1959).

3.1.2 Structural characteristics of the Douglass tower

The Douglass lighthouse is a masonry structure comprising 2171 blocks of granite (Fig. 3.4a), vertically arranged on 89 courses (rows of stones). Each block was dovetailed to the next on all its faces (i.e. both in the horizontal and vertical plane) and liquefied mortar was poured to fill the remaining voids in the grooves.

The geometrical configuration of the lighthouse consists of two parts: a solid cylindrical base, 13.4 m in diameter, with a tapered tower on top of it (Fig. 3.4). The base of the tapered tower is 10.8 m in diameter. These different diameters were chosen in order to reduce the wave run up by breaking the vertical water motion (Douglass, 1878). The overall height of the lighthouse is 49 m. The height of the cylindrical base varies from 6.0 and 7.5 m because the structure is erected on the top of an irregular rock. The tapered tower is about 41.5 m high and its diameter is approximately 7 m at the top.

The geometrical configuration of the lighthouse varies with the height of the structure. The cylindrical base and the first 4 m of the tapered tower are of solid construction (Fig. 3.4b). Then, the lighthouse has internal spaces arranged on 9 levels (plus one small water tank under the 1^{st} level), where walls tend to become thinner with increasing height; the thickness of the walls varies from 2.6 m at the bottom to 0.7 m at the top (Fig. 3.4b). Above these levels comes the lantern room and a helideck which is supported on a latticework of steel attached to the top courses of masonry (Fig. 3.4).

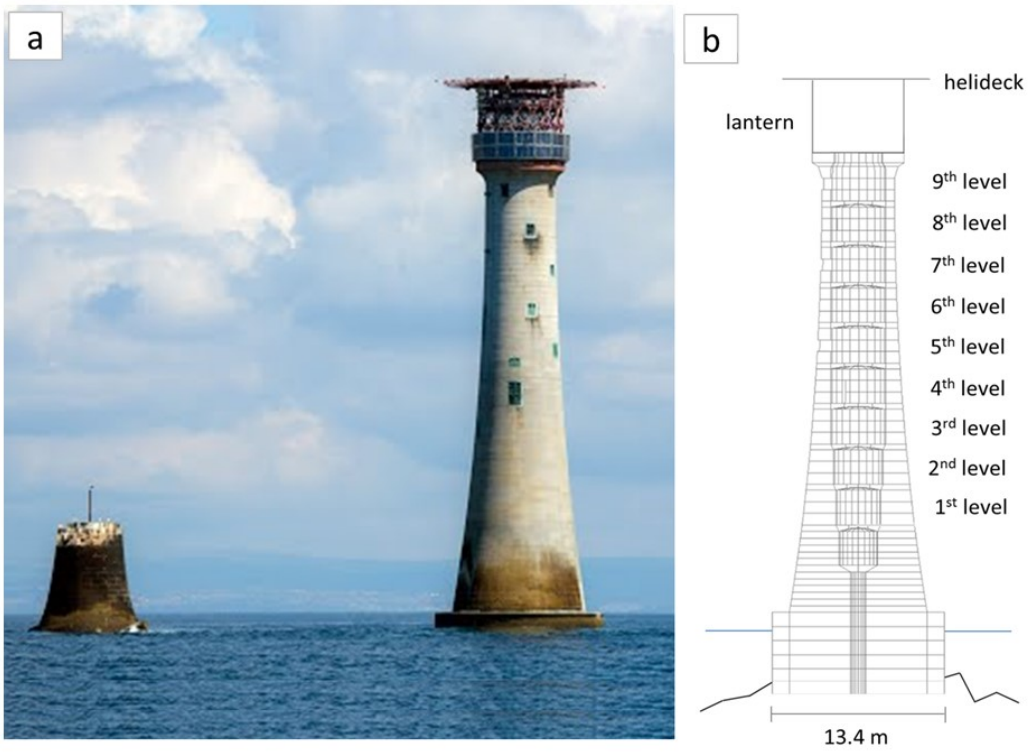

Figure 3.4: The Douglass tower: (a) photo (Mapio.net, n.d.); (b) sketch of the central section.

The helicopter landing pad was built in 1980 to enable maintenance personnel to land. The lighthouse is a structure held in place by gravity. The cylindrical base is 'framed' into the rock (Fig. 3.4b). The average weight of each block, approximately 0.5-0.6 m in height, is 2-3 metric tonnes, thus the total weight of the stone construction is approximately 5500 metric tonnes.

Finite Element model of the Eddystone lighthouse

As part of a wider project, a structural model of the Eddistone lighthouse was developed in order to evaluate the stability of the tower (Trinh et al., 2016). The Finite Element (FE) model (Fig. 3.5), which was modelled by Trinh, was constructed using the LUSAS package. Structural dimensions and material properties (density, Young's modulus, compressive strength) were obtained from historical archive drawings and from the literature that describes the construction (Douglass, 1878).

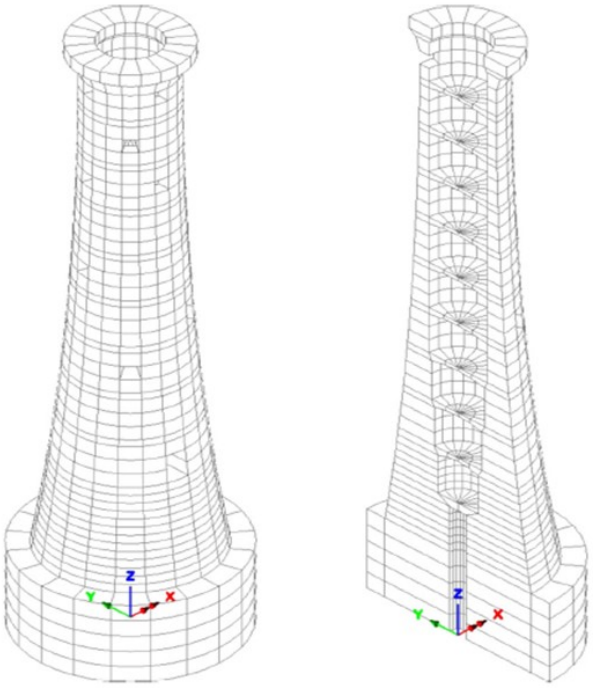

Figure 3.5: Finite Element model of the Eddystone lighthouse (Trinh et al., 2016).

Complex structures[2] have different modes of vibration, which are called natural frequencies of the structure. A shock (impulsive) load, when followed by the free motion of the structure, tends to excite all natural frequencies of the structure, although to different extents. Thus, these are characterised by fixed values and their amplitudes vary according to the frequency content of the wave load. In particular, higher load frequencies tend to excite the higher natural frequencies of the structure and lower load frequencies tend to excite the lower natural frequencies (Clough & Penzien, 1975). Spectra analysis using Fourier transformation allows the determination of the modes of vibration of a structure from its structural response[3]. Therefore, the model was calibrated using geophone signals, from which it was possible to determine both the damping and the natural frequencies of the Eddystone lighthouse. In particular, the damping and the natural frequencies were calibrated in the model by adjusting the mass of both lantern and helideck, which were modelled through a fictitious roof. The

[2]Real structures are defined complex because they are characterised by multiple degrees of freedom (which depend on the geometrical and mechanical properties of the structure).

[3]The structural response is the oscillation of the structure with a motion that includes the frequencies of its natural vibration modes.

mass of the roof (i.e. the last course of stones in Figure 3.5) was varied in order to obtain structural natural frequencies similar to those given by geophone signals.

With regard to the boundary conditions, the bottom surface of the lighthouse was considered as fully fixed. With reference to the original structure, this would certainly be the most obvious condition since all the blocks of granite in the lowest course were fixed to the rock through bolted iron brackets (Nicholson, 1995). In today's situation, it is reasonable to assume that the connections are no longer effective due to a deterioration of the bolts. In this regard, the analyses presented in Trinh et al. (2016) show how the base is always in compression and friction alone is able to globally resist the critical wave load. These results supported the choice of a perfect bond between the base of the tower and the reef.

3.1.3 Instrumentation and wave data

Geophones

Two geophones (RDL/Vibe system) were installed on the Eddystone lighthouse in 2013 in order to monitor the vibration of tower. The structure was monitored by using the RDL/Vibe system because this offered several useful features i.e. wireless mobile connectivity to set the device online remotely, long battery life, trigger alarming by email, access to data online and resistance to damage through accidental external overloading on the device.

Similarly to accelerometers, the geophone consists of a spring-mounted magnetic mass moving within a wire coil to generate an electrical signal. However, the signal is calibrated on the basis of the velocity of the mass, rather than the acceleration as an accelerometer would.

The two geophones, which were connected to a control box powered by a battery pack (Fig 3.6), were secured at the 68^{th} course in perfect line to the horizontal plane (X-Y). The 68^{th} course is the floor of the subsidiary light room (7^{th} level in Figure 3.4), which is

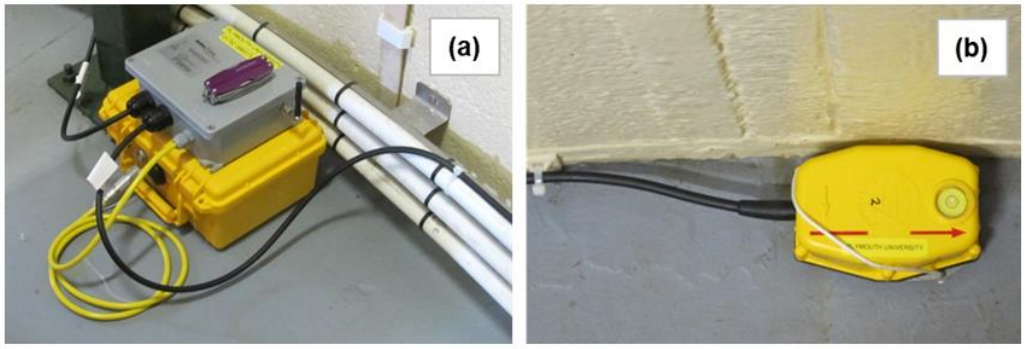

Figure 3.6: RDL Vibe geophone system: (a) battery and control box; (b) geophone No. 2.

located approximately 25 m from the base of the tapered tower. Two geophones were used so that their outputs could be compared, faults detected, and as an insurance against failure.

Each geophone provided the three orthogonal velocity components (in the three dimensional space) of the lighthouse as it oscillated in response to wave impacts. In addition, the system recorded also the time of occurrence of the event. The system was automatically activated when one of the vibration measurements, related to the discrete position where the device was located, exceeded a threshold value. This was set to 0.32 mm/s (the threshold of 0.18 mm/s is the minimum level before ambient noise triggers the equipment). Each instrument was limited to recording a maximum of 1032 data points. The acquisition rate was set to balance the temporal resolution, to capture the dynamic oscillation, with the time duration necessary to capture the signal decay. Almost all the events were recorded at 500 Hz, resulting in an acquisition period of the event of about 2 seconds. Just a few events were recorded at 100 Hz over a period of about 10 seconds. Due to the fact that the maximum frequency of the signal was observed at 28 Hz, both the sampling frequencies (100 and 500 Hz) satisfied the Nyquist criterion. This ensures the results do not suffer from the aliasing phenomena which can cause a distortion of the signal. Adhering to this criterion, the signal must be sampled with an acquisition rate equal to 2-3 times the maximum frequency present in the signal.

The geophone systems communicated by way of the global system for mobile communications so that alerts could be received and data remotely downloaded. Data acquisition features such as the threshold level and acquisition rate could also be changed without visiting the lighthouse.

Cameras

Four DC-powered video cameras, controlled remotely by internet connection, were installed on the top part of the Eddystone lighthouse as part of the wider project. They were attached underneath the helideck structure using four scaffold poles which stick out from the lighthouse (Fig. 3.7).

The four cameras were aligned along three different directions (SW, NNW and ESE), as shown in Table 3.1, in order to have the surrounding view of the tower. For each direction there was one camera that aimed at the base of the lighthouse in order to observe the evolution of the waves, from the breaking point to the run up. Another camera was placed along the SW direction (corresponding the longest fetches), angled towards the 'far-field' to provide observations about the wave transformations (mainly shoaling and refraction). All four cameras had overlapping fields of view to permit tracking of incoming waves (Fig. 3.8).

The cameras were set up to capture video images at a rate of 1 Hz. The sampled frequency increased to 5 Hz when one of the three near-field cameras recorded a

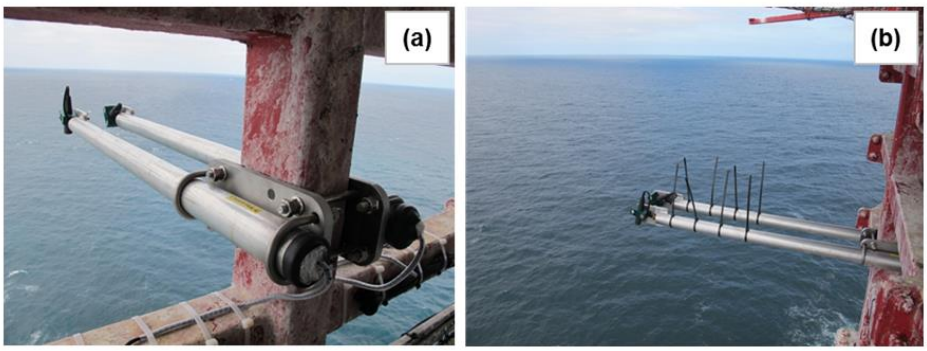

Figure 3.7: Cameras: (a) poles attached to the helideck structure; (b) cables ties to inhibit sea birds.

Table 3.1: Orientation of cameras

Camera No.	Direction	Near- or far-field
1	SW (225°)	Far
2	NNW (337.5°)	Near
3	ESE (112.5°)	Near
4	SW (225°)	Near

sudden change at the base of the tower caused by waves running up the structure. The cameras acquired data at 5 fps for a period of at least 30 s and continued at this higher recording rate while evidence of run up in that region persisted.

By using the remote internet control, it was possible both to both activate/deactivate video recording and to check live video acquisition. Video images were recorded on an external hard disk. A full disk comprised 1862 GB corresponding to approximately 950 hours of video images with effective pixels 768 H X 494 V. In order to preserve the hard disk memory, the cameras were set up to capture video images only during day light hours (from 6:00 GMT to 20:00 GMT).

Statistical offshore wave data

Hourly statistical wave data were available from the E1 buoy as mentioned earlier. This buoy is some 15 km south-west of the lighthouse, in line with the longest fetches (Fig. 3.1). The buoy provided the following offshore measurements of use here:

- significant wave height $H_{s,o}$ [m];
- peak period T_p [s];
- wave direction β [° to true N].

Water levels

The vertical distance between the bottom of the seabed at the toe of the lighthouse and the top surface of the cylindrical base, which is framed on an irregular rock, varies

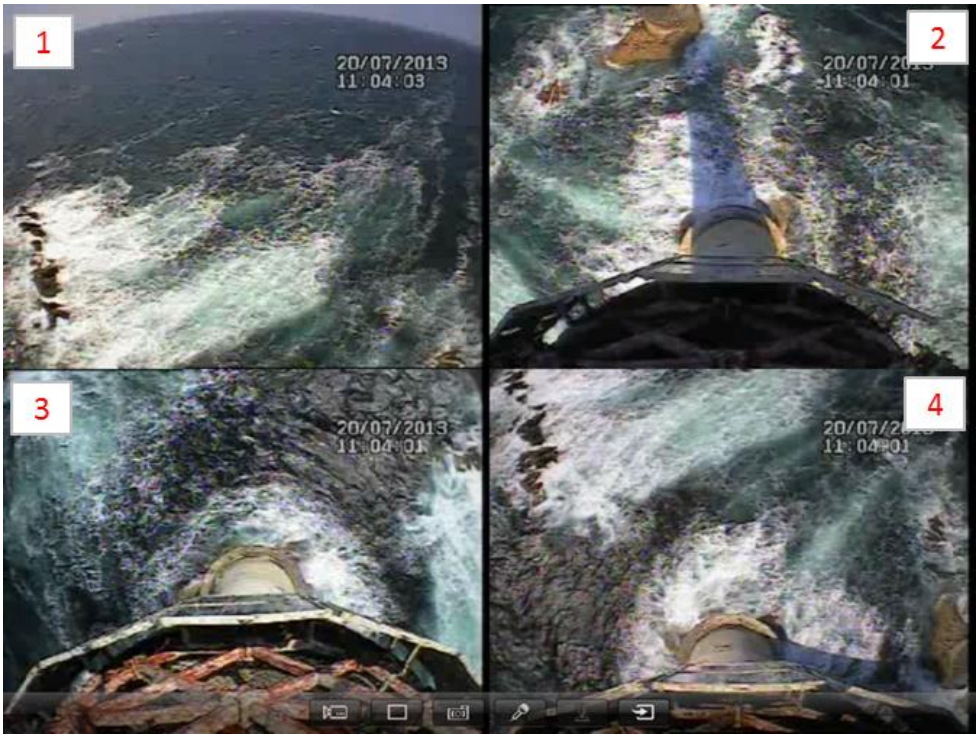

Figure 3.8: View from the four cameras situated under the helideck of the lighthouse.

between 5.0-7.0 m. As a consequence, the lighthouse is situated in limited water depths. The Eddystone Reef tends to be submerged at most states of the tide. In 2015, the maximum tidal range was estimated to be 5.9 m (in Devon area) from the National Oceanography Centre (prediction for the period 2008-2026). Therefore, it is reasonable to expect that the local wave climate, at the Eddystone Reef, is strongly affected by the tidal level.

The British Oceanographic Data Centre (BOCD) provides water levels from the Devon Area at Plymouth. The data frequency is 15 minutes and the values are referenced to Admiralty Chart Datum (CD). Instantaneous water levels were obtained by a linear interpolation between two consecutive data acquisitions.

Design drawings of the Eddystone lighthouse, provided from the archive of Trinity House, show the extreme tide conditions at the toe of the structure. However, the drawings date back to the time of construction (end of the 19^{th} century) and a change of tides has occurred over the years. Therefore, in order to have a better estimation,

the water depth at the toe of the structure was related to the BOCD's measurements using photography with the cylindrical base in full view. The photo, taken during calm sea conditions (21/05/13 at 11:17 am), is shown in Figure 3.9. Because the exact hour of the photo is known, it was possible to relate the BOCD's measurement with the vertical distance between the water level in the photo and the top surface of the cylindrical base ($z = 0$). From the design drawings it is then possible to determine the vertical distance from the top surface of the cylindrical base and the bottom of the seabed for each direction. Consequently, the instantaneous BOCD's measurements can be related to the relative water depth at the toe of the lighthouse for any direction. At highest astronomical tide, the cylindrical base is almost completely submerged and there is only approximately 0.25 m of freeboard. However, it should be noted that the tide may have not been at the level predicted at the time of the photo. For example, the level is affected by atmospheric pressure. Thus, all the structural elevations are estimates.

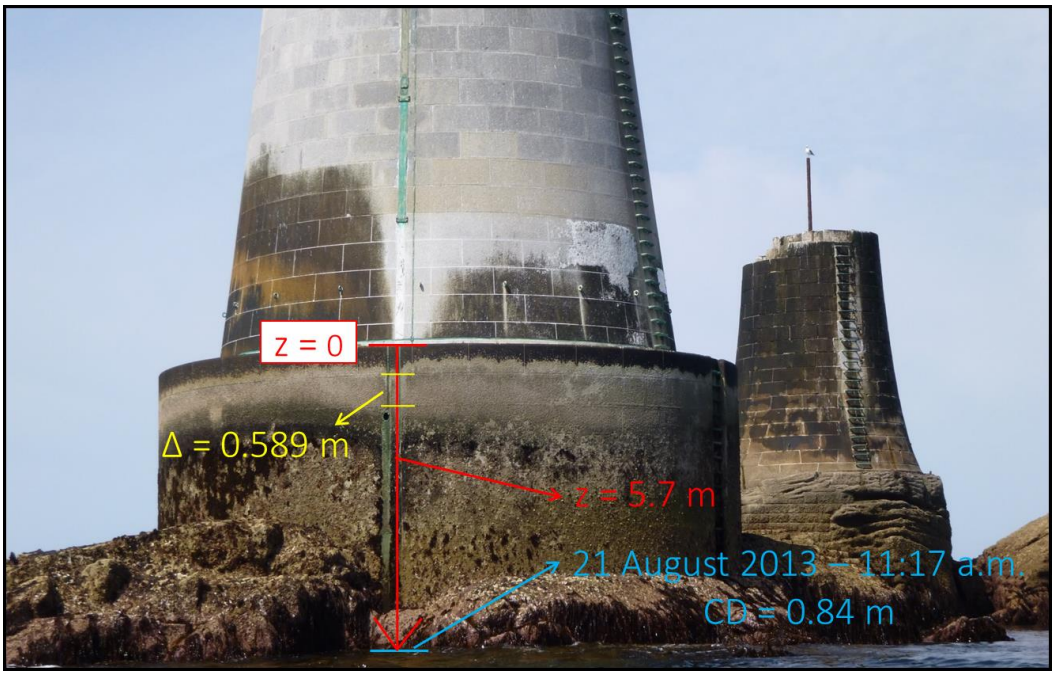

Figure 3.9: Identification of the water level from the top surface of the cylindrical base (photo reproduced with kind permission of Helen Nance).

3.2 Design of the physical hydraulic model

Interpretation of the field data was aided by a physical modelling investigation under controlled hydraulic conditions. Small scale-tests were carried out in the 35 m long x 0.6 m wide x 1.2 m deep sediment wave flume of the COAST Laboratory of Plymouth University. The wave flume has a force feedback absorbing wavemaker that absorbs incoming waves by measuring the force on the front of the paddle and producing compensating motion. Additionally, a passive absorption system is provided by a permeable foam filter located at the end of the wave flume (which enlarges with a circular shape).

Two physical models of the lighthouse were used to analyse the wave-structure interactions. The models were designed to obtain local pressure and overall force using pressure transducers and load cells respectively. The choice of using two models for the different test phases was done in order to produce a higher measurement accuracy. This is related to the fact that load cells must be connected to a model that is light and rigid as far as is possible, so that its inertial movement are limited. The simultaneous location of pressure transducers would have increased the mass of the model, whose imperceptible movements could be also constrained by transducer cables. In addition, pressure measurements need to be integrated into a model which is rigidly connected to a fixed position, to limit resonance effects of the transducers.

3.2.1 Setup of the experiments

The experiments were conducted at 1:70 length scale (Froude scaling) compared to the prototype. As shown in Figure 3.10, the bathymetry was modelled with two average slopes, 1:20 and 1:8, according to the South-West direction, which coincides with the prevailing wind direction and the longest fetches in the prototype.

The gentler slope (1:20) horizontally extended for 7.85 m and the steeper uppermost slope (1:8) horizontally extended for 1.15 m. The water depths at the paddle and at

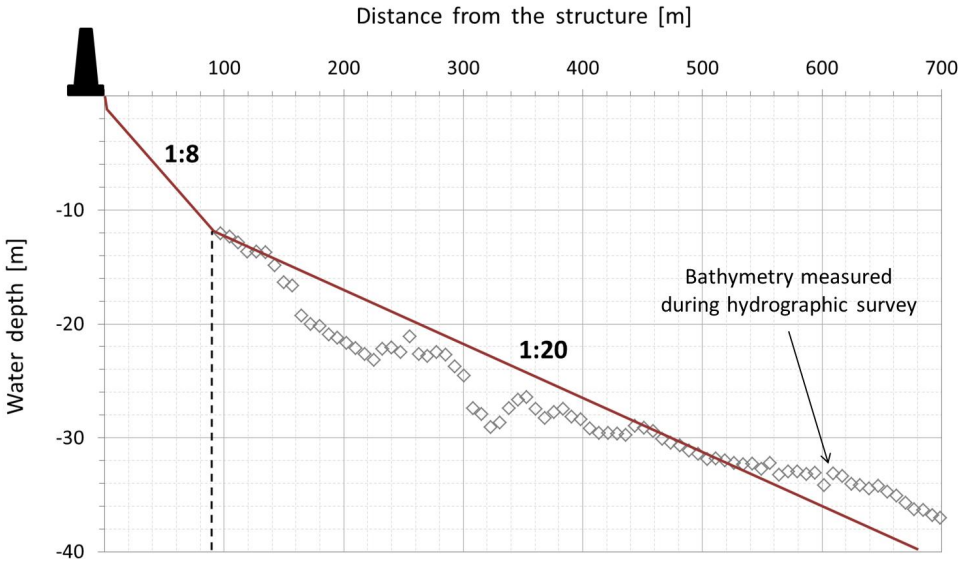

Figure 3.10: Modelling of the bathymetry on the basis of the SW direction.

the toe of the lighthouse model(s) were 0.63 m and 0.095 m respectively (Fig. 3.11), in agreement with the depths in the prototype at highest astronomical tide (i.e. 44 m and 6.65 m). The lighthouse model(s) was situated at a distance of 16.5 m from the end of the flume, located on the top of a horizontal plane (Fig. 3.11).

According to the depth limited conditions in the lee of the lighthouse (i.e. North direction), the horizontal plane was extended behind the lighthouse model for 1.3 m rather than suddenly cut. This choice was also made in order to decrease the amount of the water mass, behind the model, and so the relative movement of water caused by the splash of plunging waves. Alternatively, an inclined slope behind the lighthouse model would have limited the supply of water required by the rush down affecting the circulation of the water around the cylinder. Submerged rubble stones, used as a permeable filter, were located about 0.3 m behind the model in order to decrease the oscillation of the water, which could not spread laterally due to the presence of the walls of the flume.

Nine resistance wave gauges were located, as shown in Figure 3.11 (red lines), in order to measure the wave height offshore and the subsequent transformations. The surface elevations were sampled at 128 Hz.

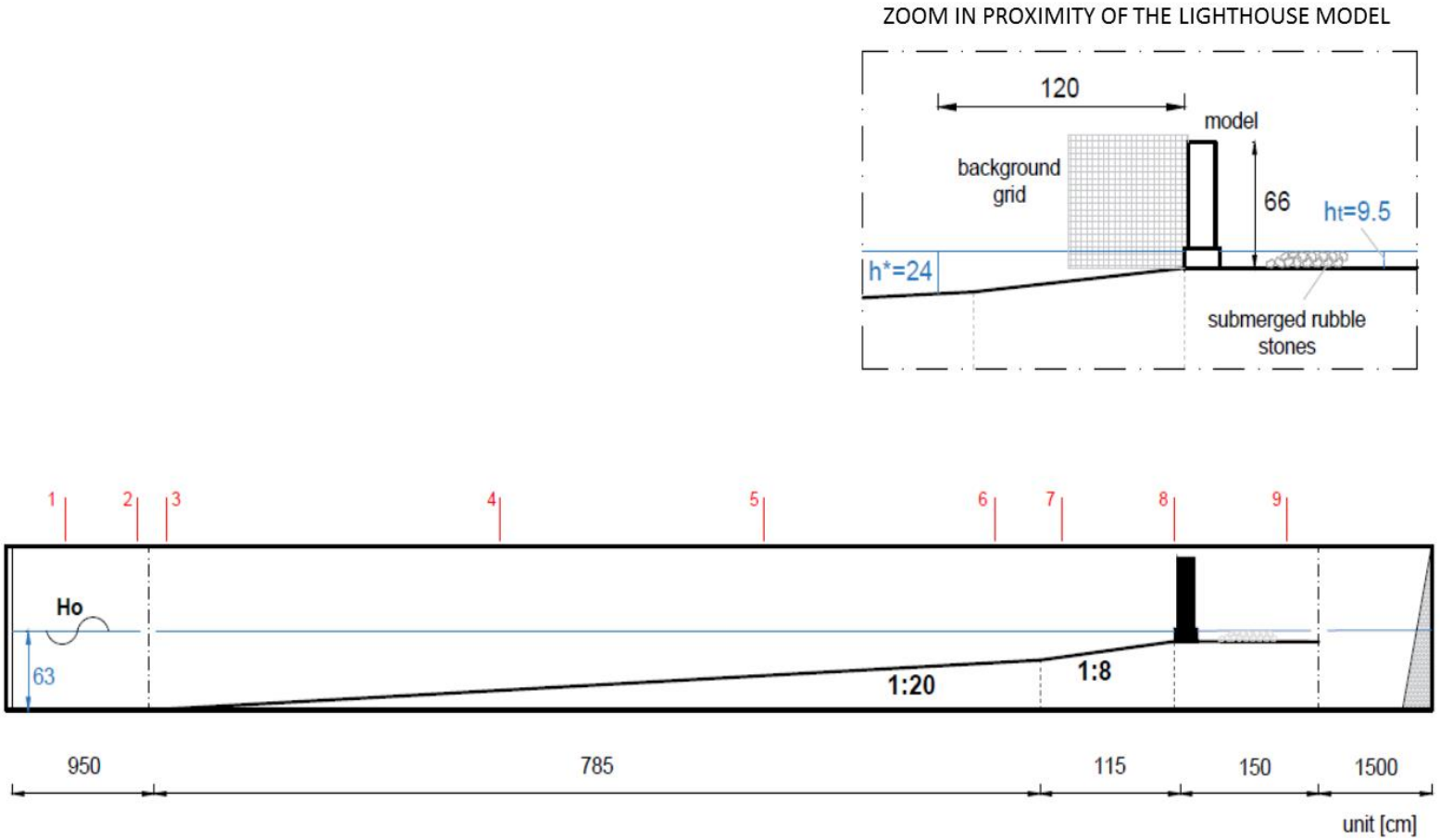

Figure 3.11: Setup of the experiments with locations of wave gauges indicated (red lines). Note all dimensions are in cm.

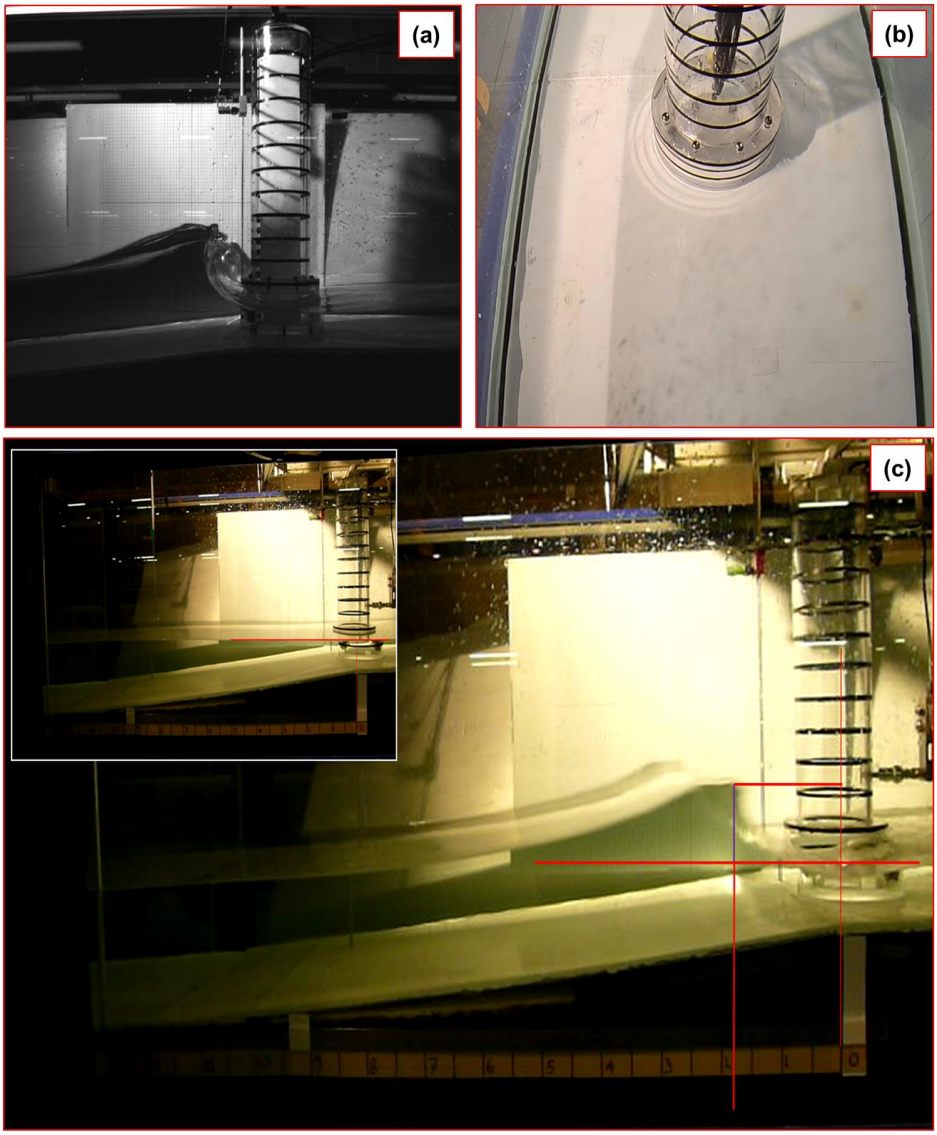

Figure 3.12: Video frames from: (a) high-speed camera (b) GoPro on the top and (c) and wide field of view camera.

Three different cameras were used in order to have different visual observation of waves approaching the lighthouse model(s).

1. A high speed (3600 fps) and high definition (1024 x 1024 resolution) camera was used to analyse: the effects of the lighthouse model on water flow, the breaking wave height at breaking point and the breaking shape at the moment of impact (Fig. 3.12a). The breaking wave height was not determined by using wave gauges, to avoid affecting the wave in close proximity to the lighthouse model.

2. A waterproof GoPro camera was located on the top of the model to have a plan view of the circulation of the water around the cylinder (Fig. 3.12b).

3. Another high definition camera with a wider field of view, covering a horizontal extent of 1.6 m, was placed to record the wave transformations and the wave that broke farther from the lighthouse model (Fig. 3.12c). Small photo in the left corner of Figure 3.12c shows the undisturbed water level before the test generation (Fig. 3.12c).

3.2.2 Physical models of the lighthouse and instrumentation

The tests were conducted using two models that were dimensionally identical, but one could be disassembled (pressure model) and the other was an indivisible rigid structure (force model). Both comprised two circular cylinders (one above the other) having different diameters. The cylindrical base had a diameter of 0.20 m and a height of 0.10 m (according to the height of the prototype at SW direction). The upper cylinder was 0.55 m high with a diameter of 0.155 m (according to the base of the tapered tower of the prototype). The thickness of the cylinders was 0.01 m and they were manufactured in Plexiglas in order to be simultaneously waterproof, rigid and light.

Pressure model

As just mentioned, the pressure model could be disassembled into two rigid parts (Fig. 3.13), so that pressure transducers could be installed. One part consisted of the cylindrical base without the top surface; while the second part consisted of an upper cylinder with a ring which, rigidly attached on the base, was coincident with the diameter of the cylindrical base (Fig. 3.13). The two parts of the lighthouse model were connected using eight screws. A perfect watertight fit was ensured with an additional layer of Plexiglas under the holes screws layer and by locating absorbing paper and petroleum jelly between the two parts.

Figure 3.13: Photo of the pressure model that could be disassembled to install pressure transducers.

Nine 10 mm diameter threaded holes were manufactured on the Plexiglas model in order to give flexibility in where transducers could be placed for best test description of the wave impacts. Pressure signals were measured by six dynamic piezoelectric pressure sensors of type XP1102 which had a range of up to 1 bar and a resonance frequency of 50 kHz. Data was acquired at a sampling rate of 1.8 kHz. The transducers were fixed into 10 mm diameter threaded holes on the seaward side of the model (Fig. 3.14). Three of the machined holes were on the cylindrical base and six were on the upper cylinder (Fig. 3.14). Around these holes, the internal surface of the cylinders was manufactured flat to ensure the perfect installation of the transducers. In order to provide the most detailed spatial resolution, two consecutive holes were spaced at intervals of 25 mm (between hole interaxis). The holes covered an extent of 0.215 m on the surface of the model, so that the impact area was fully instrumented. Pressure transducer cables were inserted through another hole of 40 mm diameter on the leeside of the upper section model. The lighthouse model was screwed down to the uppermost horizontal plane of the bathymetry (Fig. 3.11).

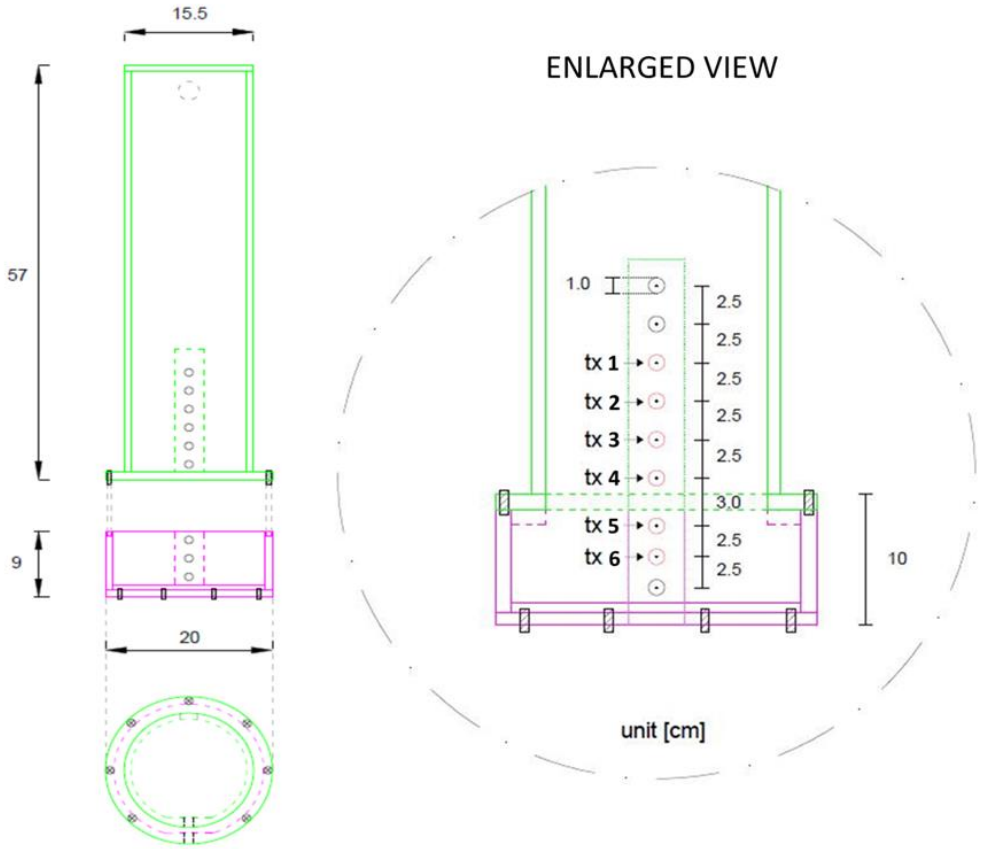

Figure 3.14: Sketch of the two parts of the pressure model and pressure transducer locations.

Force model

Tests were conducted in order to obtain the horizontal components of the force in-line with the wave direction; to this end, two unidirectional load cells (FSLB) were used. The FSLB is a stainless steel platform load cell (beam type) able to measure compression and tension force, in-line to the application point of the device. When forces are dynamically applied, a load cell with a nominal capacity of at least 2 times the maximum measured force is recommended. Thus, for the experiment two FSLB with a nominal capacity of 890 N, sealed at a waterproof level of IP67 and an accuracy of 0.02% of the maximum capacity, were identified. Data were acquired with the same sampling rate of the pressure transducer, i.e. at 1.8 kHz.

The Plexiglas model, an indivisible rigid structure, was connected to the two load cells

through two rigid supports placed on its leeside (Fig. 3.15a). The model, independent from the bathymetry, was supported at the top by a sliding-pivot (in line with the wave direction) (Fig. 3.15b-c). This support comprised two sliding rails (circular section of low friction) and two pivots (spherical pillow blocks). The support hence avoided the weight of the model acting on the load cells. It also prevented lateral vibration (due to impulsive impacts) of the model whilst still allowing deflections in line with the load cell axes. Two axial ball joints were used to connect the model and the load cells (Fig. 3.15a). These connectors ensured that only the orthogonal component of the wave force was transferred to the application point of the unidirectional-type load cells. Both the sliding-pivot and the load cells were attached to a framework rigidly connected to the top of the wave flume.

The framework consisted of two main components: a vertical support where the load cells were attached, and a horizontal structure where the sliding support was attached (Fig. 3.16). The two components were rigidly connected and the horizontal structure rigidly attached to the wave flume by using four clamp systems. The framework was

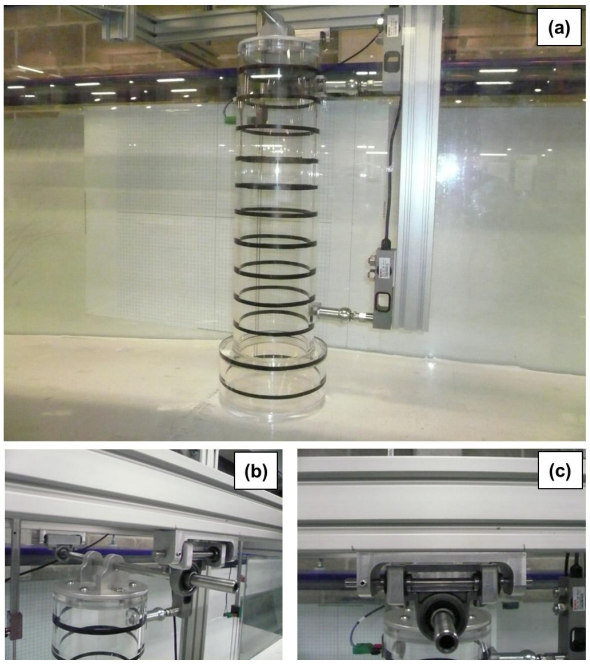

Figure 3.15: Load cells system: (a) Plexiglas model, load cells and axial ball joints; (b)-(c) sliding-pivot and supporting aluminum profile framework.

manufactured using aluminium profile (box section internally framed) with a rectangular shape in order to decrease torsional deflections; then, the profiles were assembled using angular brackets. These measures aimed to guarantee a larger stiffness of the framework with respect to the stiffness of the load cells (so that the framework did not absorb any force affecting the measurements). Four screw-feet were installed on the horizontal structure in order to adjust the level and the position of the model (with respect to the bathymetry).

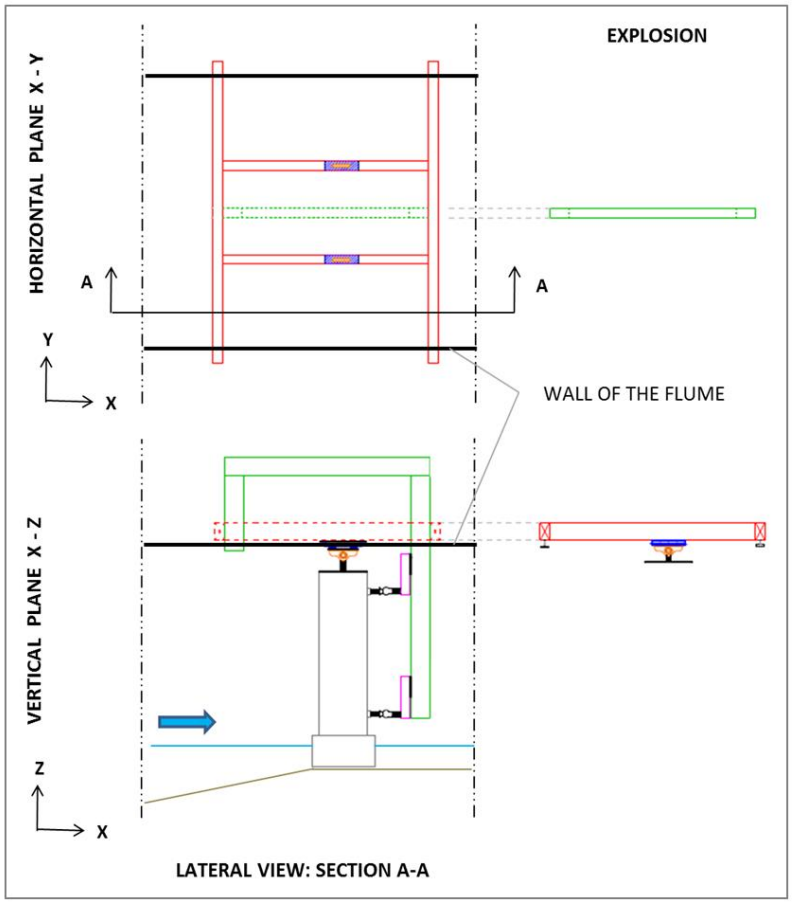

Figure 3.16: Sketch of the 2 components of the framework supporting the model. In green is the vertical support and in red the horizontal structure.

3.2.3 Test program

Tests were conducted in 2 phases reproducing the same target values of wave conditions for each model. Each experimental phase included 128 runs of regular waves

(Table 3.2), with target values of offshore wave height (H_o) and wave period (T) between 0.02-0.24 m and 0.6-3.0 s, respectively.

Table 3.2: Test program (128 run of regular waves)

Test	H_{target}	T	Test	H_{target}	T	Test	H_{target}	T	Test	H_{target}	T
1	0.02	0.6	33	0.16	1.2	65	0.08	1.8	97	0.03	2.4
2	0.05	0.6	34	0.18	1.2	66	0.1	1.8	98	0.06	2.4
3	0.08	0.6	35	0.2	1.2	67	0.12	1.8	99	0.09	2.4
4	0.11	0.6	36	0.22	1.2	68	0.14	1.8	100	0.12	2.4
5	0.03	0.8	37	0.03	1.4	69	0.15	1.8	101	0.15	2.4
6	0.06	0.8	38	0.05	1.4	70	0.16	1.8	102	0.18	2.4
7	0.08	0.8	39	0.07	1.4	71	0.17	1.8	103	0.21	2.4
8	0.1	0.8	40	0.09	1.4	72	0.18	1.8	104	0.24	2.4
9	0.12	0.8	41	0.11	1.4	73	0.2	1.8	105	0.03	2.6
10	0.14	0.8	42	0.13	1.4	74	0.22	1.8	106	0.06	2.6
11	0.03	1	43	0.14	1.4	75	0.24	1.8	107	0.09	2.6
12	0.06	1	44	0.15	1.4	76	0.03	2	108	0.12	2.6
13	0.08	1	45	0.16	1.4	77	0.06	2	109	0.15	2.6
14	0.1	1	46	0.18	1.4	78	0.08	2	110	0.18	2.6
15	0.12	1	47	0.2	1.4	79	0.1	2	111	0.21	2.6
16	0.13	1	48	0.22	1.4	80	0.12	2	112	0.24	2.6
17	0.14	1	49	0.24	1.4	81	0.14	2	113	0.03	2.8
18	0.15	1	50	0.03	1.6	82	0.15	2	114	0.06	2.8
19	0.16	1	51	0.06	1.6	83	0.16	2	115	0.09	2.8
20	0.17	1	52	0.08	1.6	84	0.17	2	116	0.12	2.8
21	0.18	1	53	0.1	1.6	85	0.18	2	117	0.15	2.8
22	0.2	1	54	0.12	1.6	86	0.2	2	118	0.18	2.8
23	0.22	1	55	0.14	1.6	87	0.22	2	119	0.21	2.8
24	0.03	1.2	56	0.15	1.6	88	0.24	2	120	0.24	2.8
25	0.05	1.2	57	0.16	1.6	89	0.03	2.2	121	0.03	3
26	0.07	1.2	58	0.17	1.6	90	0.06	2.2	122	0.06	3
27	0.09	1.2	59	0.18	1.6	91	0.09	2.2	123	0.09	3
28	0.1	1.2	60	0.2	1.6	92	0.12	2.2	124	0.12	3
29	0.11	1.2	61	0.22	1.6	93	0.15	2.2	125	0.15	3
30	0.12	1.2	62	0.24	1.6	94	0.18	2.2	126	0.18	3
31	0.13	1.2	63	0.03	1.8	95	0.21	2.2	127	0.21	3
32	0.14	1.2	64	0.06	1.8	96	0.24	2.2	128	0.24	3

The test program was designed to generate a comprehensive data set covering a broad range of wave conditions (Banfi et al., 2017a). The target wave conditions were identified thanks to a type of breaking map, which was obtained in a dimensionless plane given by the combination of *Iribarren number* and *momentum flux* of Hughes, as shown in Figure 3.17. On the horizontal axis, the *Iribarren number* (Equation 2.7) was determined according to the uppermost slope ($\alpha = 1/8 = 0.125$) and the offshore wave steepness (H_o/L_o). On the vertical axis, the *momentum flux* was determined according to Equation 2.10 and setting $H = H_o$. As may be observed from Figure 3.17, the test program is enclosed by three limiting conditions: the two breaking limits for wave steepness (H/L) and wave height (H/h), and the shallow water limit (h/L).

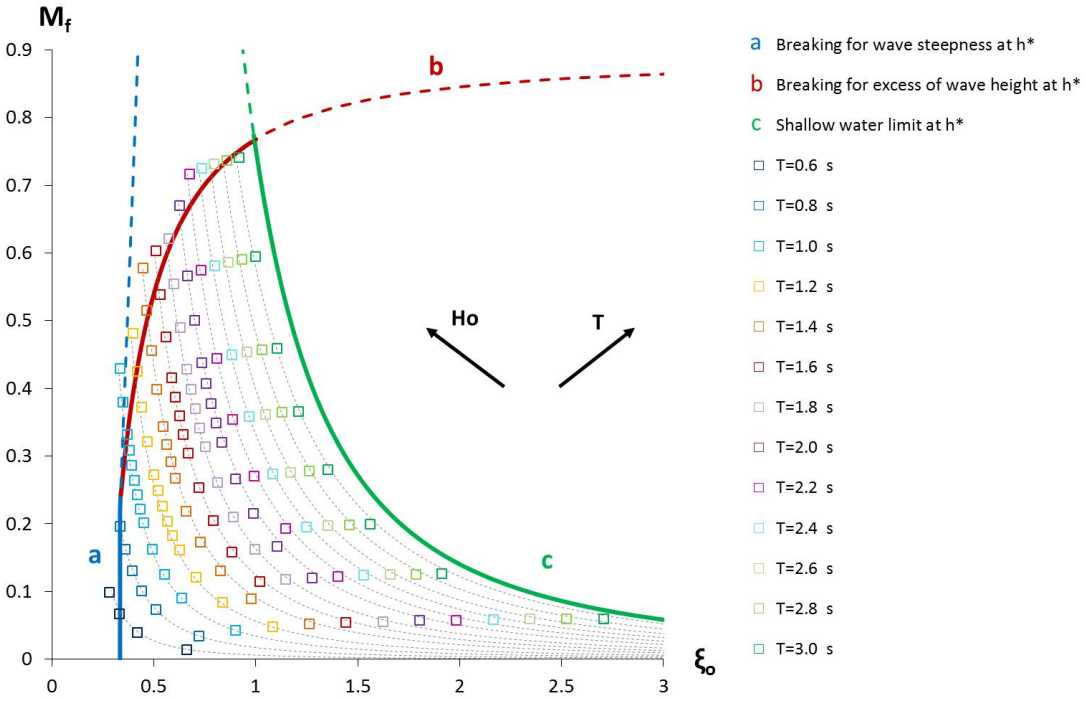

Figure 3.17: Region on the theoretical ξ_o - M_f plane used for defining test program parameters. The region is enclosed by 3 curves: (a) wave steepness limit, (b) breaking wave height limit and (c) shallow water limit.

For determining the three limits, it was first necessary to identify the section at which the *momentum flux* is calculated, i.e. the value of the water depth h that must be inserted into Equation 2.10. It was decided to select the depth section at a distance from

the model of 5 times the maximum offshore wave height ($H_o = 0.24$ m); above this value the wave tends to dissipate most of the energy (Goda, 1974). Thus, the location was identified at a distance of 1.2 m from the lighthouse model(s), where the water depth was $h^* = 0.24$ m and the slope was 1:20 (Fig. 3.11). As a consequence, the three limiting conditions were identified at h^* according to linear Airy wave theory. Below, the procedures used for their identification are described.

Breaking limit according to wave steepness

The wave steepness limit ($H/L = 0.14$) was estimated by setting the breaking water depth h_b to $h^* = 0.24$ m. A reduction coefficient of 0.91 was introduced to take into account the maximum possible decrease of the offshore wave height H_o for shoaling (Fig. 2.6). On this basis, the limit was determined as follows.

1. Define the wave steepness limit at h_b equal to $0.91H_o/L_b = 0.14$.
2. Select a value for T, e.g. $T = 0.1$ s.
3. Calculate L_o and L_b[4] at h_b using the linear dispersion relationship (Eq. 2.4).
4. Determine H_o from step 1 above.
5. Repeat steps 2-4 by defining different values of T (with an interval $\Delta T = 0.1$ s).

Finally, the blue curve (a), shown in Figure 3.17, was drawn according to ξ_o= f (H_o , L_o) and M_f = f (H_o, T, h^*).

Breaking limit according to wave height

The breaking wave height H_b, on the 1:20 slope at h_b=$h^* = 0.24$ m, was estimated as follows.

[4] L_b denotes the wave length calculated at the breaking water depth h_b

1. Define the breaking relationship between H_b/h_b and H_b/gT^2 from the diagram of Weggel (1972) shown in Figure 2.8, i.e. $H_b/h_b = 1.13 - 26.5H_b/gT^2$.

2. Select the first value of relative wave height, $H_b/h_b = 0.01$, with its relative value of H_b/gT^2 (from step 1).

3. Since $h_b = 0.24$ m, define H_b and, then, the associated T (from step 2).

4. Determine both L_o and L_b at h_b using the linear dispersion relationship (Eq. 2.4).

Once these local variables were determined at the breaking location, it was necessary to calculate their relative offshore values, as explained below.

1. Knowing h/L (i.e. h_b/L_b from step 4), identify the ratio $H_{(h)}/H_o$ from the shoaling curve (Fig. 2.6).

2. Determine the value of H_o from step 5, where $H_{(h)} \equiv H_b$.

3. Repeat steps 2-6 by varying the values of H_b/h_b (with an interval $\Delta = 0.01$).

Finally, the red curve (b), shown in Figure 3.17, was drawn according to ξ_o= f (H_o , L_o) and M_f = f (H_o, T, h^*).

Shallow water limit

The wave period T, which implies the shallow water limit at $h^* = 0.24$ m, was calculated according to $h^*/L_{(h^*)} = 0.05$, where the wavelength$L_{(h^*)}$ was determined using the linear dispersion relationship (Eq. 2.4).

Therefore, the blue limit (c), shown in Figure 3.17, represents the curve at constant period ($T = 3.2$ s) that causes the shallow water limit at $h^* = 0.24$ m.

Chapter 4

Measurements acquired and processing of data

THIS chapter illustrates information that were extracted from the field and laboratory measurements acquired. Procedures used to process data are described. Data manipulation and programming codes were developed in the LabVIEW environment (Appendix A).

4.1 Field data

4.1.1 Geophone signals

From October 2013 to March 2014, 3098 geophone events were recorded by each one of the two devices. The average difference between the peaks of the velocity maxima was 2.5% giving confidence in the reliability of the data set; just 20 data records have a differences higher than 10% due to electronic noise (vertical spikes) in the signal and, thus, they were not included in the analyses.

Each geophone measured 3 velocity components of the oscillation of the lighthouse. A typical velocity component time history is shown in Figure 4.1. When wave impacts cause a structural deflection of the lighthouse, the tower starts to vibrate. The displacement oscillations can occur with different velocities and, consequently, with different accelerations. Displacements and accelerations of the lighthouse were determined by integrating and differentiating, respectively, the velocity signals obtained from the geophones.

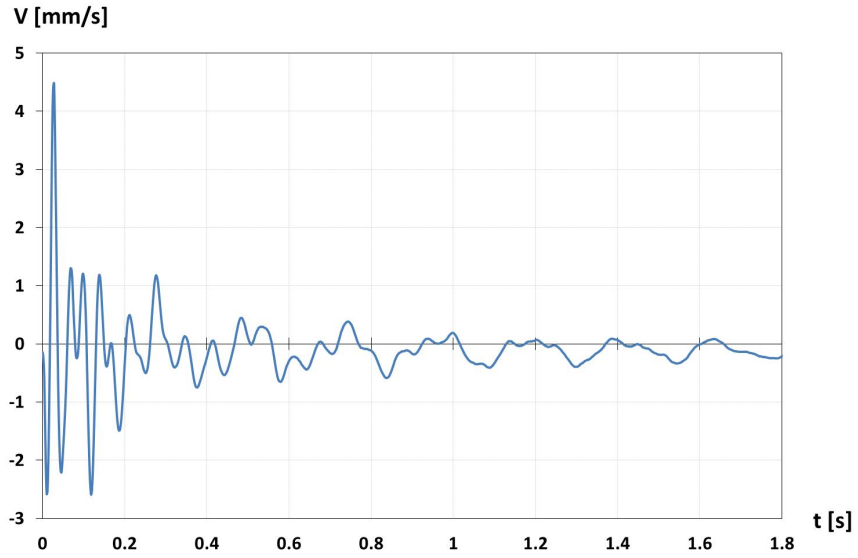

Figure 4.1: A typical response event showing a velocity component (on the horizontal plane)

There are certain practical restrictions imposed upon differentiating and integrating operations arising from electronic signals of acceleration, velocity or displacement measured in experimental vibration studies. These arise due to:

- an offset with respect to zero of the signal;
- eletronic noise that can cause vertical spikes in signals.

Therefore, two operations are required on the signal before its integration or differentiation: subtracting the mean and filtering. The mean subtraction is necessary to remove the offset; whilst the filtering to remove possible electronic noise (high frequencies) or non-null contribution at 0 Hz. The latter represents low frequency component in the background of the oscillation of the signal (Appendix B). This low frequency can be a sample rate effect or it can be also caused by an acquisition period too short compared to the duration of the event analysed. In the present investigation, the acquisition period (approximately 2 s at 500 Hz) was sufficient to detect the maximum dynamic peak, but it was too short to detect the maximum quasi-static peak in phase with the wave surface elevation (2-5 s). As a consequence, a non-null contribution at

0 Hz was present in the signal. Thus, a high-pass filter was used in order to eliminate the non-null contribution at 0 Hz.

Mean removal

In order to compensate for the non-zero mean, the offset was calculated and then that value was subtracted from the signal. The instrument was limited to recording a maximum of 1032 data points. With a sampling rate of 500 Hz, the signal was acquired for slightly more than 2 seconds. Only the first portion, about 0.6 seconds long, presented an irregular nature (impulsive transient); in the second portion the signal decays. The signal was corrected by subtracting the mean value obtained from its last portion, precisely from the last 516 points. In Figure 4.2 it is possible to see the slight shifting between the raw (Vr) and the same signal with mean removal (Vrm).

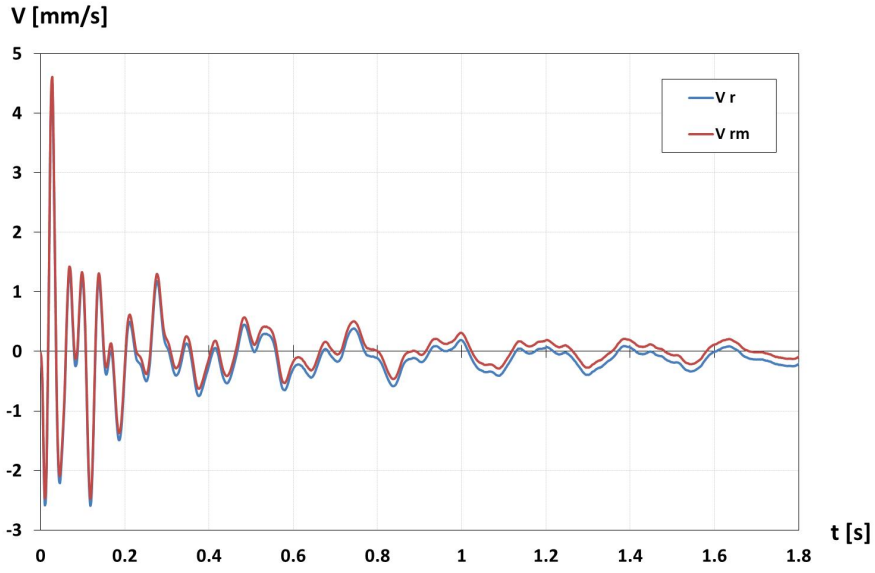

Figure 4.2: In blue (Vr) the raw velocity signal; in red (Vrm) the same signal with mean removal.

Filtering

The non-null frequency at 0 Hz was eliminated by passing the signals through a high-pass filter. The filtering was performed using an IIR (Infinite Impulse Response) Butterworth filter of order 3 (Appendix C). A satisfactory result was found using a cut-off

frequency of 0.5 Hz (equal to 0.1% of the sampling frequency 500 Hz). The choice of this value allowed eliminating the zero frequency without altering the energy contribution of the signal. In Figure 4.3 it is possible to see the comparison between the raw signal with mean removal (Vrm), shown in Figure 4.2, and the same signal after the filtering (Vrmf). The filtering causes a negligible reduction in the peak of about 1%.

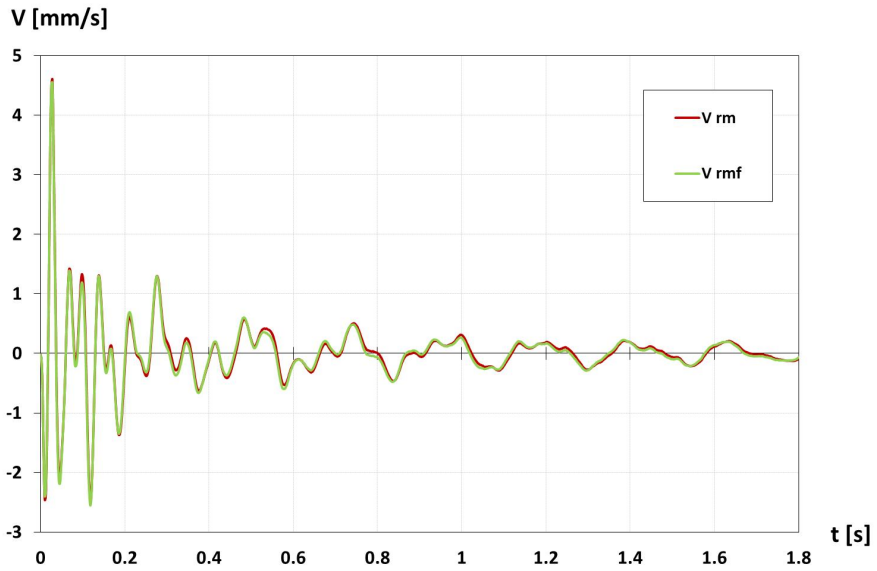

Figure 4.3: In red (Vrm) the raw signal with mean removal; in green (Vrmf) the same signal after the filtering.

Integration and differentiation

Velocity signals were integrated and differentiated using Simpson's rule (3 point-formula) and 2^{nd} order central method respectively.

According to Simpson's rule, the integral $y(t) = \int x(t)\ dt$ obtains the elements of y as follows.

$$y_i = \frac{1}{6} \sum_i (x_{i-1} + 4x_i + x_{i+1})\ dt$$

According 2^{nd} order central method, the derivative $y(t) = dx(t)/dt$ provides the elements of y as follows.

$$y_i = \frac{1}{2\,dt}\ (x_{i+1} - x_{i-1})$$

A cross-check has been carried out by applying different integration derivation (4^{th} order central) and integration methods (Trapeziodal Rule, Simpson's 3/8 Rule, Bode Rule). The different methods caused a maximum peak difference of 1%.

Frequency analysis

Frequency oscillations of the structural responses (accelerations, velocities and displacements) were determined with power spectra analysis.

4.1.2 Video images

A geo-referenced grid was drawn on the video frames with AutoCAD in order to make the best possible estimation of run up elevation. The distortion of the images was determined by interpolating points on the surface of the tower at known locations, identified with a physical target held outside the windows (Fig. 4.4a).

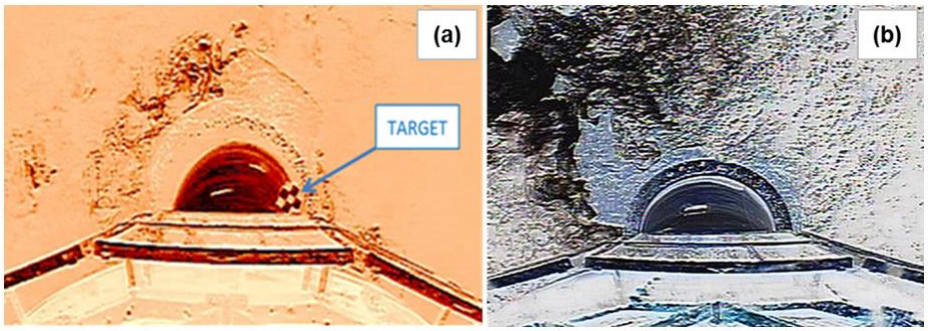

Figure 4.4: Processing of the distorted video-frame in order to (a) highlight the target and (b) the masonry courses.

Then, the images were processed to highlight the boundaries, along the circumference, of the masonry courses that enclosed the windows and the base of the tapered tower (Fig. 4.4b). The final grid drawn on the tower surface is shown in Figure 4.5; the vertical step between two consecutive red curves is 5 m.

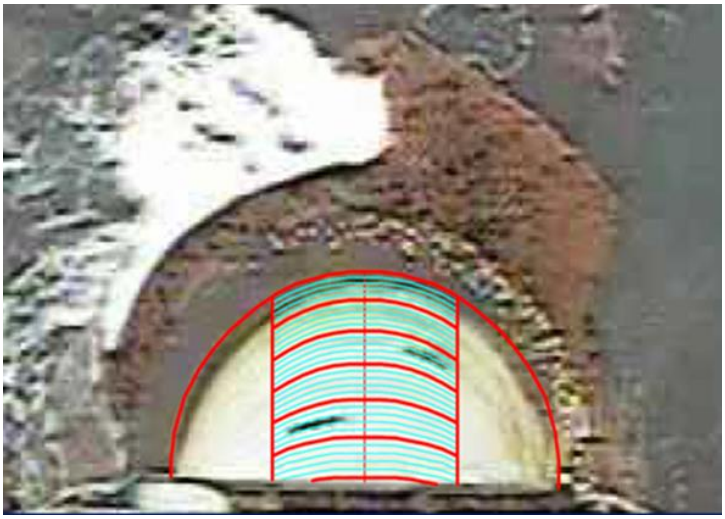

Figure 4.5: Grid construction on the tower surface (red curves are spaced at 5 m vertical intervals).

4.2 Laboratory data

The first three waves in each wave train were omitted from the analysis, as they had not reached the required amplitude; instead the subsequent 10-15 waves were analysed depending on the wave period.

4.2.1 Pressure measurements

Definition of pressure parameters

From pressure signals the following parameters were extracted from each individual event:

- p_1 and t_1: pressure and time of the beginning of the event;
- p_{max} and t_{max}: pressure and time of the maximum peak;
- p_2 and t_2: pressure and time at the end of the dynamic impulse (if the event was identified as impulsive);
- p_3 and t_3: pressure and time end of the event.

The beginning of the event was identified when the difference between two consecutive values of pressure was larger than a percentage of the maximum peak, i.e. $p_{i+1} - p_i > \%p_{max}$. The percentage was set at 0.01% for the 4 transducers above the SWL; while it was set at 0.005% for the 2 transducers under the still water level. Sometimes pre-oscillations, with the same frequency of the sampling occurred before the beginning of the event (Fig. 4.6a). These oscillations may be due to a resonance effect of the pressure transducer (natural frequency of 50 kHz), from imperceptible vibration of the bathymetry caused by the incoming wave. Thus, a further condition was given in order not to take them into account; i.e. $p_{i+2} - p_{i+1} > 0$ (so that the subsequent pressure step had to be positive).

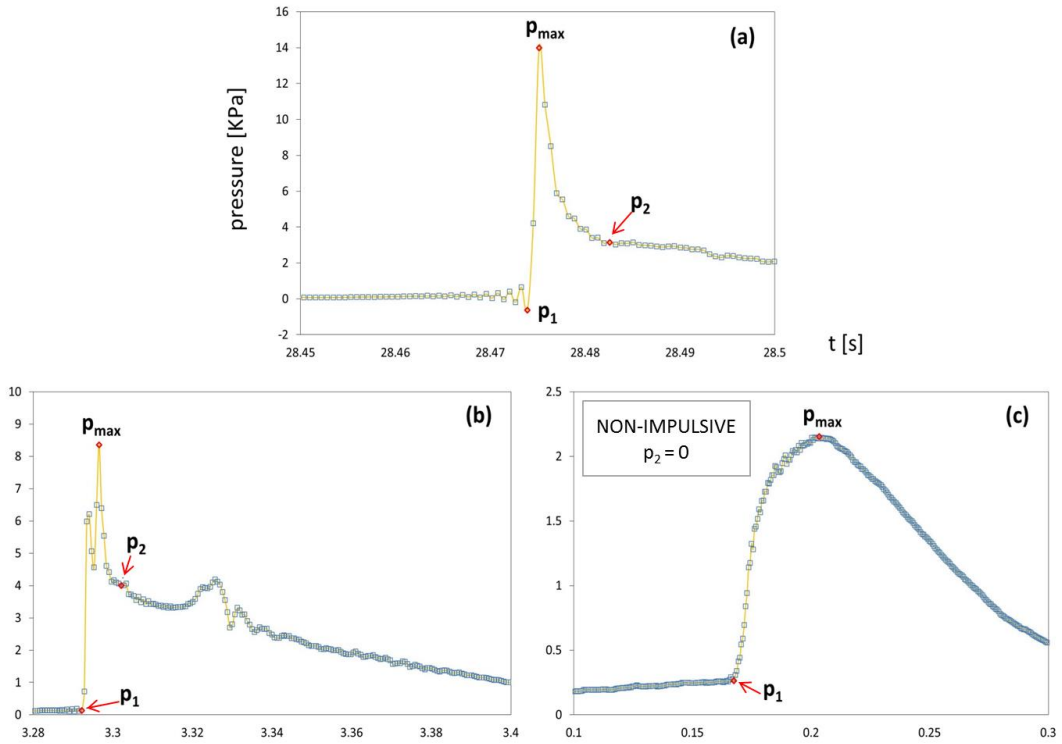

Figure 4.6: Three examples of pressure events: (a) and (b) are defined impulsive, (c) non-impulsive.

The end of the dynamic impulse was identified when the sum of two consecutive pressure steps (in absolute value) was lower than a fixed pressure value δ, i.e. $|p_{i+1} -$

$p_i| + |p_{i+2} - p_{i+1}| < \delta$ (Fig. 4.6a-b). The value of δ was set at 0.1 kPa ($\approx$ 0.01 m). If $p_{i+1} - p_i < 25\% p_{max}$, the event was then classified as non-impulsive and p_2 set to 0 (Fig. 4.6c).

The end of the event was identified when $p_3 = p_1$.

Vertical spatial distribution and time history of the line of action of the force

Vertical spatial distributions were determined by applying a linear interpolation between the measured pressures. As shown in Figure 4.7a, the spatial distribution was vertically extrapolated below the lowest transducer to the bottom and it was not extrapolated above the upper sensor. The spatial distribution was truncated on the top in order to avoid an unrealistic extrapolation above the measured run up on the model.

Elevations of the application force point were obtained by determining barycentre time histories (Z_G) of the vertical spatial distributions. In particular, the barycentre time history is the vertical component (Z) of the barycentre point calculated instant by instant according to the vertical spatial distribution defined above.

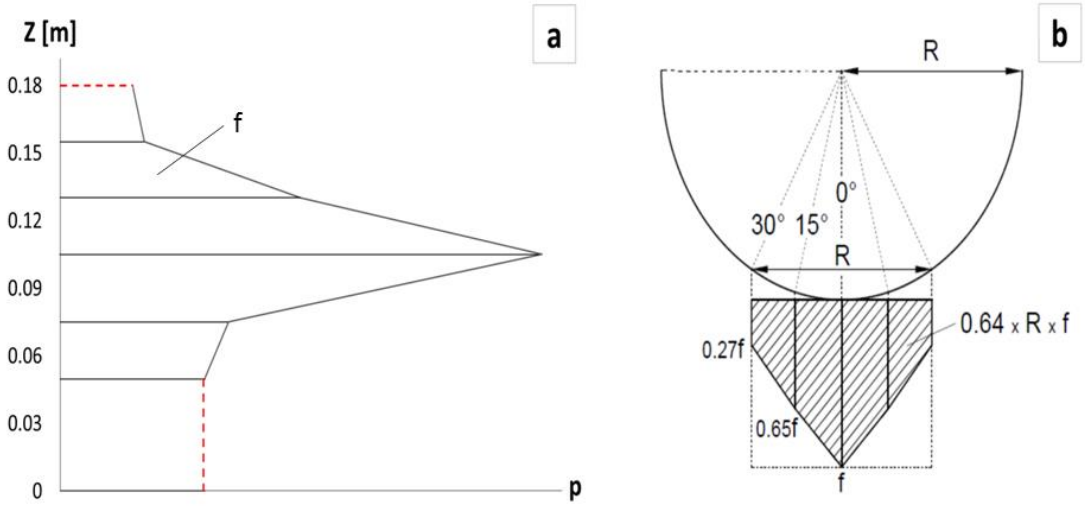

Figure 4.7: (a) Linear interpolation used to calculate the vertical spatial distribution and related in line force f; (b) azimuthal distribution for the estimation of the overall force F.

Azimuthal distribution and estimation of the overall force

The spatial integration of the pressure measurements gives the in-line force (f) at the front line of the cylindrical model (Fig. 4.7a). An estimation of the overall force (F_{int}) was obtained according to the azimuthal distribution derived from pressure measures shown in Wienke & Oumeraci (2005). They measured pressures around the vertical cylinder and they found that the pressures at $\pm 15^{\circ}$ and $\pm 30^{\circ}$ were 0.65 and 0.27 times lower than the pressure in line with the wave direction (i.e. at 0°). As a consequence, their azimuthal integration result is 0.64 times the size of a force line equally distributed along a horizontal extension equal to the radius of the cylinder (Fig. 4.7b). Note that the distance between $+30^{\circ}$ and -30° coincides with the radius of the cylinder (R) and for the present analysis it was fixed equal to 0.10 m. This value coincides with the radius of the cylinder which is continually under the SWL.

4.2.2 Load cells measurements

Horizontal force measured by load cells

The wave loads acted on the model with an overall force that caused deflections of the load cells. The load cells deflection subsequently caused a variation of the electronic signals (outputs) that are converted to force through the calibration. The two outputs represent the two horizontal components that balance the orthogonal component of the external load i.e. wave force. The sliding-pivot and the axial ball joints avoided the model being statically indeterminate (or hyperstatic). If this was the case, the horizontal component of the wave force would have not been totally absorbed by the load cells and, so, measurements would have been inaccurate. The horizontal wave force can be obtained by solving instant by instant the isostatic[1] scheme shown in Figure 4.8. In particular, it is possible to determine instant by instant the horzontal force (F_X) and its line of action (b_O) thanks the the equilibrium relationships (Equation 4.1 and 4.2).

[1] A structure is defined isostatic when the number of constraints equals the number of degrees of freedom of the structure.

$$F_X + R_1 + R_2 = 0 \tag{4.1}$$

$$M_O = F_X\, b_O + (R_2 - R_1)\, b = 0 \tag{4.2}$$

In the present investigation, the time history of the line of action of the horizontal force was determined on the basis of pressure spatial distributions due to the fact that the natural frequency of the load cell system did not enable the force-time history of the highly impulsive part of each impact event to be accurately recorded.

However, it should be noted that load cells provide the overall force (horizontal) that acts on the whole lighthouse model; instead the pressure integration provides an estimation of the overall force obtained from a force line (N/m). As a consequence, the maximum force peaks obtained by load cells are more robust when compared to the overall peak forces obtained by pressure integration.

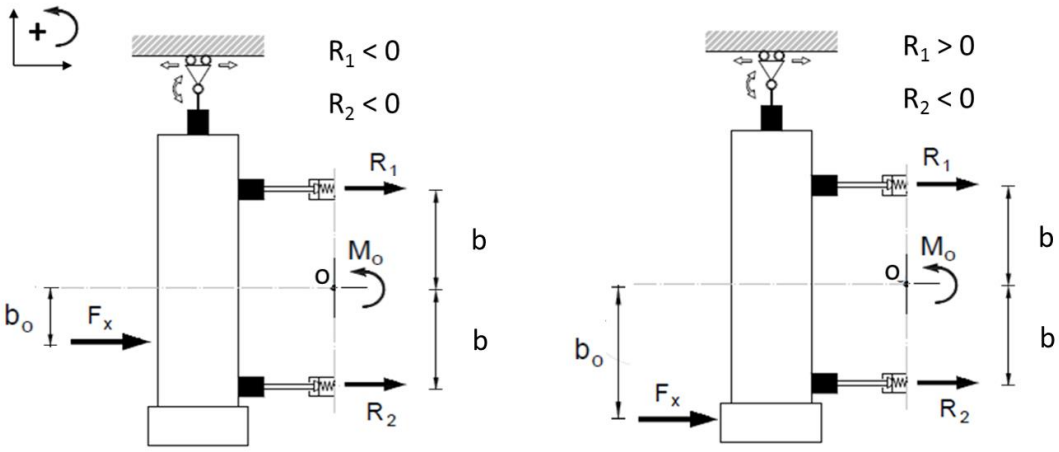

Figure 4.8: The structural isostatic scheme that allows the determination of the horizontal component of the wave force (Fx) by summing the load cells outputs (R1 and R2) simultaneously.

Natural frequencies of the system

The load cells are slightly deformable and the other components of the system (model,

framework and connectors) have a stiffness (K) that detracts from the ideal condition of infinite rigidity ($K = \infty$); thus, the whole system has its own natural frequency (f_n). The characteristics of the system do not affect the measurements when load frequencies (f_l) are lower than the natural frequencies of the system (i.e. for quasi-static events). However, for impulsive events, the load frequencies tend to increase and other forces (inertial, elastic and damped) occur when $f_l > f_n$. These forces generate in the signal a transient that depends on the characteristics of the system. Unfortunately, the transient tends to overlap the information related to the time history of the external force. In extreme cases, when $f_l = f_n$, the system enters into the resonance vibrations and the signal tends to be amplified, to infinity in an ideal condition i.e. $K = \infty$. It is not possible to analyse the natural frequency of the system from a theoretical point of view. This is because the stiffness of the system (K) and the water mass, involved during the breaking process, are not known. Thus, the frequency response of the system was empirically determined from the free oscillation of the model.

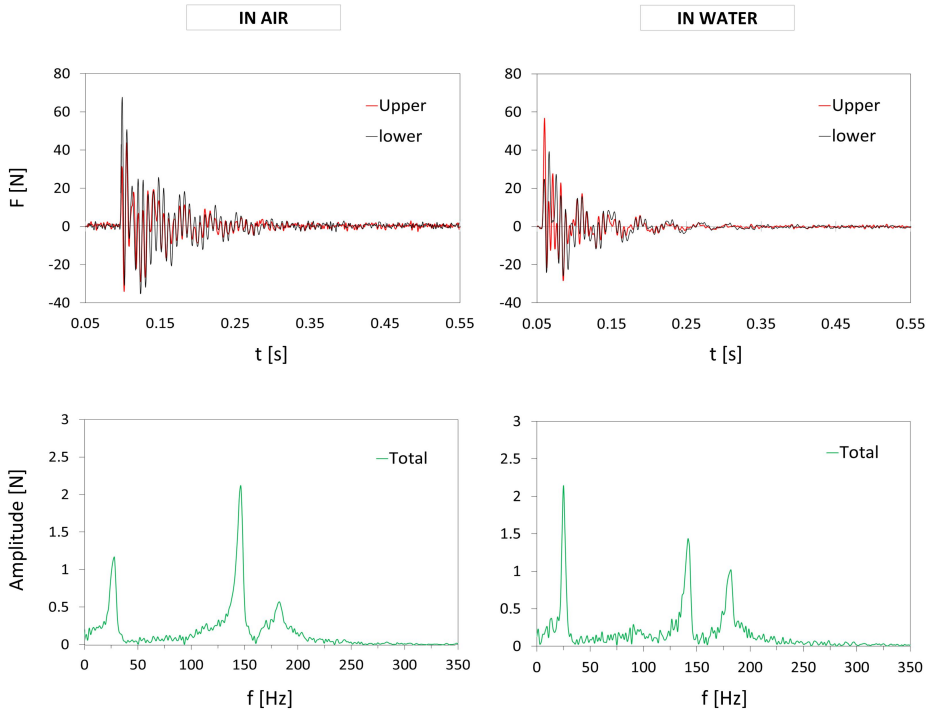

Figure 4.9: Load cells time histories for tap testing in order to obtain the natural frequencies of the system: in air (left) and in water (right).

The vibrations were caused by a total of 20 rapid and strong taps, applied on different points of the lighthouse model. This procedure was carried out both in air (with the flume empty) and in water (at the test depth); the results gave the same natural frequencies but with different amplitudes, as shown with two examples in Figure 4.9. The higher peak occurs at 140 Hz in air (i.e. oscillation period of 0.00714 s); while the higher peak is at 26 Hz (i.e. 0.038 s) when the model is slightly submerged to a depth of 0.095 m. This means that force peaks in time histories should not be followed by resonance oscillations when impact durations are longer than 0.038 s.

Calibration

Load cells are pre-calibrated by the supplier. However, in the present investigation, where forces were applied to the model and not directly to the devices, ad hoc calibrations were performed. Thus, vertical weight-forces were horizontally applied to the model using a pulley system (Fig. 4.10). Three different calibrations were performed applying the force at three different points on the model (1st case, 2nd case and 3rd case), as shown in Figure 4.10.

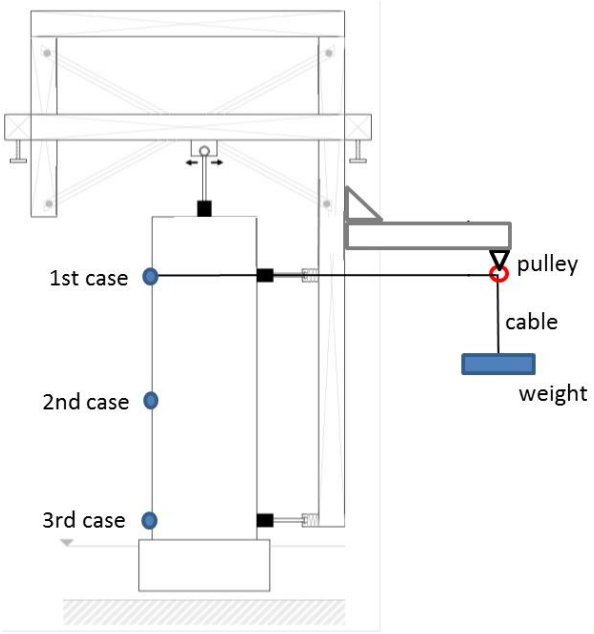

Figure 4.10: Sketch of the pulley system used for the calibration in 3 different points.

For each calibration, data were acquired using five weights. The angular coefficients given by the calibration are 0.0016 for the lower load cell and 0.0018 for the upper load cell (Fig. 4.11). The values provided by the supplier are 0.00157 and 0.00176 respectively, thus 1.9% and 2.3% lower. This discrepancy could be given by several factors, e.g. friction in the pulley system, stiffness of the load cell system and pully cables that are different from the ideal condition of infinity, different extension of the load cell cables and different environments of electronic noise.

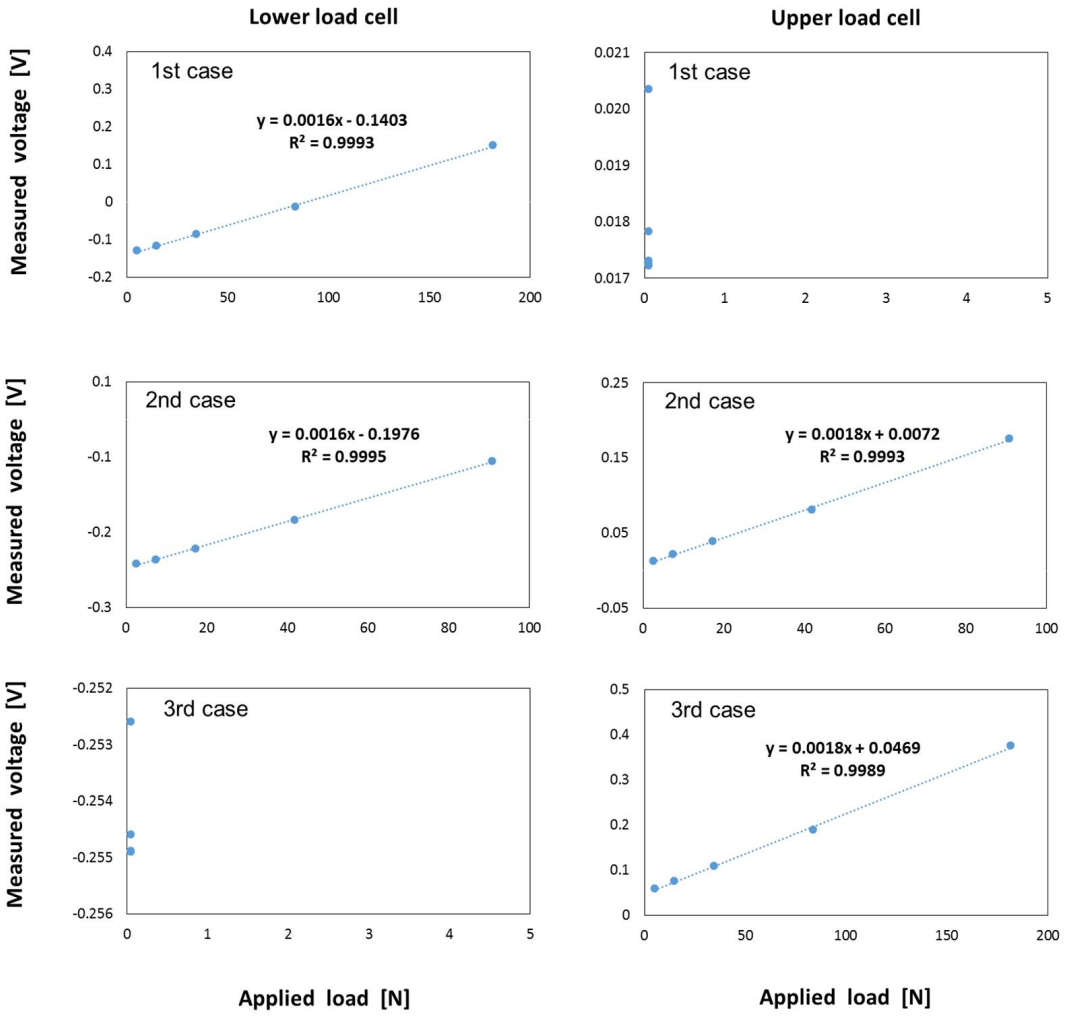

Figure 4.11: Result of the three different calibrations.

Note that the two graphs in the corners (upper right and lower left) are related to the

two load conditions (1st case) and (3rd case). In these conditions the measurement should be 0 for the unloaded load cell. The difference in measurements is related to the small variations of the average value of the signal due to the electronic noise.

Filtering

Load signals were passed through a low pass filter with a cut-off frequency set at 250 Hz, so that only the high frequency electronic noise was eliminated. The filtering was performed using a Butterworth filter of order 3.

Chapter 5

Structural response of the Eddystone lighthouse

THE UK winter storms of 2013-2014 caused more than 3000 geophone-registered events on the Eddystone lighthouse (see Raby et al., 2015). The oscillation of the Eddystone lighthouse, in terms of accelerations and displacements, were obtained from the velocity signals recorded by the geophones as previously described. These signals may be considered as three outputs generated by an input, i.e. the impulse of the wave ($I = \int F\ dt$). This way, the structure may be considered to be a 'filter' that transforms the input signal (Fig. 5.1).

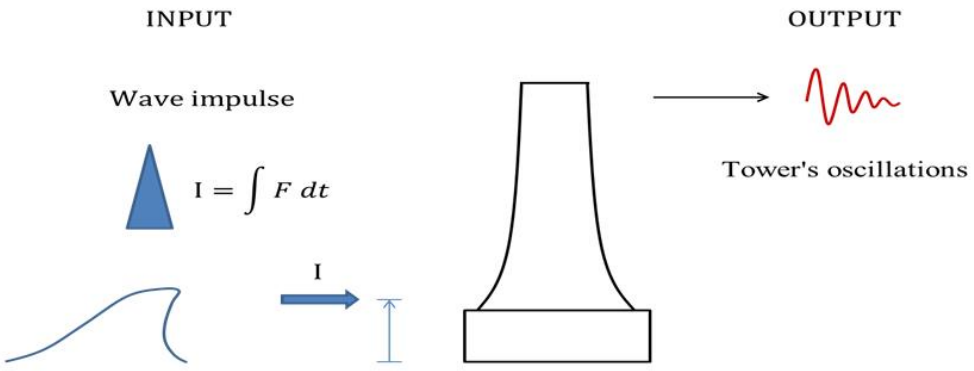

Figure 5.1: Wave impulse (input) and tower oscillations (output).

In this Chapter the structural responses of the Eddystone lighthouse are analysed and described. In particular, Section 5.1 illustrates three analysis steps that led the identification and classification of four main structural response types. The dynamic response classification is provided on the basis of the impulsivity of geophone signals. Then, the

structural responses are related to the video images in order to provide a qualitative description of the wave field. Finally, the effects of statistical wave data on the structural responses are investigated in Section 5.2. As it will be shown in Section 5.2, the random sea-state tends to mask any trend for velocities or displacements under 2 mm/s or 0.02 mm respectively. As a consequence, most of the observations provided in this Chapter are related to an extreme portion of the data set. This portion includes 164 geophone-registered events that have velocities or displacements larger than 2 mm/s or 0.02 mm respectively.

5.1 Identification and classification of the structural responses

Visual observation and structural behaviours

The first step of the structural analysis consisted of a visual observation of geophone signals. As for the wave load time histories described in the literature review, the structural responses of the Eddystone lighthouse show different behaviours to wave impacts. Although the structural responses vary gradually in their behaviour, four main types can be identified and they are shown in Figure 5.2. As may be observed from Figure 5.2, shapes of peaks in signals (displacement, velocity and acceleration) tend to be generally less sharp moving from Type 1 to Type 4. Simultaneously to the previous observation, the contribution of higher frequency contents decreases moving from Type 1 to Type 4 (Figure 5.3).

Thanks to the visual observations of frequency signals (power spectra), it was noted that higher frequencies in the structural response tend to show a predominant sharp peak in the velocity time history. Both sharp peaks and higher frequencies have been often used as an indicator of the impulsivity (Sections 2.2.3 and 2.4.3). In particular, the ratio of the two maximum peaks is used in the parameter map to categorise wave loading either in impact or non-impact (Kortenhaus & Oumeraci, 1998) (Section 2.4.2). Similarly, higher frequencies in structural responses are related to rapid shock loads (Clough & Penzien, 1975; Loraux, 2013) (Sections 2.4.3 and 3.1.2).

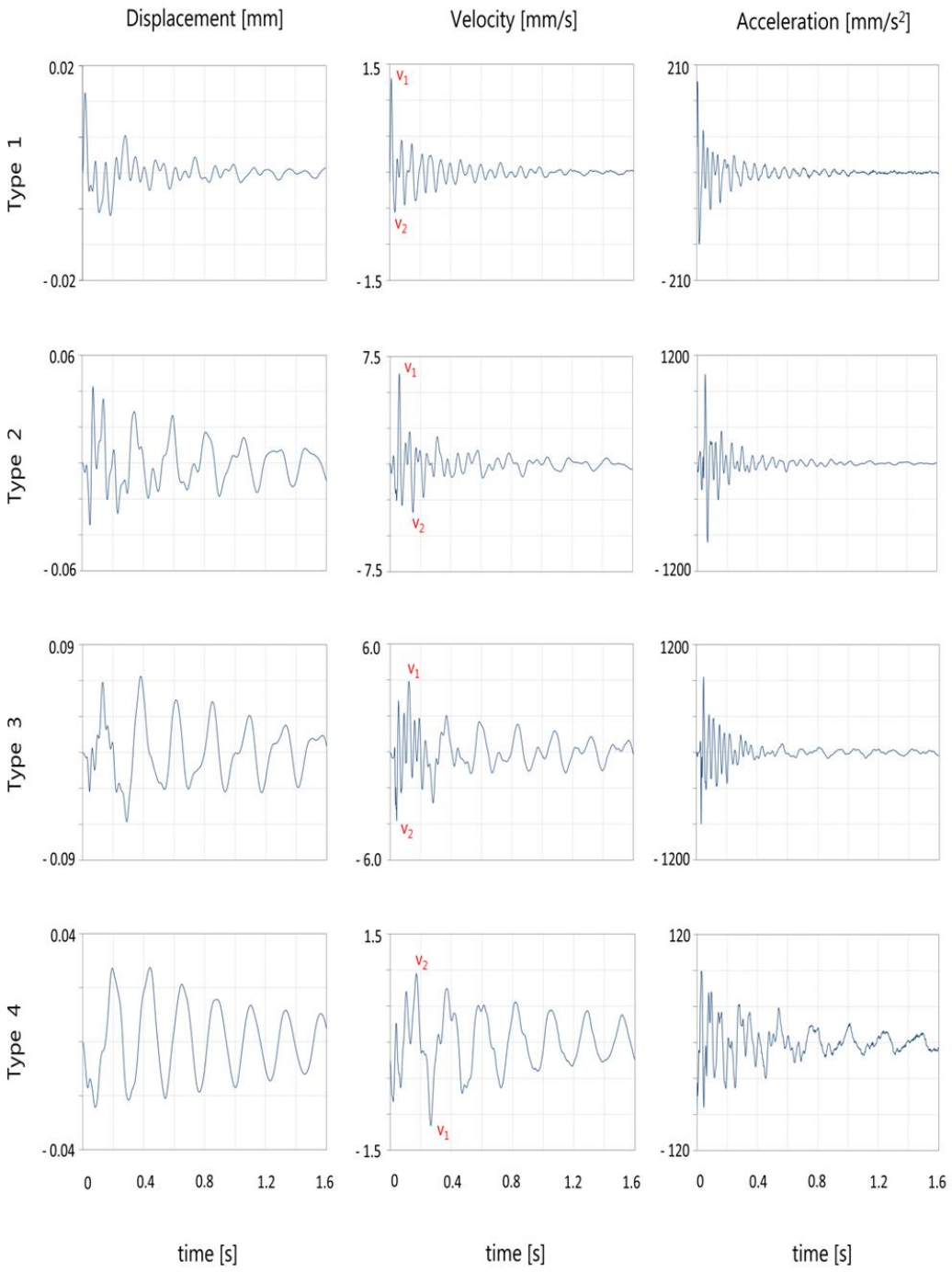

Figure 5.2: Comparison between displacement, velocity and acceleration time histories of the four representative structural types. Note that vertical axes have different maximum values.

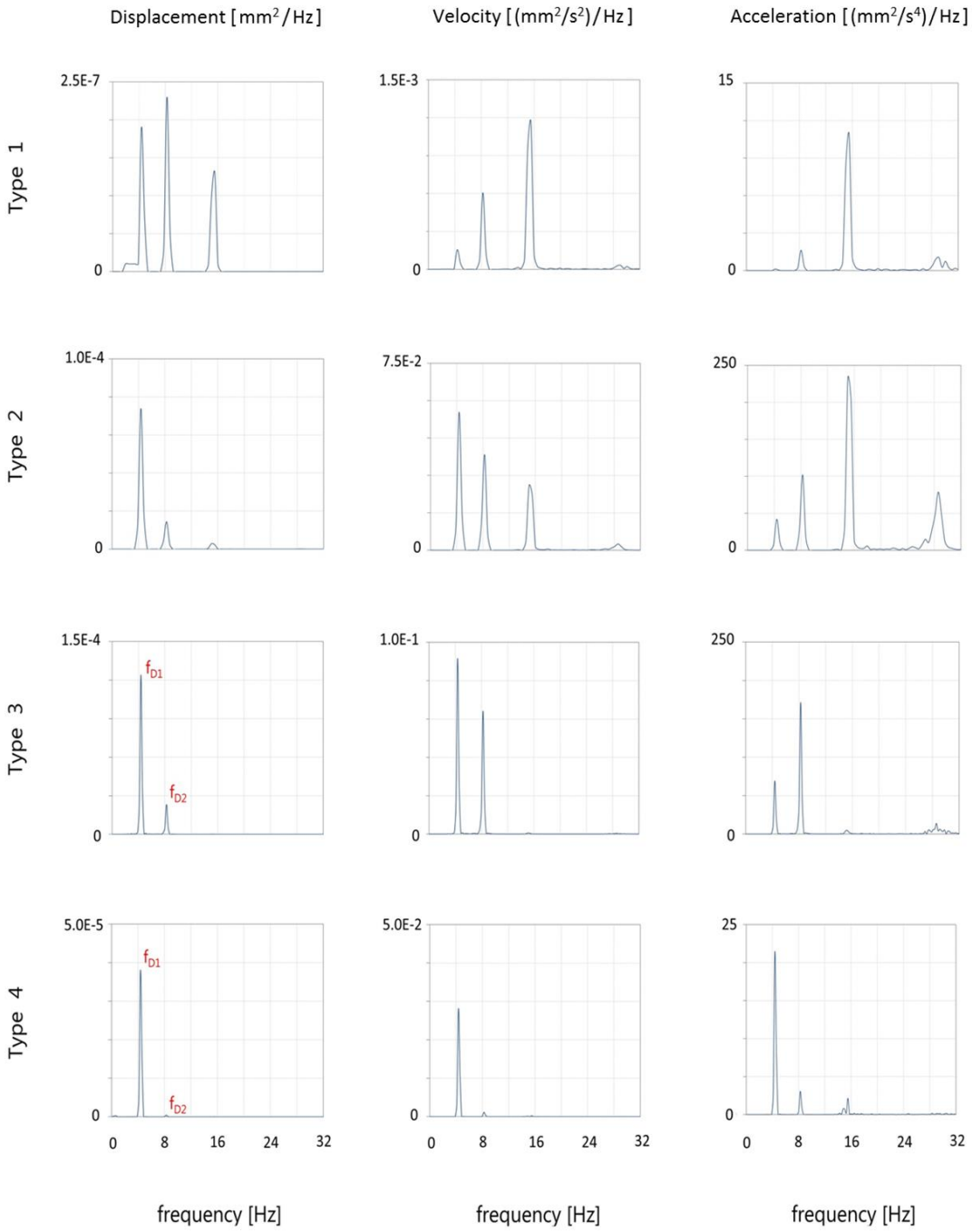

Figure 5.3: Comparison between the displacement, velocity and acceleration power spectra of the four representative structural types. Note that vertical axes have different maximum values.

Repeatability of structural characteristics

The second step of the structural study consisted in analysing quantitative characteristics of geophone signals. It was noted that structural responses exhibit a systematic repeatability of signal characteristics according to the different behaviours observed. In particular, the repeatability of characteristics includes:

- time of occurrence of the maximum peak in structural velocity time history;
- harmonic contributions related to structural frequencies;
- time of occurrence of the maximum peak in structural displacement time history;
- magnitude of the maximum peak in structural displacement time history;

In more detail the repeatability of characteristics for the four main types is as follows.

Type 1: structural responses are characterised by high frequency content. Both maximum velocity and displacement peaks occur before 0.1 s. Although the maximum velocity peak can have relatively high values (3-4 mm/s), the maximum displacement peak is relatively small (less than 0.02 mm).

When the previous characteristics occur, the velocity time history has usually an extreme sharp predominant peak and a very high oscillation frequency.

Type 2: structural responses are characterised by high frequency content. Both maximum velocity and displacement peaks occur before 0.2 s and they can have high values, i.e. 5-12 mm/s and at least 0.02 mm respectively.

When the previous characteristics occur, the velocity time history is characterised by a predominant sharp peak and high oscillation frequencies.

Type 3: structural responses are characterised by high and low frequency contents. The maximum velocity occurs before 0.2 s; in contrast the maximum displacement peak occurs after 0.2 s. Velocity peak can have modestly large values (5 mm/s) and displacements can be larger than 0.02 mm.

When these characteristics occur, the velocity time history is characterised by an initial irregular oscillation, which occurs with overlapping high frequencies, followed by a smaller damped low frequency oscillation.

Type 4: structural responses are characterised by low frequency content. Maximum velocity and maximum displacement occur after 0.2 s. Despite velocity peaks being relatively low (less than 3 mm/s), displacemet peaks can be larger than 0.02 mm.

When the previous characteristics occur, the velocity time history is characterised by a damped oscillation that gradually decays with a low frequency.

Classification criteria

The third step of structural analysis consisted of identifying a methodology to categorise the four structural behaviours according to repeatability of the signal characteristics described above. A classification based on video images from cameras, which are located on the top of the lighthouse, would not have allowed classifying the structural responses in a quantitative and systematic manner due to the difficulty of obtaining accurate estimations of local hydraulic variables (breaking wave height, mean water level, etc.). As a consequence, the classification has been developed on the basis of ratios of peaks in the structural responses.

As previously mentioned, higher frequencies in the structural response are associated with a predominant peak in the velocity time history. Thus, the ratio of the two highest peaks (in absolute value) in the velocity time history, i.e. $|V_1/V_2|$, has been found to be a robust discriminator for Type 1 and 2. Type 3 and 4 are not characterised by a predominant peak in velocity time histories; thus, they have been classified on the basis of the ratio of two highest peaks in the displacement power spectrum (f_{D1}/f_{D2}). The transition values of the ratio limits are shown in Table 5.1. The values have been identified by analysing the repeatability of the time of occurence of the maximum velocity and displacement peak for the extreme portion of data set i.e. for the events with velocities or displacements larger than 2 mm/s or 0.02 mm respectively.

Table 5.1: Ratio limits ($|V_1/V_2|$, f_{D1}/f_{D2}) and percentage of events exhibiting the following structural characteristics: t (V_1), t (D_1), V_1 and D_1

Type	t (V_1) [s]	t (D_1) [s]	V_1 [mm/s]	D_1 [mm]	$\lvert V_1/V_2\rvert$	f_{D1}/f_{D2}	% events
1	< 0.1	< 0.1	< 5	< 0.02	≥ 2	N/A	100%
2	< 0.2	< 0.2	< 12	> 0.02	1.5 - 2	N/A	92%
3	< 0.2	> 0.2	< 5	> 0.02	≤ 1.5	≤ 10	86%
4	> 0.2	> 0.2	< 3	> 0.02	≤ 1.5	> 10	89%

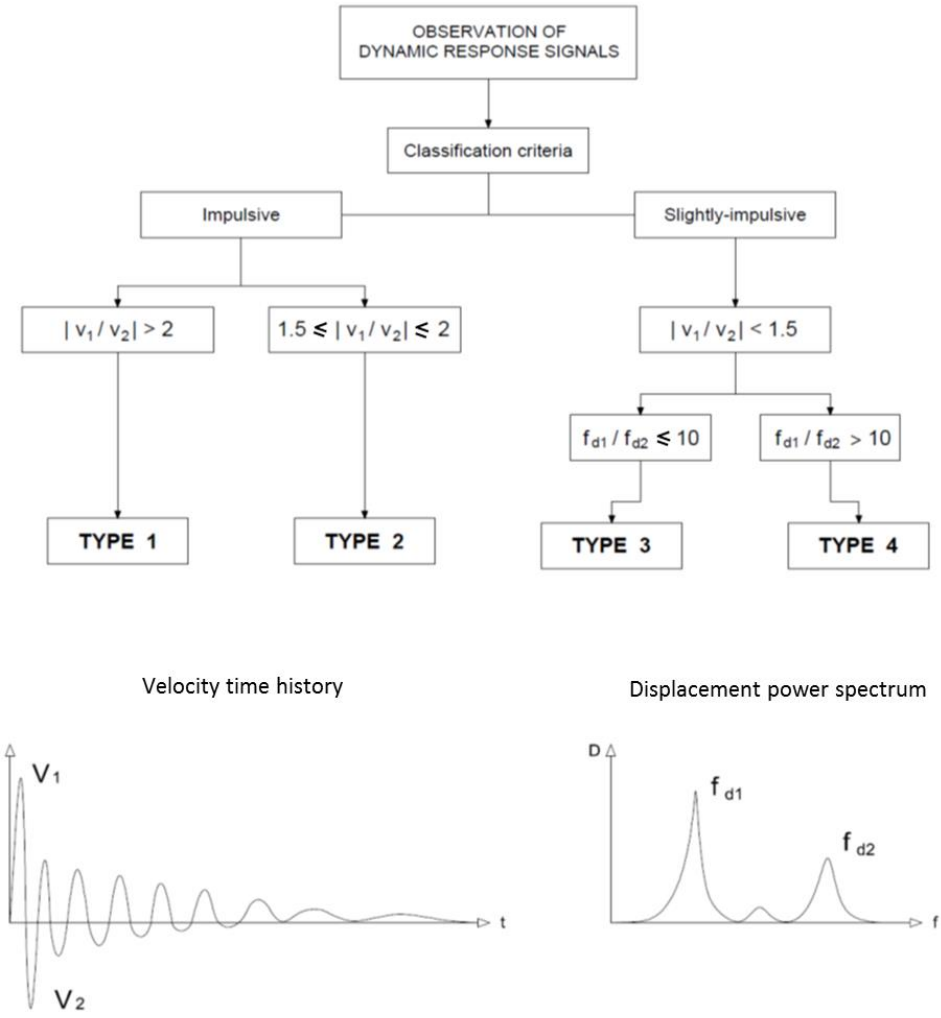

Figure 5.4: Procedure and criteria for the response type classification.

As can be observed from Table 5.1, 100% of the events have the time characteristics described in Type 1 when $|V_1/V_2| > 2$; 92% of the events have the time characteristics described in Type 2 when $1.5 \leq |V_1/V_2| \leq 2$. When $|V_1/V_2| < 1.5$, 86% of the events have the time characteristics described in Type 3 if $f_{D1}/f_{D2} > 10$ and 89% of the events have the time characteristics described in Type 4 if $f_{D1}/f_{D2} \leq 10$. Concerning Type 3 and 4, a good distinction was found by setting the ratio between the two maximum peaks in the velocity power spectra equal to 10. However, for a few transition events, a better discriminator was found by applying the same ratio to the displacement power spectra. Thus, the dynamic responses have been classified in the four final types with the procedure shown in Figure 5.4. Due to the fact that Type 1 and 2 are characterised by a predominant sharp peak and higher frequency content, they are defined *impulsive*, in contrast Type 3 and 4 are defined *slightly-impulsive*.

5.1.1 Description of four representative structural events

The four representative structural events used to exibhit the different structural behaviours in Figure 5.2 and 5.3, are here described in more detail in order to highlight the different nature of the response types in terms of displacements, velocities and accelerations. Because the vertical components (Z) of the geophone signals are negligible compared to those from the horizontal plane (X-Y), signals are presented from oscillations along the principal direction in the horizontal plane, determined by Principal Component Analysis (Appendix D). The types of the structural responses are described from Type 1 to Type 4 (i.e. following the impulsivity order). The four events have been chosen within the structural events that occurred during the daylight, so that their corresponding video images can be discussed. Observations related to the largest events associated with the four types will be discussed in Section 5.1.3.

- **Event 1**: $|V_1/V_2| > 2$

Figure 5.5 shows an event as representative of Type 1. As may be observed from

Figure 5.5a, the maximum displacement peak is more than double any other peak. Moreover, it is the first peak of the whole signal.

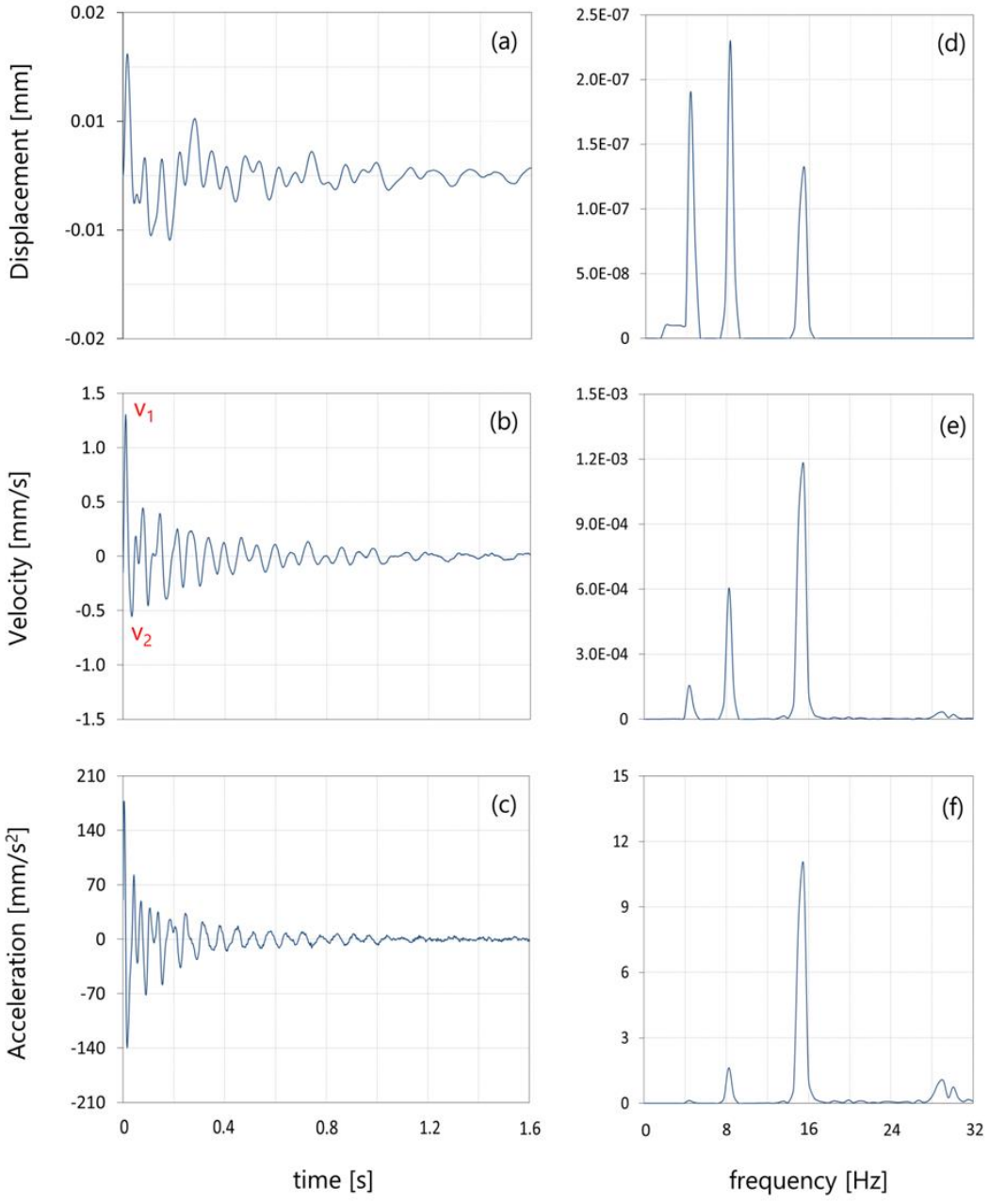

Figure 5.5: Structural response classified as Type 1: (a) displacement (b) velocity and (c) acceleration time histories; (d) displacement (e) velocity and (f) acceleration power spectra.

Similarly, the velocity signal is characterised by a single sharp peak (1.3 mm/s) that is

more than twice any other peak in absolute value (approximately 2.2 times the second highest peak) (Figure 5.5b). The maximum velocity peak is the first peak of the signal, which then decays gradually with very small amplitudes and very high frequencies.

The acceleration signal tends to show a symmetric signal with a sharp negative peak with a similar value to the larger positive one (175 mm/s^2) (Fig. 5.5c).

The displacement power spectrum is characterised by components at frequencies of about 4, 8 and 15 Hz (Fig. 5.5d). In the velocity power spectrum a component at 28 Hz is also slightly visible (Fig. 5.5e). The component at 28 Hz is more visible in the acceleration power spectrum, whilst the one at 4 Hz tends to disappear (Fig. 5.5f). Therefore, as may be observed, the four harmonics of the structure are at approximately 4, 8, 15 and 28 Hz (Section 3.1.2). The highest frequencies tend to be less evident moving from acceleration to displacement. This is mainly an effect of the integration process given by the fact that when the displacement has completed a quarter of cycle, the velocity has completed half cycle and the acceleration one cycle (Appendix E). In addition, due to the fact that the integrated signal is the variation of the area under the starting signal, flickering variations of the starting signal tend to generate negligible variation over the whole area.

As may be observed from Figure 5.5, the amplitude of the first natural frequency of the structure, at 4 Hz, is never the largest in any of the three power spectra. Consequently, this event is characterised by predominant high frequencies and, hence, it is caused by a strong impulsive shock load as required for a Type 1 event (Section 3.1.2).

- **Event 2**: $1.5 \leq |V_1/V_2| \leq 2$

Figure 5.6 shows an event as representative of Type 2. This type shows larger peak values with respect to Event 1. However, both events share a number of similarities.

As in Event 1, maximum displacement and velocity (0.042 mm and 6.1 mm/s) occur in the first part of the signals, approximately at 0.1 s, and they are correlated (Fig. 5.6a-b).

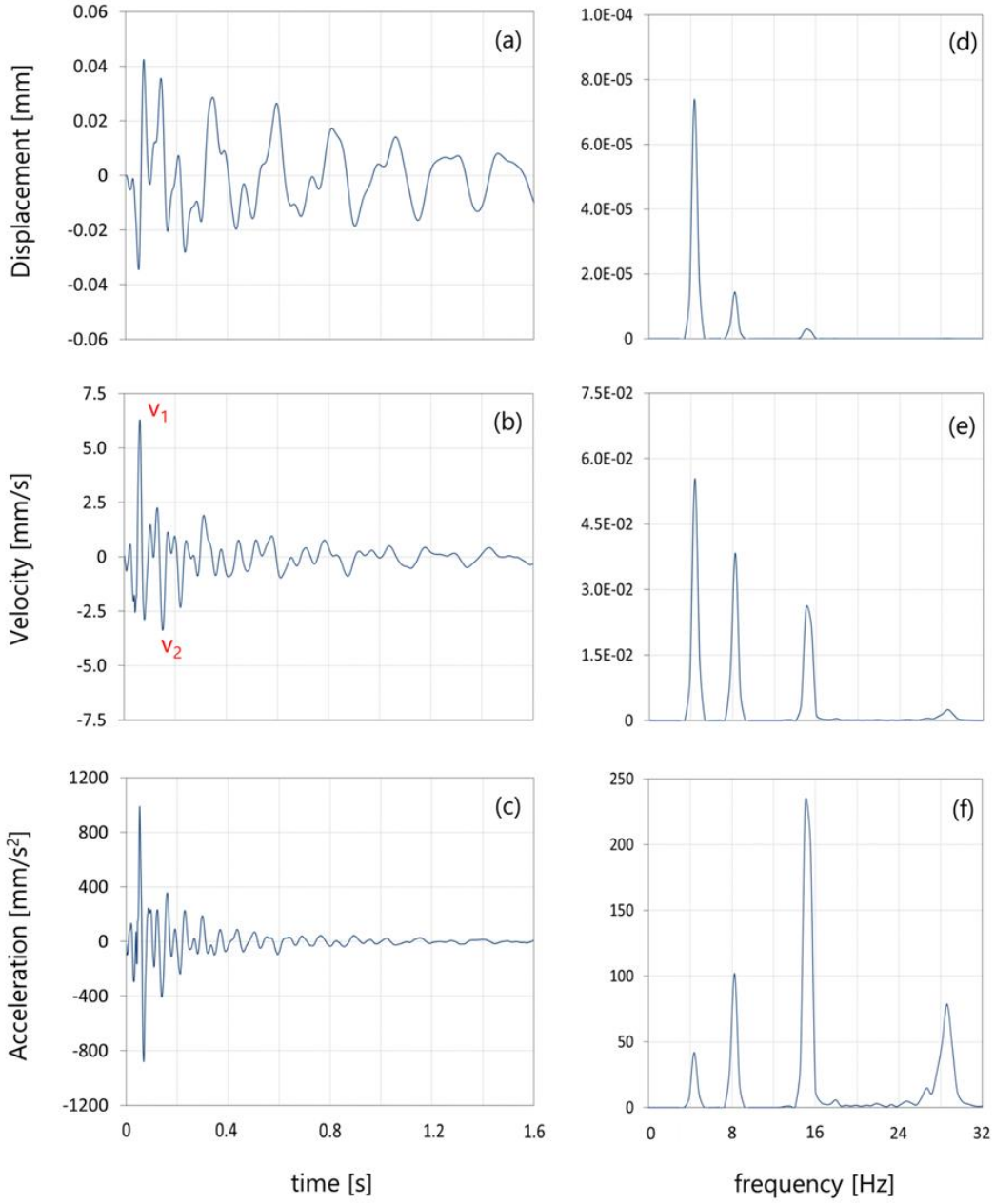

Figure 5.6: Structural response classified as Type 2: (a) displacement (b) velocity and (c) acceleration time histories; (d) displacement (e) velocity and (f) acceleration power spectra.

Note that when the displacement is maximum, the velocity is null; thus, the maximum displacement is related to the previous peak in the velocity time history (Appendix E). However, these two peaks do not occur immediately as in Event 1 and in the velocity signal the ratio between the two largest peaks is less than 2 (approximately 1.8 in

Figure 5.6b). Moreover, while the velocity signal of Event 1 tends to decay gradually, Event 2 tends to be more irregular after the first peak.

The acceleration signal has a double symmetric sharp peak ($\pm$ 1000 mm/s^2); then, the signal is dramatically damped (Fig. 5.6c).

Also, the power spectra of Event 2 tends to show all the same four frequency components of Event 1, i.e. 4, 8, 15 and 28 Hz (Fig. 5.6d-e-f). However, amplitudes at the highest frequencies tend to be lower in Event 2 especially for the displacement and velocity power spectra.

- **Event 3**: $|V_1/V_2| < 1.5$ and $f_{D1}/f_{D2} > 10$

Figure 5.7 shows an event as representative of Type 3. The similarities exhibited by Event 1 and 2 tend to disappear in Event 3. The maximum displacement peak (0.064 mm) does not occur at the beginning of the signal, but at approximately 0.4 s (Fig. 5.7a). Before this maximum peak, the displacement signal is dominated by two main frequency components. Then, the signal slowly decays with a dominant frequency component (Fig. 5.7a).

The velocity signal is characterised by two distinct phases (Fig. 5.7b). The first part, until approximately 0.3 s, exhibits irregular oscillations with high frequencies and the ratio of the two highest peak is lower than 1.5, as was the case in Event 1 and 2. Subsequently, the decay of the signal is gradual and, with low frequencies and with relatively high amplitudes. As a result of this lower frequency, the maximum displacement occurs in this second part of the velocity signal.

As may be observed from Figure 5.7b, the maximum velocity peaks, of approximately 4 mm/s, occur at 0.05 s and 0.12 s, but the maximum displacement occurs at 0.4 s and is related to a velocity peak of 2 mm/s (Fig. 5.7a). Consequently, this means that, from a mathematical point of view, the decrease of the oscillation frequency is fundamental to generate the maximum displacement peak. From a physical point of view,

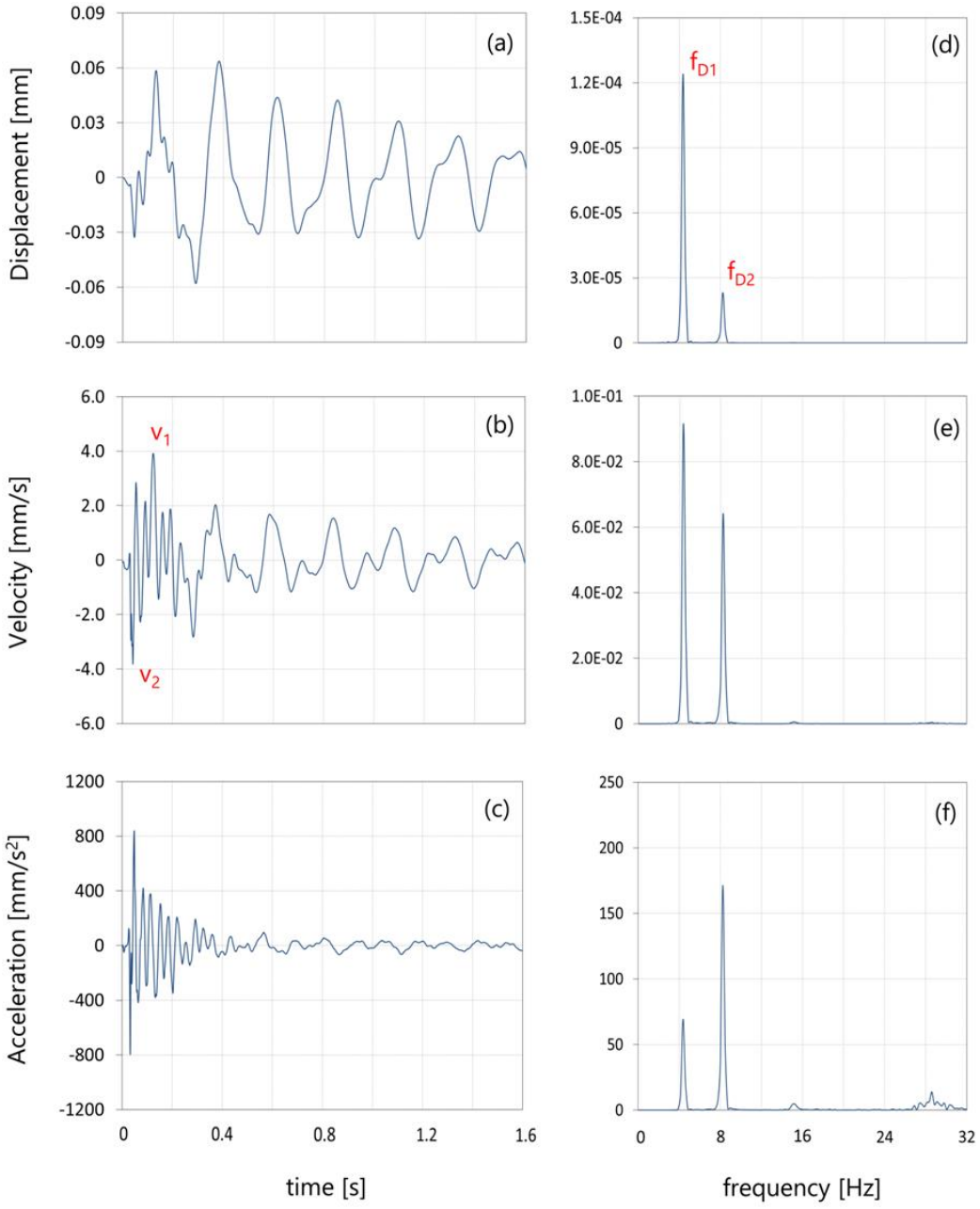

Figure 5.7: Structural response classified as Type 3: (a) displacement (b) velocity and (c) acceleration time histories; (d) displacement (e) velocity and (f) acceleration power spectra.

the lighthouse starts to vibrate with small amplitudes and high velocities; subsequently, the displacement amplitudes increase and, simultaneously, the velocity oscillations decrease.

The acceleration signal is characterised by a compact oscillation (Fig. 5.7c); after the maximum symmetric peaks ($\sim$ 800 mm/s^2) a gradual decay can be observed.

The frequency component at 15 Hz, which is visible in Event 1 and 2, tends to disappear in the displacement and velocity power spectra of Event 3 (Fig. 5.7d-e). The frequency at 4 Hz is the predominant one in both spectra, although the frequency contribution at 8 Hz is similar to the one at 4 Hz in the velocity. In the acceleration power spectrum, the component at 8 Hz is predominant (Fig. 5.7f); whilst the components at 15 and 28 Hz become less evident.

Note that Event 3 shows a greater displacement (0.064 mm) if compared to Event 2 (0.042 mm), even if Event 2 is characterised by larger velocity and acceleration (6 mm/s and 1000 mm/s^2) with respect to Event 3 (4 mm/s and 800 mm/s^2).

- **Type 4**: $|V_1/V_2| < 1.5$ and $f_{D1}/f_{D2} \leq 10$

Figure 5.8 shows an event as representative of Type 4. Like Event 1 and 2, Event 3 and 4 also exhibit several similarities between them. The maximum displacement peak (0.028 mm) does not occur at the beginning of the signal, but at 0.3 s, even if the previous peak is very similar (Fig. 5.8a). Compared to Event 3, the displacement signal is essentially given by only one frequency component. Consequently, it appears as a damped sinusoidal signal. Moving from Event 1 to Event 4, the decay of the displacement signals occurs with oscillations that tend to be essentially dominated by one frequency component.

Similarly to Event 3, in the velocity signal the ratio between the two highest peaks is lower than 1.5 (Fig. 5.8b). The maximum peak (-1.15 mm/s) occurs in the first part of the signal; i.e. at 0.3 s. In this first part, the signal is given by the composition of two low frequencies; then, the oscillations become increasingly dominated by one low frequency component. The velocity peak, related to the maximum displacement (0.4 s), is relatively low (0.8 mm/s) (Fig. 5.8a).

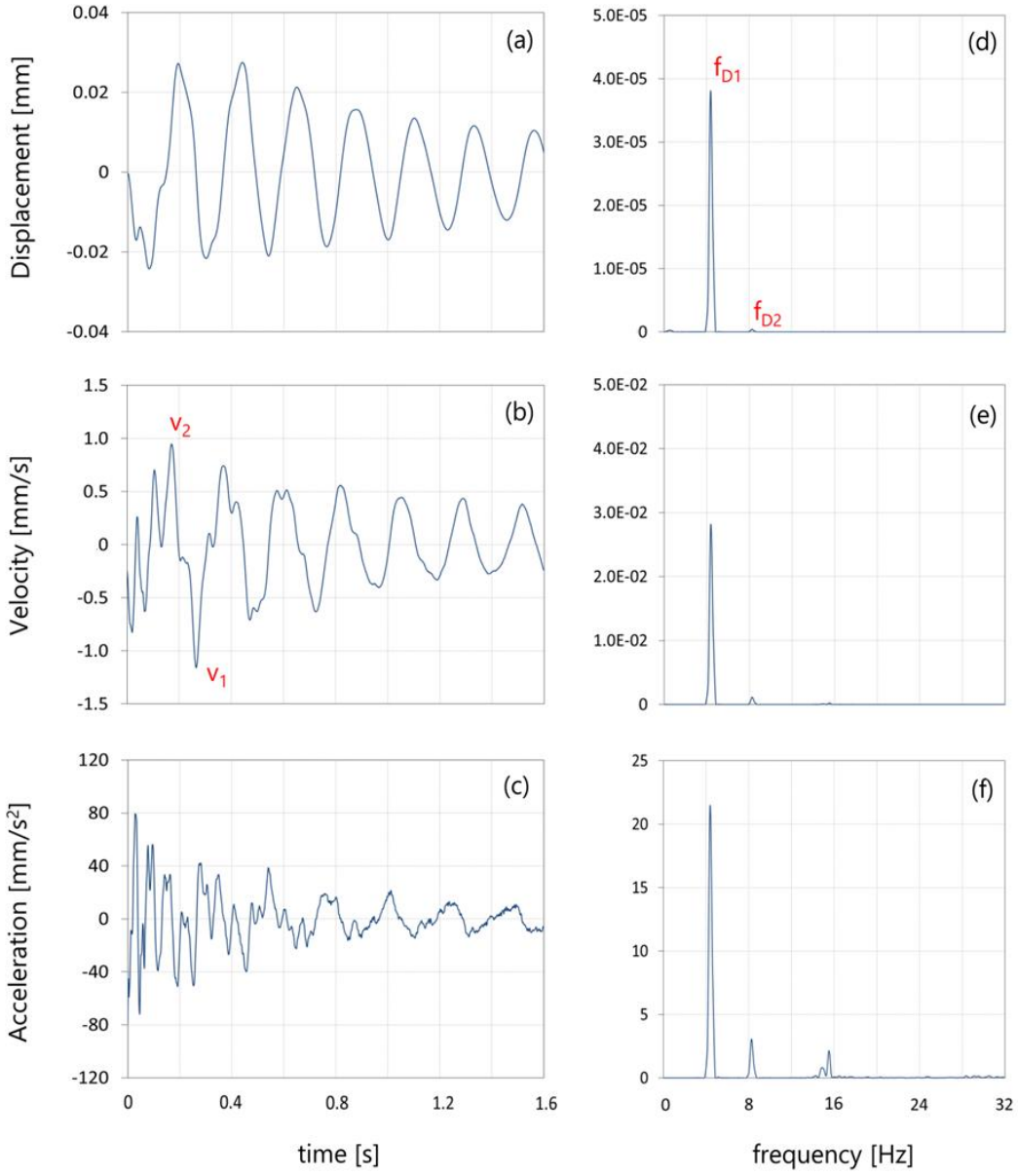

Figure 5.8: Structural response classified as Type 4: (a) displacement (b) velocity and (c) acceleration time histories; (d) displacement (e) velocity and (f) acceleration power spectra.

The acceleration signal of Event 4 is quite different compared to the previous three events: there is no symmetric double sharp peak (Fig. 5.8c). Instead, the signal appears quite flickering with some sudden small spikes. Usually, the maximum value is relatively low (-75 mm/s^2).

In contrast to Event 3, for Event 4 the frequency contribution at 8 Hz tends to disappear

in the displacement and velocity power spectra, which are only characterised by the low natural frequency at 4 Hz (Fig. 5.8d-e). In the velocity power spectrum the component at 8 Hz is barely visible; however, this is one order of magnitude lower than that one at 4 Hz. In the acceleration power spectrum, the components at 8 and 15 Hz tend to increase, even if they are still very low compared to the predominant frequency at 4 Hz (Fig. 5.8f). In addition, the power spectra show that the higher frequencies tend to disappear passing from Type 1 to Type 4.

Note that the Event 4 shows a larger displacement (0.028 mm) when compared to Event 1 (0.011 mm), even if Event 1 is characterised by larger velocity and acceleration (1.3 mm/s and 175 mm/s^2) with respect to Event 4 (1.15 mm/s and 75 mm/s^2).

5.1.2 Field observations on wave hydrodynamics

Low frame-rate (5 Hz) video images of the four representative impact events, used to describe the four response types in Section 5.1.1, are shown in Figures 5.9 to 5.12. The four events occurred in different phases of the two severest storms (Petra and Hercules) that occurred in 2013-2014 winter. During this period, the southwest coast of England was hit by an unprecedented sequence of very energetic wave conditions, including four extremely energetic and named storms. According to the Met Office, the storm Hercules on 6 January 2014 was a 1:5 to 1:10 year wave event, whereas the storm Petra on 5 February 2014 was probably the most damaging storm in terms of coastal impact on the south coast of Devon and Cornwall for the last 50 years (Metoffice, 2016). Furthermore, analysis of modelled and measured wave data showed that the 8-week sequence of storms from mid-December 2013 to 10 February 2014 represented the most energetic period of waves to have hit the southwest coast of England since 1950 (Metoffice, 2016). According to Draper (1991) (as cited by BGS, 1996), in the Eddystone region maximum winter (local) wave heights exceed 3 m for 10 % of the time with a 1:50 year maximum wave height greater than 20 m. Offshore details ($H_{s,o}$, T_p, β) of the four events, with their respective date/time and instantaneous water level,

are given in Table 5.2. The water levels refers to BODC's measurement (CD).

Table 5.2: Storm details for the four representative impact types.

Type	Storm	Date and time	$H_{s,o}$ [m]	T_p [s]	CD [m]	β [°]
1	*Hercules* (W) Beginning of the storm	04/02/2014 11:36 a.m.	1.81	11.9	4.41	220
2	*Petra* (SW) Peak of the storm	06/01/2014 08:34 a.m.	3.21	10.5	5.96	230
3	*Hercules* (W) Peak of the storm	05/02/2014 09:13 a.m.	5.95	13.3	6.06	233
4	*Petra* (SW) After the storm	06/01/2014 01:34 p.m.	3.11	18.2	2.44	237

Simple sketches at the top of Figures 5.9-5.12 indicate, with blue lines, the field of view of each of the four cameras (see Section 3.1.3 for more details of their orientation). The two cameras aligned to SW, from which larger waves attack the structure (blue arrow on the top of the figures), correspond to Columns 1 and 2. Column 1 corresponds to the camera with the view towards the 'far-field', whereas Column 2 corresponds to the frames from the camera angled downwards. Both Columns 3 and 4 show downwards-pointing views from cameras aligned ESE and NNW, respectively (to the lateral sides with respect to the wave attack).

In order to compare the different events, each subsequent row of the four Figure 5.9-5.12 shows video frames with the same time step (1 s). In addition, the wave front is highlighted with a red line, which is solid when the wave front is stable and dashed when the wave is broken.

- **Event 1**

Figure 5.9 shows the wave event that corresponds to the structural response used to describe Type 1. This event occurred at the beginning of storm Hercules on 4/2/2014

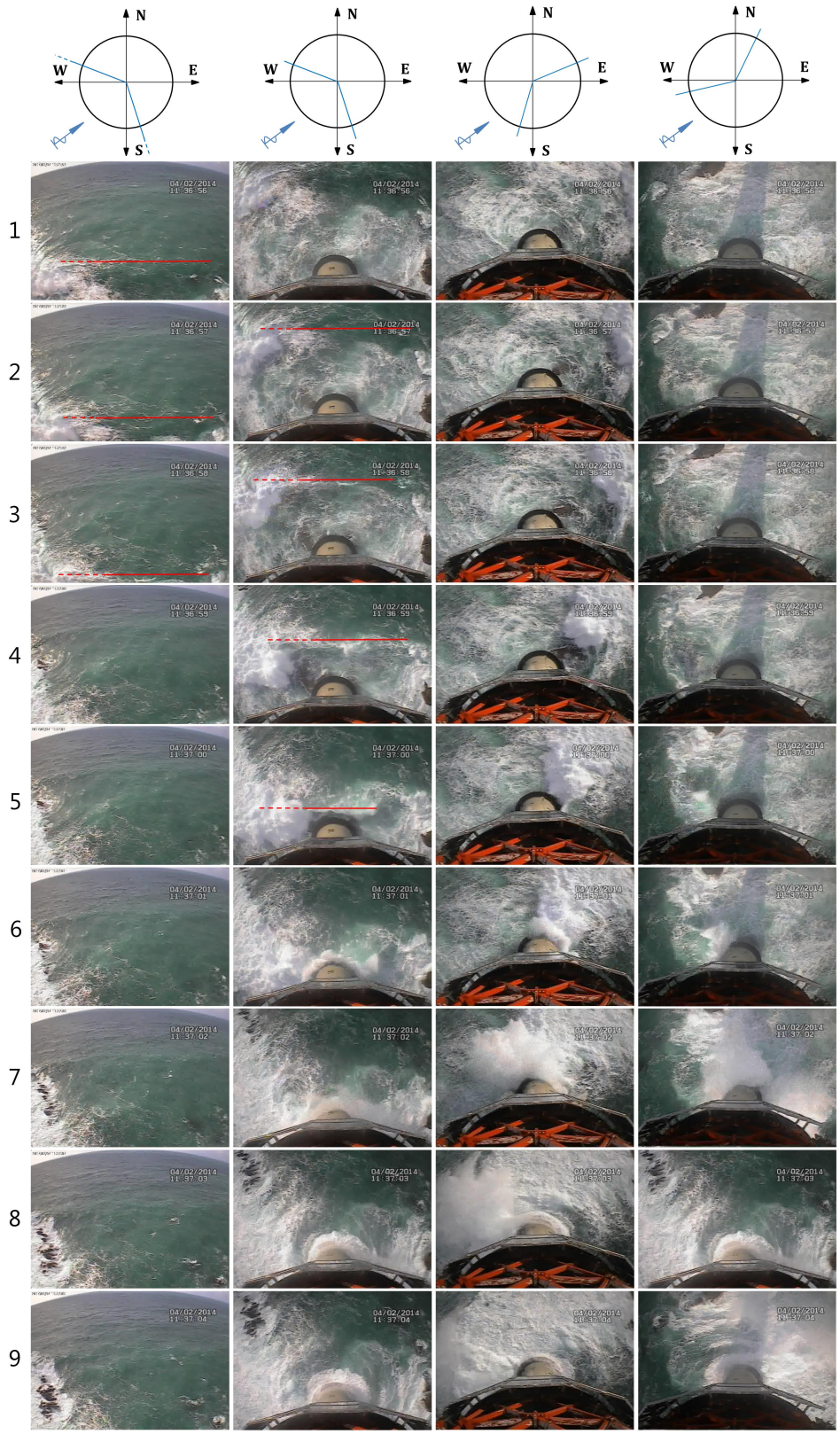

Figure 5.9: Video frames for the wave event used to describe the structural response of Type 1.

while the weather was still bright and the sea was fairly calm (Table 5.2). In the distance only small wavelets can be seen, their appearance being glassy, with no breaking.

Column 1 shows an imperceptible wave front advancing towards the lighthouse. Column 2 shows that, closer to the lighthouse, the wave height suddenly increases (Row 3-4). The rapid increase of the wave height suggests the occurence of a plunging impact. The central portion of the wave front is still unbroken when it is in close proximity to the structure (Row 5); then the wave breaks at the tower (Row 6). The development of this breaking is in good agreement with the structural response of Event 1 that has a highly impulsive nature. In fact, plunging waves with short breaking distances are related to shock loads charcaterised by a sharp predominant peak highly localised in both time and space. Also, from Column 3 it can been seen that the wave front is just broken to the left due to the presence of the rock to south (Rows 4-5), whilst the front is stable in the central portion when it breaks on the lighthouse and very limited quantities of spray are visible along this portion. Smaller amounts of air are associated to shorter impact durations and, hence higher structural frequencies as required for a Type 1 event. Similarly, from Column 4 (Row 5) it is possible to appreciate the stability of the wave front at the impact time. After the impact (Rows 6), the wave clearly wraps itself around the tower (Rows 7).

The wave causes some 14 m of run up (from the top surface of the cylindrical base) as estimated by video images. As the following trough moves in (see subsequent frames of Column 1-2), exposed reefs can be seen. The reef to south, on which the Douglass tower stands, is to the left; whilst to west, where the Smeaton stump stands, is to the right and it encloses the water mass at a distance from the lighthouse of approximately one diameter of the cylindrical base (Column 2, Row 9). This can also been seen to the top-left of Column 4.

- **Event 2**

Figure 5.10 shows the wave event that corresponds to the structural response used to

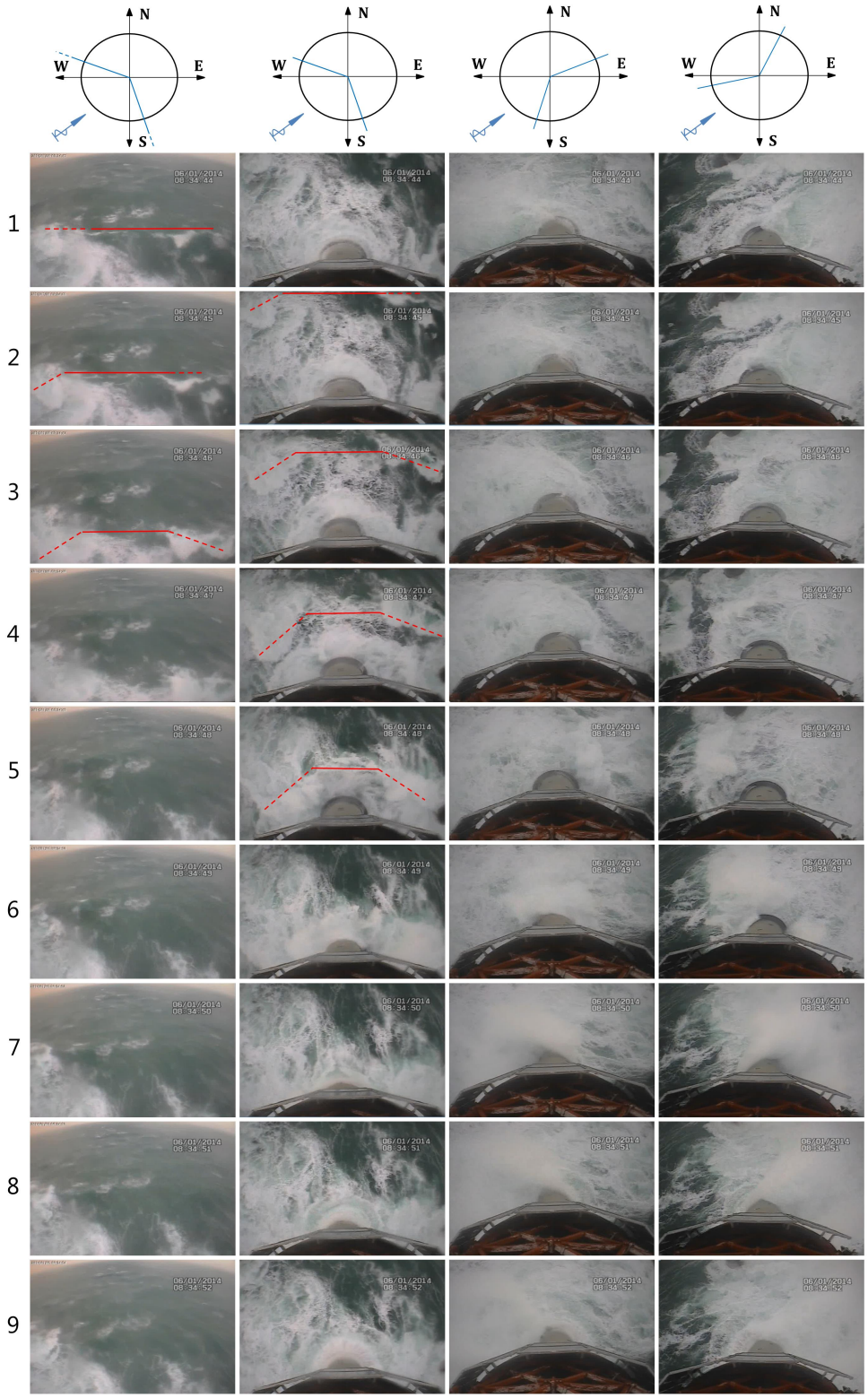

Figure 5.10: Video frames for the wave event used to describe the structural response of Type 2.

describe Type 2. Here, the video frames were captured at the peak of Storm Petra on 6/1/2014 (Table 5.2).

Looking firstly at Column 1, a large wave can be seen advancing towards the lighthouse with a little white-capping on the right side of the wave front (West) and a little white foam on the left side (South). Focusing closer to the tower (Rows 2 and 3 of Column 2), the wave front initially breaks to either side of the central field of view due to the presence of rocks but a stable central wave front (Rows 4-5) proceeds towards the tower. Between the frames shown in Rows 5 and 6, a plunging jet is suddenly shot at the tower with a relatively short breaking distance.

Event 2 is characterised by a clear wave front that breaks farther from the structure when compared to Event 1. As a consequence, Event 2 should be characterised by a larger wave that involves higher level of aeration. This would imply a longer impact duration that would cause a decrease of the structural impulsivity on one hand. On the other one, a larger wave would lead to larger peaks in the structural response as required for a Type 2 event.

The impact generates a significant vertical run up, some 20 m above the cylindrical base (Row 7), subsequently receding back down the tower, creating petal-shaped white water at the base (Rows 8 and 9). Column 3 and 4 capture the two clouds of spray related to the already-broken edges of the wave front. The violence of the impact is evidenced by the large amounts of spray visible in the surrounding area of the lighthouse (Rows 7, 8 and 9).

Due to higher tide levels for this event (6.29 m c.f. 4.74 m for wave Event 1), the exposed reefs are not visible.

- **Event 3**

Figure 5.11 shows the wave event that corresponds to the structural response used to describe Type 3. This event was recorded at the peak of the storm Hercules on

5/2/2014 (Table 5.2).

Column 1 shows that the wave is extremely large and it advances rapidly. Consequently, the wave front appears unstable and irregular. In particular, it seems that on the left part of Column 1 (South), the wave front slows down and simultaneously it increases its wave height. Conversely, on the right side (West), the wave front is faster and seems to rotate due to the refraction[1] (Section 2.5). Consequently, the right side of the wave front (West) tends to break closer to the lighthouse and with higher velocity, when compared to the left side (South). This different behaviour suggests that the wave front moves on different water depths i.e. shallower to South and deeper to West. This would be in agreement with the 3D bathymetry described in Section 3.1.1, which showed lower depth to the south due to a submerged vertical cliff (Fig. 3.3). Column 2 shows that, although the wave breaks far from the lighthouse (Row 5), the plunging jet is so violent that it is able to hit the tower with a high level of spray (Row 6). Then, the wave acts for long time and over a large area on the structure (Row 6-7).

Plunging impacts characterised by larger breaking distance are generally associated with less impulsive loads that can show several peaks in the overall force time history. In addition, higher levels of aerations tend to increase the load impact duration. Although the structural response of Event 3 is characterised by an irregular initial part of the velocity signal with a high frequency of oscillation, the impulsivity of the structural response tends to decrease when compared to Event 2. This may be given by the fact that the breaking distance increases and a large amount of air seems to be entrapped by the plunging jet. However, the structural response of Event 3 is characterised by a low frequency content that lead a larger displacement with respect to Event 2. The larger displacement should be a consequence of a longer impact duration and a larger amount of water mass that acts over a larger area of the structure.

This impact generated an extremely high run up that reached the location of the camera (some 40 m above the cylindrical base). The wave height alone may not justify

[1] The celerity of the wave front is larger in deeper depths and lower in shallower depths. As a consequence, the wave front tends to change direction (refraction) during the wave propagation.

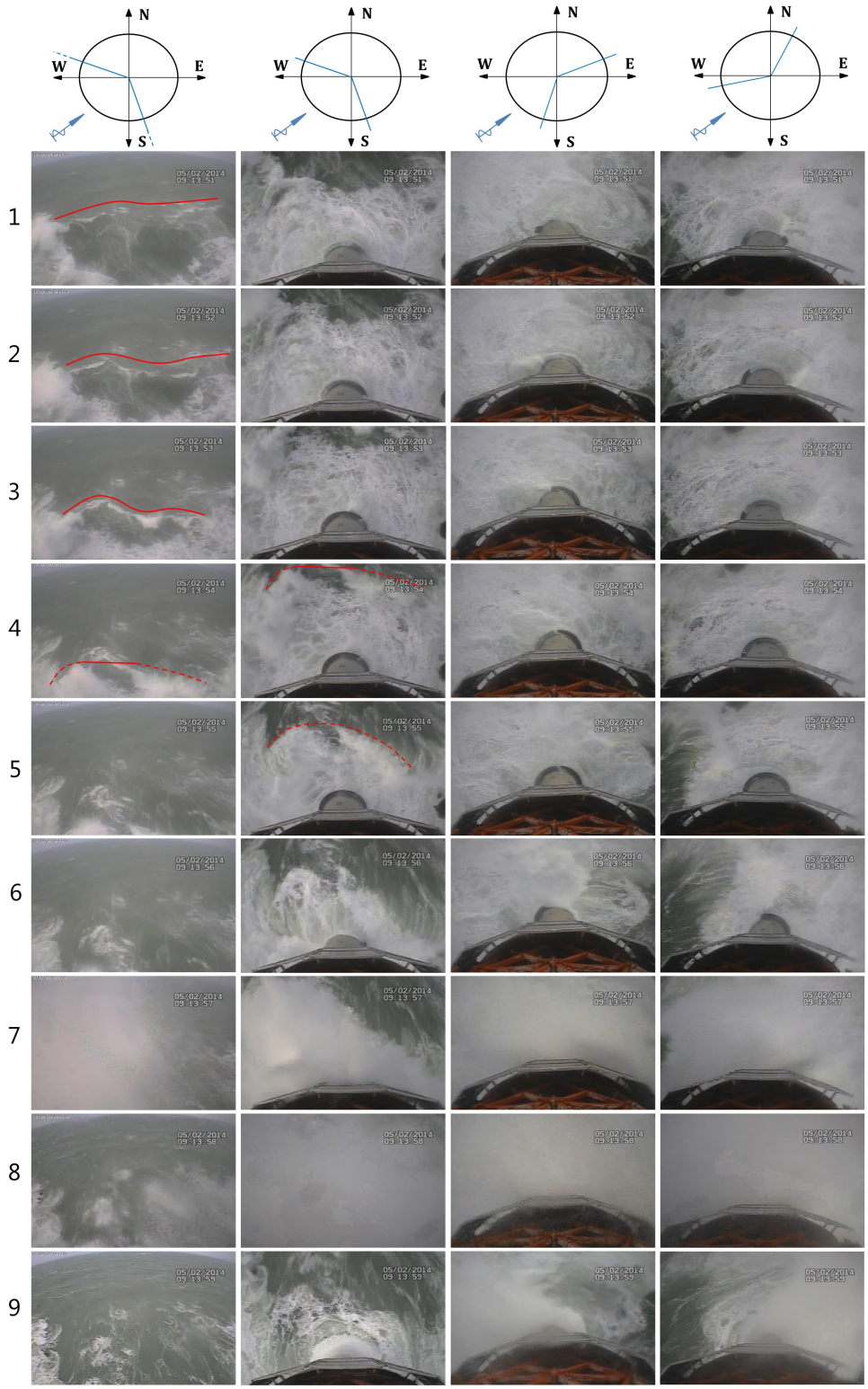

Figure 5.11: Video frames for the wave event used to describe the structural response of Type 3.

this immense run up; the particular configuration of the bathymetry and the wind could have a considerable bearing. Due to the fact that the seabed is very steep and it is constrained at the sides by two reefs (Fig. 3.3), the bathymetry may behave like a bottleneck and so the water could be shot upward by the huge mass of water involved. Then, the strong winds may contribute in pushing the water to this great height. Column 3 and 4 show the violence of the plunging jet that envelops the lighthouse with large amounts of spray.

- **Event 4**

Figure 5.12 shows the wave event that corresponds to the structural response used to describe Type 4. This event occurred the day after the peak of the storm Petra and its long wave period is typical of post-storm swell seas (Table 5.2).

From Column 1, it is possible to appreciate the rotation of the wave front (refraction) caused by the bathymetry configuration. As can be seen in Columns 1 and 2, the plunging jet is completely developed and it breaks far from the lighthouse (Rows 3 and 4); consequently large amounts of spay are visible (Row 5). The breaking distance is so large that the impact is caused by large amount of turbulent water, which seems to act for a long time on the structure with high residual velocity (Rows 6, 7 and 8).

Due to the fact that the plunging wave is fully developed, the impact is caused by a broken wave. This is associated to non-impulsive and low frequency load as required for a Type 4 event, which has low frequency structural response and velocity oscillations relatively low (i.e. structural velocities caused by a non-violent load event).

This event is characterised by lower water levels compared to the three previous events (Table 5.2); however, its run up is much lower, i.e. some 6 m from the top surface of the cylindrical base. Columns 3 and 4 show the large amount of spray that surrounds the lighthouse. Moreover, due to the low tide, a large portion of the dry rock that protects the lighthouse for waves coming from west can be seen (Column 4). Both the rocks tend to enclose the water mass on the two lateral sides (Column 2, Row 1).

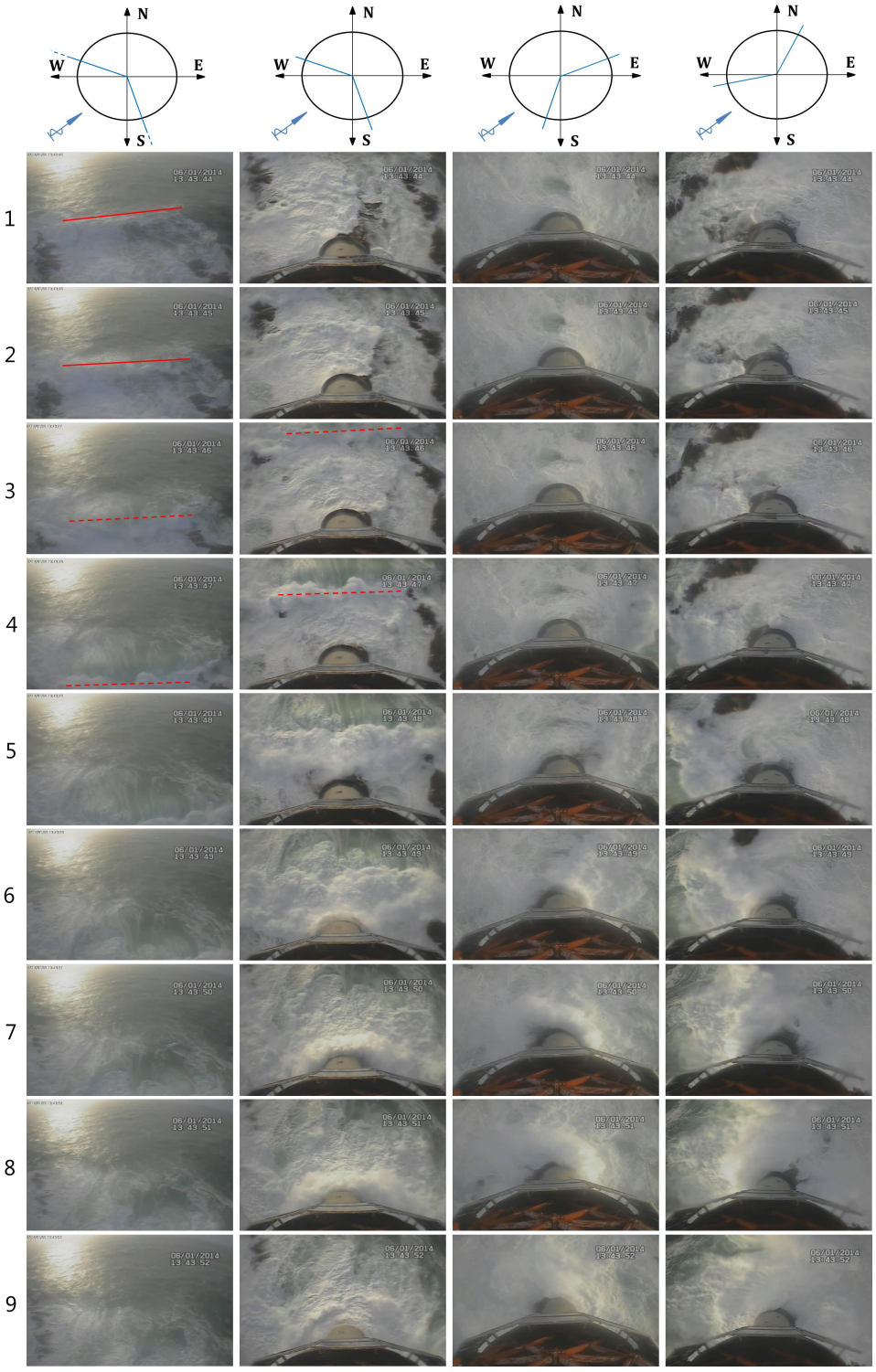

Figure 5.12: Video frames for the wave event used to describe the structural response of Type 4.

5.1.3 Considerations and observations on the field data set

Dynamic responses

The maximum deflection of the tower, which was measured during the winter storms of 2013-2014, was approximately 0.08 mm. This event occurred during the night so no video images are available. The dynamic responses (time histories and peak spectra), related to this event, are shown in Figure 5.13.

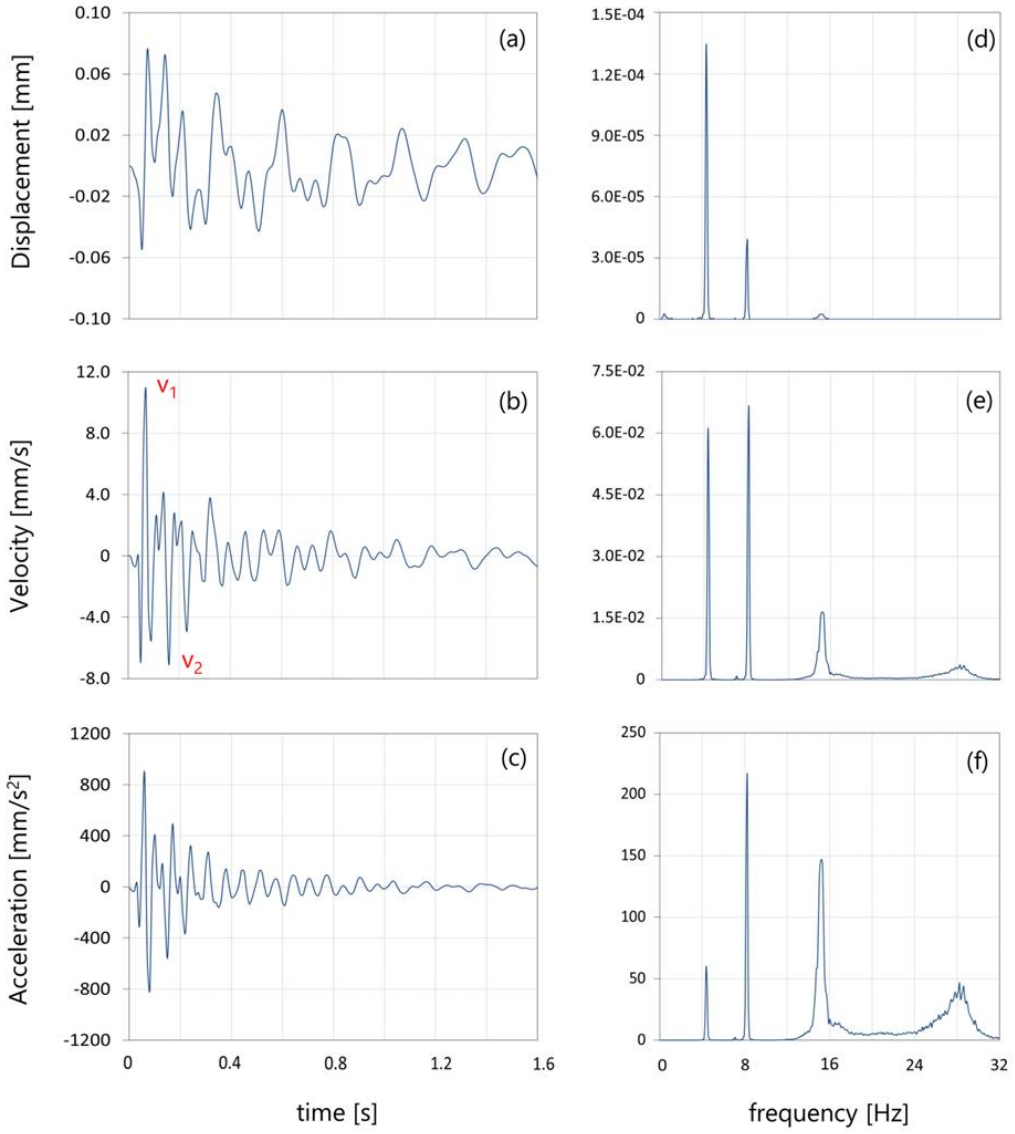

Figure 5.13: Maximum structural deflection recorded. This is classified as Type 2.

As may be observed, the ratio between the two highest peaks is about 1.6; consequently, this event falls within the Type 2 category. Just 4.5% of structural events caused deflections larger than 0.02 mm corresponds to the 25% of the maximum displacement. The histogram in Figure 5.14 shows the distinction, for structural types and displacement classes, of this extreme portion of the data set (141 events out of 3078).

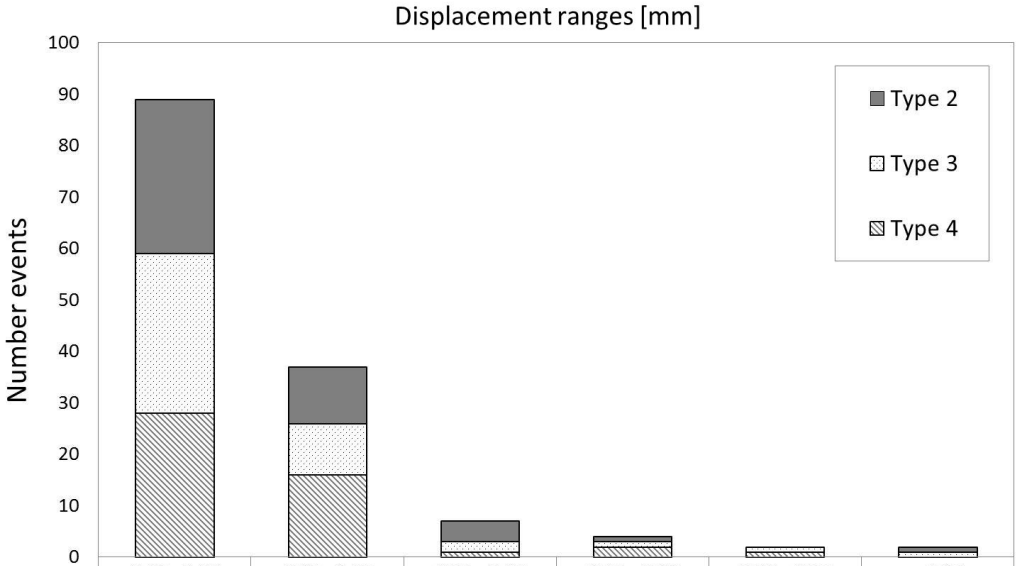

	0.02 - 0.03	0.03 - 0.04	0.04 - 0.05	0.05 - 0.06	0.06 - 0.07	> 0.07
Type 2	30	11	4	1	0	1
Type 3	31	10	2	1	1	1
Type 4	28	16	1	2	1	0

Figure 5.14: Occurrence of the extreme portion of the structural data set (141 events that cause deflections larger than 0.02 mm). They are distinguished on the basis of displacement ranges and structural responses.

As may be observed from Figure 5.14, Type 1 are absent and hence only generate displacements lower than 0.02 mm and Type 2, 3 and 4 can generate similar displacements to each other.

Three observations may be made on the basis of results obtained by the structural response:

1. higher structural velocities/accelerations do not necessarily lead to the larger structural displacements;

2. Type 1 is only able to generate small deflections (lower than 0.02 mm), despite its nature being highly impulsive (Fig. 5.14);

3. Types 2, 3 and 4 can generate similar amplitudes of deflection; even if their oscillations tend to occur with different velocities (the velocity tends to decrease moving from Type 2 to Type 4).

Structural stability of the Eddystone lighthouse

The largest tower deflections are relatively low, i.e. of the order of a tenth of a mm. This value gives an idea about the imposing rigidity of the Eddystone lighthouse.

The FE model (Section 3.1.2) indicates that both structural response signals and amplitude spectra obtained from numerical simulations are in agreement to those extracted from the geophones (Trinh et al., 2016). In particular, the FE model is able to capture the harmonics of approximately 4 Hz, 15 Hz and 28 Hz, even though it is slightly more flexible than the actual structure, since the frequencies of the numerical analysis are slightly lower than those obtained from the geophone. A significant difference between the two spectra is that the 8 Hz frequency is not evident from the FE analysis. There are a number of possible reasons for the absence of this vibration mode. The most likely cause is the simplistic representation of the combined helideck structure and lantern room at the top of the structure (Trinh et al., 2016). On the basis of the numerical agreement, the FE model has been used to evaluate the stability of the lighthouse. As shown by Trinh et al. (2016), the lighthouse is stable with regard to material failure; for failure mechanisms of structural overturning and sliding there are factors of safety of 6.3 and 8.0 respectively. Considerations on the wave that could cause the structural failure condition will be discussed in Section 5.2.2.

Maximum accelerations are close to $0.1g$ (Fig. 5.6c). The United States Geological Survey developed an Instrumental Intensity scale (Table 5.3) which maps peak ground acceleration and peak ground velocity on an intensity scale similar to the Mercalli scale. According to this classification, just a couple of wave impact events would be felt as

Table 5.3: Accelerations and velocities caused by earthquake on the ground (Instrumental Intensity scale developed by United States Geological Survey)

Instrumental intensity	**Acceleration (g)**	**Velocity (mm/s)**	**Percived shaking**	**Potential damage**
I	< 0.0017	< 1	Not felt	None
II - III	0.0017 - 0.014	1 - 11	Weak	None
IV	0.014 - 0.039	11 - 34	Light	None
V	0.039 - 0.092	34 - 81	Moderate	Very light
VI	0.092 - 0.18	81 - 160	Strong	Light
VII	0.18 - 0.34	160 - 310	Very strong	Moderate
VIII	0.34 - 0.65	310 - 600	Severe	Moderate to heavy
IX	0.65 - 1.24	600 - 1160	Violent	Heavy
X+	> 1.24	> 1160	Extreme	Very heavy

'Strong' (level VI). The effects of the earthquake levels are based on eyewitness reports, felt shaking and observed damage. However, the accelerations and the velocity of the earthquake are strongly affected by the ground characteristics. Therefore, there is not a relationship between the velocity and acceleration ranges of the lighthouse (characterised by particular value of mass, damping and stiffness) when compared to one of the ground shown in Table 5.3. In fact, the maximum accelerations of the lighthouse should be in class VI, whilst maximum velocities between classes III and IV. In addition, the time duration of the earthquake, typically several tens of seconds or more, affects strongly the structural damage and short time durations tend not to generate damage.

Interpretation obtained from field video images

Although previous wave descriptions (Section 5.1.2) are rather qualitative, the nature of the dynamic responses seem to be affected by the way in which waves approach the

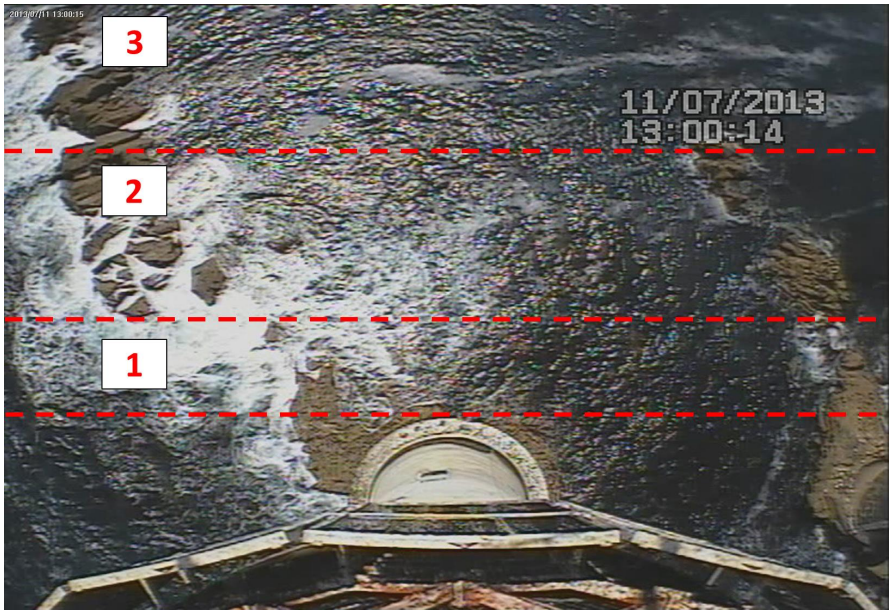

Figure 5.15: Breaking distances and structural response types.

reef and in particular by the breaking distance. Within the extreme portion of data (i.e. $V > 2$ mm/s and $D > 0.02$ mm), 41 events out of 164 occurred during the daylight. The occurrence of this extreme data set has been analysed depending on the breaking distance in accordance with the 3 zones shown in Figure 5.15. Breaking distances have been estimated with respect to the central portion of the wave front; Table 5.4 shows a summary of the results.

Table 5.4: Breaking distance ranges and percentage of structural response types

Type	Zone 1	Zone 2	Zone 3
1	100%	0%	0%
2	64%	36%	0%
3	21%	43%	36%
4	11%	33%	64%

As may be observed from Table 5.4, 100% of events classified as Type 1 occur in Zone

1; 64% of events classified as Type 2 occur in Zone 1 and 36% in Zone 2. The spread increases for Type 3, for which 21% of events occur in Zone 1, 43% in Zone 2 and 36% in Zone 3. Finally, 11% of events classified as Type 4 occur in Zone 1, 33% in Zone 2 and 64% in Zone 3.

Results in Table 5.4 show that the same structural response type can occur within a wide range of breaking distances. This is given by the fact that the breaking distance is not dimensionless with respect to the wave height due to difficulty of estimating both wave height and water level from video images. However, the impulsivity of structural responses tends to increase with decreasing breaking distance (moving from Type 1 to Type 4). Generally, video images indicate that Type 1 are characterised by smaller waves that break in proximity of the structure, while the impact of Type 4 is caused by a turbulence mass of water. It is not possible to set a clear distinction between Type 2 and 3 from video images. However, both tend to be characterised by a plunging jet that hits the tower.

Although video images are in good agreement with the coastal literature (Sections 2.2.3 and 2.3.1), which has demonstrated that shock loads are usually caused by waves that break on or just in front of the structure (Chan & Melville, 1988; Oumeraci et al., 1993; Wienke & Oumeraci, 2005), only small displacements are generated by waves that break at the Eddystone lighthouse; even if they show highly impulsive structural responses. Thus, while video images indicate that the nature of the structural responses (clear sharp peak and frequency content) is affected by the type of wave impact, it is reasonable to presume that the magnitude of the structural deflection is affected by both wave characteristics and application point of the wave load. Their effects will be discussed in subsequent sections.

In addition, video images suggest that waves, which generated geophone events, tended to approach the lighthouse from an approximately SW direction. Along this direction, waves do not break on rock outcrops and the breaking point mainly seems influenced by the variation of the three variables, namely, wave $H_{s,o}$, T_p and water level.

Quantitative estimations of the run up are difficult due to the location of the cameras, which do not enable the cloud of spray to be distinguished from the vertical flow on the structure. However, video images suggest that broken waves generated lower run up (estimated from the top surface of the cylindrical base). This is in agreement with experimental investigations on both vertical walls and vertical cylinders (Section 2.3.3). Instead, larger run up tended to be caused by larger waves that hit the tower with a plunging jet. Within this type of breaking waves, the run up tends to increase with the increasing celerity of the wave front. Thus, it is reasonable to presume that larger run up is characterised by larger periods (which is in agreement with the coastal investigations). Although there are these similarities with coastal structures, the Eddystone Reef seems to increase the run up on the lighthouse if compared to laboratory investigations on smooth and plane walls (Section 2.3.3). In particular, the configuration of the steep reef (at SW), could channel all the wave energy inside the submerged corridor. This may limit the escape of the water flow, increasing the vertical water flux with respect to investigations on mild slopes in 2D.

5.2 Factors affecting the tower's structural response

The E1 buoy data have been assumed to be representative of conditions offshore from the Eddystone Reef (Figure 3.1 in Section 3.1) and the waves reaching the lighthouse will be mainly modified by shoaling, refraction and breaking. As these processes are likely to have a major influence on how a wave finally impacts the lighthouse they will also have an indirect influence on the structure's response.

However, the methods of application of the wave variables and final considerations are as much a matter of engineering judgement as mathematical rigour. This is due to the fact that statistical wave data ($H_{s,o}$, T_p, β) are related to the individual structural events recorded by the geophone system. Therefore, it is reasonable to expect that changes occur gradually in the results rather than suddenly because an irregular sea-state encompasses a wide range of individual waves. Moreover, it is also necessary

to take into account the intrinsic random nature of wave loads, which is given by the complexity of the breaking process with its unknown mixture of expelled, entrapped and entrained air (Bullock et al., 2001).

Therefore, the present section aims to detect general behaviour based on the entire data set rather than directly relating a particular response to a particular load case. The 3078 events recorded during an exceptional six months of storms covered a wide range of different hydraulic conditions. A maximum of 15-20 events were recorded in each one hour interval during the severest storms and no more than 3-4 of them caused significant deflections (larger than 0.02 mm). As it will be shown later, the random sea-state tends to mask any trends for deflections under 0.02 mm.

The wave parameters are calculated according to the idealised bathymetry profile along the SW (Fig. 5.16), which is the direction of main significance as suggested by video images.

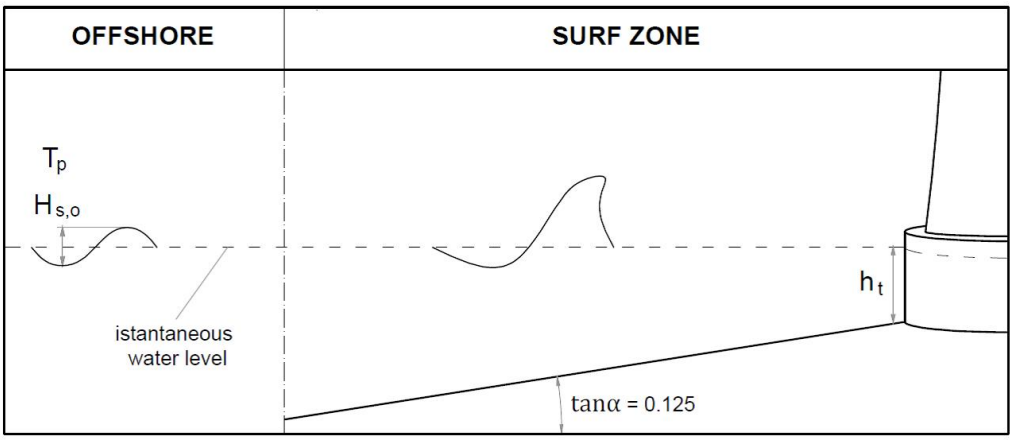

Figure 5.16: Assumed profile at SW

Figure 5.17 shows the displacement peaks (D) against the related velocity peaks (V), both obtained in the horizontal plane X-Y, of the tower's response (3078 events).

As may be observed from the graph (Fig. 5.17), the amplitudes of the tower's deflection can occur with different velocities of the oscillation. According to Loraux (2013) and Chollet (2014), larger load impulses (caused by an increase in load duration) re-

sult in a decrease in the frequency of the structural response. As a consequence of larger impulses, which decrease the impulsivity of the load, the structural deflections increase and the velocities/accelerations decrease. Therefore, analyses are presented by comparing the maximum displacements (D) and velocities (V) in order to take into account the effects of the frequency of the structural response. In particular, for two identical displacement amplitudes (Fig. 5.17), the one which has a higher velocity, is the result of a more impulsive structural event i.e. it is characterised by dynamic responses with a higher dominant frequency.

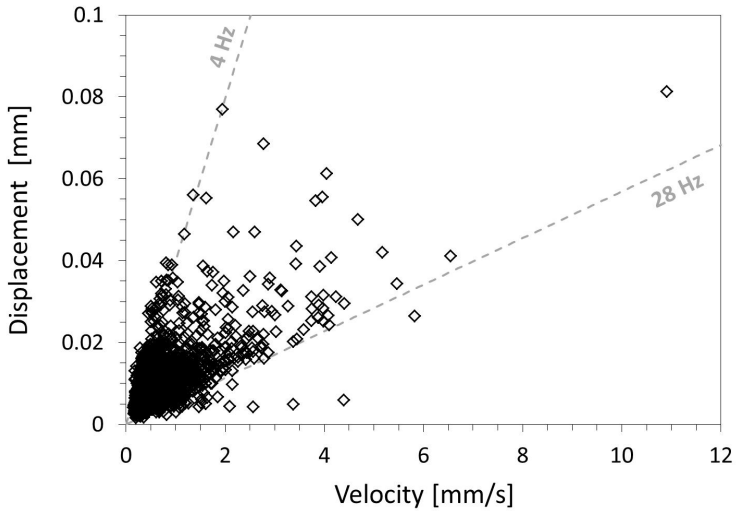

Figure 5.17: Structural displacements against structural velocities. Data, related to the 3078 geophone events, are the maximum peaks obtained in the horizontal plane X-Y.

5.2.1 Dependence on dimensional hydraulic variables

The results are presented in this order: wave direction β, significant wave height $H_{s,o}$, wave period T_p and water level (CD) obtained from BODC's measurement at Devonport. Concerning the offshore wave data, $H_{s,o}$ and T_p were characterised by gradual variations between two consecutive hourly measurements. In contrast, the wave direction was rather variable and it could result in wide changes (i.e. 30°- 35°) from one hour to the next. The water levels are instantaneous values assumed constant during the impact event recorded by the geophone system. The maximum variation could be

at most about 4 mm in 10 s (acquisition period at 100 Hz). This value is one magnitude order lower than the measurements; thus, the water level can be safely assumed constant at the time of the event. Estimation of the water depth – at the toe of the lighthouse (SW) – can be obtained adding 0.33 m to the BODC's measurement (based on the procedure described in Section 3.1.3).

Direction of wave attack

Maximum structural velocities and displacements as a function of offshore wave directions (β) are plotted in Figure 5.18. Some 93.3% of the events (i.e. 2871 in 3078) occur for a range of directions centered approximately at South-West (209° to 255°). The number of the events tends drastically to reduce beyond the two red lines drawn at 209° and 255°. This result could be expected. On one hand, the longest fetches and the prevailing winds are from a South-West direction; on the other, the rock outcrops represent a natural protection for the lighthouse (Section 3.1.1). In fact, the video images indicate that waves from directions greater than 255° tend to break on the rock to West; conversely, waves from directions less than 209° tend to break on the rock in line to the South direction.

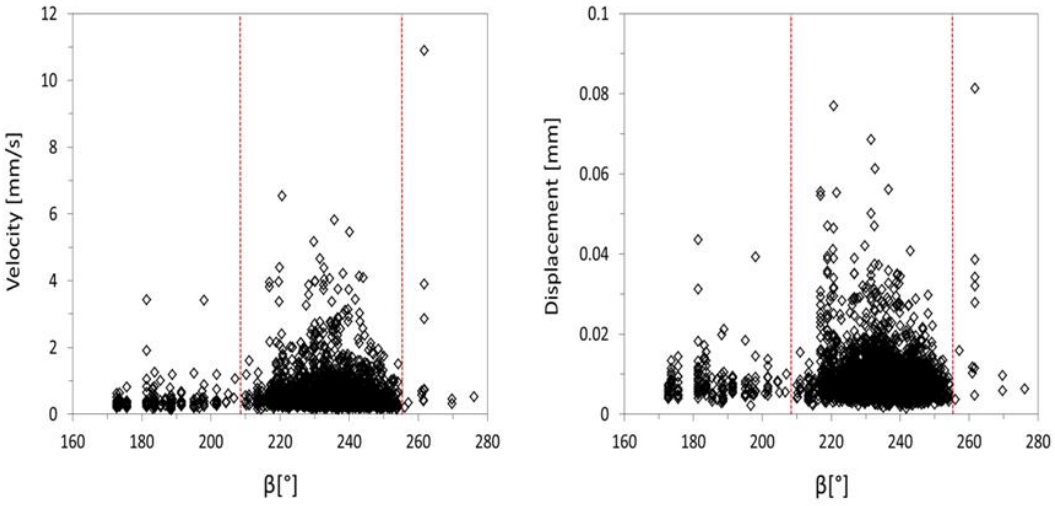

Figure 5.18: Structural velocity and displacement against offshore wave direction.

As may be observed from Figure 5.18, larger displacements tend to occur at 220° when compared to those close to 245°. The different breaking process, as suggested by video images, may explain this difference. Although the submerged rock to the South tends to cause the breaking, the wave is however able to hit the tower with a plunging jet. Instead, the dry rock to West tends to cause breaking farther from the lighthouse and, so, just turbulent water reaches the tower; consequently, it is reasonable to suppose that much more energy is dissipated (Goda, 1974; Oumeraci et al., 1993; Bullock et al., 2007). In addition, the rock to West, which tends to be partially emerged, may act as an obstruction for the amount of the water mass under the mean water level.

The 4.6% of data inside the 2 red lines has a displacement larger than 0.02 mm. Outside the 2 red lines, the percentage of displacements larger than 0.02 mm is 3.8% (i.e. 8 events in 207). Unfortunately, video images are not available for these 8 events. Generally, when video images are available for the other events outside the 2 red lines, waves tend however to approach the lighthouse approximately from the SW. Concerning the largest displacement, this and the other 4 large displacements at 260° are related to the same measurement hour where directions changed from 260° to 232° in the following hour. Due to the dry rock outcrops to West, it is reasonable to believe that the strongest event approached the lighthouse from a direction closer to SW.

Significant wave height and peak period

Maximum velocities and displacements as a function of significant wave height ($H_{s,o}$) are plotted in Figure 5.19. The events with $H_{s,o} < 3$ m are 52.7% of the data set (i.e. 1622 in 3078) and 1.1% of them (18 in 1622) have velocity values larger than 3 mm/s. Similarly, 1.1% of events (17 in 1456) have $V > 3$ mm/s when $H_{s,o} \geq 3$ m. Different behaviour is shown by displacement. In fact, one event in 1622 has a displacement larger than 0.04 mm when $H_{s,o} < 3$ m; instead, 15 in 1456 have $D > 0.04$ mm when $H_{s,o} \geq 3$ m. Therefore, higher velocities can be generated by a wide range of $H_{s,o}$; in

contrast, larger displacements tend to occur for larger wave heights (i.e. $H \geq 3$ m). This is reasonable because larger wave height are characterised by larger amounts of energy.

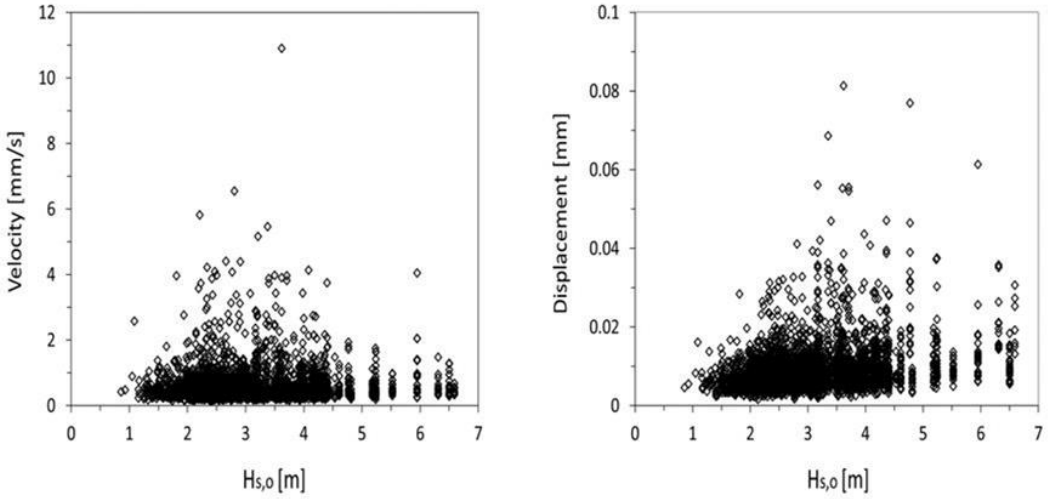

Figure 5.19: Structural velocity and displacement against significant wave height.

Maximum velocities and displacements as a function of offshore wave period (T_p) are plotted in Figure 5.20.

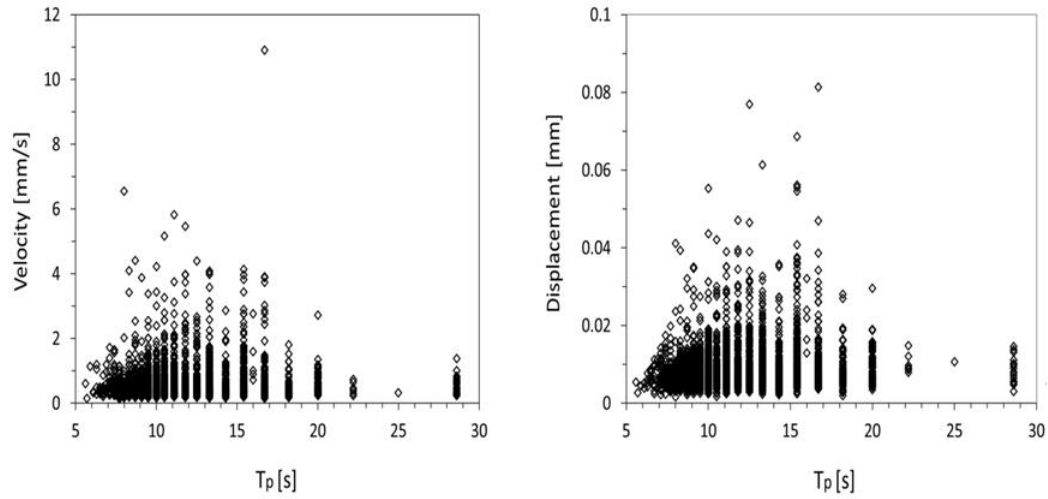

Figure 5.20: Structural velocity and displacement peaks against peak wave period.

As may be observed from Figure 5.20, larger peaks ($V > 4$ mm/s and $D > 0.04$ mm) can occur within a large wave period range i.e. 7.7 s $< T_p <$ 16.8 s. This range covers the 90.6% of the data set (i.e. 2789 events in 3078). Both displacement values and their occurrence drastically decrease when $T_p \geq$ 16.8 s (184 events in 3078). Generally, when $T_p \geq$ 16.8 s, video images indicate that waves tend to be broken or long and mild waves. As a consequence, it is reasonable to believe that their violence tends to decrease.

Water level

Figure 5.21 shows the maximum structural velocities and displacements against the instantaneous water level (CD) measured at Devonport (Section 3.1.3).

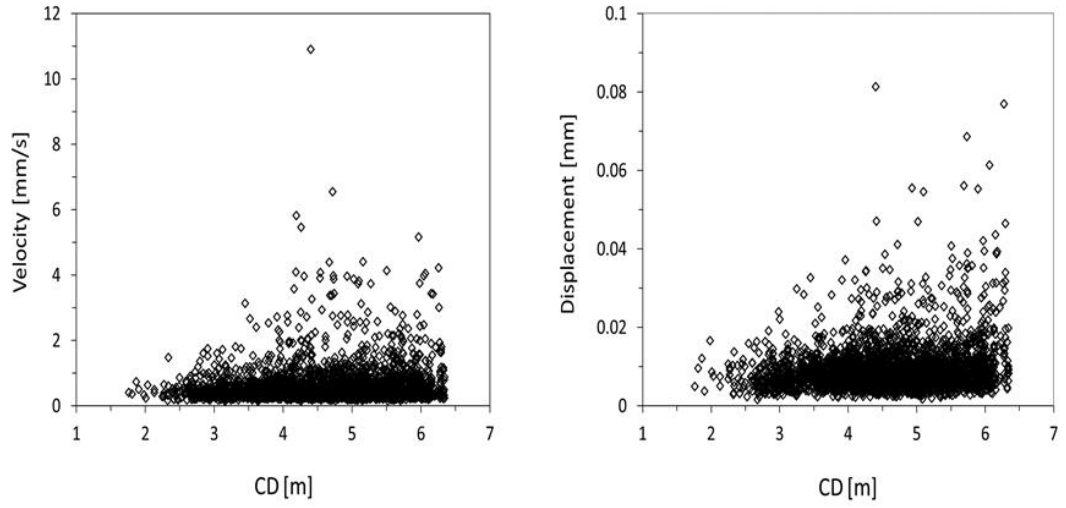

Figure 5.21: Structural velocity and displacement peaks against water level.

As can be seen from Figure 5.21, the occurrence of the strongest events tends to increase for higher values of the water level. This is not surprising since the tidal range (5.9 m) is similar to the maximum water depths estimated at the toe of the structure (6.8 m at SW). Therefore, larger waves are able to break closer to the lighthouse at higher tide conditions. Video records show that, when the water level is less than 3

m, the cylindrical base of the lighthouse tends to be largely out of the water. Thus, it tends to be hit only by residual turbulent masses of water (broken waves), which cause lower deflections. By comparing the two graphs in Figure 5.21, the displacement peaks tend to show a rather steep linear upper limit. Furthermore, in contrast to the significant wave height and peak period (Fig. 5.19-5.20), the displacements tend to show a monotonic tendency with water level. As a consequence, in comparison to H_s and T_p, the magnitude of the tower's deflection tends to be proportional to the water level.

It is reasonable to believe that higher water levels would affect responses in three ways:

- larger waves are able to approach closer to the structure;
- the submerged portion of the lighthouse increases resulting in a larger wave load area;
- higher mean water levels raise indirectly the load application point on the tower.

Concerning the application point of the wave force, its effects on the structural deflection has been investigated with the structural simulations (Trinh et al., 2016) and results are shown in the following sub-section.

5.2.2 Dependence on the line of action of the wave force

Numerical simulations have been carried out in order to analyse the effects on the structural displacements caused by different load directions (Trinh et al., 2016). In particular, different load conditions have been simulated by varying both the wave directions in the horizontal planes (i.e. direction of wave attack) and the vertical elevations (i.e. mean water level). As described below, several methods have been used in order to estimate: the force time history (dynamic component related to the impact), the spatial distribution, the breaking wave height and a reduction coefficient for the breaking distance.

Force time history of the dynamic component of the wave load

The dynamic component of the wave force has been calculated in agreement with the model for vertical cylinders provided by Wienke & Oumeraci (2005) (Section 2.4.1). They assume that the impact wave causes a maximum line force at the impingement instant; then, it decreases to 0 with a composite time history (Fig. 5.22).

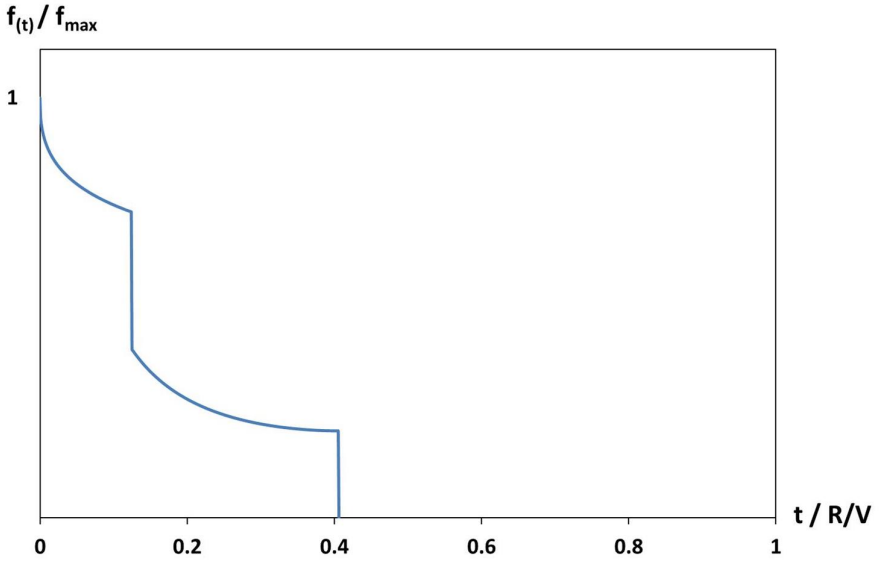

Figure 5.22: Time history of the force line (along the horizontal section of the cylinder) proposed by Wienke & Oumeraci (2005).

The maximum line force (f_{max}) is the total force, in N/m, along the circumference and it is determined as follows:

$$f_{max} = \rho \, 2\pi \, R \, V^2 \tag{5.1}$$

Wienke & Oumeraci (2005) identify a total impact duration equal to 0.406 R/V, where R is the radius of the circular structure and V the velocity of the water jet acting on the cylinder. As described in Section 2.4.1, Wienke & Oumeraci (2005) estimated the force peak with strain gauges, the composite time history by means of a pressure measure and the impact duration using pressure transducers along the circumference.

Spatial distribution

Wienke & Oumeraci (2005) provide a simplified vertical spatial distribution, i.e. with the force line equally distributed along the vertical extent of the impact. The impact height Δz is set equal to $\lambda\ \eta_b$, which represents the fraction (λ) of the maximum crest elevation ($\eta_b = 0.78 H_b$) over which the jet impingement acts (Fig. 2.4a in Section 2.4.1). On the basis of their experimental tests, Wienke & Oumeraci (2005) estimated a curling factor $\lambda = 0.46$ for vertical cylinders. However, according to several pressure investigations on cylinders (Zhou et al., 1991; Chan et al., 1995; Tanimoto et al. (1986), the vertical distribution tends to be triangular for plunging waves. Thus, in the current study, the overall force has been calculated with Wienke & Oumeraci (2005), but it has been applied with a vertical triangular distribution, symmetrical to the impact height ($\Delta z = 0.46$ $0.78\ H_b$). As a consequence, the maximum peak of the vertical distribution is twice the force line proposed by Wienke & Oumeraci (2005), as shown in Figure 5.23.

The azimuthal distribution has been calculated on the basis of the pressure values recorded along the circumference in the experiments of Wienke & Oumeraci (2005), as illustrated in Figure 5.23.

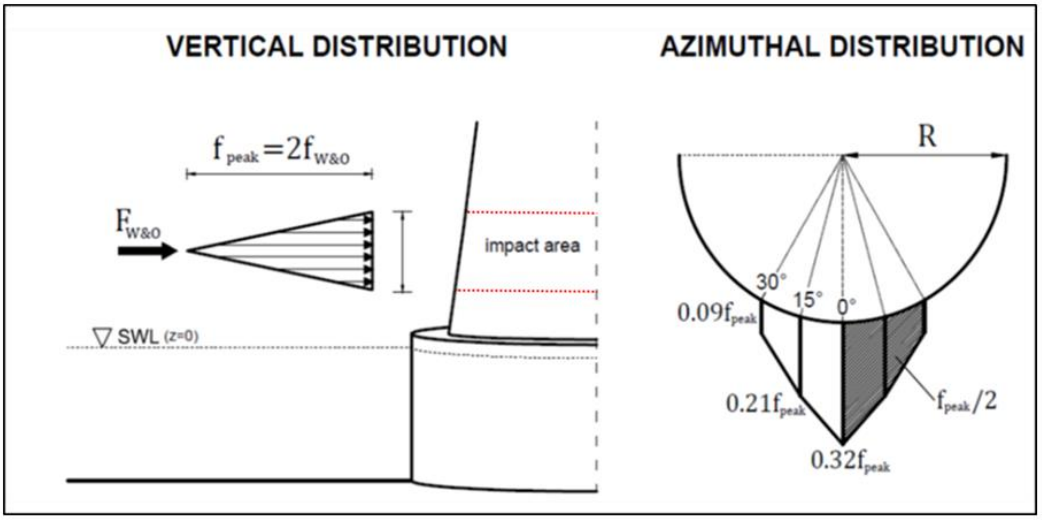

Figure 5.23: Triangular vertical distribution according to Tanimoto et al. (1986) and azimuthal distribution according to the pressure measurements recorded by Wienke & Oumeraci (2005).

Breaking wave height

As may be observed from Equation 5.1, the load formulation of Wienke & Oumeraci (2005) is proportional to the velocity of the water jet that hits the cylinder. The Authors suggest to assume the velocity of the water jet equal to the celerity of the wave at the breaking point ($c_b = L_b/T$). This assumption derives from the fact that when the velocity of the particle in the crest equals the celerity of the wave, the wave overturns and breaks. For plunging waves at breaking point, the water velocity is usually calculated with the wave celerity assuming the shallow water relationship. Since at breaking point the wave height and the water depth have similar size ($H_b/h_b \approx 1$), it is possible to find in the coastal literature two different expressions that are equivalent, i.e. $c_b \approx \sqrt{gh_b} \approx \sqrt{gH_b}$. In the current study, the wave celerity has been estimated on the basis of the breaking wave height thanks to the diagrams for irregular wave transformation in the surf zone proposed by Goda (2010) (Figure 5.24).

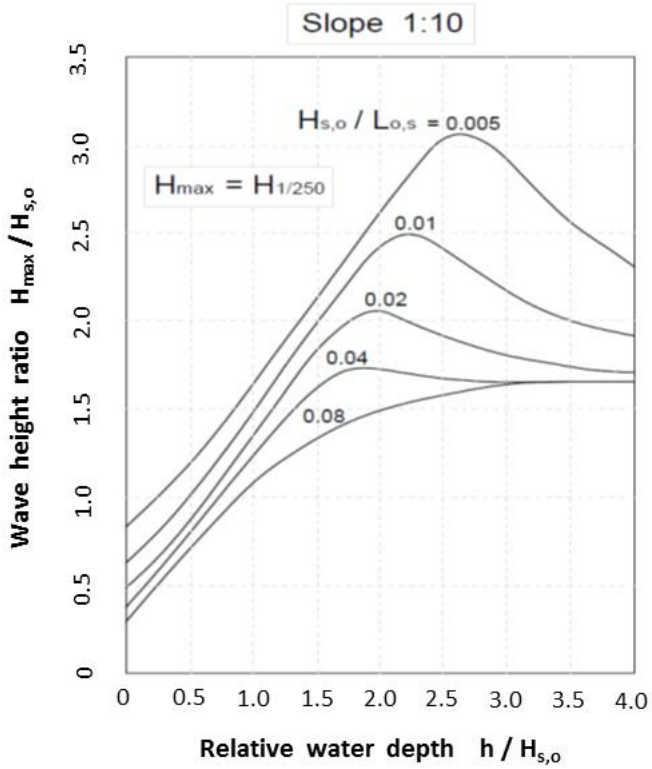

Figure 5.24: Wave transformation in the surf zone for 1:10 slope (based on Goda, 2010).

Goda (2010) identifies the maximum breaking wave height ($H_{1/250,b}$), for several slopes, depending on the significant wave steepness in deep water ($s_{s,o} = H_{s,o}/L_{o,s}$). In particular, Figure 5.24 shows the surf zone diagram for the 1:10 slope and in Table 5.5 are the values of the breaking coefficients.

Once the breaking wave height was identified on the basis of the offshore significant wave height (E1 buoy), it was possible to determine: the maximum force line value at the impact instant (f_{max}), the time duration of the load history (0.406 R/V) and the spatial extent of the load on the structure ($\Delta z = 0.46\ 0.78\ H_{max,b}$).

Table 5.5: Breaking coefficients proposed by Goda (2010) (slope 1:10)

$s_{s,o}$	0.005	0.01	0.02	0.04
$H_{s,o}/h_b$	0.38	0.45	0.50	0.53
$H_{max,b}/H_{s,o}$	3.05	2.48	2.04	1.72

Breaking distance coefficient

As said above, the maximum water velocity is reached just prior to breaking, i.e. when the velocity of the particle in the crest equals the celerity of the wave; then the wave overturns and breaks. The relationship of Wienke & Oumeraci (2005) was developed under this condition, which occurs when the wave breaks immediately in front of the cylinder. Therefore, in order to take into account the effects of the breaking distance, a reduction coefficient has been applied to their formulation.

The reduction coefficient has been determined on the basis of the results obtained by Irschik (2012), who shows the dimensionless force decreasing as a function of the relative breaking distance (Fig. 5.25).

The relative breaking distance ($d = x/H_b$), estimated according to the breaker index proposed by Goda (Tabble 5.5), has been then verified with the breaking distance (x) ob-

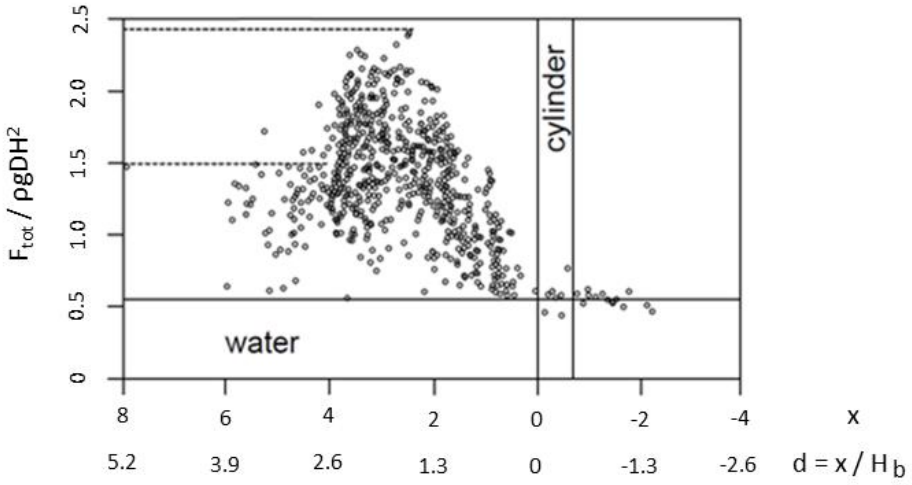

Figure 5.25: Dimensionless wave force against the relative breaking distance measured by Irschik (2012) (Trinh et al., 2016).

tained from video images. Figure 5.26 shows the estimation of the relative breaking distance depending on the relative wave height at the toe of the lighthouse ($H^* = H_{s,o}/h_t$).

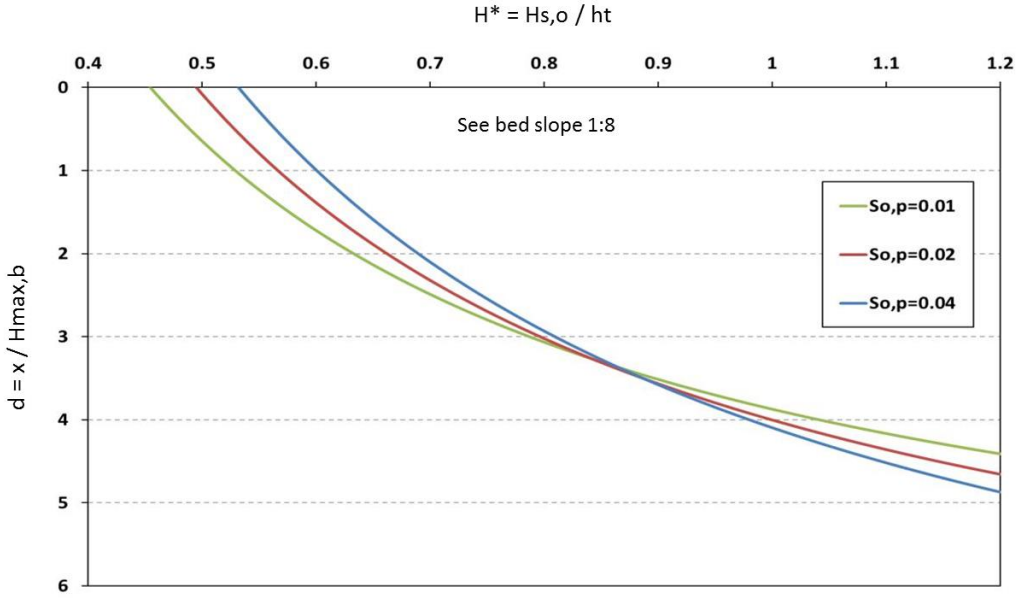

Figure 5.26: Relative breaking distance (d) against the relative wave height at the toe of the lighthouse (H^*). Values estimated according to the breaking coefficients proposed by Goda (2010).

Quasi-static component of the wave load

Breaking wave loads comprise two components, dynamic and quasi-static, each of which are characterised by a different nature of time history. An impact will generate an initial impulsive load (dynamic component), which causes a transient on the structural response (depending on the structural characteristics). The impact force duration is very short; typically 0.02-0.01 times the wave period T (local impact pressure can also have a duration one order lower i.e. 0.001 T). In contrast, the quasi-static component acts more slowly on the structure according to the wave elevation (maximum elevation approximately at 0.25 T).

For vertical cylinders, the quasi-static force is usually determined according to Morison et al. (1950). However, this method is typically applied in non-impulsive situations. For geophone signals affected by breaking waves, an attempt to extract the quasi-static displacement may be undertaken by applying the method proposed by Irschik et al. (2004). They filter the force signal, obtained by strain gauges in laboratory investigations on cylinders, in order to decompose the raw data into its quasi-static component (low pass filter) and the dynamic one (high pass filter) (Fig. 5.27).

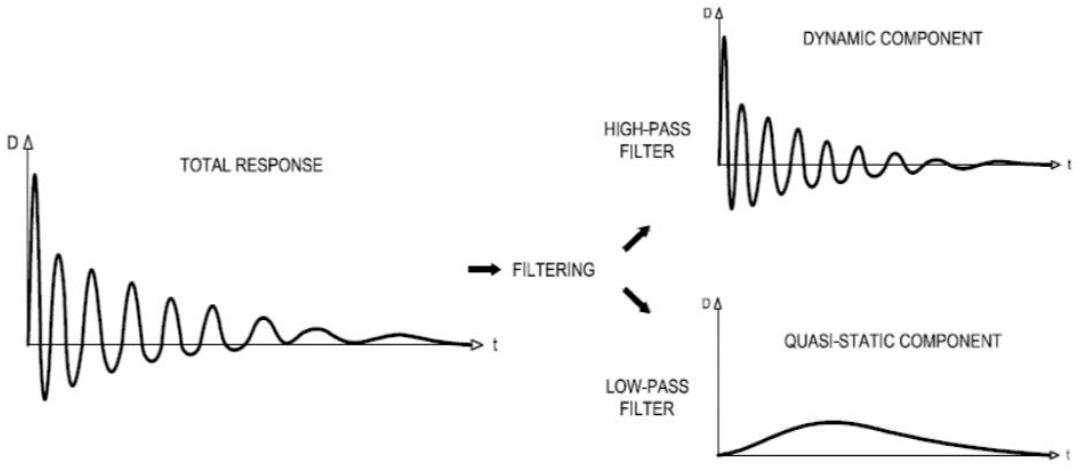

Figure 5.27: Signal filtering to share the dynamic component (high-pass filter) and the quasi-static one (low-pass filter).

However, the maximum displacement of the lighthouse is related only to the initial im-

pulsive impingement and it is not affected by the quasi-static component, which varies according to the surface elevation (Fig. 5.27). Therefore, only the dynamic component of the load has been applied.

Different load scenarios: variation of the application point of the force

As mentioned earlier, the same external load has been applied from different directions and at different elevations. While the load direction does not have a significant effect on the structural deflection, it is highly influenced by the height at which the impact occurs (Trinh et al., 2016). In particular, results show that maximum displacements have steep linear trends with impact height (Fig. 5.28). The increase in displacements is explained by the fact that the cylindrical base, which has a larger diameter, can be considered a massive structure that is more rigid; while, the upper part of the lighthouse tends to be more slender and, so, less rigid (Trinh et al., 2016).

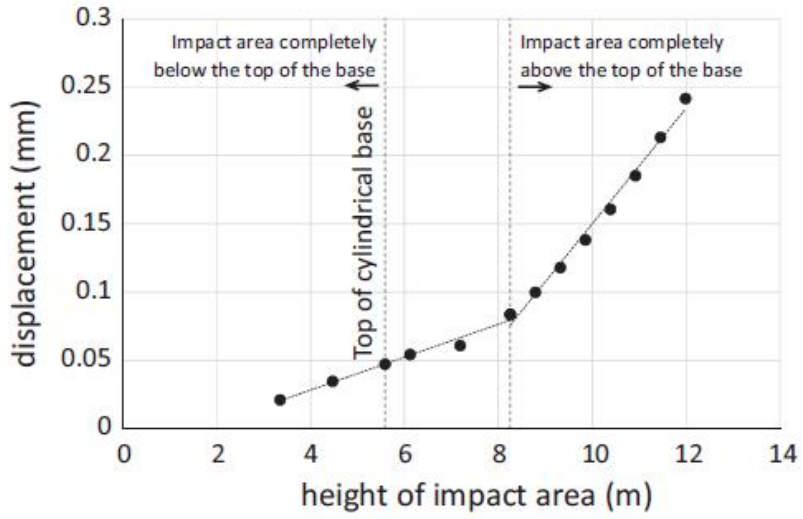

Figure 5.28: Relationship between maximum displacement and height of the impact area (Trinh et al., 2016).

As a consequence, the variation of the water level can be of critical importance in determining the magnitudes of the structural deflection related to the three impact types (Type 2-3 and 4, as shown in the histograms of Figure 5.14). Thus, while the nature

of the signal may be affected by the breaker type (as suggested by video images), the magnitude of the displacement is highly influenced by the application point on the structure.

Concerning the structural stability, on the basis on the load formula proposed by Wienke & Oumeraci (2005), a hypothetical wave of 17.5 m height should break at the structure to cause the failure of the lighthouse for overturning (Trinh et al., 2016). However, such hypothetical wave would not be able to break at the structure due to the fact that the maximum water depth, at the toe of the lighthouse, is approximately 6.8 m. As a consequence, the wave would break farther from the lighthouse dissipating both its height and part of its energy. An estimation of the maximum wave height at the toe of the Eddystone lighthouse may be obtained on the basis of the breaking coefficeints proposed by Goda (2010). Assuming a wave steepness of 0.04 (Table 5.5), the breaking coefficients result to be $H_{s,o}/h_b = 0.53$ and $H_{max,b}/H_s = 1.78$. Therefore, the maximum wave height can be estimated on the basis of the maximum water depth at the toe of the lighthouse as follows:

$$H_{max,b} = 1.78 \cdot 0.53 \cdot h_t = 1.78 \cdot 0.53 \cdot 6.8 = 6.42$$

Once estimated the maximum wave height, the maximum impact height on the structure can be estimated as follows:

$$h_{impact} = h_t + \eta_b = h_t + 0.78 \cdot H_{max,b} = 6.8 + 5.00 = 11.80$$

5.2.3 Dependence on dimensionless coastal parameters

Dimensional analyses in sub-section 5.2.1 has pointed out that structural displacements are strongly affected by the water level. In this sub-section structural responses are related to dimensionless coastal parameters. In particular, structural velocities and displacements have been plotted against the *Iribarren number* and *momentum flux*.

Offshore wave data, obtained at the E1 buoy (Fig. 3.1), have been substituted into the irregular relationships described in Section 2.5.2.

Iribarren number for irregular waves

For the purpose of this investigation, the *Iribarren number* is defined for irregular waves using the uppermost slope (1:8) of the idealised bathymetry at SW (Fig. 5.16) and offshore wave values ($H_{s,o}$ and $L_{o,p}$) as follows:

$$\xi_{o,p} = \frac{\tan(1/8)}{\sqrt{H_s/L_{o,p}}} \tag{5.2}$$

where $L_{o,p} = gT_p^2/2\pi$ is the offshore wave length calculated using peak period T_p.

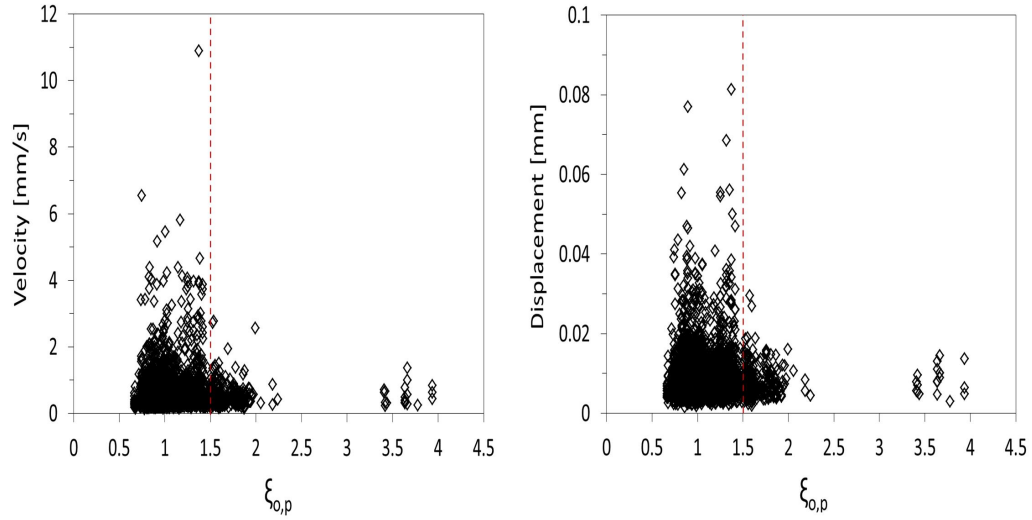

Figure 5.29: Structural velocity and displacement against *Iribarren number*.

As may be seen from Figure 5.29, almost the totality of the strongest events ($V > 2$ mm/s and $D > 0.02$ mm) occur for $\xi_{o,p} < 1.5$. This could be expected, given that wave steepness is an indicator of the breaker violence through the well-known classification of Galvin (1968) (Section 2.5.1) – note that the *Iribarren number* is inversely proportional to the wave steepness. However, the events with $\xi_{o,p} < 1.5$ are 90.0% of the data

set. Therefore, when $\xi_{o,p} \geq 1.5$, there is a drastic decreasing of both number of events and their structural magnitudes.

Thanks to video images, it is possible to distinguish four main Iribarren ranges as follows.

1^{st} *RANGE* : $\xi_{o,p} < 0.6$

No structural responses are recorded. Video images show calm sea conditions or white capping conditions attributable to weak spilling breakers.

2^{nd} *RANGE* : $0.6 < \xi_{o,p} < 2.2$

Almost the totality of the events (99.4%) occur in this range. Due to the fact that the *Iribarren number* does not take into account the variability of the water depth, it is possible to distinguish two different breakers: plunging and broken. The former group shows the detachment of plunging jet that hits the tower, whilst for the latter the plunging is completely developed and large amount of turbulence hits the structure with high residual velocity. Similarly, Blenkinsopp & Chaplin (2008) pointed out that, during their laboratory tests, breaking waves are strongly influenced by the water level variation over the crest of a submerged reef. Although the Eddystone Reef tends to be submerged at higher tide conditions, the water level variation may generate a range of hydraulic conditions as found by Blenkinsopp & Chaplin (2008).

3^{rd} *RANGE* : $2.2 < \xi_{o,p} < 3.3$

No responses are recorded in this range. Small wave conditions or turbulent mixtures of water-air are visible from video images. This may be explained by the fact that increasing *Iribarren numbers* imply the increase of the wave period and/or the decrease of the wave height. On one hand the occurrence of longer wave periods tend to be rare. On the other hand longer periods result in mild waves when wave heights are small,

or they break farther from the lighthouse when the wave heights are larger. Both the situations should give wave conditions that are not able to lead structural deflections.

4^{th} *RANGE* : $\xi_{o,p} > 3.3$

Exceeding the value of 3.3, a surprising cluster of weak events can be seen. These events have the same wave period T_p of 28.2 s, which was continuously measured during a period of 24 hours. As a consequence of this long period, wave should break far from the lighthouse. However, this period does not seem to be in agreement with video images, which show small waves that break close to the lighthouse.

Dimensionless *momentum flux* for irregular waves

As for the *Iribarren number*, the dimensionless relationship of the irregular *momentum flux* (Hughes, 2004a) M_F is defined using the offshore significant wave height ($H_{s,o}$) and the peak period (T_p) as follows:

$$M_F = A_o \left(\frac{h}{g {T_p}^2} \right)^{-A_1} \tag{5.3}$$

where

$$A_o = 0.64 \left(\frac{H_{s,o}}{h} \right)^{2.02} \quad \text{and} \quad A_1 = 0.18 \left(\frac{H_{s,o}}{h} \right)^{-0.39} \tag{5.4}$$

The instantaneous water depths h are estimated at the SW toe of the lighthouse (h_t), as illustrated in Figure 5.16 $-$ note that the values are obtained adding a constant value of 0.33 m to the BODC's measurements (CD).

Figure 5.30 shows the maximum structural velocities and displacements against M_F. Almost the totality of the largest displacements occur when $M_F = 0.6$-1.6 (which is 53.1% of the data set). In contrast, displacements tend to be lower than 0.04 mm when $M_F < 0.6$ (which is 34.1% of the data set) and when $M_F > 1.6$ (which is 12.8%

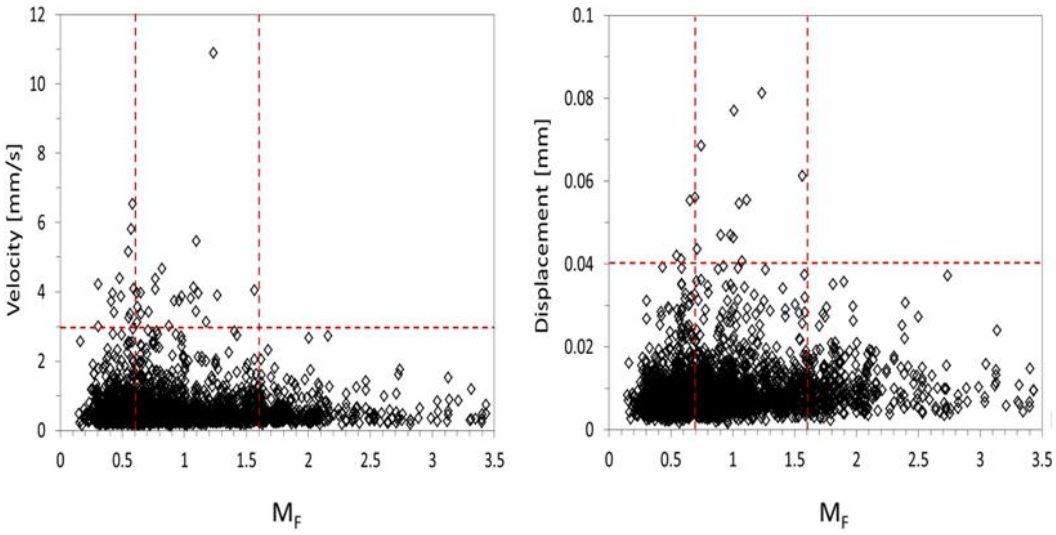

Figure 5.30: Structural velocity and displacement peaks against *momentum flux*.

of the data set). Although $M_F < 0.6$ and $M_F > 1.6$ lead to similar maximum deflections (i.e. 0.04 mm), velocities are much larger when $M_F < 0.6$ if compared to those with $M_F > 1.6$. As a consequence of previous observations, two results can be detected by comparing velocities and displacements of Figure 5.30.

- Maximum velocities occur in both ranges i.e. $M_F < 0.6$ and $M_F = 0.6$-1.6, but the range $M_F = 0.6$-1.6 is characterised by much larger displacements.
- The ranges $M_F < 0.6$ and $M_F > 1.6$ tend to have similar maximum displacements, but the range $M_F < 0.6$ is characterised by much larger velocities.

As a consequence of the previous two results, there is a general tendency for which the frequency of the structural response decreases as the *momentum flux* increases. According to Loraux (2013), shorter impact durations, which increase the frequency of the structural response, result in higher structural velocities but lower deflections when compared to those caused by longer impact durations (Section 2.4.3). For their part, video images indicate that the breaking distance tends to increase with increasing M_F.

Chapter 6

Wave loading at small scale

THE different structural response types shown in Chapter 5 require different wave load impulsivities, which are related to the breaker shape and aeration level in the coastal literature. In addition, structural numerical simulations in conjunction with field data suggest that the tower's deflection is strongly affected by the line of action of the wave force. However, in the previous chapter it has also been pointed out that more impulsive structural responses can generate smaller deflections even when the water level is higher. As a consequence, it is reasonable to suppose that other load variables contribute to affect the tower's deflection e.g. maximum instantaneous force, impact duration, extent of the spatial distribution. Small-scale model tests have been carried out in order to have a better understanding about the effects of the limited depth condition on the wave loading and how this is affected by the different breaker shapes. Because statistical field wave data have been related to individual geophone events, the structural responses may be related to laboratory tests on the basis of video images. To this end, regular waves have been used so that the wave shape could be investigated in a well-controlled condition.

This Chapter includes a description of the different breaking shapes at the lighthouse model. In addition, the influence of the wave parameters on the wave loading characteristics is provided and the occurrence of the different breaking shapes on the $\xi_o - M_{\mathrm{f}}$ plane is illustrated.

6.1 Breaker shape and load characteristics

As described in Section 3.2.3, the test program was designed to generate a comprehensive data set covering a broader range of wave conditions.

The different combinations of H_o and T (128 run tests) result in different wave shapes. Load time histories (pressure and overall force) tend to show different characteristics that gradually vary according to the wave shape. As a consequence, they have been distinguished on the basis of the relative breaking distance ($d = x/H_b$); except for spilling, non-breaking and slightly breaking.

Non-breaking is a mild wave with small amplitude, while slightly breaking occurs when an incipient breaking is visible in line with centre of the lighthouse model. Spilling breakers can occur within a wide range of breaking distances; however, the wave force is small because the wave steepness reaches its breaking limit. Consequently, the breaking is slow (spray rolls on the wave crest) and no detachment-jets are visible.

The other wave shapes are categorised in four types as follows.

- *Weak impact* ($x = 0.1$ - $0.5\ H_b$)
- *Violent impact* ($x = 0.5$ - $1.5\ H_b$)
- *Large air pocket* ($x = 1.5$ - $3.5\ H_b$)
- *Broken* ($x > 3.5\ H_b$)

Load characteristics from pressure measurements

Presented below are typical characteristics of the four significant breakers: *weak impact*, *violent impact*, *large air pocket* and *broken*. In particular, load data provided in the following Figures 6.2-6.5 correspond to the four impacts shown in Figure 6.1.

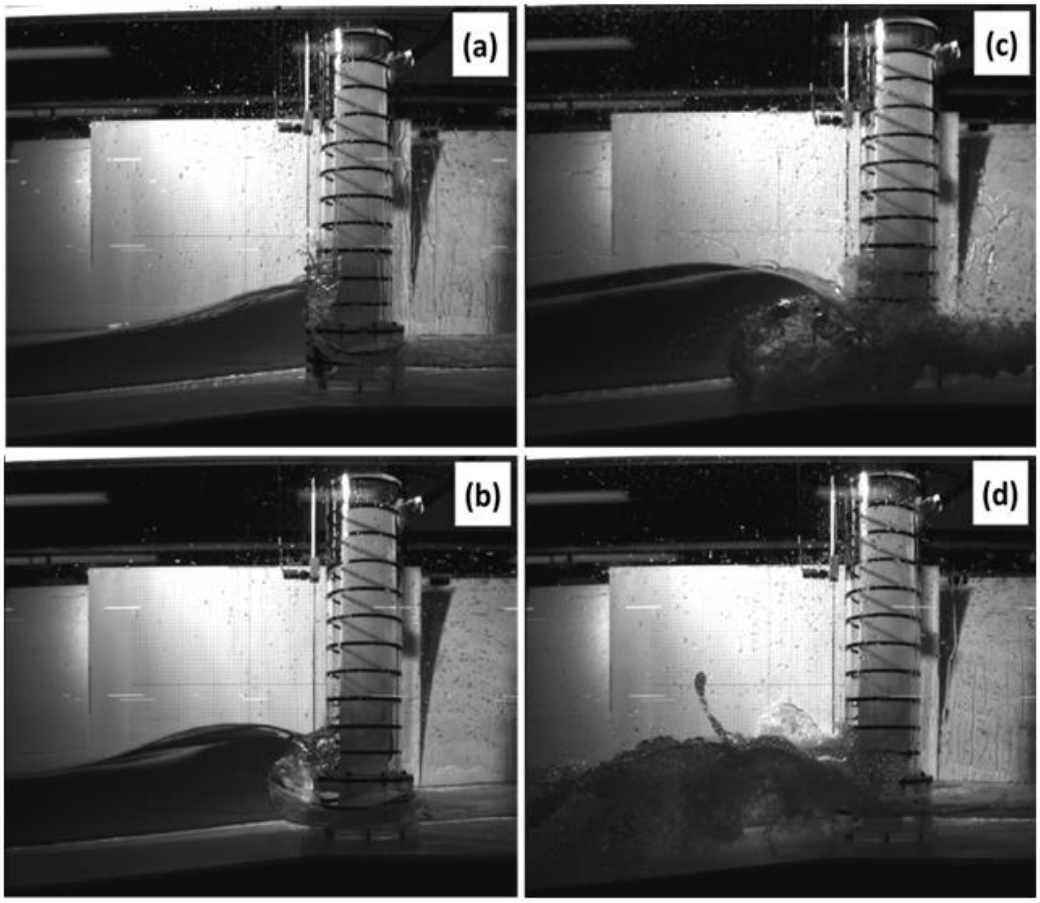

Figure 6.1: (a) *Weak impact* ($H_o = 0.11$m, $T = 1.4$s); (b) *violent impact* ($H_o = 0.13$m, $T = 1.8$s); (c) *large air pocket* ($H_o = 0.17$m, $T = 2.2$s); (d) *broken* ($H_o = 0.22$m, $T = 2.4$s).

- ***Weak impact***: $x = 0.1$ - $0.5\ H_b$

This is a small plunging impact that breaks approximately at the model with the wave front almost vertical (Fig. 6.1a).

Impulsive pressure time histories (i.e. $p_2 \neq 0$ as described in Section 4.2.1) are highly localised in space and they tend to occur in the proximity of transducer 3 (above SWL). Here, the impinging jet causes a rapid pressure spike, followed by the quasi-static component of the wave surface (Fig 6.2a). Usually, the other pressure transducers (below and above the area hit by the small plunging jet) do not exhibit the occurrence of a pressure spike (i.e. $p_2 = 0$). The maximum measurements, related to the pressure transducers under SWL, occur first, followed by quasi-static loads measured above the

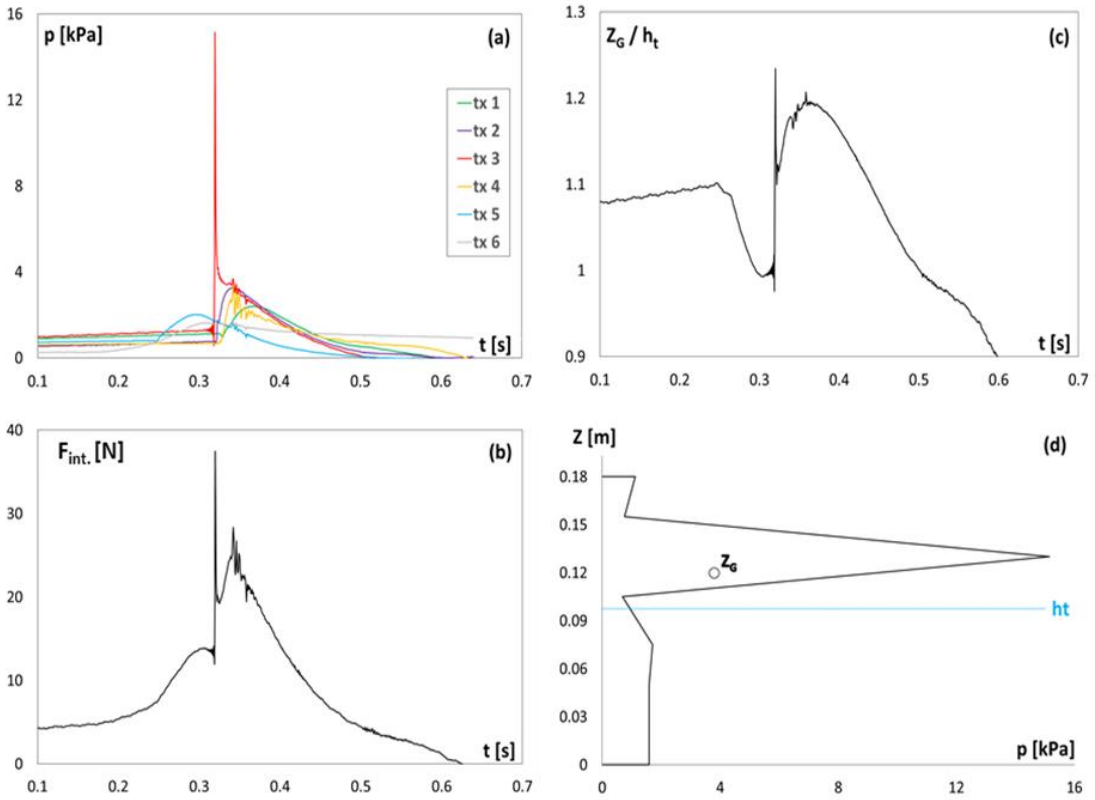

Figure 6.2: Weak impact ($H_o = 0.11$m, $T = 1.4$s): (a) pressure times histories; (b) integrated force; (c) time history of the line of action; (d) spatial distribution at the instant of the force peak.

impact area from the subsequent run up. Very often, the pressure records show high frequency oscillations at the location just below the occurrence of the impulsive peak. These oscillations, which occur later than the impulsive peak, suggest the presence of a small amount of air (transducer 4 in Fig. 6.2a).

The integrated force (F_{int}), estimated in Newton (N) as described in Section 4.2.1, exhibits a sharper peak highly localised in time (Fig. 6.2b). The instant of the maximum force is coincident with the instant of the maximum peak in the barycentre time history (dimensionless with respect to the water depth at the toe of the lighthouse, i.e. $h_t = 0.095$ m) (Fig. 6.2c) – note that the time history of the line of action of the horizontal force will be referred to as the barycentre time history. At the instant of the maximum force peak, the spatial distribution tends to be a sharp triangle with the peak above SWL (Fig. 6.2d).

- ***Violent impact***: $x = 0.5$ - $1.5\ H_b$

With respect to the previous breaker, this is a larger plunging impact that breaks relatively close to the model (Fig. 6.1b).

Impulsive pressures (i.e. $p_2 \neq 0$) tend to occur over all the pressure transducers, also for those under the SWL (Fig. 6.3a). All the pressure time histories tend to have a well-defined triangular shape and, frequently, extreme spikes are visible on the top of the triangular peaks (Fig. 6.3a). The maximum pressure peak, highly localised in the time, occurs randomly between the four pressure transducers above SWL (i.e. tx1, tx2, tx3 and tx4) depending on the direction of the forward jet. Minimal frequency oscillations after maximum peaks indicate the presence of a small volume of air (Fig. 6.1b).

The integrated force (F_{int}) results in a triangle with a sharp spike on the top (Fig. 6.3b).

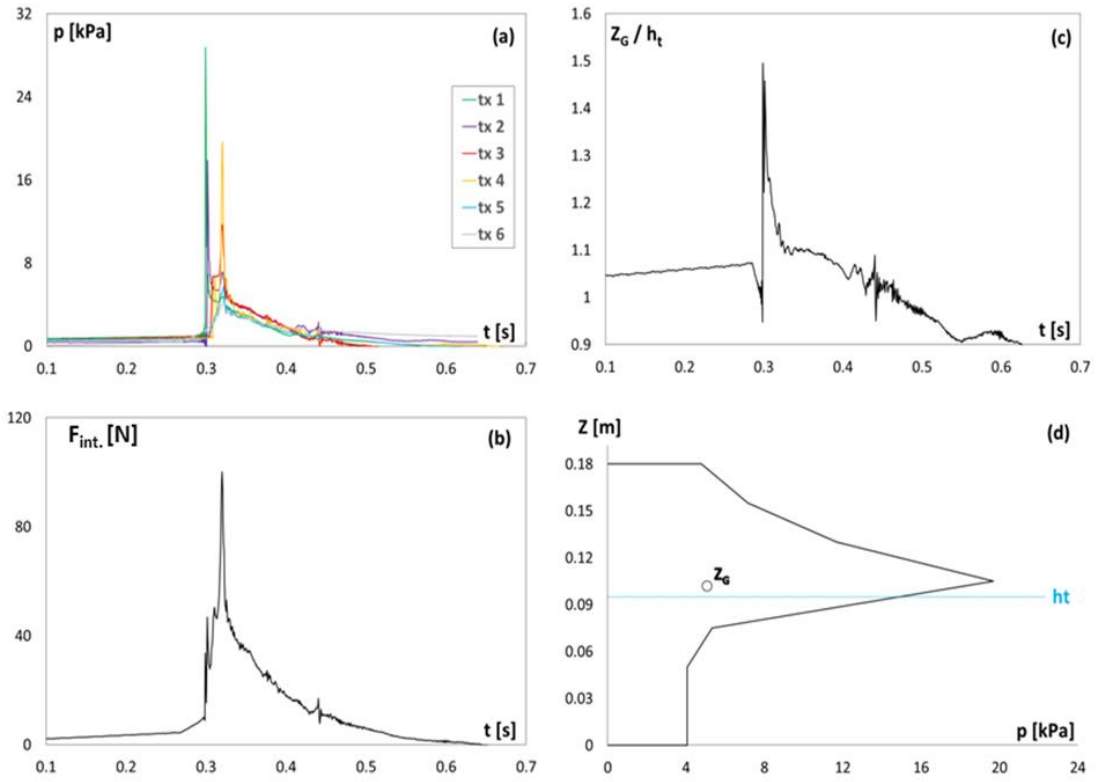

Figure 6.3: Violent impact ($H_o = 0.13$m, $T = 1.8$s): (a) pressure times histories; (b) integrated force; (c) time history of the line of action; (d) spatial distribution at the instant of the force peak.

Often, the first pressure spike, which occurs for the highest pressure transducers (i.e. tx1 and tx2), is so localised (in time and space) that it loses its effects when the pressures are integrated over the whole interface of the cylinder (Fig. 6.3b). As a consequence, the maximum peaks in the barycentre (Z_G/h_t) and force time (F_{int}) histories do not occur at the same instant (Fig. 6.3b-c). However, spatial distributions, at the instant of the maximum peak force (F_{int}), tend to be triangular; but the shape tends to be wider than that of the weak impact and with the peak just slightly above SWL (Fig. 6.3d).

- ***Large air pocket***: $x = 1.5$ - $3.5\ H_b$

This is a large plunging wave that breaks farther from the lighthouse model due to the limited water depth condition. The wave crest, which overturns and hits the model as it falls down, can entrap a large air pocket (Fig. 6.1c). This is an air-water mixture that extends over the whole depth at the toe of the lighthouse. Maximum run up, approximately 4 times the water depth h_t, occurred for this breaker type. However, this value is lower with respect to the maximum run up observed in the 3D situation of the field (Section 5.1.2).

This breaker exhibits two distinct temporal phases. The first phase is caused by the falling-down jet, which generates impulsive pressures above the SWL; the second phase is caused by the incoming wave that generates impulsive pressures under the SWL (Fig. 6.4a). Although the maximum pressure peak can occur in both the phases, it tends to be smaller and wider when compared to those recorded for violent impact type. In addition, the effects of the entrapped air generate irregular oscillations, recorded under SWL, after the secondary peaks (Fig. 6.4a).

As consequence of the distinct phases, the force time history (F_{int}) shows several peaks and its shape is less triangular than that of the violent impact type (Fig. 6.4b).

The barycentre time history (Z_G/h_t) shows the line of action moves from above to under SWL (Fig. 6.4c). Despite the repeatability of the barycentre time histories, two different spatial distributions can be associated with this breaker depending on whether the max-

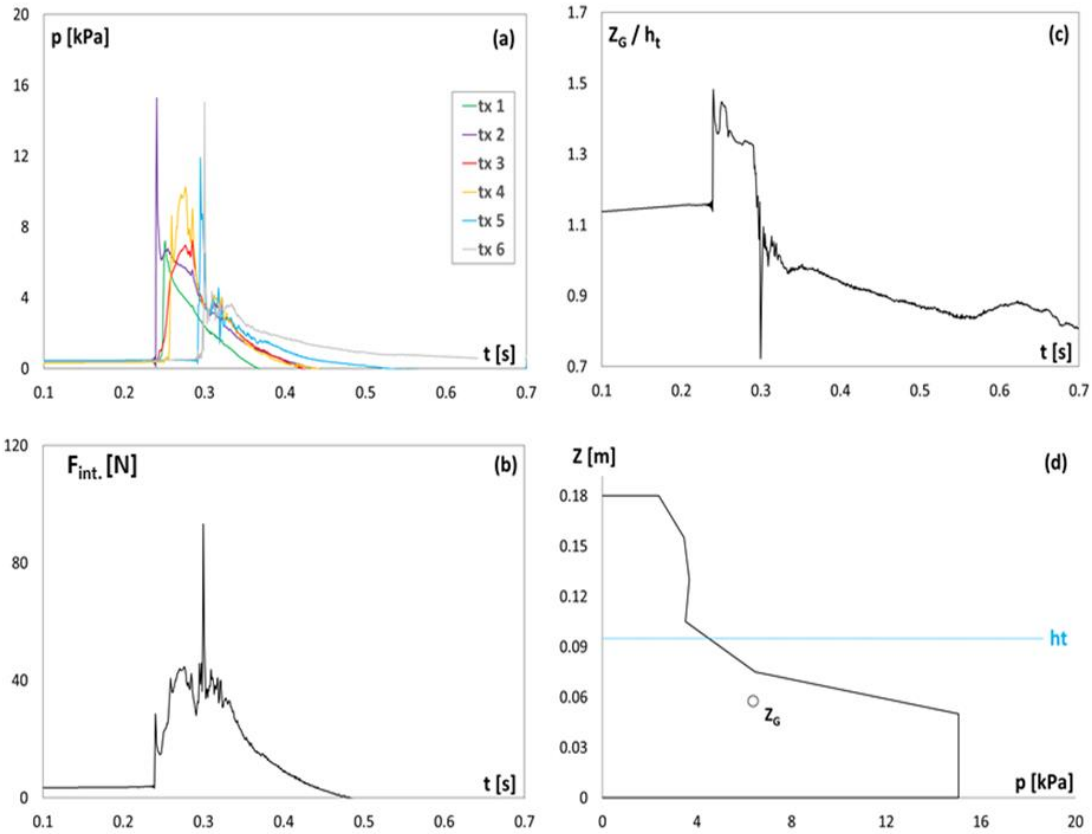

Figure 6.4: Large air pocket ($H_o = 0.17$m, $T = 2.2$s): (a) pressure times histories; (b) integrated force; (c) time history of the line of action; (d) spatial distribution at the instant of the force peak.

imum peak force occurs in the first or in the second phase. When the maximum force peak is related to the falling-down jet, the spatial distribution has a triangular shape similar to that of the violent impact type (Fig. 6.4d). Alternatively, when the maximum force peak is caused by the incoming wave, the spatial distribution is characterised by a wide area under the SWL (Fig. 6.4d).

- ***Broken***: $x > 3.5\ H_b$

The wave crest strikes the water and the cylinder is subsequently hit by a turbulent mass of water with high residual velocities (Fig. 6.1d). This breaker tends to cause lower run up, even if these wave impacts tend to persist for longer durations.

All the pressure transducers tend to show a highly variable signal characterised by

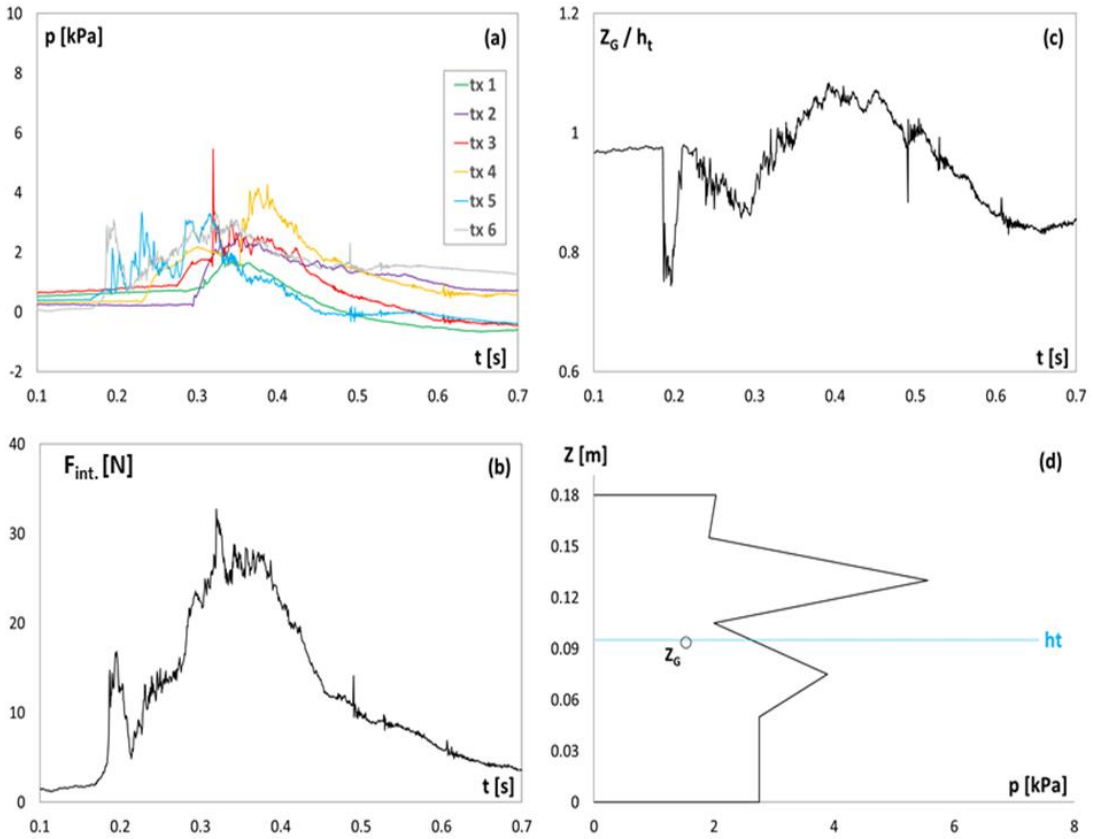

Figure 6.5: Broken ($H_o = 0.22$m, $T = 2.4$s): (a) pressure times histories; (b) integrated force; (c) time history of the line of action; (d) spatial distribution at the instant of the force peak.

random peaks due to the impact of the air-water mixture (spray) and secondary small jets (Fig. 6.5a). The pressure measurements are not in phase with each other and the pressure event moves gradually from tx6 (lower transducer) to tx1 (upper transducer) due to the turbulent bore that runs up the model (Fig. 6.5a).

The integrated force (F_{int}) shows a quasi-static noisy signal (Fig. 6.5b); usually, two peaks can be observed because pressures are not simultaneous.

The barycentre of the spatial distributions moves from under to above SWL (Fig. 6.5c). Due to the fact that pressure magnitudes from tx3, tx4 and tx5 tend to be similar, the maximum spatial distributions can occur slightly under or above SWL. Although they tend to be characterised by a more uniform distribution over the whole impact extent, the shape is completely random (Fig. 6.5d).

Load cells measurements

Figure 6.6 shows video images and load cells measurements for the four wave conditions previously described. Note that the maximum values of the vertical axes are not the same. Maximum load peak related to the four breaker types will be discussed in Section 6.3.

As may be observed from Figure 6.6a-b, the impinging front of the *weak impact* causes a rapid force peak, followed by the quasi-static component of the wave surface.

Similarly, the time history of the *violent impact* shows an initial clear sharp peak followed by high frequency oscillations (Fig. 6.6c-d). However, these oscillations, which occur after the maximum peak of Figures 6.6b and 6.6d, are similar to the natural frequency of the system (25 Hz). As a consequence, these oscillations are likely to be the response of the load cell system rather the instantaneous wave-induced force.

With respect to the force time histories of the *violent impact*, *large air pocket* tends to be characterised by a longer rise time; as a consequence its dynamic impulse can increase even when the force peak is lower (Fig. 6.6e-f). As may be observed from Figure 6.6f, the maximum force value does not occur at the beginning of the signal event, but the time history shows a wide dynamic peak that tends to be symmetric. This occurs with an overlap of irregular oscillations that may be an aeration effect. Immediately after the wide peak, a long lasting quasi-static component occurs. Compared to the force obtained by the pressure integration (Fig. 6.4b), the load cell signal is smoother because the pressure spikes tend to be very localised and the resolution of the pressure transducers (i.e. their spacing) prevents a smooth result.

The force time history of the *broken* wave is similar to that of the large air pocket. Also this breaker exhibits a wide and symmetric dynamic peak that occurs with secondary oscillations, although these tend to be smoother (Fig. 6.6g-h). As may be observed by comparing Figures 6.6b and 6.6h, the force peak of the broken wave is slightly lower than that of the weak impact, but the rise time and the rise impulse tend to increase drammatically.

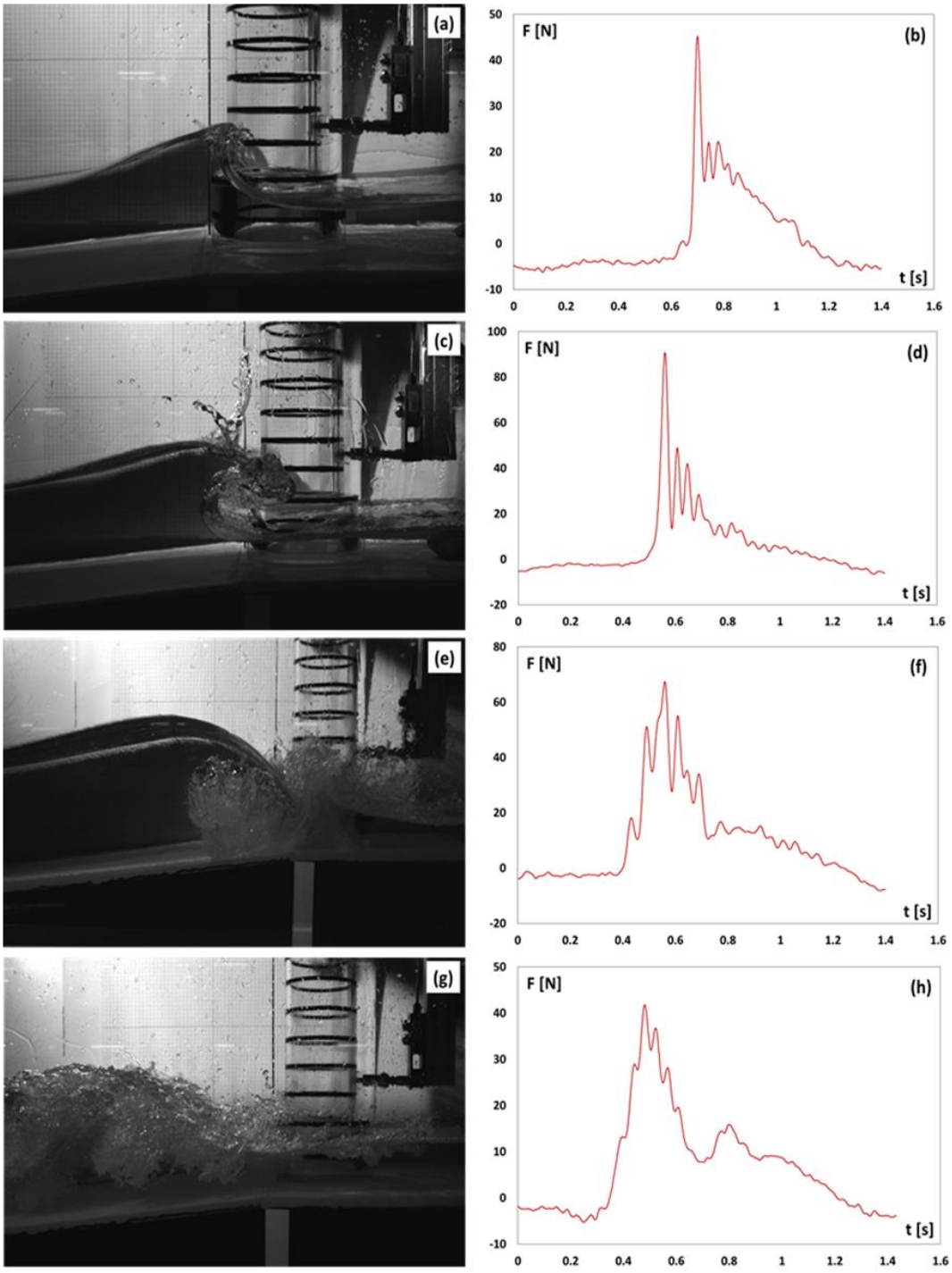

Figure 6.6: Video images and horizontal force time measured representative of the four breaker type: (a) *weak impact* ($H_o = 0.11$m, $T = 1.4$s); (b) *violent impact* ($H_o = 0.13$m, $T = 1.8$s); (c) *large air pocket* ($H_o = 0.17$m, $T = 2.2$s); (d) *broken* ($H_o = 0.22$m, $T = 2.4$s). Note: the vertical axes have a different scale.

6.2 Load characteristics and dimensionless coastal parameters

Load peak characteristics (pressure, overall force and line of action) are investigated on the basis of the *Iribarren number* ξ_o and *momentum flux* M_f (dimensionless coastal relationships for regular waves described in Section 2.5). Figure 6.7 shows dimensional and dimensionless pressure peaks against ξ_o and M_f. The peaks are the maximum values recorded for each test by each pressure transducer (six in total). The dimensional values are in kPa, while the dimensionless values (usually used as an indicator of the impulsivity) are obtained by dividing the pressure by the specific weight of the water (γ) and the offshore wave height (H_o) i.e. measured before the wave transformation that occurs on the 1:20 slope.

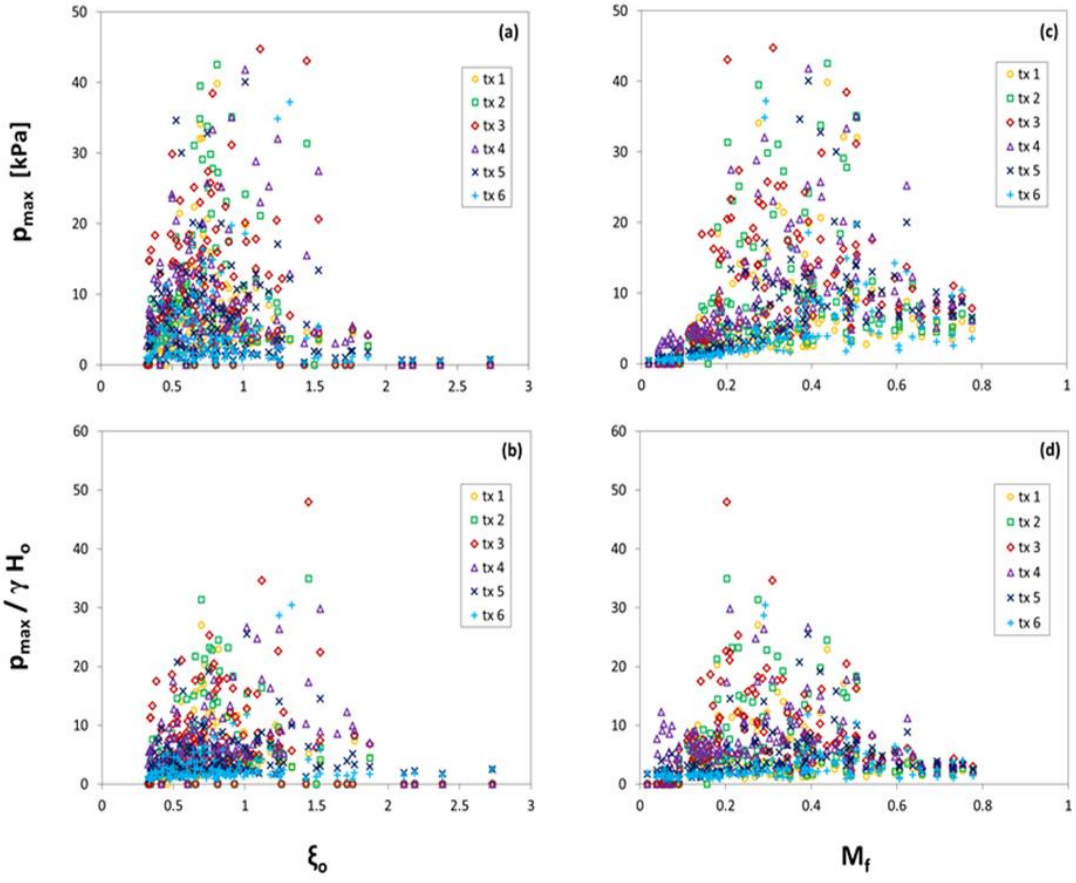

Figure 6.7: Maximum pressure peaks against ξ_o (left) and M_f (right). On the top are dimensional values and on the bottom dimensionless values. The p_{max} are distinguished from tx1 (upper transducer) to tx6 (lower transducer).

As may be observed from Figure 6.7a-b, pressure peaks are quite random when plotted against ξ_o. Also, similar maximum values (dimensional and dimensionless) can occur over a large range ($0.4 < \xi_o < 1.5$). However, the pressures are much smaller when $\xi_o > 1.5$. This is due to the fact that plunging waves can occur if $\xi_o < 1.5$, instead only non-breaking/slightly breaking waves occur when $\xi_o > 1.5$. When $1.0 < \xi_o < 1.5$, dimensionless values tend to show a relatively larger scatter because they are characterised by stronger wave transformation (maximum values observed $H_b/H_o = 1.6$).

When plotted against M_f, most of the highest dimensional pressure peaks occur over the range 0.2-0.6 (Fig. 6.7c). This is given by the fact that non-breaking/slightly breaking waves occur only if $M_\mathrm{f} < 0.2$, while broken waves occur when $M_\mathrm{f} > 0.6$. Except for the lower values in the first part ($M_\mathrm{f} < 0.2$), where waves are non-breaking/slightly breaking, the dimensionless pressure shows a tendency to decrease with the increase in M_f.

Figure 6.8 shows dimensional and dimensionless maximum integrated force against ξ_o and M_f. The dimensionless values are obtained by dividing the force line (f) by the specific weight of the water (γ), the offshore wave height (H_o) and the water depth at the toe of the cylinder ($h_t = 0.095$ m). As for the dimensional and dimensionless pressures, most of the highest force peaks tend to occur for $\xi_o < 1.5$ and $0.2 < M_\mathrm{f} < 0.6$ (Fig. 6.8).

As may be observed by comparing Figure 6.8c and 6.8d, M_f below 0.2 show a scatter moving from dimensional to dimensionless value. This portion of data includes slightly-breaking waves, which are characterised by small offshore wave heights that become steeper in the proximity of the model. As a result, they cause small impulsive load peaks with respect to the offshore wave heights. However, the dimensional forces are rather small because these waves are so small that the two upper transducers did not record the pressure event. Moreover, events with $M_\mathrm{f} > 0.6$ generate larger forces (dimensional values) with respect to those with $M_\mathrm{f} < 0.2$, even if the latter exhibit stronger impulsivity i.e. larger dimensionless values.

Although with different peak values, overall forces obtained by load cells generally tend to exhibit the same tendencies previously described for the integrated forces (Fig. 6.9).

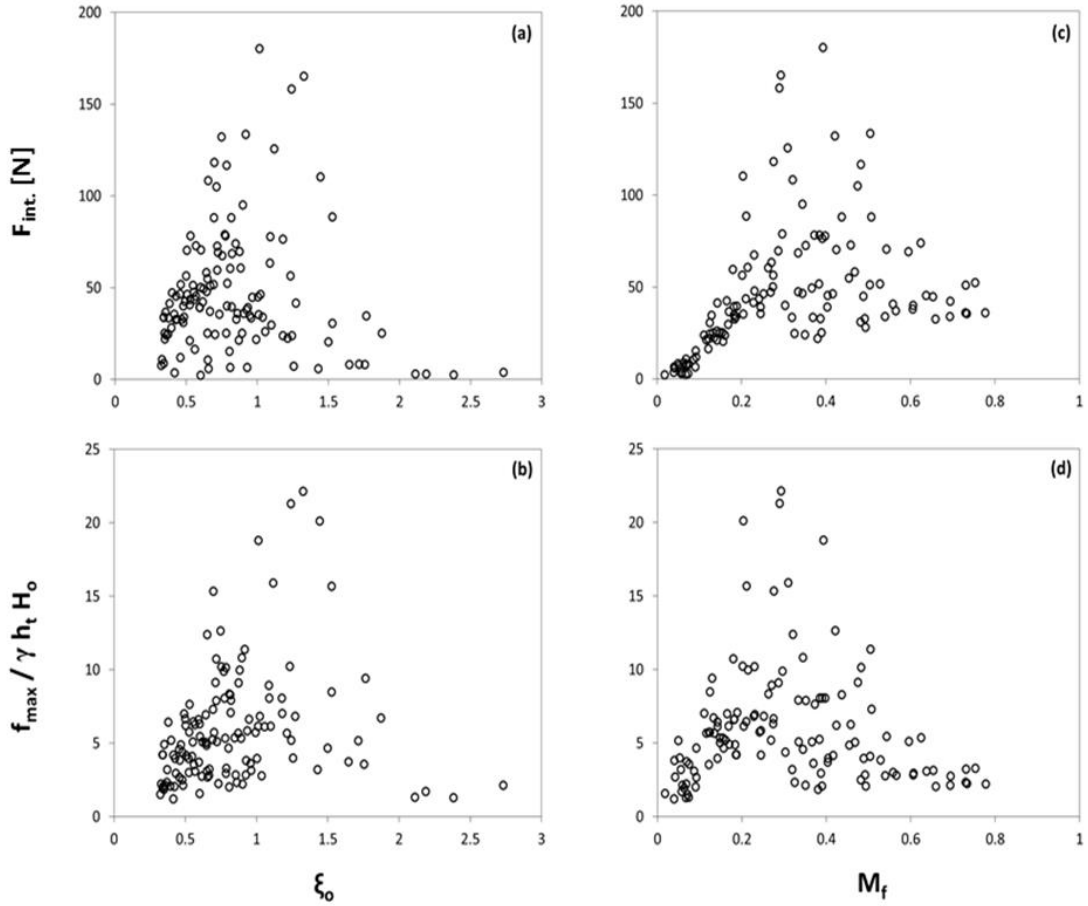

Figure 6.8: Maximum force peaks (obtained by the pressure integration) against ξ_o (left) and M_f (right). On the top row are dimensional values and on the bottom dimensionless values.

However, the tendencies are slightly clearer and, in agreement with the pressure rather than the integrated force, the dimensionless force peaks tend to show a slightly decreasing trend when they are plotted against M_f (Fig. 6.9d). Note that the dimensionless force is obtained by dividing the force F (in N) by four terms: (γ, H_o, h_t and the average diameter D_{av} (i.e. 0.175 m).

By comparing the dimensionless forces, i.e. Figures 6.8c and 6.9c, the values obtained from load cells exhibit a tendency to be larger compared to the integrated forces when $M_\mathrm{f} > 0.6$. As a consequence, the spatial azimuthal distribution, used to estimate the overall force from pressure measures (Section 4.2.1), may provide an underestimation of the overall force acting on the circular model when waves tend to be *broken*.

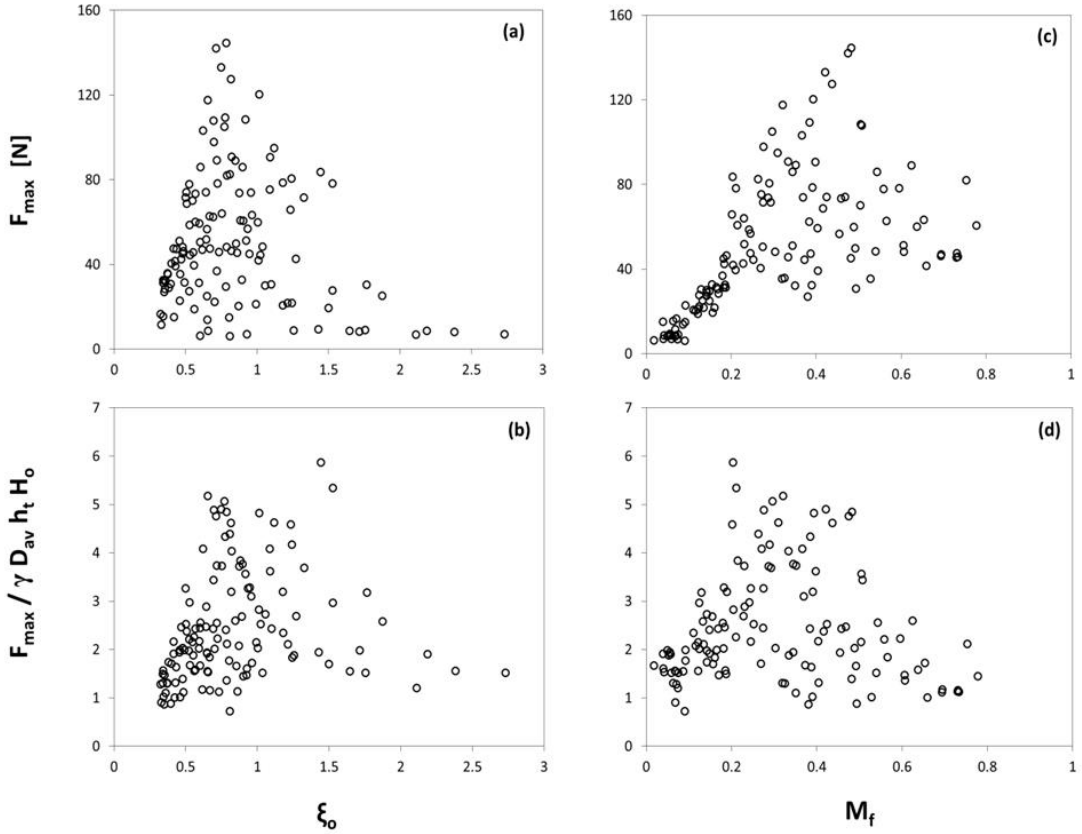

Figure 6.9: Maximum force peaks (obtained by the load cell system) against $\xi_{o,p}$ (left) and M_f (right). On the top row are dimensional values and on the bottom dimensionless values.

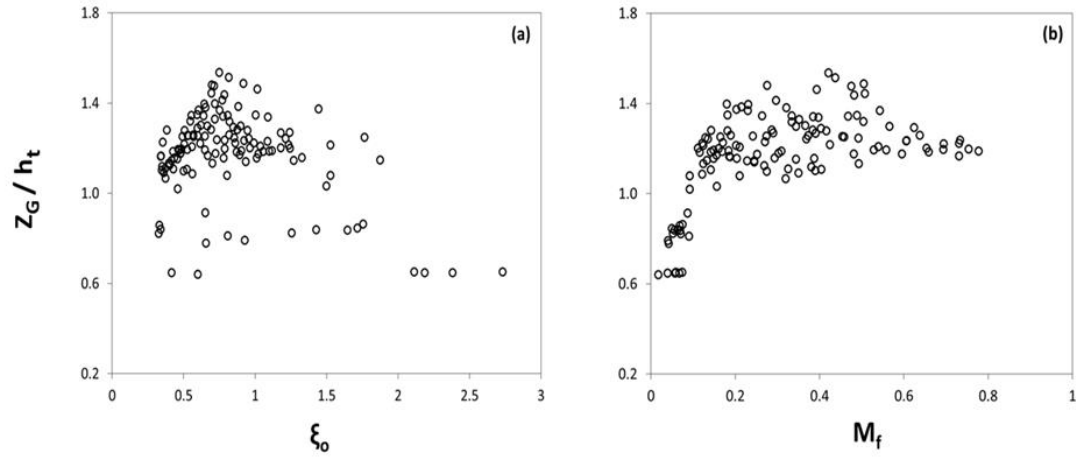

Figure 6.10: Maximum dimensionless barycenter peaks against $\xi_{o,p}$ (left) and M_f (right). On the top row are dimensional values and on the bottom dimensionless values.

In the previous Section 6.1, spatial distributions that occur at the instant of the maximum force have been described. Figure 6.10 shows the maximum peaks of the barycentre time history plotted against the *Iribarren number* and *momentum flux*. As may be observed, the *Iribarren number* does not show a clear trend (Fig. 6.10a). However, when plotted against the *momentum flux*, the lowest barycentre peaks occur for $M_f < 0.2$, then the highest values (approximately 1.5) occur over the range 0.2-0.6 and they tend to 1.2 when $M_f > 0.6$ (Fig. 6.10b).

6.3 Occurrence of the breaker types on the breaking plane

Figure 6.11 shows the breaker plotted on the dimensionless plane $\xi_o - M_f$ according to the measured offshore wave height H_o (i.e. before the wave transformations that occur on the 1:20 slope). It should be note that the position of the breaker on the plane depends on the location of the depth section used to calculate the *momentum flux*. As illustrated in Section 3.2.3, the depth section (h^*) has been identified at a distance from the lighthouse model equal to $5(H_o)max$. As may be observed in Figure 6.11, the same value of the *Iribarren number* or *momentum flux* can generate different type of impacts. As a consequence, a better characterisation of the event is obtained by plotting data on the breaking map used to define the program test.

Analysing Figure 6.11, waves break for wave steepness (spilling) far from the lighthouse model when the *Iribarren number* is low ($\xi_o < 0.4$); while the waves approach the lighthouse with minor breaking (non-breaking and slightly-breaking) for larger values ($\xi_o > 1.5$). Plunging waves (i.e. *weak impact*, *violent impact*, *large air pocket* and *broken*) are enclosed between $0.4 < \xi_o < 1.5$. However, the full development of the plunging jet does not occur if the *momentum flux* is lower than 0.15-0.2; in this case, waves are non-breaking or slightly-breaking. In contrast, an excessive increase of the *momentum flux* ($M_f > 0.6$) does not lead to larger forces because the breaking point tends to move seawards from the structure with increasing M_f. As a consequence, despite the large offshore wave heights, most of the wave energy tends to be dissipated

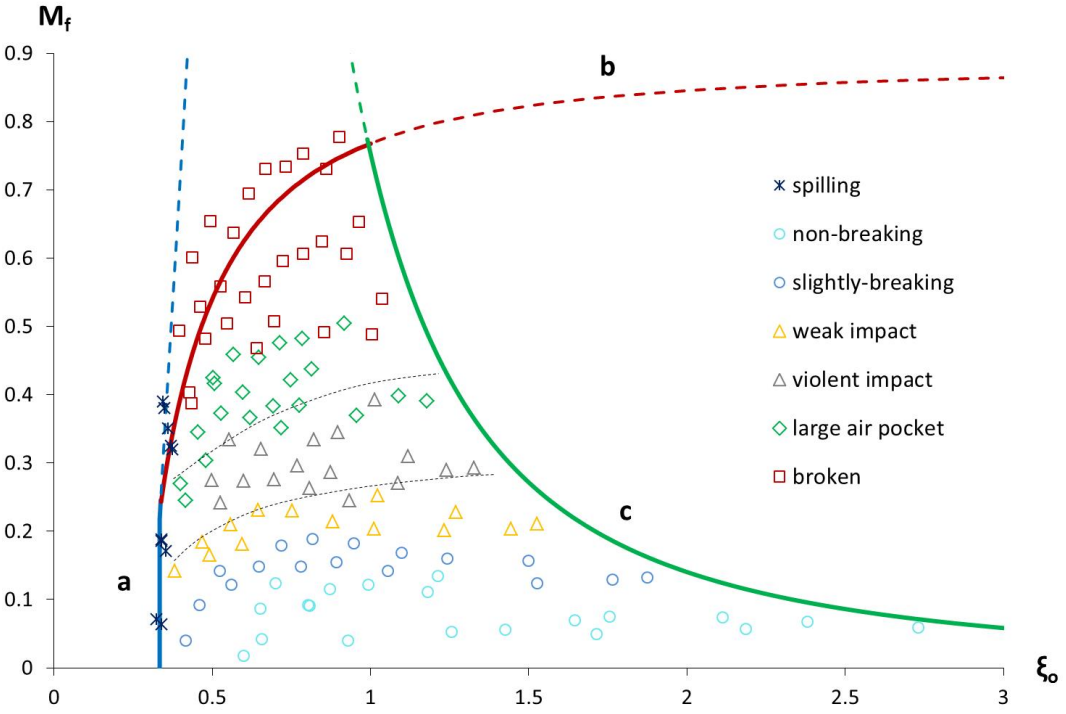

Figure 6.11: Impact type occurrence on the breaking map delimited by the three limits: (a) wave steepness, (b) breaking wave height and (c) shallow water. Most violent impacts are enclosed by the two black dashed lines.

before reaching the lighthouse model.

It should be noted that the transition of breakers occurs for higher values of M_f when $1.0 < \xi_o < 1.5$. Consequently, the relative breaking distance increases moving horizontally from right to left. This is caused by the fact that the wave height increases moving horizontally from right to left i.e. the breaking point tends to move seawards. In addition, gentler waves i.e. higher ξ_o are affected by stronger wave transformations that cause larger breaking wave height. As a consequence, the relative breaking distance tends to decrease moving from left to right, even when the breaking point moves farther from the structure.

Histograms in Figure 6.12 show maximum peak range (smallest and largest value) recorded for the four breaker types distinguished on the basis of the relative breaking distance from video images i.e. *weak impact* (14 tests), *violent impact* (17 tests), *large air pocket* (22 tests) and *broken* (28 tests). Pressure and overall forces peaks

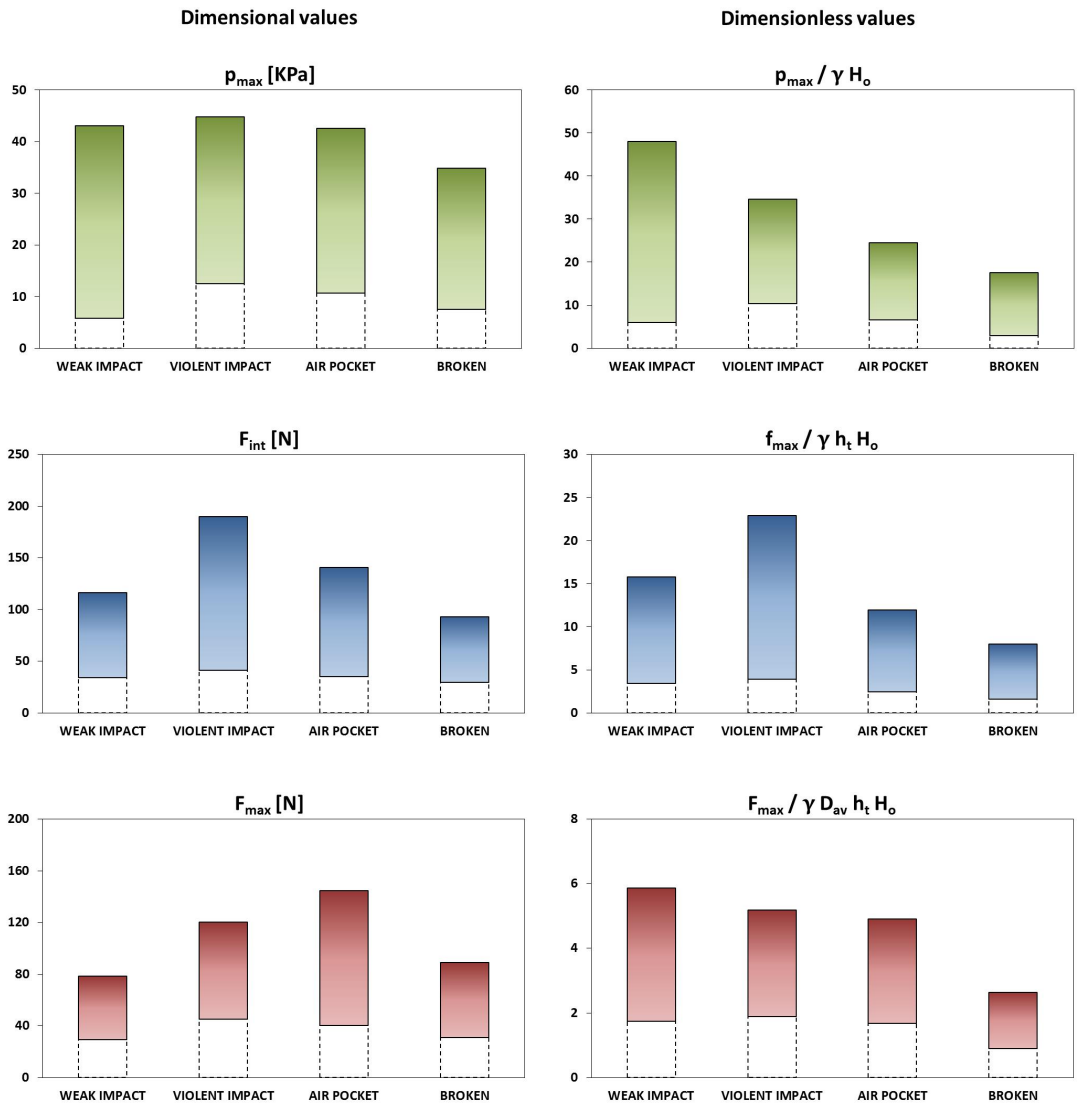

Figure 6.12: Histograms of the maximum peak ranges of pressure (top), integrated force (middle) and load cells force (bottom). Dimensional (left) and dimensionless values (right).

are shown for both dimensional (left) and dimensionless values (right). As may be observed in Figure 6.12, *weak impact*, *violent impact* and *large air pocket* are able to generate similar dimensional pressures. In contrast, the dimensionless pressures decrease from *weak impact* to *broken*. Consequently, the impulsivity of the pressure signals tends to decrease with increasing of the relative breaking distance. This means that smaller waves (*weak impact*), characterised by smaller masses, can generate

pressures similar to those generated by larger wave heights. Thus, due to the fact that pressure transducers provide spatially localised measurements, the pressures may be more affected by the acceleration of the water than by the amount of the water mass.

In contrast with pressure, dimensional integrated forces exhibit larger difference among the four breaker types, and maximum values (both dimensional and dimensionless) are given by *violent impact* (Fig. 6.12). This result is caused by the fact that a couple of vertical spikes tend to be almost simultaneous over two pressure transducers for the *violent impact*. As a consequence, the integrated force tends to show a strong vertical spike highly localised in time. Although the weak impact types arise from a plunging wave that breaks at the structure with the wave front almost vertical, it causes lower forces when compared to breaker characterised by larger breaking distances. This is explained by the fact that the lighthouse model is in depth limited conditions and only small plunging waves are able to break at the structure. Thus, even if larger plunging waves break farther from the lighthouse, they are characterised by larger wave heights and periods that generate larger forces.

In contrast with the forces estimated from pressure measurements, dimensional force obtained from load cell show maximum values in this order: *large air pocket*, *violent impact*, *broken* and *weak impact*. Thus, larger plunging waves cause the maximum forces acting on the whole lighthouse model; even if they are characterised by larger breaking distances. As for the dimensionless pressure, the dimensionless force (obtained by load cells) also decreases from *weak impact* to *broken* (Fig. 6.12). Consequently, the impulsivity of the force signals tends to decrease with increases of the relative breaking distance as well.

6.4 Comparison with previous laboratory studies on plunging impacts

The present laboratory investigation provides agreement with much of the laboratory findings described in the coastal literature. For example, although wave pressure peaks exhibit their intrinsic random nature, the behaviour of the load time history tends to

be repeatable with the breaker shape at the lighthouse model, as found in laboratory studies on plane walls (Chan & Melville, 1988; Oumeraci et al., 1993; Hattori et al., 1994; Hull & Müller, 2002) and vertical cylinders (Tanimoto et al., 1986; Zhou et al., 1991; Chan et al., 1995).

As indicated by field video images, the laboratory tests show that the lighthouse can be exposed to violent breaking waves, with extreme pressure peak between 30-50 ρgH recorded during the experiments. This range is in agreement with the maximum pressures noted by Zhou et al. (1991) and Chan et al. (1995) in their laboratory studies on vertical cylinders (i.e. 30-40 ρc^2)[1].

Similarly to the findings described by Zhou et al. (1991) and Chan et al. (1995), the extreme peaks recorded on the lighthouse model are highly localised in space and time. In addition, in the present investigation pressure oscillations after extreme peaks are observed. It is likely that the oscillations are an aeration effect (Zhou et al., 1991; Chan et al., 1995).

Impulsive loads were observed to occur when the wave breaks at or near the lighthouse model; then, the impact duration and the violence of the impact decreases with increasing breaking distances. This result is in agreement with several investigations on vertical cylinders (Tanimoto et al., 1986; Zhou et al., 1991; Chan et al., 1995; Wienke & Oumeraci, 2005).

Another similarity with previous investigations on vertical cylinders (e.g. Tanimoto et al., 1986; Zhou et al., 1991; Chan et al., 1995) is related to the spatial distribution of the overall force – defined impulsive in the coastal literature if the maximum peak is 2.5 times the hydrostatic force related to the quasi-static component (Kortenhaus & Oumeraci, 1998). Plunging impacts are characterised by a triangular spatial distribution and the line of action of the overall force (quasi-static and dynamic) is at approximately 0.5 times the water depth (h) at the toe of the lighthouse model (from the still

[1] Note that the two pressure relationships $p = \rho gH$ and $p = \rho c^2$ are similar because in shallow water the wave celerity is $c = \sqrt{gh}$ and the breaking wave height limit is about $H/h \approx 1$. As a consequence, $p = \rho c^2 \approx \rho gh \approx \rho gH$.

water level) – with maximum dynamic peaks about 6 times the quasi-static component. The value of the line of action of the force is in agreement with those related to the dynamic spatial distribution suggested by Tanimoto et al. (1986) and Wienke & Oumeraci (2005) i.e. $0.57H_b$ – note that at the breaking point $H/h \approx 1$.

However, the present investigation shows a significant difference when compared to the previous investigations on vertical cylinders. Plunging impacts at the lighthouse model and broken waves are characterised by similar dimensional force peaks, although with a different impulsivity (i.e. impact duration). This is explained by the fact that the present investigation is characterised by a limited water depth at the toe of the lighthouse model. This aspect is analysed in depth in the following chapter.

Chapter 7

Wave impacts on the Eddystone lighthouse and assessment procedures

BASED on the insights obtained from the laboratory tests, this Chapter provides an interpretation of the field data. In addition, practical advice, which can be applied for the particular case of study of the Eddystone lighthouse, are suggested.

7.1 The effects of the depth-limited condition on wave impacts

The laboratory tests indicate that breaker load classifications, based on the breaker shape on vertical or 'near' vertical walls (Chan & Melville, 1988; Oumeraci et al., 1993; Hattori et al., 1994; Hull & Müller, 2002), may not be applicable in conditions for which the structure is on the top of a steep slope and in limited water depths. In particular, the limited depth conditions strongly affect the impulse and the impulsivity of the different breaker shapes. Usually, the severest load situations are related to waves that break on or just in front of the structure (plane walls or offshore cylinders). This result does not occur for the present laboratory tests, where the limited water depth allows the breaking at the toe of the lighthouse model only for small plunging waves. Larger waves that break further away can impose a greater overall impulse due to the longer duration of the load, even when the maximum force peak is lower. In contrast, the impulsivity (shock load) tends to decrease with the increase of the relative breaking distance; this result is in good agreement with the coastal literature.

For field data, *impulsive* structural responses (Type 1 and 2) tend to be caused by

waves that break on or just in front of the Eddystone lighthouse. However, such loads do not necessarily lead to the largest displacements when compared to *slightly-impulsive* responses (Type 3 and 4). In particular, higher structural velocities and accelerations can result in lower structural deflections. According to Loraux (2013), shorter impact durations, which increase the frequency of the structural response, result in higher structural velocities but lower deflections when compared to those caused by longer impact durations (Section 2.4.3). As a consequence, the longer impact duration may explain the larger deflection arising from broken waves when these occur at lower tide conditions, which should imply both smaller impact extents and lower application points of the wave force.

From an engineering point of view, the structural responses of the Eddystone lighthouse tend to be caused by plunging waves, which can hit the lighthouse with a plunging jet or with turbulent masses of water (when the plunging is completely developed). However, the *Iribarren number* fails in identifying the impulsivity of the wave force. This is given by the fact that the *Iribarren number* cannot take into account the wide tide variations that characterise the Eddystone Reef. In contrast, the *momentum flux* appears as a better indicator of the wave impulsivity when compared to the *Iribarren number*. In particular, the laboratory tests at constant water level indicate that the relative breaking distance tends to increase with increasing *momentum flux* (Fig. 6.11).

At this stage, in the absence of any guidelines for circular structures located on the top of steep slopes, an attempt to identify the wave impulsivity may be obtained by correlating the irregular *momentum flux* of Hughes (Equation 7.1 and 7.2) with a qualitative estimation of the relative breaking distance.

$$M_F = A_o \left(\frac{h}{g {T_p}^2} \right)^{-A_1} \tag{7.1}$$

where

$$A_o = 0.64\left(\frac{H_{s,o}}{h}\right)^{2.02} \quad \text{and} \quad A_1 = 0.18\left(\frac{H_{s,o}}{h}\right)^{-0.39} \tag{7.2}$$

For this purpose the irregular breaking coefficients of Goda (2010) may be used as described in the following procedure.

Breaking and estimation of a *momentum flux* threshold $M_{F,b}$

1. Define the slope and identify the breaking coefficients $H_{1/250,b}/H_{s,o}$ and $H_{s,o}/h_b$ provided by Goda (2010). In this investigation the values related to 1:10 slope have been used (Table 7.1).

Table 7.1: Goda's coefficients (2010) for a 1:10 slope

$s_{s,o}$	0.01	0.02	0.04
$H_{s,o}/h_b$	0.45	0.50	0.53
$H_{max,b}/H_{s,o}$	2.48	2.04	1.72

2. The values of the breaking coefficients, which depend on both slope and offshore wave steepness s_o, can be inserted in Equation 7.1 and 7.2 with appropriate transformations of the relative water depth as shown by Equation 7.3.

$$\left(\frac{h}{gT^2}\right) = \left(\frac{h_b}{H_{s,o}}\right)\left(\frac{s_{s,o}}{2\pi}\right) = \left(\frac{h_b}{H_{s,o}}\right)\left(\frac{H_{s,o}\,2\pi}{gT_s^2\,2\pi}\right) \tag{7.3}$$

3. Once the values of the breaking coefficients have been determined, calculate the value of the *momentum flux* ($M_{F,b}$) as explained in step 2. As shown in Table 7.2, for the 1:10 slope $M_{F,b}$ varies between 0.48-0.51 (depending on $s_{s,o} = H_{s,o}/L_{o,s}$).

Table 7.2: Momentum flux threshold ($M_{F,b}$)

$s_{s,o}$	0.01	0.02	0.04
$H_{s,o}/h_b$	0.45	0.50	0.53
$M_{F,b}$	0.48	0.49	0.51

Step 3 implies that the breaking limits provided by Goda (2010) are reached when $M_F = M_{F,b}$ =0.48-0.51 (for a 1:10 slope). As a consequence, the breaking limits are reached at the depth section h, used to calculate M_F, if $M_F = M_{F,b}$ =0.48-0.51.

Identification of the depth section where M_F is determined

The following steps use the breaking coefficients of Goda (2010) in order to estimate the value of h_b that generates a generic relative breaking distance $d(h_b)$ e.g. a qualitative slightly-impulsive limit equal to 2-3 times $H_{1/250,b}$.

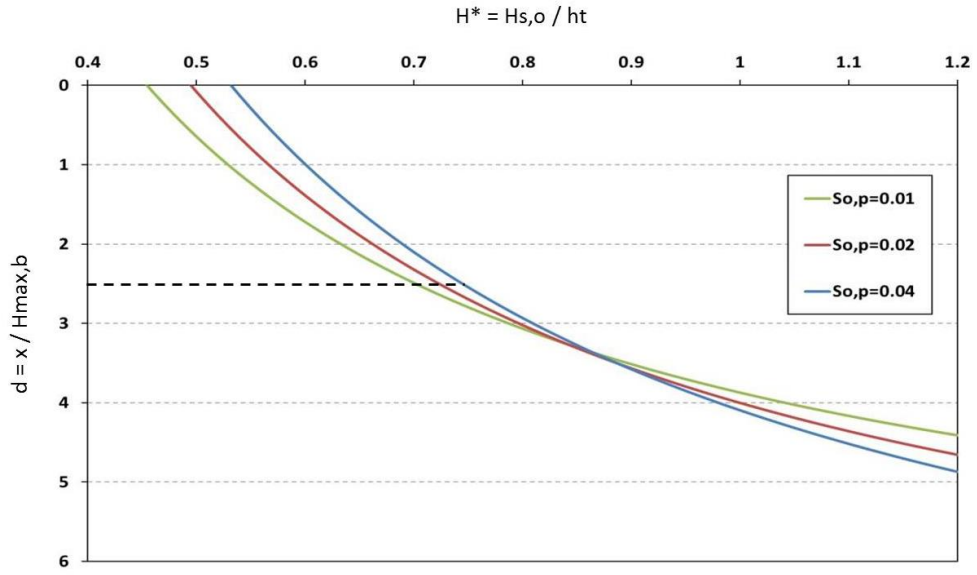

Figure 7.1: Relative breaking distance (d) against the relative wave height at the toe of the lighthouse (H^*). Values estimated according to the breaking coefficients proposed by Goda (2010).

1. Using to the breaking coefficients provided by Goda (2010), it is possible to link $H_{1/250,b}/h_b$ with $H_{s,o}$ and the slope α. As a consequence, it can be estimated the relative breaking distance ($d = x/H_{1/250,b}$) as function of the relative water depth at the toe of the lighthouse ($H^* = H_{s,o}/h_t$) and wave steepness ($s_{s,o}$), as shown in Figure 7.1.

2. Identify a significant value of the relative breaking distance $d(h_b)$. In this investigation a qualitative slightly-impulsive limit equal to 2.5 times $H_{1/250,b}$ has been chosen (Fig. 7.1). On the basis of Figure 7.1, the value of $H^* = H_{s,o}/h_t$ has then been extrapolated for any value of the wave steepness $s_{s,o}$ (between 0.01 and 0.04), as shown in Figure 7.2.

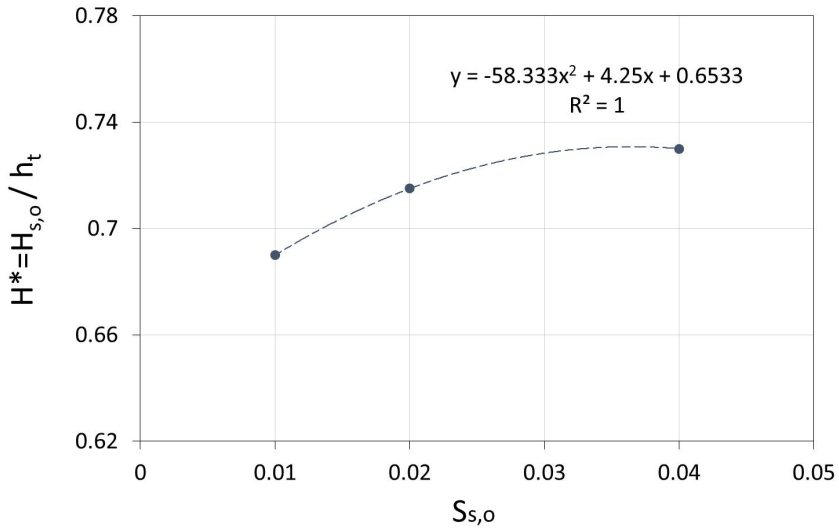

Figure 7.2: Relative wave heights at the toe of the lighthouse (H^*) and wave steepnesses related to relative breaking distances d =2.5.

3. Given a specific wave event ($\overline{H_{s,o}}$, $\overline{T_s}$, $\overline{h_t}$), calculate its offshore wave steepness $s_{s,o}$. Then, from step 2 estimate the value of $H^* = H_{s,o}/h_t$ (which causes $d = x/H_{1/250,b}$ =2.5).

4. Knowing the values of the water depth at the toe of the lighthouse $\overline{h_t}$ for the specific event ($\overline{H_{s,o}}$, $\overline{T_s}$), from step 3 estimate the value of $H_{s,o}$ that would break at h_b i.e. at a distance x from the lighthouse equal to 2.5 $H_{1/250,b}$.

5. Knowing the values $H_{s,o}$, estimate the value of h_b from the breaking coefficients provided by Goda (2010). On the basis of Table 7.1, the coefficient $H_{s,o}/h_b$ has been extrapolated for any value of the wave steepness $s_{s,o}$ (between 0.1 and 0.4) as shown in Figure 7.3.

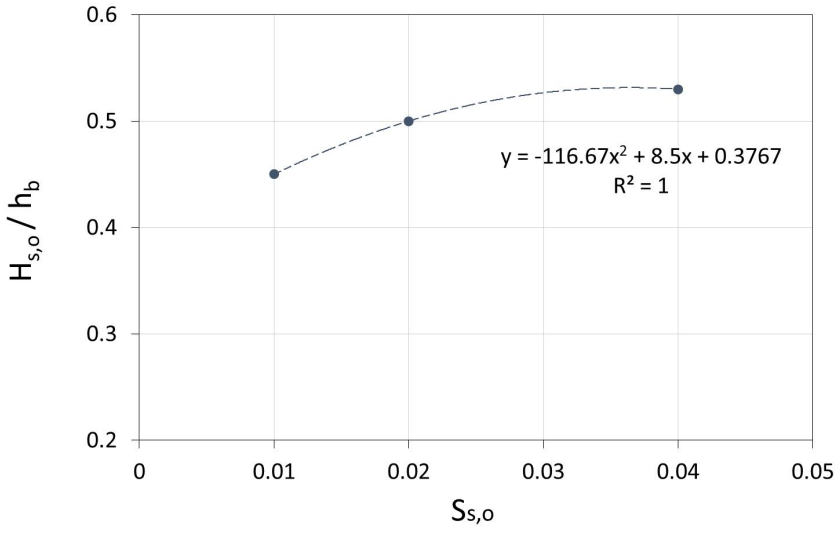

Figure 7.3: Relative wave heights at the breaking point and wave steepnesses.

Momentum flux of a specific event $\overline{M_F}$ and estimation of the relative breaking distance

If the *momentum flux* of a specific event $\overline{M_F}$ is determined fixing $h = h_b$ (step 5), the comparison between $M_{F,b}$ and $\overline{M_F}$ would give a qualitative indication concerning the relative breaking distance. In particular, because $\overline{M_F}$ increases with increasing $\overline{H_{s,o}}$ and/or $\overline{T_s}$, $\overline{d}$ would tend to be larger than $d(h_b)$ =2.5 when $\overline{M_F} > M_{F(d=2.5)}$ =0.48-0.51 (where $M_{F(d=2.5)} = M_{F,b}$ =0.48-0.51 for a 1:10 slope).

The above procedure has been applied to the extreme portion of the field data set and results are shown in the following subsection. Due to the fact that different hydraulic conditions ($H_{s,o}$, T_p, h_t)[1] can give the same value of $\xi_{o,p}$ or M_F, a better characterisation of the wave event has been obtained by the simultaneous combination of $\xi_{o,p}$ and M_F.

[1] Note that $T_p \approx T_s$.

Combination of the *Iribarren number* and *momentum flux*

Figure 7.4 shows field events plotted on a *momentum flux* versus *Iribarren number* plane, where the *momentum flux* has been related to the relative breaking distance as described above. The plane shows only the events that produced strong structural responses, i.e. $V > 2$ mm/s and/or $D > 0.02$ mm, because these are the most significant data from an engineering point of view. In addition, data are distinguished according to the different response types classified on the structural impulsivity (Section 5.1).

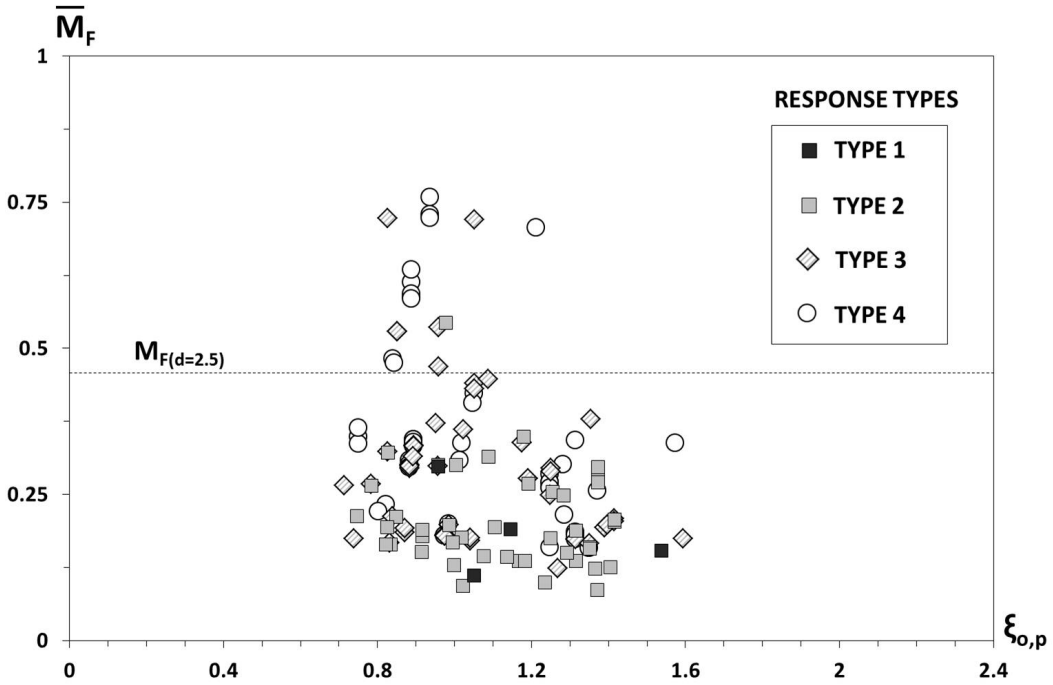

Figure 7.4: Significant events (145 events) distinguished according to the 4 response Types on the $\xi_{o,p} - \overline{M_F}$ plane.

As may be observed in Figure 7.4, there is a large spread of the structural response when $\overline{M_F} < 0.48$; in particular, 50 events are *impulsive* (Type 1 and 2) and 76 are *slightly-impulsive* (Type 3 and 4). In contrast, the occurrence of impulsive events show a dramatic decrease when $\overline{M_F} > 0.48$; in fact, 18 are *slightly-impulsive* and only 1 is *impulsive*.

Although significant events are rare for $\xi_{o,p} > 1.6$, the *Iribarren number* is not able to

give information concerning the occurrence of the structural response types, which are seemingly randomly distributed within the range $0.7 < \xi_{o,p} < 1.6$. This could be expected, because $\xi_{o,p}$ does not take into account the water depth. Therefore, identical offshore wave steepness can result in different kinematics and breaking distances depending on the water level; as a consequence, they generate different type of impacts on the structure. Therefore, while the *Iribarren number* is a valid parameter to describe the breaker shape (*spilling*, *plunging* and *surging*), it cannot be considered on its own in the present investigation, which is characterised by significant tide variations. Instead, $\overline{M_F}$ results in a better indicator for describing the impulsivity of signals – related to the relative breaking distance for wave impacts (Chan & Melville, 1988; Oumeraci et al., 1993; Wienke & Oumeraci, 2005) – when compared to $\xi_{o,p}$. This is in agreement with the considerations of Hughes (2004a), which describes M_F as a better parameter for surf-zone processes i.e. where h plays a fundamental role (Section 2.5.2).

7.2 Breaker shapes and characteristics of the wave dynamic force

Field video images indicate that the strongest structural responses ($V >$ 4 mm/s and $D >$ 0.04 mm) tend to be caused by larger waves that are still able to hit the lighthouse with a plunging jet. These waves may be characterised by relatively large force peaks (related to larger wave heights and periods) and simultaneously by wave impulses that persist longer on the structure. However, it is difficult to define the breaker that can cause the tower's largest deflection due to the fact that this is not only affected by the maximum instantaneous force, but also by the impact duration, extent of the load area and line of action of the dynamic wave force (Banfi et al., 2017b).

At this stage, the coastal literature provides poor indications concerning the dynamic analysis of circular structures in depth-limited conditions. A first approximation of the dynamic wave force on the Eddystone lighthouse may be obtained by using the relationship proposed by Wienke & Oumeraci (2005) for offshore cylinders. However, this dynamic formula assumes that the wave breaks at the cylinder. In contrast, field

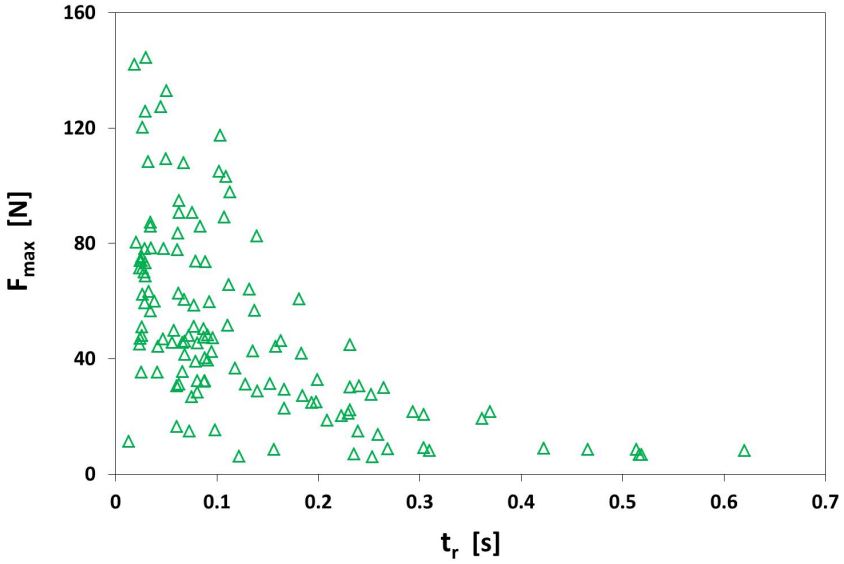

Figure 7.5: Dimensional force peaks and rise time obtained by load cell measures.

data suggests that longer impact durations and different spatial distributions can play a fundamental role in terms of structural deflection. As found in previous laboratory investigations (Weggel et al., 1970; Blackmore & Hewson, 1984; Kirkgöz, 1990; Witte, 1990; Hattori et al., 1994; Bullock et al., 2001; Cuomo et al., 2011), the maximum peak load and the rise time exhibit an exponential relationship (Fig. 7.5). Therefore, a characterisation of the wave dynamic force on the Eddystone lighthouse to the different breaker shapes is provided as follows. Based on the load cells measurements (Fig. 7.5), maximum overall forces are related to the rise time by means of a dimensionless relationship. The prediction formula can be applied for three different breaker types (dimensionless with respect to the relative breaking distance) as descibed below.

Definition of the three main breaker groups

The four significant breaker types (Section 6.1) have been divided in three main groups:

- *weak impact*
- *violent impact* and *large air pocket*
- *broken*

As shown in Figure 7.6, empirical formulae have been developed in order to enclose these three groups in different areas on the $\xi_o - M_f$ plane (regular waves).

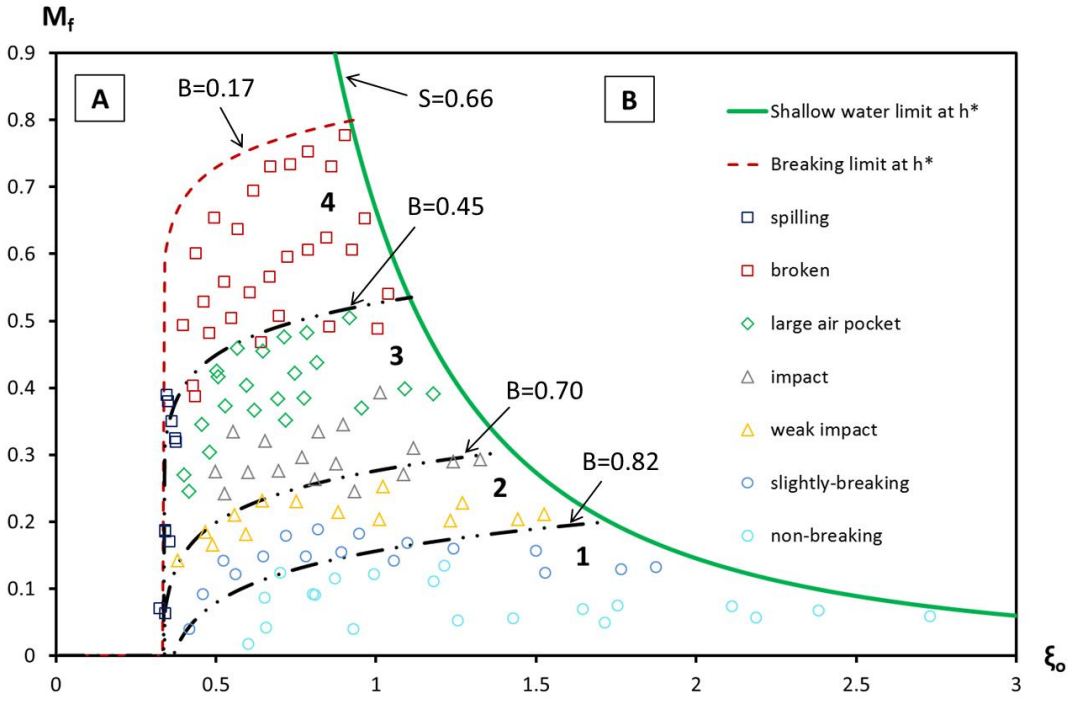

Figure 7.6: The significant breaker types grouped into 3 main Areas (2, 3 and 4).

Firstly, the shallow water limit at h^* (curve c in Figure 6.11) has been found to be well represented with the following equation:

$$M_f = 0.66\,\xi_o^{-2.2} \tag{7.4}$$

as a consequence, the plane is divided in two parts: **A** (left) and **B** (right). The test program is enclosed on the left side of the plane (**A**). This part is then divided in 5 sub-areas by means of four equations that have the following form:

$$M_f = (\xi_o - 0.33)^{3/50} - B \tag{7.5}$$

where the coefficient B assumes the values shown in Table 7.3.

Table 7.3: The values of the coefficient B for the different transition curves.

Transition curve	**Coefficient B**	**Breakers limits**
Area 1-2	0.82	*non-breaking* and *slighty-breaking*
Area 2-3	0.70	*weak impact*
Area 3-4	0.45	*violent impact* and *large air pocket*
Top limit Area 4	0.17	*broken*

From Equations 7.4 and 7.5 can be obtained two parameters, S and B respectively, based on the *Iribarren number* and *momentum flux* as shown in Equations 7.6 and 7.7

$$S = M_{\mathsf{f}} \cdot \xi_o^{2.2} \tag{7.6}$$

$$B = (\xi_o - 0.33)^{3/50} \; - \; M_{\mathsf{f}} \tag{7.7}$$

Thus, the location of the breakers (regular waves) on the plane varies according to the values assumed by S and B, and their occurrence can be estimated as follows:

- **AREA 1** ($S < 0.66$ and $B > 0.82$): *non-breaking* and *slightly-breaking*
- **AREA 2** ($S < 0.66$ and $0.70 < B \leq 0.82$): *weak impact*
- **AREA 3** ($S < 0.66$ and $0.45 < B \leq 0.70$): *violent impact* and *large air pocket*
- **AREA 4** ($S < 0.66$ and $0.17 < B \leq 0.45$): *broken*

When $S < 0.66$ and $B \leq 0.17$, waves break for wave steepness or relative wave height far from the lighthouse model (at h^*), generating much lower wave loadings.

According to the histograms of Figure 6.12, Table 7.4 shows the upper limits of dimensionless force (F'$= \mathsf{F}_{\mathsf{max}}/\gamma\, \mathsf{D}_{\mathsf{av}}\, h_t\, H_o$) and the relative breaking distances ($d = x/H_b$)

for Areas 2, 3 and 4. Note that the force peak (F_{max}) has been divided by the specific weight of the water (γ), the water depth at the toe of the cylindrical model (h_t), the average value of the two diameters (D_{av}) and the offshore wave height (H_o). Due to the fact that maximum breaking wave heights H_b were approximately 1.6 times H_o, the dimensionless force F' can be express in terms of the local wave height by setting $H_o = H_b/1.6$.

Table 7.4: Relative breaking distance (d) and maximum dimensionless force (F') for Area 2, 3 and 4.

Area	**Breakers**	***d***	**F'**
2	*weak impact*	0.1-0.5	5.9
3	*violent impact* and *large air pocket*	0.5-3.5	5.1
4	*broken*	> 3.5	2.6

Overall force peak and rise time

A formula covering the range of the tested condition, i.e. $0.8 < H_o/h_t < 2.8$ (limited water depths at the toe of the lighthouse), is developed to predict the relationship between force peak (F_{max}), which takes into account the total force given by the contribution of both quasi-static and dynamic component, and rise time (tr). The formula is expressed in terms of dimensionless values (F'$= F_{max}/\gamma\, D_{av}\, h_t\, H_o$ and $t' = t_r/T$). The rise time, which is the time taken to get to F_{max} from 0, is divided by the wave period T. As shown in Figure 6.12, the relationship between dimensionless force peak and rise time has been predicted with the 3^{rd} order polynomial shown in Equation 7.8 (used to envelope the force data obtained by regular wave conditions).

$$F' = 495\, t'^3 - 183\, t'^2 - 3\, t' + 6.1 \tag{7.8}$$

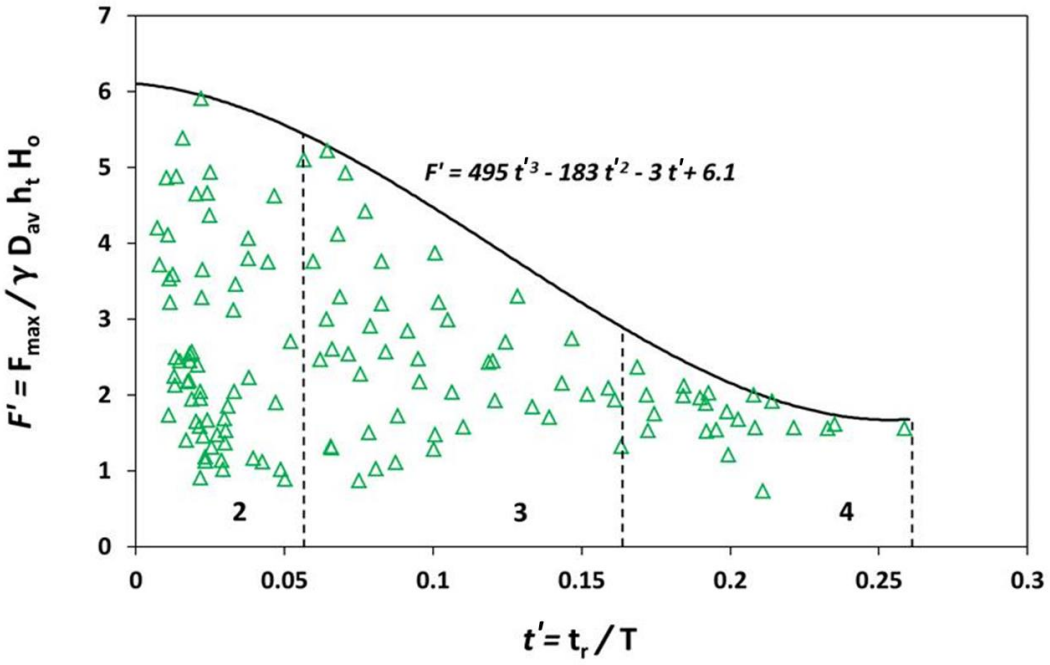

Figure 7.7: Dimensionless relationship between of F' and *t'* (regular waves).

The dimensionless relationship can be distinguished in three different ranges on the basis of the upper dimensionless force limits shown in Table 7.4. Thus, the breakers are linked to the predicted formula according to the relative breaking distance as follows:

- $0.005 < t' \leq 0.055 \quad \rightarrow \quad 0.1 < x/H_b \leq 0.5$ (*weak impact*)
- $0.055 < t' \leq 0.16 \quad \rightarrow \quad 0.5 < x/H_b \leq 3.5$ (*violent impact* and *large air pocket*)
- $0.165 < t' \leq 0.26 \quad \rightarrow \quad x/H_b > 3.5$ (*broken*)

Temporal distribution and impact duration

In dynamic analysis, the definition of simplified time-history loads is required. Idealised load-histories are usually represented by a symmetric triangle (Cuomo, 2005). Thus, the dynamic impulse of the wave may be characterised by a triangular load with an impact duration equal to $2t_r$, as shown in Figure 7.8.

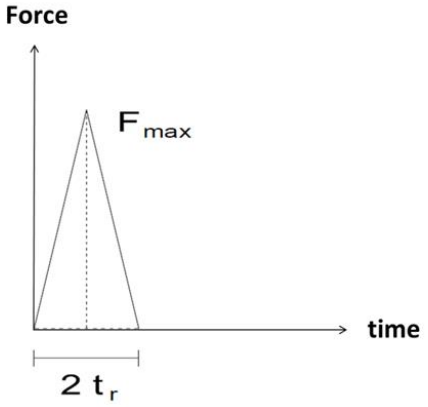

Figure 7.8: Idealised dynamic impulse of the wave.

Spatial distributions and line of action of the force

The Eddystone lighthouse is a tapered tower on the top of a solid cylindrical base. For this reason, as described in Section 5.2.2, the deflection of the lighthouse depends strongly on the extent of the load area on the structure. Therefore, in order to provide a more accurate parameterisation of the wave-structure interaction, three different spatial distributions are proposed for the three ranges that characterise the force-rise time formula (Fig. 7.7). In order to ensure a precautionary estimation of the line of action of the force, the three idealised spatial distributions, which are shown in Figure 7.9, have been developed on the basis of the maximum dimensionless barycentres recorded for the different breakers (Figure 6.10 in Section 6.2).

For Area 2, which is characterised by small plunging that break at the structure (*weak impact*), the vertical spatial distribution results in a sharp triangle with maximum elevation of the barycenter recorded at 1.4 h_t (Fig. 7.9).

Area 3 is characterised by larger waves that hit the lighthouse with a plunging jet (violent impact and large air pocket). Depending on the direction of the plunging jet, two main vertical distributions can occur with the barycenter under or above the SWL. When the barycenter is above the SWL, the spatial distribution is similar to those of Area 2, but the triangle is wider (Fig. 7.9). Due to the fact that Area 3 is characterised by larger waves, the maximum barycenter elevation recorded is at 1.5 h_t (Fig. 7.9).

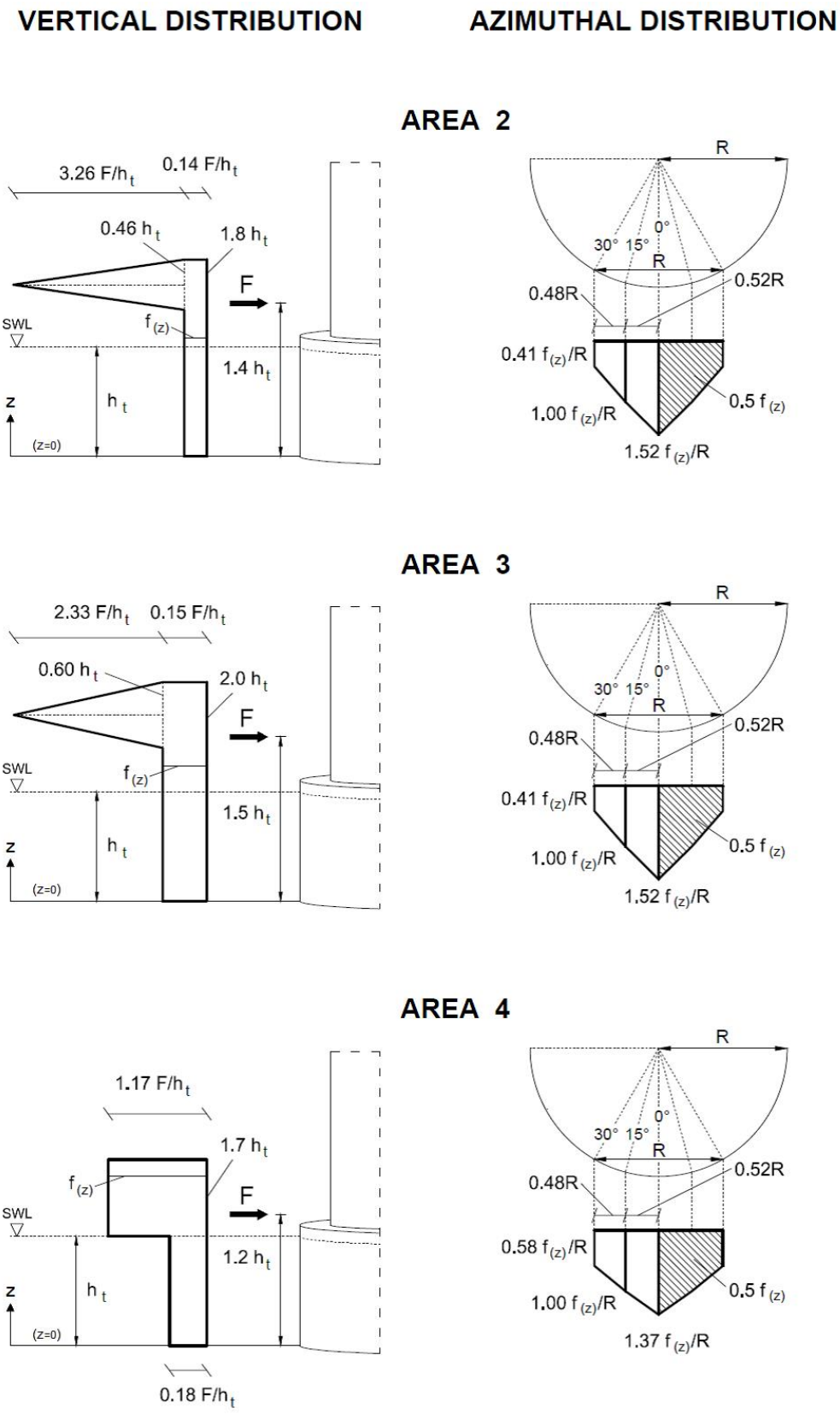

Figure 7.9: Idealised spatial distributions.

For Area 4, which is characterised by broken waves that cause more uniformly distribution over the lighthouse, the vertical spatial distribution has been idealised with two rectangular shapes (Fig. 7.9). The maximum barycenter elevation recorded is at 1.2 h_t (Fig. 7.9).

In Figure 7.9, the vertical line distributions represent the overall force acting along the circumference of the lighthouse. Thus, these overall forces may be distributed along the surface of the cylinder on the basis of the azimuthal distributions shown on the right side of Figure 7.9. The azimuthal distribution of Area 3 and 4 are developed according to the pressure measures recorded by Wienke & Oumeraci (2005).

The comparison of the integrated forces with the load cells measurements suggests that the azimuthal distribution used for Area 2-3 may be underestimated for Area 4 (*broken*) (Section 6.2). Thus, a more uniform azimuthal distribution is suggested for Area 4 (Fig. 7.9).

Considerations on the prediction formulae

Currently, the coastal literature does not provide a load description for breaking waves in limited water depths ($H_o/h_t > 1$). The small-scale tests have given more insight into the very complex phenomena of breaking wave forces on a cylindrical structure on the top of a steep slope. However, the previous prediction formulae covering the range of tested conditions ($0.8 < H_o/h_t < 2.8$) may be applied for conditions not too different from those of the model tests, i.e. steep slopes and limited water depth. It should be noted that:

1. Both slope and depth condition at the toe of the structure strongly affect the wave transformations and, hence, the load characteristics related to the different breaker shapes;

2. As a consequence of the previous consideration, the occurrence of the breaker types on the dimensionless $\xi_o - M_{\mathrm{f}}$ plane is also affected by the slope and water

depth. In addition, both dimensionless limits and location of the breaker types are influenced by the choice of the water depth section identified to determine the dimensionless momentum flux of Hughes. In this study, the depth section (h^*) was fixed at a distance from the model of 5 times the maximum offshore wave height.

3. In irregular wave analyses, the breaker prediction on the plane cannot be estimated through the plane of Figure 7.6. However, load characteristics are related to extreme individual events that have been distinguished on the basis of the relative breaking distance (dimensionless values at breaking point).

7.3 Circular structure and deformation of the wave front

The cylindrical base of the Eddystone lighthouse has a diameter larger than water depths and local wave heights at the toe of the structure. Depending on the tide condition, the water depth can be few cm up to 6-7 m. As a consequence, the diameter (13.4 m) is approximately twice the water depth at highest tide conditions. According to the field video images, three main phenomena seem to be generated by this particular depth-limited condition, i.e. rush-down on the top of the reef, back-flow around the cylindrical base and deformation of the wave front.

As may be observed from Figure 7.10, the rush-down can be distinguished by incoming wave (blue line in video frames 3 and 4 of Figure 7.10) causes the emergence of the rock at the toe of the lighthouse.

As may be observed from Figure 7.11, laboratory tests showed that during the rush-down the water level was slightly higher in the centre-line on the lee and offshore sides of the model's surface. Thus, while on the back the higher level should be a rush down effect, on the front line it may be a reflection effect caused by the incoming wave. Chaplin et al. (1997) and Rainey & Chaplin (2003) have also observed these small run up during their experiments on slender cylinders.

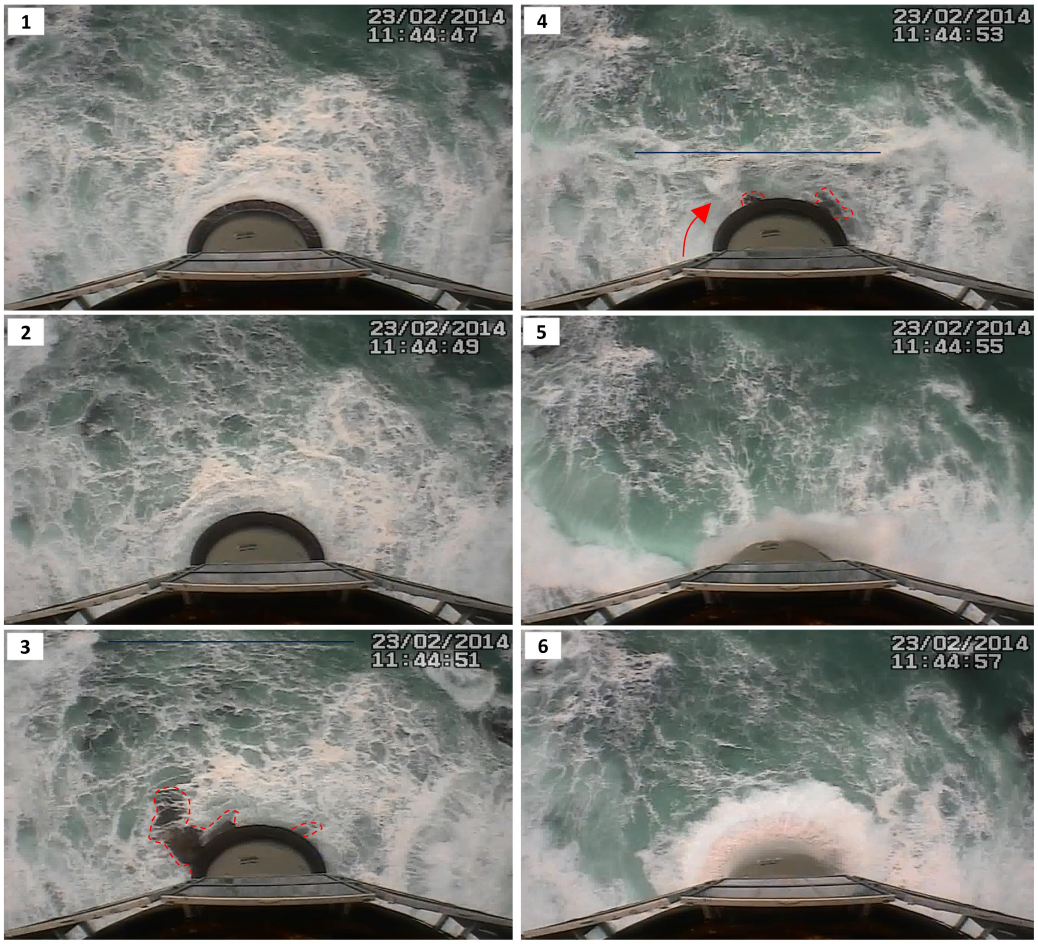

Figure 7.10: The incoming wave (blue line) uncovers the rock at the base of the Eddystone lighthouse.

As may be observed from Figure 7.11, the rush-down is caused by the fact that the incoming wave is of the same order of the water depth. Therefore, the wave trough causes a depression, which is uniformly extended over the whole water depth at the toe of the model because this is in shallow water (Airy theory). Due to the depression in the trough phase, the water velocity has a velocity with opposite direction respect to the incident wave (Airy theory). Figure 7.12 indicate that a back-flow occurs after the wave impact in the field. In addition, the spray on the water surface, caused by the fall of the previous run up, tends to move seawards. As a consequence, it is likely that the back-flow is mainly an effect of the depression related to the trough phase, which tends to 'attract' the water from the lee of the lighthouse (note that the local

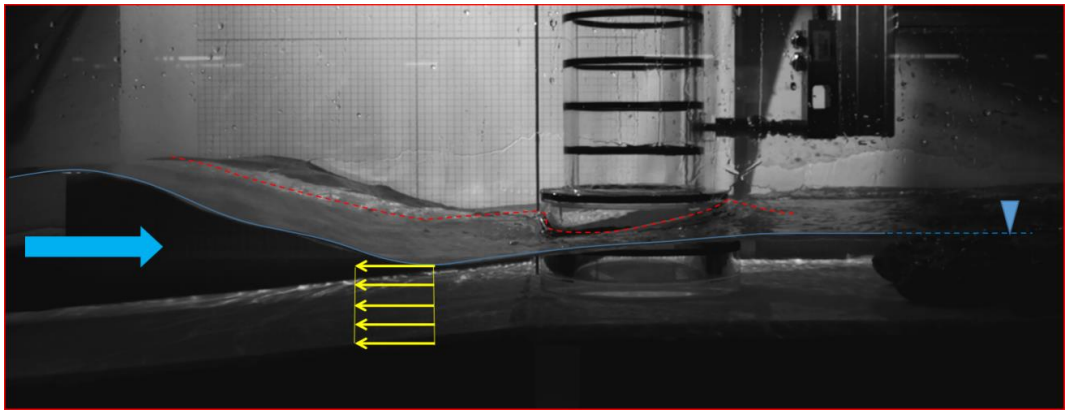

Figure 7.11: Decreasing of the still water level in the front line of the cylinder during the trough phase.

breaking wave height should tend to be larger than the water depth at the toe of the lighthouse). However, other aspects could contribute to generate the back-flow, e.g. a back-wave caused by the previous plunging jet, water current at the Eddystone Reef, water-flow affected by the two lateral rocks (to South and to West), refraction from the rock outcrops.

As may be observed from Figure 7.12, the back-flow tends to circumnavigate the lighthouse due to the circular shape of the base; then, it seems to cause a deformation of the wave front, which appears more stable and steeper in the middle. In particular, video images suggest that both backflow and the incoming wave tend to compress the water just in front of the lighthouse (video frames 5-6 of Figure 7.12), while the breaking tends to occur earlier on the two lateral sides (video frames 4-5 of Figure 7.12 and see also Figures 5.9 and 5.10 in Section 5.1.2). Although the physical modelling has been simplified with a 2D bathymetry, a similar deformation of the wave front has been observed during the laboratory tests for some small waves able to approach closer to the cylindrical model. The deformation evolves in two distinct phases. In the first phase the wave front assumes a concave shape, i.e. the two lateral sides tend to be higher and faster compared to the central portion of the front (Fig. 7.13a). This may be caused by the two lateral back-flows that may roll on the two lateral surfaces of the wave front. Then, when the wave is in proximity to the model, the water level tends to increase just

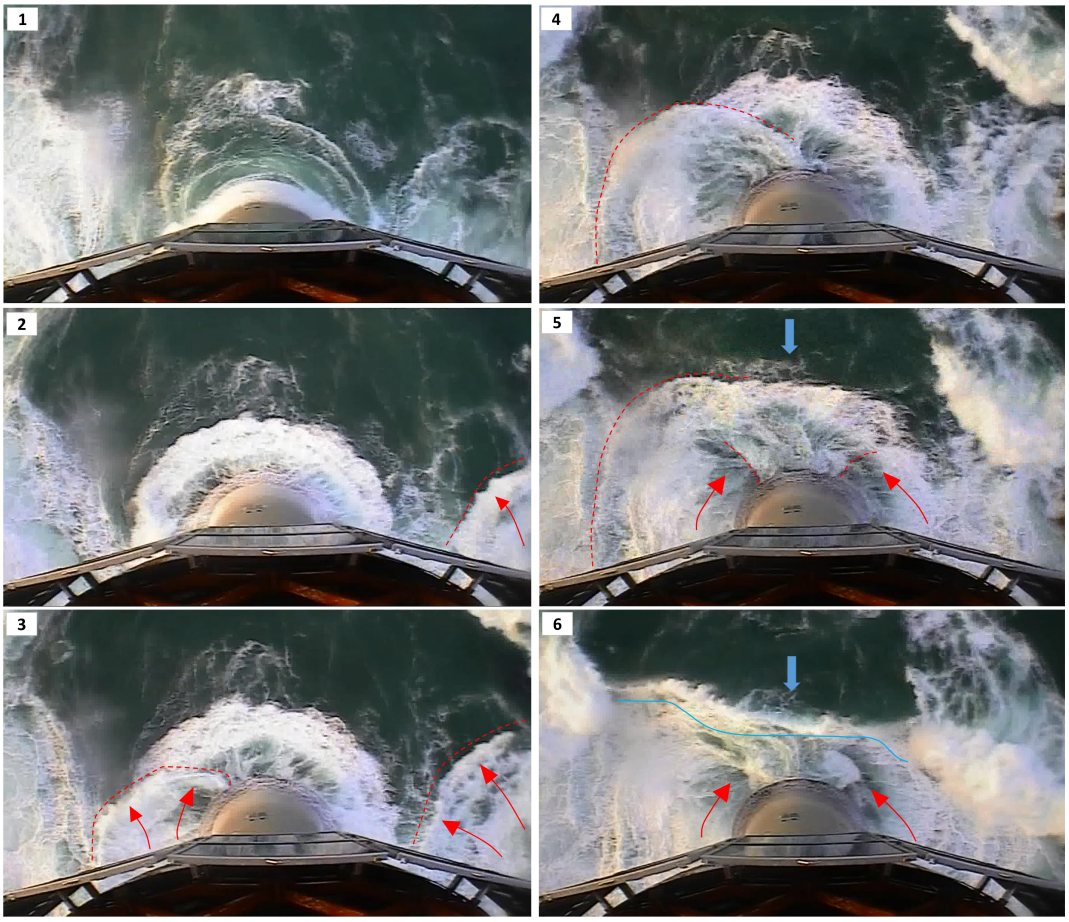

Figure 7.12: Back-flow and steepening compression of the wave just in front of the lighthouse.

in front of the cylinder due to the reflection, and the wave height increases just at the middle of the wave front, i.e. assuming a convex shape (Fig. 7.13b).

It is likely that this wave front deformation may cause accentuated run up on the cylinder compared to plane surface and this aspect could be an interesting subject of study for future investigations. However, concerning the Eddystone lighthouse, it is reasonable to believe that both the particular configuration of the steep reef and the wind have had a dominant role in generating the extreme run up observed in the field (Section 5.1.2 and Section 6.1).

Figure 7.14 shows two other examples of different wave front deformations which caused a violent forward jet. As may be observed in Figure 7.14a, the breaking starts

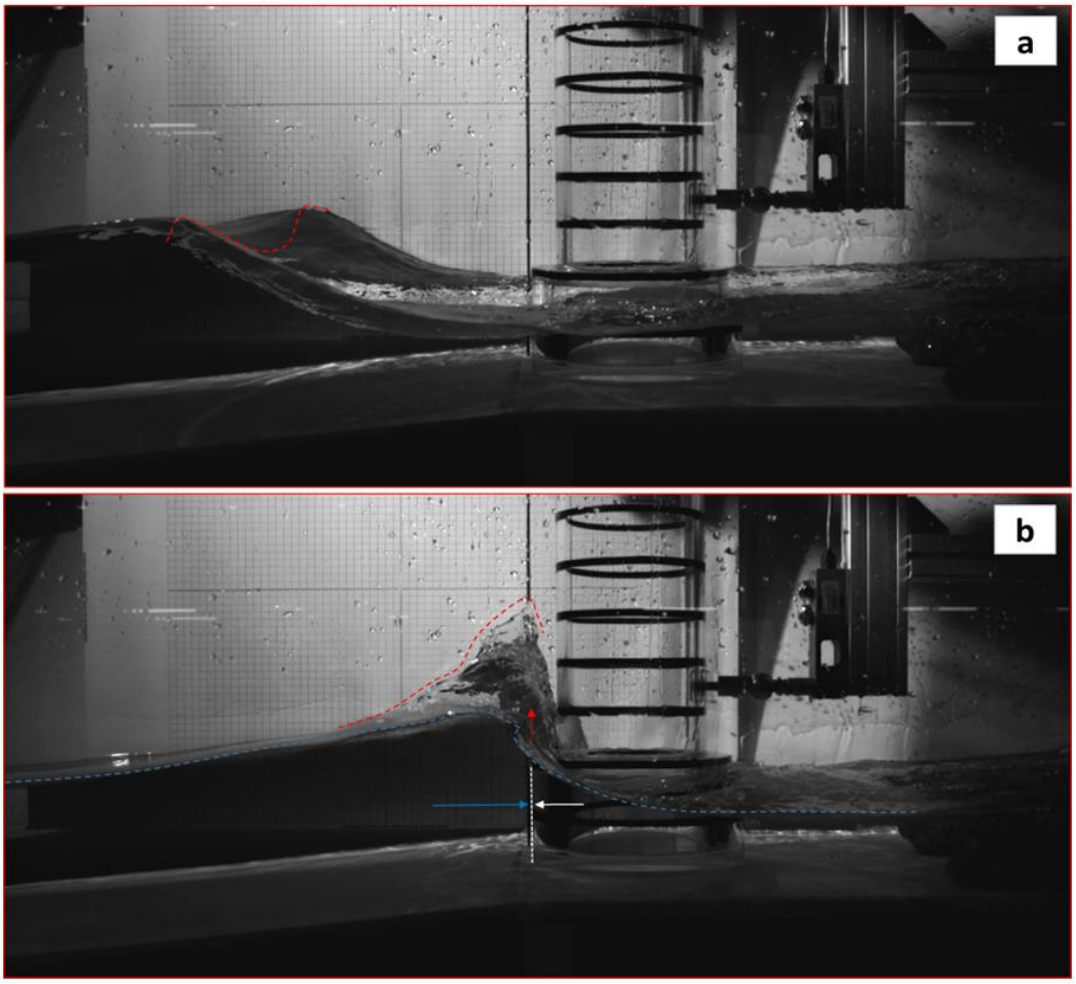

Figure 7.13: Deformation of the wave front: (a) 1^{st} phase; (b) 2^{nd} phase.

on the two lateral sides and then the detachment of a jet occurred from the middle of the wave crest. Although the location of the breaking point was approximately the same from one wave to the next in a train of regular waves, the forward jet could occur with different accelerations and directions. In particular, the jet could suddenly be shot upward with a velocity higher than that of the wave front, as shown in Figure 7.14b. It is likely that this increase in velocity may be caused by the crash between the incident wave and the back-flow. Although it is reasonable to expect that the reasons were different in the field (e.g. reef configuration), similar breaking characteristics were observed at the Eddystone lighthouse. As described in Figure 5.9 and 5.10 of Section 5.1.2, the detachment of the jet, from the middle of the wave front, was able to hit the

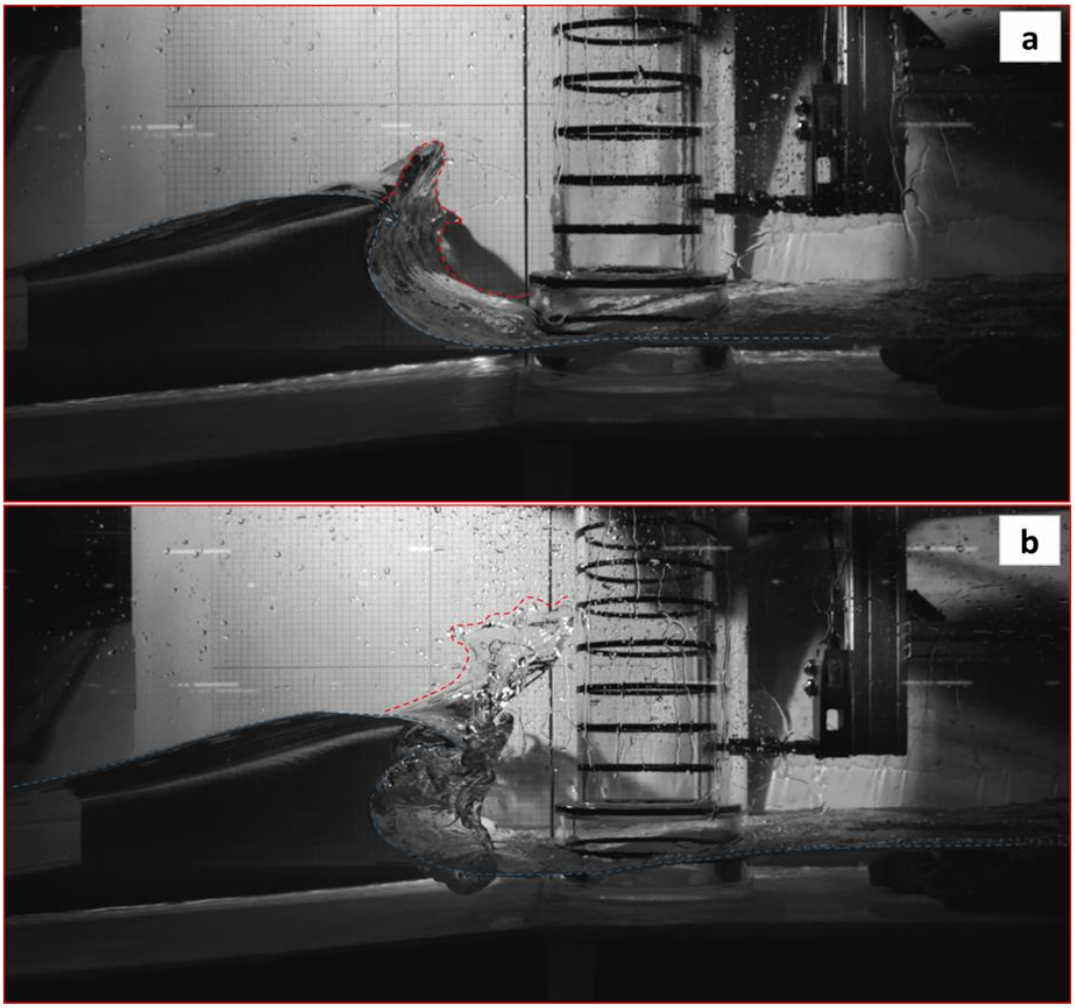

Figure 7.14: Occurrence of the vertical jets for small and milder plunging waves.

lighthouse before breaking had occurred on the two lateral sides.

Although in different ways with respect to the 3D situation of the Eddystone Reef, most of the previous depth-limited effects were observed in the field. However, unrealistic oscillations of the still water level occurred during the experiments on the lee of the lighthouse model due to the splash of larger plunging waves. This is a laboratory effect given by the fact that water could not escape due to the walls of the channel. In contrast, it is reasonable to suppose that oscillations of the still water level could be spread in the field. Rubble stones were used as a submerged filter in order to limit the oscillations of the still water level on the lee of the lighthouse model so that horizontal

stability of the water level could be increased (Fig. 7.14).

Chapter 8

Conclusions and recommendations

8.1 Impulsivity of the dynamic responses and their classification

MORE than than 3000 events were recorded by the geophone system during the UK winter storms of 2013-2014. Various dynamic responses have been identified and higher structural frequencies, which are related to rapidly varying loads (i.e. shock loads with shorter impact durations) (Clough & Penzien, 1975; Loraux, 2013), tend to show a predominant sharp peak in the velocity time histories. As a consequence, the dynamic responses of the Eddystone lighthouse have been classified into four types on the basis of the impulsivity of the signals (using the ratio of peaks in velocity time histories and displacement peak spectra).

The structural response types are classified in Types 1-2 (*impulsive*) and Types 3-4 (*slightly-impulsive*). Types 1-2 are characterised by a clear sharp velocity peak that is connected to the maximum peak in the displacement time history. Both the peaks tend to occur at the beginning of the signal (before 0.2 s). For Types 3-4, which are not characterised by a clear sharp peak, the maximum velocity peak is not related to the maximum displacement peak and this does not occur at the beginning of the signal, but later (after 0.2 s).

Higher velocities/ accelerations do not necessarily lead to the larger displacements. In addition, structural velocities tend to decrease from Type 2 to Type 4; while the contribution of higher structural frequencies tends gradually to decrease moving from Type 1 to Type 4. As a consequence of the decreasing of the frequency, Types 2, 3 and 4 can generate similar structural deflections, even if they are characterised by different

velocity oscillations. Type 1 causes just smaller velocities and displacements, despite it being characterised by highly impulsive signals. Maximum structural deflections of $\sim$0.1 mm, related to acceleration of 0.1g, were recorded during the period 2013-2014. These deflections give an idea about the structural rigidity of the Eddystone lighthouse.

8.2 Dynamic response types and impact waves

Video images and hydrodynamic wave data, which have been related to the geophone events, indicate that the different types of response are caused by different types of wave impacts. Due to the bathymetric configuration of the reef, impact events are mainly caused by waves which came from a sector centered approximately at SW. Along this sector, which coincides in addition with the prevailing wind directions, the mean gradient of the sea bottom is quite regular with a slope approximately of 1:8. The steep slope strongly affects the wave transformation due to shoaling. This causes the rapid increasing of wave height and wave steepness generating violent plunging breakers. Due to the limited water depth at the toe of the lighthouse, only small waves are able to break close to the structure (Type 1). Larger waves cannot break at the structure because the standard breaking criteria (H_b/h_b) implies that the breaking point moves seawards. Waves result, then, in violent impacts if they are able to hit the tower with a plunging jet, as happens for Type 2 and 3. If compared to Type 3, Type 2 tends to be characterised by lower heights and periods, which tend to cause lower breaking distances. Type 3 tends to be characterised by larger waves and periods and, so, by larger breaking distances. When wave heights exceed the water depth far from the lighthouse, usually when the water level tends to decrease, the plunging is completely developed and waves break on the reef. Consequently, these waves are already broken and, so, just turbulent amounts of water reach the structure; these are Type 4. As a consequence, video images indicate that the impulsivity of the dynamic responses decrease with the increasing of the breaking distance (from Type 1 to Type 4). This is in agreement with the coastal literature, which associates the impulsivity

of wave loading with the relative breaking distance. Generally, for coastal structures the maximum loads are caused by waves that break at the structure. Waves, which break closer to the lighthouse (Type 1), tend to generate smaller deflections, despite showing highly impulsive responses. This is essentially explained by the depth-limited conditions, which allow the breaking at the structure only for small waves. According to the small scale tests, larger waves cause larger loads despite increasing relative breaking distance and decreasing of the impulsivity.

Thus, while the impulsivity of the dynamic response tends to be affected by the impact types, the magnitude of the deflections depend on both load extent of the spatial distribution and impact duration.

The magnitude of the deflection tends to increase with increasing water level and, according to the numerical simulations (Trinh et al., 2016), the displacement amplitudes of the Eddystone lighthouse tend to be gained depending on the vertical elevation of the impact area on the composite structure of the tower. Thus, the increasing of the water level would tend to raise the wave impact area in proximity of smaller tapering diameter of the lighthouse and, in addition, the portion of the structure submerged increases and the load area tends to be larger. As a consequence of this double effect, higher water levels tend to cause larger deflections.

Field data show that less impulsive responses, characterised by lower velocities/ accelerations, can lead to larger structural deflections. However, these larger deflections can occur also when they are characterised by lower water levels. Consequently, higher elevations of the impact area could not always justify the larger structural deflections. Numerical simulations on Jument lighthouse (Loraux, 2013; Chollet, 2014) have shown that longer load durations – which decrease the structural response frequency – increase the deflection but decrease the velocity/acceleration. According to the small-scale tests, larger waves, which break farther from the lighthouse model, tend to be characterised by a longer rise time. Consequently, the dynamic impulse can increase, even when the force peak is lower. Although broken impacts have been

generally dismissed as not being very important, Bullock et al. (2007) have pointed out that this type of loading could well be of engineering significance because impact pressure could have much longer durations and they can act over larger load areas. For the present investigation, characterised by limited water depth, *slightly-impulsive* events (Type 3 and 4) can cause significant structural deflections, suggesting that the load duration would play an important role in their generation. Generally, field video images indicate that the strongest structural responses ($V >$ 4 mm/s and $D >$ 0.04 mm) tend to be caused by larger waves, but still able to hit the lighthouse with a plunging jet. These waves may be characterised by relatively large force peaks (related to larger wave heights and periods) and simultaneously by wave impulses that persist longer on the structure. However, it is difficult to define the breaker that can lead the largest tower's deflection. As mentioned earlier, this is not only affected by the impact duration, but also by the maximum instantaneous force, extent of the load area and line of action of the dynamic wave force.

Laboratory tests indicate that the line of action of the force tends to be above the SWL for plunging waves that break closer to the lighthouse model. The application point shifts from above to below the SWL for larger waves; thus, it can occur above or below the SWL depending on the instant of the maximum force peak. For broken waves the line of action shifts from below to above the SWL and it tends to occur around the SWL at the instant of the maximum force.

Concerning the run up, extreme field values were not found during the laboratory test. As a consequence, the reef configuration may have a fundamental role for their generation. However, observed run up of some 40 m (from the top surface of the cylindrical base) seems still excessive and the storm winds could have a considerable bearing.

8.3 Occurrence of the structural response types

The strongest structural responses tend to occur when the irregular *Iribarren number* ($\xi_{o,p}$) is lower than 1.4. This is explained by the fact that the *Iribarren number* is an indi-

cator of the violence of the breakers (Galvin, 1968) and the wave steepness increases with decreasing $\xi_{o,p}$. This result is in agreement with video images, which indicate that the structural responses are caused by plunging waves. However, this parameter is not able to give information about the occurrence of the response types, which are random within the range $0.5 < \xi_{o,p} < 1.4$. Blenkinsopp & Chaplin (2008) explained that breakers are strongly influenced by the water level over the crest of a submerged reef. In fact, same values of $\xi_{o,p}$ can occur with different kinematic and breaking distance from the structure generating different wave loads – depending on the relative breaking distance that is affected by the instantaneous value of the water depth h.

Video images indicate that waves tend to break farther from the lighthouse for larger values of the irregular wave *momentum flux* M_F (Hughes, 2004a). When plotted against M_F, structural responses show the following two results.

- The comparison between structural velocities and displacements indicates a general tendency for which the frequency values of the structural response tend to decrease with increasing M_F.
- *Impulsive* structural responses (Type 1 and 2) tend to occur for lower M_F within the extreme portion of the data set ($V > 4$ mm/s and $D > 0.04$ mm).

These two results are in agreement with field video images. In fact, on one hand higher structural frequencies are related to shock loads (Clough & Penzien, 1975; Loraux, 2013), on the other hand impulsive loads are related to shorter breaking distances for wave impacts (Chan & Melville, 1988; Oumeraci et al., 1993; Wienke & Oumeraci, 2005). Laboratory tests indicate clear trends in breaker type when results, obtained with a constant depth of water, are plotted in the regular $\xi_o - M_\mathrm{f}$ plane and the relative breaking distance tends to increase with the regular *momentum flux*. This result is in agreement with the considerations of Hughes (2004a), who describe the dimensionless *momentum flux* as a better indicator for wave-structure interactions in surf-zone (i.e. where h plays a fundamental role) with respect to the *Iribarren number*. Therefore,

if compared to $\xi_{o,p}$, $H_{s,o}$, T_p or water level, M_F may be a better indicator to describe the impulsivity of signals.

8.4 Recommendations

The present study on the Eddystone lighthouse has given insights concerning wave impacts on a structure located on the top of a steep reef and in limited water depths. These environmental conditions are poorly investigated in the coastal literature and a better understanding is needed. Some possible future research directions are indicated below.

1. Although in the past dynamic analysis has been poorly considered for the design of coastal defence structures, shock impulses due to plunging waves lead to structural deflections of the Eddystone lighthouse. In addition, due to the wide tidal range and the limited depth conditions at the Eddystone Reef, broken waves can generate significant structural responses of the tower. The use of geophones could give in the future more insight about the effects of these waves on other type of structures.

2. The load classification based on the wave shape on plane walls may be not applicable when slopes are steep and the water depths are limited. The effects of the different breaker shapes on the wave loading should be investigated over different slopes and depth conditions.

3. Compared to the *Iribarren number*, the dimensionless *momentum flux* of Hughes appears as better indicator of wave impulsivity when wide variation of the water level occurs. A better hydraulic description of the breaker has been obtained thanks to the breaking map given by the simultaneous use of the *Iribarren number* and *momentum flux*. The usefulness of dimensionless breaking map should be investigated in irregular wave conditions and over different slope values.

4. The azimuthal spatial distributions would seem strongly affected by the type of

breaker on the cylinder. Furthermore, the wave front may be subjected to particular deformations when waves break in proximity of circular structures located in limited water depths. This aspect should be investigated with PIV techniques.

Appendix A

LabVIEW

LABVIEW (Laboratory Virtual Instrument Engineering Workbench) is a graphical programing language, also referred to as G, from National Instruments.

LabVIEW is composed of two main parts:

- The front panel is the interactive user interface. This may contain controls to set the analysis processes and graphs or indicators to view the results produced by the program.
- The block diagram is the actual executable program. Execution is determined by the structure of a graphical block diagram on which the programmer develops the codes using different functions and cycles (for and while loops, if case structures, etc.).

LabVIEW is specifically designed for data acquisition, instrument control, analysis and signal processing.

Appendix B

Quasi-static and dynamic component

WHEN the impact wave occurs, the total response measured by geophones shows a high increase of the signal, followed by an oscillation that is governed by the dynamic characteristics of the structure (transient phenomena). Figure C.1 shows a sketch of a typical displacement signal caused by a wave impact. The black line represents the total response, which is given by the sum of the quasi-static and dynamic component. In the graph is also shown the quasi-static component (red line) caused by the transit of the wave. This component tends to be obscured in the total response because it is covered by the oscillation of the dynamic component (transient) that represents the oscillation of the structure due to the impact. This oscillation depends by the dynamic characteristics of the structure. The static component is visible in the total response just for the asymmetry of the total response with respect to the time axis.

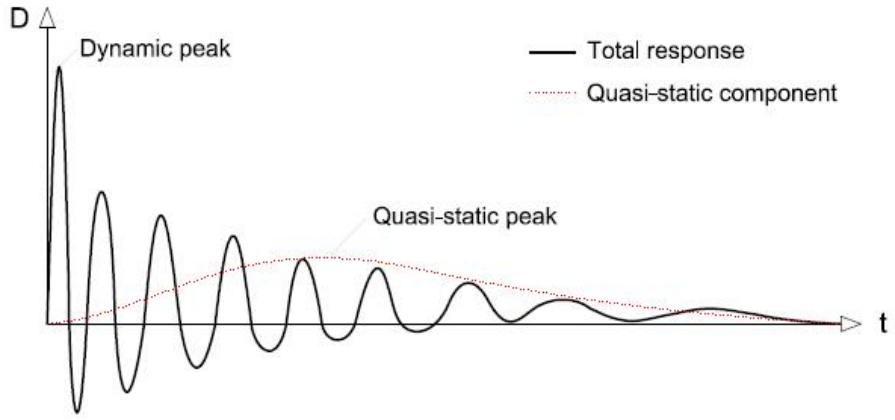

Figure B.1: Sketch of a typical impulsive displacement signal.

Appendix C

Filtering

THE most common types of ideal filters include low-pass filter, high-pass filter and band-pass filter (by combining the first two filters). The term 'ideal' implies that the magnitude of the signal passing through the filter is not attenuated over the desired passband of frequencies. However, in the case of non-ideal filters, a fraction of intermediate frequency signal content is removed by the filter.

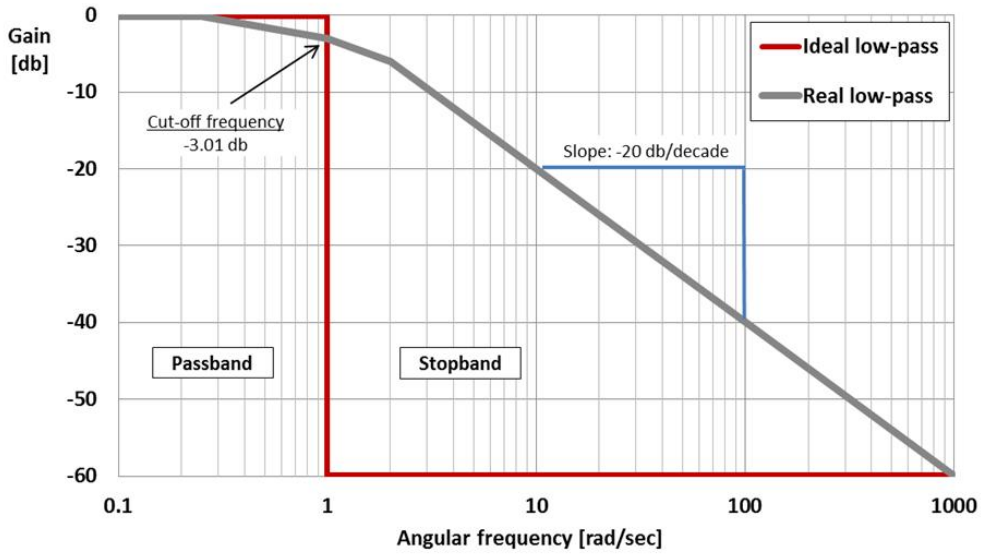

Figure C.1: Comparison between an ideal low pass filter (red) and a real (gray). In particular the real filter is the low-pass Butterworth of first order.

Digital filters operate on a digitally converted signal. In Figure C.1 it is possible to see the difference between an ideal filter (red line) and a real one (grey line) for a low pass filter. This shows the gain on a logarithmic scale as a function of the angular frequency

ω (rad/sec) where the value 1 rad/sec represents the cut-off frequency.

It is clear that an ideal filter passes sharply with a gain of 1 for the frequencies below the cut-off value (passband), to a gain very close to 0 for the frequencies immediately after the cut-off value (stopband). For a real filter this transition is gradual and for the cut-off frequency, the gain is less than 1. In particular, the real filter shown in the graph is a low-pass Butterworth filter of order 1. As it is possible to see more clearly from the Figure C.1, in correspondence with the cut-off frequency the gain is about 0.7 (-3.01 db). For a first-order filter its response slowly decreases at -20 db per decade. A second-order filter decreases at 40 dB per decade, a third-order at 60 dB and so on. The frequency response of the Butterworth filter is maximally flat in the passband and smoothly decreases towards zero in the stopband with a monotonic trend.

Appendix D

Principal Components Analysis

PRINCIPAL components analysis (PCA) is commonly used to reduce the number of variables and avoid multicollinearity. In particular, PCA uses an orthogonal transformation to convert a data set of variables into a set of values called principal components. The number of principal components is less than or equal to the number of original variables. This transformation is defined in such a way that the first principal component (PC1) has the largest possible variance. As a consequence, PC1 accounts for as much of the variability in the data as possible. Then, each succeeding component in turn has the highest variance possible in way that it is orthogonal to the preceding components.

In order to determine the principal components (PCs) it is necessary to determine the Eigenvalues and the Eigenvectors of the covariance matrix of the set variables. For a two dimensional data set $\mathbf{A} = (\mathbf{x}, \mathbf{y})$ the covariance matrix $\mathbf{C}$ is:

$$\mathbf{C} = \begin{bmatrix} var\ \mathbf{x} & cov\ \mathbf{xy} \\ cov\ \mathbf{xy} & var\ \mathbf{y} \end{bmatrix}$$

where $var\ \mathbf{x}$ and $var\ \mathbf{y}$ are the variance of $\mathbf{x}$ and $\mathbf{y}$ respectively, while $cov\ \mathbf{xy}$ is the covariance of $\mathbf{xy}$.

The Eigenvalues (λ_1 and λ_2) are determined by solving the determinant of the matrix

$(\mathbf{C}-\lambda\mathbf{I})$ − where $\mathbf{I}$ is the identity matrix − i.e. the characteristic polynomial of $\mathbf{C}$:

$$\lambda^2-(var\ \mathbf{x}+var\ \mathbf{y})\lambda+(var\ \mathbf{x}\ var\ \mathbf{y}-cov\ \mathbf{xy}^2)$$

To determine the Eigenvectors ($\vec{\lambda_1}$ and $\vec{\lambda_2}$) it is necessary to solve the linear homogeneous system. Thus, the two components (λ_1^1 and λ_1^2) of $\vec{\lambda_1}$ are determined by solving $(\mathbf{C}-\lambda_1\mathbf{I})[\vec{\lambda_1}]$, where $(\lambda_1^1+\lambda_1^2)=1$. Note: the solution of the linear homogeneous system for λ_2 gives $\lambda_2^1=\lambda_1^2$ and $\lambda_2^2=-\lambda_1^1$.

Finally, the new coordinates $\mathbf{A}^*$ according to the PCs (i.e. $\vec{\lambda_1}$ and $\vec{\lambda_2}$) is given by multiplying the original data set for to the Engine vectors matrix, i.e.:

$$\mathbf{A}\begin{bmatrix}\lambda_1^1 & \lambda_2^1\\ \lambda_1^2 & \lambda_2^2\end{bmatrix}=\mathbf{A}^*$$

Figure D.1 shows the PCs (in the horizontal plane X-Y) for a typical structural velocity event. PC1 is the first principal direction and it is characterised by having the largest possible variance; PC2 is orthogonal to PC1. Figure D.2 shows the velocity value in the time plotted along the 2 principal directions (PC1 and PC2). Note: the vertical component (Z), which is proportional to the values on the horizontal pane (X-Y), is omitted because it is one order smaller.

As may be observed from Figur D.2, the velocity values along PC2 tend to be one order smaller than those along PC1.

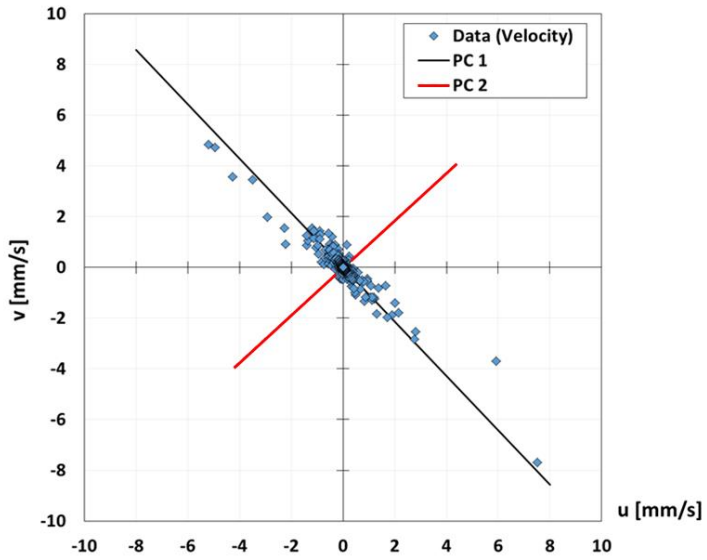

Figure D.1: Velocities taken by the lighthouse on the plane X-Y during a typical impact process.

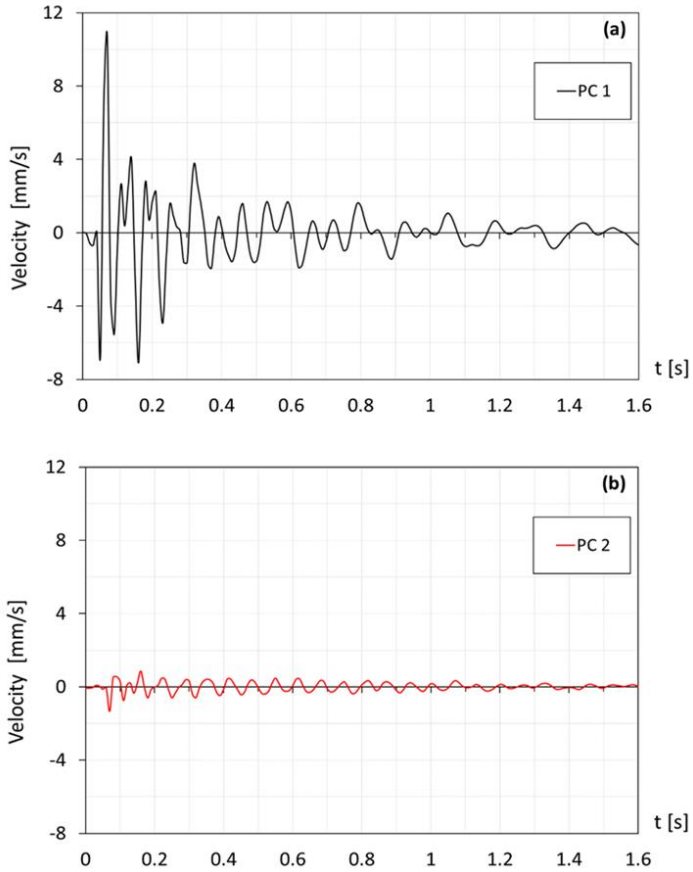

Figure D.2: Typical velocity time histories plotted along (a) PC1 and (b) PC2.

Appendix E

Integration and differentation

FOR a sinusoidal signal the relationship between acceleration, velocity and displacement is shown in Figure E.1. As may be observed, the integration process implies the decreasing of the frequency moving from acceleration to displacement. When the displacement is a maximum, the velocity and the acceleration are zero; while the acceleration is zero when the velocity is maximum.

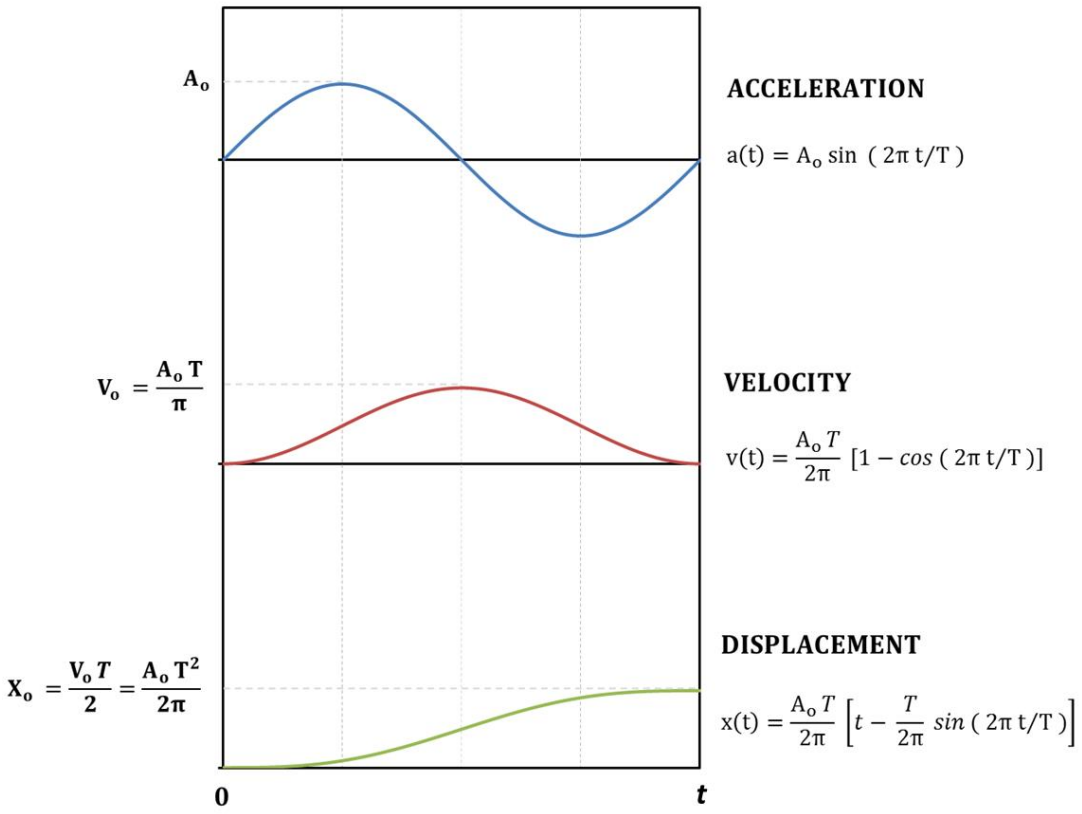

Figure E.1: Relationship between acceleration, velocity and displacement for a sinusoidal signal.

Nomenclature

α	Average slope of the bathymetry or structure slope
β	Offshore wave direction with respect to true North
γ	Specific weight of the water
η	Instantaneous sea surface elevation relative to still water level
ξ	Iribarren number or surf similarity parameter ($\tan\alpha/\sqrt{H/L}$)
ξ_b	Local Iribarren number ($\tan\alpha/\sqrt{H_b/L_o}$) $-$ regular wave
ξ_o	Deepwater Iribarren number ($\tan\alpha/\sqrt{H_o/L_o}$) $-$ regular wave
$\xi_{o,m}$	Deepwater Iribarren number with T_m ($\tan\alpha/\sqrt{H_{s,o}/L_{o,m}}$) $-$ irregular wave
$\xi_{o,p}$	Deepwater Iribarren number with T_p ($\tan\alpha/\sqrt{H_{s,o}/L_{o,p}}$) $-$ irregular wave
ρ	Mass density of the water
c	Wave celerity (L/T)
D	Highest structural response peak in the displecemt time history (absolute value)
D	Diameter of the cylinder
D_{av}	Average of the two diameters of the physical model (lab test)
d	Relative breaking distance (x/H_b)
F	Overall force obtained by the load cells system (lab test)
F_{int}	Overall force obtained by pressure integration (lab test)
F_{max}	Maximum overall peak force of the test (load cells system)

F' Dimensionless value of the maximum peak force of the load cells system ($F_{max}/\gamma D_{av} h_t H_o$)

f Vertical line force (N/m) obtained by pressure integration (lab test)

f_{max} Maximum integrated force peak of the test (integration of pressures)

f_{D1} Frequency of the highest structural peak in the displacement peak spectrum

f_{D2} Frequency of the 2^{nd} highest structural peak in the displacement peak spectrum

f_{V1} Frequency of the highest structural peak in the velocity peak spectrum

f_{V2} Frequency of the 2^{nd} highest structural peak in the velocity peak spectrum

f_n Natural frequencies of the load cells system

f_l Wave load frequency

g Graitational acceleration

H Wave height

H_b Breaking wave height $-$ regular wave

H_o Offshore wave height $-$ regular wave

$H_{s,b}$ Significant wave height at breaking point $-$ irregular wave

$H_{s,o}$ Offshore significant wave height $-$ irregular wave

$H_{1/3}$ Significant wave height ($\equiv H_s$) $-$ irregular wave

$H_{1/250}$ Mean of the highest 250^{th} wave heights $-$ irregular wave

$H_{1/250,b}$ Maximum wave height at breaking point $-$ irregular wave

H_{m0} Spectral significant wave height $-$ irregular wave

H^* Relative wave height at the toe of the lighthouse ($H_{s,o}/h_t$)

h Water depth

h_b Water depth at breaking point

h_s Water depth at the seaward toe of the structure

h_t Instantaneous water depth at the toe of the lighthouse or at the toe of the model

h^* Water depth at the section used to calculate the momentum flux for lab tests

H/h Relative wave height

H/L Wave steepness $-$ also H/gT^2

H_b/h_b Relative wave height at breaking point $-$ regular wave

h/L Relative water depth $-$ also kh or h/gT^2

K Stiffness of the load cells system

k Wave number $(2\pi/L)$

L Local wave length

$L_{(h)}$ Local wave length at the depth h $(L_o \tanh kh)$

L_o Offshore wave length $(gT^2/2\pi)$ $-$ regular wave

$L_{o,m}$ Offshore wave length with with T_m $-$ irregular wave

$L_{o,p}$ Offshore wave length with with T_p $-$ irregular wave

m_f Instantaneous flux of horizontal momentum acros a unit area

$m_{f,int}$ Depth-integrated wave momentum flux across a unit width

M_f Maximum dimensionless regular wave momentum flux $\left(\frac{m_{f,int}}{\rho g h^2}\right)$

M_F Maximum dimensionless irregular wave momentum flux

$M_{F,b}$ Irregular momentum flux calculated according to the breaker indexes of Goda

$\overline{M_F}$ Value of the irregular momentum flux determined at $h = h_b$

p_d	Instantaneous wave dynamic pressure
p_i	Generic pressure value (lab test)
p_{max}	Maximum pressure peak related to the pressure event (lab test)
p_1	Pressure value related to the beginning of the pressure event (lab test)
p_2	Pressure value related to the end of the impulsive pressure event (lab test)
p_3	Pressure value related to the end of the pressure event (lab test)
p_{max}	Maximum pressure peak of the test for a generic pressure transducer (lab test)
R	Radius of the cylinder
s_o	Offshore significant wave steepness $(H_{s,o}/L_o)$ – irregular wave
T	Wave period
T_m	Mean wave period – irregular wave
T_p	Peak wave period – irregular wave
T_s	Significative wave period – irregular wave
t	time
t_i	Instant of the generic pressure value (lab test)
t_{load}	Wave load duration related to the dynamic component
t_{max}	Instant of the maximum pressure peak (lab test)
t_r	Rise time (lab test)
t_1	Instant of the beginning of the pressure event (lab test)
t_2	Instant of the end of the impulsive pressure event (lab test)
t_3	Instant of the end of the pressure event (lab test)

t'	Dimensionless rise time (t_r/T)
tx*(i)*	Pressure measurement (signal) related to the pressure transducer no. i (i=1,...,6)
u	Instantaneous horizontal water velocity
V_1	Highest structural response peak (absolute value) in the velocity time history ($\equiv V$)
V_2	2^{nd} highest structural response peak in the velocity time history (absolute value)
V	Water velocity in the wave load formula of Wienke and Oumeraci (2005)
Vr	Raw velocity signal from geophones
Vrm	Velocity signal with mean removal (geophone)
Vrmf	Velocity signal with mean removal and filtered (geophone)
x	Breaking distance
X	Signal component on the horizontal plane (geophone)
Y	Signal component on the horizontal plane (geophone)
Z	Vertical signal component (geophone)
Z_G	Barycentre time history obtained by the integrated force (lab test)

Bibliography

Ahrens, J. P. (1981), 'Irregular wave runup on smooth slopes', *US Army, Corps of Engineers* .

Allsop, N., Durand, N. & Hurdle, D. (1998), 'Influence of steep seabed slopes on breaking waves for structure design', *Coastal Engineering Proceedings* **1**(26).

Allsop, N. & Hettiarachchi, S. (1988), 'Reflections from coastal structures', *Coastal Engineering Proceedings* **1**(21).

Allsop, N., McKenna, J., Vicinanza, D. & Wittaker, T. (1996c), 'New design methods for wave impact loading on vertical breakwaters and seawalls', *Coastal Engineering Proceedings* **1**(25).

Allsop, N. & Vicinanza, D. (1996), 'Wave impact loadings on vertical breakwaters: development of new prediction formulae', *Proc. 11th Int. Harbour Congress, Antewerp, Belgium* .

Allsop, N., Vicinanza, D., Calabrese, M., Centurioni, L. et al. (1996b), 'Breaking wave impact loads on vertical faces', *The Sixth International Offshore and Polar Engineering Conference* .

Allsop, W., Vicinanza, D. & McKenna, J. (1996a), 'Wave forces on vertical and composite breakwaters', *HR Wallingford Ltd* .

Andersen, T. L., Frigaard, P., Damsgaard, M. & De Vos, L. (2011), 'Wave run-up on slender piles in design conditionsŮmodel tests and design rules for offshore wind', *Coastal Engineering* **58**(4), 281–289.

Bagnold, R. (1939), 'Interim report on wave-pressure research', *Institution of Civil Engineeris* .

Banfi, D., Raby, A. & Simmonds, D. (2017a), 'Characterisation of breaking waves on the eddystone lighthouse: a laboratory investigation on wave pressure', *Coastal Engineering Proceedings* **1**(35), 15.

Banfi, D., Raby, A., Simmonds, D., Rafiq, Y. & Bullock, G. (2017b), 'Wave impacts on the eddystone lighthouse: a field and laboratory investigation', *ICE Coasts, Marine Structures and Breakwaters Conference. Liverpool, September 2017* .

Battjes, J. (1974a), 'Surf similarity', *Coastal Engineering Proceedings* **1**(14).

Battjes, J. A. (1971), 'Run-up distributions of waves breaking on slopes', *Journal of the waterways, harbors and coastal engineering division* **97**(1), 91–114.

Battjes, J. A. (1974b), Computation of set-up, longshore currents, run-up and overtopping due to wind-generated waves, PhD thesis, Delft University of Technology.

BGS (1996), 'Wind and water - chapter 2.3', *Coasts and seas of the United Kingdom - Region 10 South-west England: Seaton to the Roseland Peninsula - Peterborough, Joint Nature Conservation Committee* .

Blackmore, P. & Hewson, P. (1984), 'Experiments on full-scale wave impact pressures', *Coastal Engineering* **8**(4), 331–346.

Blenkinsopp, C. & Chaplin, J. (2007a), 'Validity of small-scale physical models involving breaking waves', *Power* **12**, 16.

Blenkinsopp, C. & Chaplin, J. (2007b), Void fraction measurements in breaking waves, *in* 'Proceedings of the Royal Society of London A: Mathematical, Physical and Engineering Sciences', Vol. 463, The Royal Society, pp. 3151–3170.

Blenkinsopp, C. & Chaplin, J. (2008), 'The effect of relative crest submergence on wave breaking over submerged slopes', *Coastal Engineering* **55**(12), 967–974.

Blenkinsopp, C. & Chaplin, J. (2011), 'Void fraction measurements and scale effects in breaking waves in freshwater and seawater', *Coastal Engineering* **58**(5), 417–428.

Bredmose, H., Bullock, G. & Hogg, A. (2015), 'Violent breaking wave impacts. part 3. effects of scale and aeration', *Journal of Fluid Mechanics* **765**, 82–113.

Bredmose, H., Peregrine, D. & Bullock, G. (2009), 'Violent breaking wave impacts. part 2: modelling the effect of air', *Journal of Fluid Mechanics* **641**, 389–430.

Buccino, M., Banfi, D., Vicinanza, D., Calabrese, M., Giudice, G. D. & Carravetta, A. (2012), 'Non breaking wave forces at the front face of seawave slotcone generators', *Energies* **5**(11), 4779–4803.

Bullock, G., Crawford, A., Hewson, P., Walkden, M. & Bird, P. (2001), 'The influence of air and scale on wave impact pressures', *Coastal Engineering* **42**(4), 291–312.

Bullock, G., Obhrai, C., Müller, G., Wolters, G., Peregrine, H. & Bredmose, H. (2003), Field and laboratory measurements of wave impacts, *in* 'Proc.. Coastal Structures Conference'.

Bullock, G., Obhrai, C., Peregrine, D. & Bredmose, H. (2007), 'Violent breaking wave impacts. part 1: Results from large-scale regular wave tests on vertical and sloping walls', *Coastal Engineering* **54**(8), 602–617.

Calabrese, M. (1997), 'Onset of breaking in front of vertical and composite breakwaters', *The Eighth International Offshore and Polar Engineering Conference* .

Calabrese, M. & Allsop, N. (1997), 'Impact loadings on vertical walls in directional seas', *Proceedings 2nd Task 1 Workshop, MAST III, PROVERBS-Project: Probabilistic Design Tools for Vertical Breakwaters* .

CEM (2003), 'Coastal engineering manual, chapter iii, estimation of nearshore waves', *US Army Engineer Waterways Experiment Station, US Government Printing Office, No. EM* pp. 1110–2.

Chan, E. & Melville, W. (1988), Deep-water plunging wave pressures on a vertical plane wall, *in* 'Proceedings of the Royal Society of London A: Mathematical, Physical and Engineering Sciences', Vol. 417, The Royal Society, pp. 95–131.

Chan, E.-S., Cheong, H.-F. & Tan, B.-C. (1995), 'Laboratory study of plunging wave impacts on vertical cylinders', *Coastal Engineering* **25**(1), 87–107.

Chan, E.-S. & Melville, W. (1989), 'Plunging wave forces on surface-piercing structures', *Journal of Offshore Mechanics and Arctic Engineering* **111**(2), 92–100.

Chaplin, J., Greated, C., Flintham, T. & Skyner, D. (1992), 'Breaking wave forces on a vertical cylinder', *Technical report, Health and Safety Executive, London, UK* .

Chaplin, J., Rainey, R. & Yemm, R. (1997), 'Ringing of a vertical cylinder in waves', *Journal of Fluid Mechanics* **350**, 119–147.

Chollet, O. (2014), 'Modélisation des effets de la houle, analyse du comportement structural et études de renforcement', *École Politechnique Fédérale De Lausanne, Institut D' Igénierie Civile. Master dissertation* .

Christensen, E. D., Bredmose, H. & Hansen, E. A. (2005), 'Extreme wave forces and wave run-up on offshore wind turbine foundations', *Proceedings of Copenhagen Offshore Wind* pp. 1–10.

Clough, R. W. & Penzien, J. (1975), 'Dynamics of structures'.

Cooker, M. & Peregrine, D. (1990), 'Computations of violent motion due to waves breaking against a wall', pp. 164–176.

Cooker, M. & Peregrine, D. (1992), Violent motion as near breaking waves meet a vertical wall, *in* 'Breaking waves', Springer, pp. 291–297.

Cuomo, G. (2005), 'Dynamics of wave-induced loads and their effects on coastal structures', *Final Dissertation PhD in Science of Civil Engineering, University of Roma TRE, Italy* .

Cuomo, G., Allsop, W., Bruce, T. & Pearson, J. (2010b), 'Breaking wave loads at vertical seawalls and breakwaters', *Coastal Engineering* **57**(4), 424–439.

Cuomo, G., Allsop, W. & Takahashi, S. (2010a), 'Scaling wave impact pressures on vertical walls', *Coastal Engineering* **57**(6), 604–609.

Cuomo, G., Piscopia, R. & Allsop, W. (2011), 'Evaluation of wave impact loads on caisson breakwaters based on joint probability of impact maxima and rise times', *Coastal Engineering* **58**(1), 9–27.

De Vos, L., Frigaard, P. & De Rouck, J. (2007), 'Wave run-up on cylindrical and cone shaped foundations for offshore wind turbines', *Coastal Engineering* **54**(1), 17–29.

De Waal, J. & Van der Meer, J. (1992), 'Wave runup and overtopping on coastal structures', *Coastal Engineering Proceedings* **1**(23).

Department, H. (1984), 'Channel pilot - isles of scilly and south coast of england from cape cornwall to bognor regis', *London, Hydrographic Office* .

Douglass, J. (1878), Note on the eddystone lighthouse., *in* 'Minutes of the Proceedings of the Institution of Civil Engineers', Vol. 53, Thomas Telford-ICE Virtual Library, pp. 247–248.

Draper, L. (1991), *Wave climate atlas of the British Isles*, Great Britain, Department of Energy.

Galvin, C. J. (1968), 'Breaker type classification on three laboratory beaches', *Journal of geophysical research* **73**(12), 3651–3659.

Goda, Y. (1973), 'Wave forces on circular cylinders erected upon reefs', *Coastal engineering in Japan* **16**, 137–146.

Goda, Y. (1974), 'New wave pressure formulae for composite breakwaters', *Coastal Engineering Proceedings* **1**(14).

Goda, Y. (1975), 'Irregular wave deformation in the surf zone', *Coastal Eng. Japan* **18**, 13–25.

Goda, Y. (2010), 'Random seas and design of maritime structures'.

Goda, Y., Haranaka, S. & Kitahata, M. (1966), 'Study on impulsive breaking wave forces on piles', *Report Port and Harbour Technical Research Institute* **6**(5), 1–30.

Guza, R. & Thornton, E. B. (1982), 'Swash oscillations on a natural beach', *Journal of Geophysical Research: Oceans* **87**(C1), 483–491.

Hansen, J. B. (1990), 'Periodic waves in the surf zone: Analysis of experimental data', *Coastal Engineering* **14**(1), 19–41.

Hanssen, A. G. & Tørum, A. (1999), 'Breaking wave forces on tripod concrete structure on shoal', *Journal of waterway, port, coastal, and ocean engineering* **125**(6), 304–310.

Hattori, M., Arami, A. & Yui, T. (1994), 'Wave impact pressure on vertical walls under breaking waves of various types', *Coastal Engineering* **22**(1), 79–114.

Hofland, B., Kaminski, M. & Wolters, G. (2011), 'Large scale wave impacts on a vertical wall', *Coastal Engineering Proceedings* **1**(32), 15.

Holman, R. (1986), 'Extreme value statistics for wave run-up on a natural beach', *Coastal Engineering* **9**(6), 527–544.

Hughes, S. A. (2004a), 'Wave momentum flux parameter: a descriptor for nearshore waves', *Coastal Engineering* **51**(11), 1067–1084.

Hughes, S. A. (2004b), 'Estimation of wave run-up on smooth, impermeable slopes using the wave momentum flux parameter', *Coastal Engineering* **51**(11), 1085–1104.

Hull, P., Müller, G. & Allsop, N. (1998), 'A vertical distribution of wave impact pressures for design purposes', *Research Report, MAST III, PROVERBS-Project: Probabilistic Design Tools for Vertical Breakwaters, Belfast, Northern Ireland, 16 pp* .

Hull, P. & Müller, G. (2002), 'An investigation of breaker heights, shapes and pressures', *Ocean Engineering* **29**(1), 59–79.

Hunt, J. & Ira, A. (1959), 'Design of seawalls and breakwaters', *Journal of the Waterways and Harbors Division* **85**(3), 123–152.

Huntley, D., Guza, R. & Bowen, A. (1977), 'A universal form for shoreline run-up spectra?', *Journal of Geophysical Research* **82**(18), 2577–2581.

Iribarren Cavanilles, R. & Casto Nogales, M. (1949), 'Protection des ports', *Pianc* .

Irschik, K. (2012), 'Belastung von zylindrischen pfahlstrukturen durch brechende und nicht brechende wellen'.

Irschik, K., Sparboom, U. & Oumeraci, H. (2004), 'Breaking wave loads on a slender pile in shallow water', **29**(1), 568.

Iversen, H. W. (1952), 'Laboratory study of breakers', *Gravity waves* p. 9.

Kamphuis, J. (1991), 'Incipient wave breaking', *Coastal Engineering* **15**(3), 185–203.

Kirkgöz, M. (1995), 'Breaking wave impact on vertical and sloping coastal structures', *Ocean Engineering* **22**(1), 35–48.

Kirkgöz, M. S. (1982), 'Shock pressure of breaking waves on vertical walls', *Journal of the Waterway Port Coastal and Ocean Division* **108**(1), 81–95.

Kirkgöz, M. S. (1990), 'An experimental investigation of a vertical wall response to breaking wave impact', *Ocean Engineering* **17**(4), 379–391.

Klammer, P., Kortenhaus, A. & Oumeraci, H. (1996), Wave impact loading of vertical face structures for dynamic stability analysis-prediction formulae, *in* 'Coastal Engineering Conference', Vol. 2, ASCE American Society of Civil Engineers, pp. 2534–2547.

Kortenhaus, A. & Löffler, A. (1998), 'Differences in estimating probability of impacts', *Status Report 2nd Overall Project Workshop MAST III (PROVERBS). Naples* .

Kortenhaus, A. & Oumeraci, H. (1998), 'Classification of wave loading on monolithic coastal structures', *Coastal Engineering Proceedings* **1**(26).

Kyte, A. & Tørum, A. (1996), 'Wave forces on vertical cylinders upon shoals', *Coastal engineering* **27**(3), 263–286.

Loraux, C. (2013), 'Comportement structural des phares en mer – étude historique sur le phare de la jument et propositions d' interventions', *École Polytechnique Fédérale De Lausanne, Institut D' Ingénierie Civile* .

Lundgren, H. (1969), 'Wave shock forces: an analysis of deformations and forces in the wave and in the foundation', *In Proc. Symp. Research on Wave Action, Delft* **2**.

Majdalany, F. (1959), *The Red Rocks of Eddystone*, [London]: Longmans.

Manjula, R., Sannasiraj, S. & Palanichamy, K. (2014), 'Experimental investigations of acceleration on slender cylindrical member under breaking waves', *The International Journal of Ocean and Climate Systems* **5**(3), 117–125.

Mapio.net (n.d.), 'The douglass tower', *n.d. photoghraph, viewed 15 November 2016, <http://mapio.net/pic/p-109786515/>* .

Mase, H. (1989), 'Random wave runup height on gentle slope', *Journal of Waterway, Port, Coastal, and Ocean Engineering* **115**(5), 649–661.

Mayer, R. & Kriebel, D. (1994), 'Wave runup on composite-slope and concave beaches', *Coastal Engineering Proceedings* **1**(24).

McAuley, P. (2013), 'Investigation into the bathymetry of the eddystone reef for use in modelling wave loading at the base of the lighthouse', *MSc dissertation, Plymouth University UK* .

McConnell, K. & Kortenhaus, A. (1997), Analysis of pressure measurements from hydraulic model tests and prototype measurements, *in* 'Proceedings 1st Overall Project Workshop, MAST III, PROVERBS-Project: Probabilistic Design Tools for Vertical Breakwaters'.

Melby, J. A. & Hughes, S. A. (2004), 'Armor stability based on wave momentum flux', *Proc. of Coastal Structures 2003* .

Metoffice (n.d.), 'Winter storms', *Available at: www.metoffice.gov.uk (14 December 2016)* .

Morison, J., Johnson, J., Schaaf, S. et al. (1950), 'The force exerted by surface waves on piles', *Journal of Petroleum Technology* **2**(05), 149–154.

Muttray, M., Oumeraci, H., Shimosako, K. & Takahashi, S. (1998), 'Hydraulic performance of a high mound composite breakwater', *Coastal Engineering Proceedings* **1**(26).

Nicholson, C. P. (1995), *Rock lighthouses of Britain: the end of an era?*, Dundurn.

Ostendorf, D. W. & Madsen, O. S. (1979), 'An analysis of longshore currents and associated sediment transport in the surf zone'.

Oumeraci, H. (1994), 'Review and analysis of vertical breakwater failuresŮlessons learned', *Coastal Engineering* **22**(1-2), 3–29.

Oumeraci, H., Bruce, T., Klammer, P. & Easson, W. (1995a), Piv measurement of breaking wave kinematics and impact loading of caisson breakwaters, *in* 'Proceedings International Conference on Coastal and Port Engineering in Developing Countries (COPEDEC)', pp. 2394–2410.

Oumeraci, H., Klammer, P. & Partenscky, H. (1993), 'Classification of breaking wave loads on vertical structures', *Journal of waterway, port, coastal, and ocean engineering* **119**(4), 381–397.

Oumeraci, H. & Kortenhaus, A. (1997), 'Wave impact loading-tentative formulae and suggestions for the development of final formulae', *Proceedings 2nd Task 1 Workshop, MAST III, PROVERBS-Project: Probabilistic Design Tools for Vertical Breakwaters* .

Oumeraci, H., Kortenhaus, A., Allsop, W., de Groot, M., Crouch, R., Vrijling, H. & Voortman, H. (2001), *Probabilistic design tools for vertical breakwaters*, CRC Press.

Owen, M. (1980), 'Design of seawalls allowing for wave overtopping', *Report Ex* **924**, 39.

Partenscky, H.-W. (1988), 'Dynamic forces due to waves breaking at vertical coastal structures', *Coastal Engineering Proceedings* **1**(21).

Peregrine, D. (1994), 'Pressure on breakwaters: a forward look', *Proc. Internat. Wkshp. on Wave Barriers in Deep Waters. Port and Harbour Research Institute, Yokosuka, Japan pp55* pp. 3–571.

Peregrine, D. & Thais, L. (1996), 'The effect of entrained air in violent water wave impacts', *Journal of Fluid Mechanics* **325**, 377–398.

PPS25 (2010), 'Planning policy statement 25: Development and flood risk'.

Raby, A., Bullock, G., Banfi, D., Rafiq, Y. & Cali, F. (2015), 'Wave loading on rock lighthouses', *Maritime Engineering* .

Rainey, R. & Chaplin, J. (2003), 'Wave breaking and cavitation around a vertical cylinder: experiments and linear theory', *Proc. 18th IWWWFB* .

Richert, G. (1968), 'Experimental investigation op shock pressures against breakwaters', *Coastal Engineering Proceedings* **1**(11).

Sainflou, G. (1928), 'Essai sur les digues maritimes verticales', *École nationale des Ponts et Chaussées* .

Seelig, W. N. (1983), 'Laboratory study of reef-lagoon system hydraulics', *Journal of waterway, port, coastal, and ocean engineering* **109**(4), 380–391.

Singamsetti, S. & Wind, H. (1980), 'Characteristics of breaking and shoaling periodic waves normally incident on to plane beaches of constant slope', *Report M1371, Delft Hydraulic Laboratory, Delft, The Netherlands* p. 142.

SPM (1984), 'Shore protection manual', *Department of the Army, Waterways Experiment Station, Vicksburg, Mississippi,* .

Stagonas, D., Warbrick, D., Muller, G. & Magagna, D. (2011), 'Surface tension effects on energy dissipation by small scale, experimental breaking waves', *Coastal Engineering* **58**(9), 826–836.

Takahashi, S., Tanimoto, K. & Shimosako, K. (1994), 'A proposal of impulsive pressure coefficient for the design of composite breakwaters', *Proc. of the International Conference of Hydro-Technical Engineering for Port and Harbour Construction* pp. 489–504.

Tanimoto, K., Takahashi, S., Kaneko, T. & Shiota, K. (1986), 'Impulsive breaking wave forces on an inclined pile exerted by random waves', *Coastal Engineering Proceedings* **1**(20).

Trinh, Q., Raby, A., Banfi, D., Corrado, M., Chiaia, B., Rafiq, Y. & Cali, F. (2016), 'Modelling the eddystone lighthouse response to wave loading', *Engineering Structures* **125**, 566–578.

Van der Meer, J. & Janssen, P. (1995), 'Wave run-up and wave overtopping at dikes, asce book on" wave forces on inclined and vertical wall structures", editor: Z'.

Van der Meer, J. W. (1988), 'Deterministic and probabilistic design of breakwater armor layers', *Journal of Waterway, Port, Coastal, and Ocean Engineering* **114**(1), 66–80.

Vicinanza, D. (1997), 'Pressioni e forze di impatto diffonde frangenti su dighe a paramento verticale e composte'.

Von Karman, T. (1929), 'The impact on seaplane floats during landing'.

Wagner, H. (1932), 'Über stoß-und gleitvorgänge an der oberfläche von flüssigkeiten', *ZAMM-Journal of Applied Mathematics and Mechanics/Zeitschrift für Angewandte Mathematik und Mechanik* **12**(4), 193–215.

Walkden, M., Crawford, A., Bullock, G., Hewson, P. & Bird, P. (1996), 'Wave impact loading on vertical structures', *Clifford, JE (Ed.), Advances in Coastal Structures and Breakwaters. Thomas Telford, London* pp. 273–286.

Weggel, J. R. (1972), 'Maximum breaker height for design', *Coastal Engineering Proceedings* **1**(13).

Weggel, J. R., Maxwell, W. et al. (1970), Experimental study of breaking wave pressures, *in* 'Offshore Technology Conference', Offshore Technology Conference.

Wiegel, R. L. (1982), 'Forces induced by breakers on piles', *Coastal Engineering Proceedings* **1**(18).

Wienke, J. & Oumeraci, H. (2005), 'Breaking wave impact force on a vertical and inclined slender pileŮtheoretical and large-scale model investigations', *Coastal Engineering* **52**(5), 435–462.

Winstanley, H. (1699), 'Eddystone lighthouse, narrative of the building', *HM Treasury, London, UK, Calendar of Treasury Papers* pp. 1702–1707.

Witte, H. (1990), 'Wave impact loading on a vertical wall with respect to structure response', *Report for the Federal Waterways and Research InstituteŮCoastal Department* .

Zhou, D., Chan, E. & Melville, W. (1991), 'Wave impact pressures on vertical cylinders', *Applied Ocean Research* **13**(5), 220–234.

Bound Copies of Published Papers

Wave Impacts on Rock Lighthouses

A. Raby, D. Banfi and D. Simmonds

Electronic version of an article published in Coastal Structures & Solutions to Coastal Disasters Joint Conference (2015)

Wave Impacts on Rock Lighthouses

Alison Raby, Dr.,*[1] Davide Banfi, Ph.D.,*[2] and David Simmonds, Dr.*[3]

*School of Marine Science and Engineering, Plymouth University, Drake Circus, Plymouth PL4 8AA, UK.

Email: [1]alison.raby@plymouth.ac.uk; [2]davide.banfi@plymouth.ac.uk; [3]dsimmonds@plymouth.ac.uk

ABSTRACT

This paper reports on a collaboration between Plymouth University and the General Lighthouse Authorities of the United Kingdom and Ireland, featuring the iconic Eddystone lighthouse. A combined field observation and structural modelling pilot study was undertaken to shed light on how exposed rock lighthouses respond to wave impacts. Constraints to traditional monitoring methods are described and the solutions, along with some preliminary results from nearly 3000 measured events, are discussed. A finite element model of the Eddystone lighthouse is briefly described and the modal frequencies are compared with the measured values from the field. These highlight a missing second modal response at 8 Hz which is the subject of on-going investigations.

INTRODUCTION

The General Lighthouse Authorities (GLAs) of the United Kingdom and the Republic of Ireland (Trinity House, the Northern Lighthouse Board and the Commissioners of Irish Lights) have a duty to deliver an aid to navigation service to assist the safety of all classes of mariners in navigation. Whilst they are committed to keeping physical aids to navigation in addition to virtual aids i.e. satellite systems, there would not (and could not) be like-for-like replacement of historic rock lighthouses should they become damaged or even destroyed by storm waves.

Motivation for the monitoring campaign came from providing a duty of care for maintenance personnel sometimes on station during storms and the increasingly hostile wave conditions that the towers will face because of climate change (Raby et al., 2015). This investigation provides an insight into both the wave loading and dynamic response of these unusual of structures which have not been the subject of any previous research. Being of tapered cylindrical geometry and situated on top of steep reefs, the wave transformation and loading characteristics are greatly complicated compared to many structures located on smoothly contoured shorelines.

The pilot field campaign deployed an array of instruments to the Eddystone lighthouse, chosen not because it is the most vulnerable asset of the GLAs, but because of its proximity to Plymouth University where the project team was based.

Structural modelling using finite element (FE) analysis, validated from field data, has given additional insight to the lighthouse behaviour in response to wave loading.

FIELD CAMPAIGN

Past field campaigns on more traditional coastal structures have used buoys or transducers to determine wave characteristics, and impact pressure measurements which provide a reasonable description of the wave loading. Here, we also require the structural response. Figure 1 shows an idealised layout of instrumentation that could be capable of determining the wave loading and subsequent response. Based upon fieldwork undertaken at the Alderney Breakwater by Bullock et al. (2003), pressure-aeration units (PAUs) could give pressure and void fraction measurements from the wave impacts, but without preliminary data it would be guesswork to know where best to site the PAUs. New developments with piezoelectric film (Stagonas et al., 2012) have suggested that more comprehensive spatial information of wave impacts might one day be available for coastal structures. Actuators could be used to apply a known disturbance to the tower and accelerometers could pick up these resulting vibrations and intermittent ones from wave impacts. Wave runup information could potentially be obtained from a novel application of runup wires if an appropriate calibration system could be developed. In addition, wave data in close proximity to the site and bathymetric information would be needed. Finally, video cameras would capture the wave-by-wave events. One camera could be placed on the stump of the old Smeaton tower (to the right of Figure 1) with a photovoltaic (PV) panel for power.

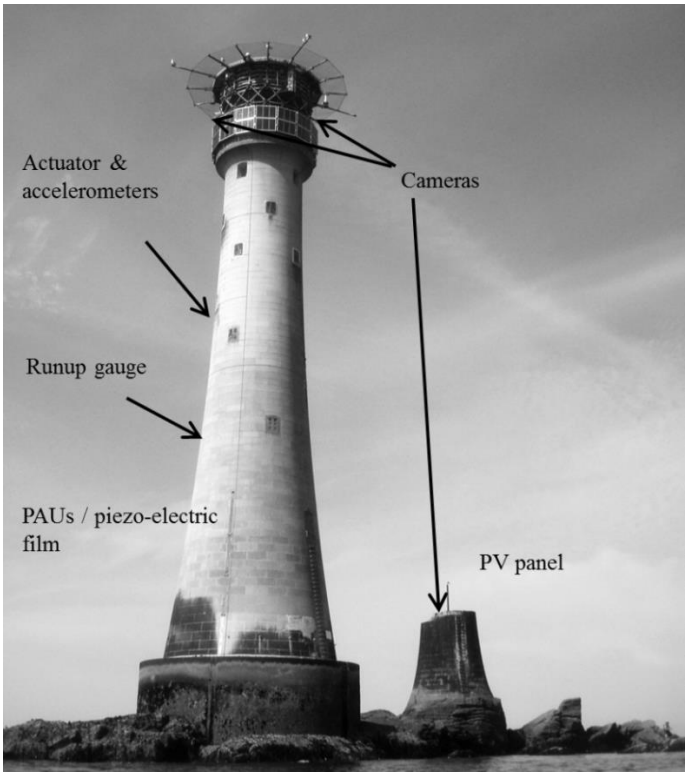

Figure 1. Idealised instrumentation of the Eddystone lighthouse.

However, due to its location, there are severe constraints to the monitoring campaign (Raby et al., 2015). Firstly, visits to the lighthouse are only possible by helicopter which is costly, both logistically and financially. Most rock lighthouses have now been fitted with helidecks onto which the maintenance personnel alight every 4 to 6 months for short-duration visits. Secondly, due to power being provided from solar PV with diesel generator back-up through periods of low light, the available power for additional instruments is very low, some 30W averaged over a year. Lastly, the hostile environment that instrumentation must withstand cannot be over-estimated. During the winter storms of 2013/14 a further three courses of interlocking stones were removed from the neighbouring Smeaton lighthouse stump (Figure 2), the tower having been moved to Plymouth Hoe in 1884 when the particular rock on which it was built was deemed to be failing.

Figure 2. Dislodged interlocking blocks on the neighbouring Smeaton's tower stump.

A pragmatic approach to the monitoring campaign was therefore devised as follows. Wave-by-wave information was obtained from four video cameras positioned around the helideck supporting structure. Two cameras pointed to the prevailing southwest, one far-field to capture the wave transformation over the reef and one downward looking to capture waves running up the structure. The other two were spaced at 120° intervals around the tower. To minimise power consumption the cameras were remotely controlled by a direct line-of-sight wireless bridge to the university. Alerts were set up from other buoys in the area, triggered when a certain threshold wave height was observed; this gave an indication on when it was prudent to turn activate the cameras. Finally, in a bid to reduce storage of video data, the cameras were programmed to record at 1 fps with the frame rate increasing to 5 fps only when waves washed over the cylindrical base of the lighthouse (an area that corresponded) to a certain region of the camera field-of-view. A snapshot from the four cameras during calm weather is shown in Figure 3. Geo-referencing the images permitted some quantification of wave runup, though it was only possible to obtain this data during daylight hours and when spray did not obscure the cameras.

To detect the structural response, tri-axial geophone systems were placed around the lighthouse. This technology is more commonly used by seismologists but it provided a convenient battery-powered method of acquiring velocity time-history

information. Furthermore, this could be sent via GSM mobile phone networks so that alerts could be sent whenever movement of the structure above a certain threshold was registered. Constraints on this system were that batteries needed to be replenished at every maintenance visit. Displacement time histories were obtained by integrating the signals and conducting principle component axis analysis.

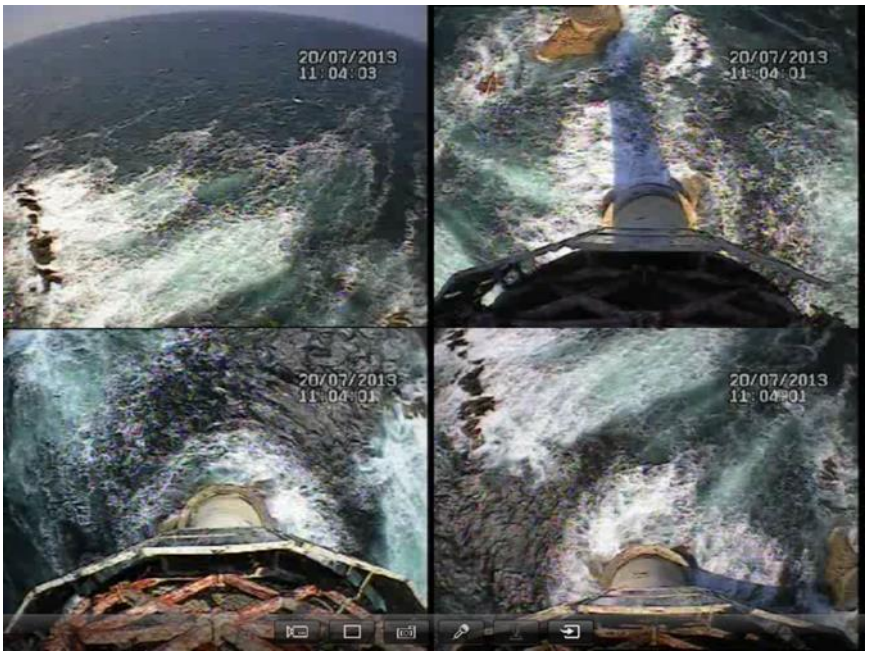

Figure 3. View from the four cameras situated under the helideck of the lighthouse. Note the Smeaton's tower stump to the top of the upper right image.

Additionally, wave data was obtained from the nearby Western Channel Coastal Observatory E1 data buoy some 16 km to the southwest (the prevailing wave direction), statistical data from 20 minute records being publicly available. Bathymetric data was obtained from a multibeam sonar survey of the area undertaken by an MSc Hydrography student at the university. Finally, water levels at the toe of the structure were obtained by relating tide levels from observation stations to date/stamped photographs taken at the Eddystone from a variety of sources.

The monitoring systems were installed in time to capture the full effects of the devastating 2013/14 winter storms which wreaked chaos across the south of the UK, disrupting the rail network and causing flooding. On the Eddystone lighthouse three thousand events above a certain threshold were recorded by the geophone systems (Raby et al., 2015). These were analysed according to: the prevailing offshore conditions e.g. wave height, wave period, wave steepness, wave direction, and the stage of the tide i.e. the local water depth at the base of the lighthouse. Most recorded events were due to 'plunging' waves as determined by the offshore Iribarren number. This is not surprising since plunging wave impacts are known to be particularly violent (Chan et al., 1995; Wienke & Oumeraci, 2005). However there were a cluster of about 20 modest events in the 'collapsing' wave breaking region. The reason for collapsing waves apparently causing measurable responses was gleaned from video images which showed that those waves broke very close to the tower. The

relationship between the size of the event and the water depth shows a steadily increasing trend with a clear linear envelope. This is due to larger water depths permitting increasingly large waves close to the tower before breaking, hence producing larger impacts. Further analysis is showing that the breaking distance from the tower is an important indicator of impact severity.

STRUCTURAL MODELLING

Alongside the field data monitoring, a structural model of the Eddystone lighthouse was developed. Archived drawings were converted into AutoCAD and imported into LUSAS Finite Element (FE) modelling software. The model (Trinh, 2015) comprised a structure with 9944 nodes, hexahedral elements and quadratic interpolation. Individual interlocking stone blocks were not modelled, instead the lighthouse was regarded to be a monolithic granite structure. Material properties of the granite were obtained from the two quarries mentioned in the historic literature (Douglass, 1883). The next stage was a validation exercise to determine the natural modes of vibration using the geophone displacement data. A comparison of the vibration modes above the fundamental demonstrated a third mode in agreement, but the FE model was unable to reproduce a response at 8Hz that was apparent in the geophone data (see Table 1). The reason for this discrepancy is the subject of on-going analysis but it may be due to the absence of a helideck in the model, or the effect of the reef on which it stands, or even a resonance of trapped air within the tower.

Table 1. First three natural modes of vibration.

Mode	*Geophone frequency (Hz)*	*Model analysis frequency (Hz)*
1	4.4	4.4
2	8.2	-
3	15.3	15.2

Following modal analysis wave loading was applied, based on estimated worst-case wave height values using depth-limited breaking criteria. The dynamic element of the load was as provided by Wienke & Oumeraci (2005) as follows:

$$F(t) = \lambda\,\eta_b \cdot \rho \cdot R \cdot V^2 \left(2\pi - 2\sqrt{\frac{V}{R}t} \cdot \operatorname{atanh}\sqrt{1 - \frac{1}{4}\frac{V}{R}t} \right)$$

for

$$0 \le t \le \frac{1}{8}\frac{R}{V}$$

and

$$F(t) = \lambda \eta_b \cdot \rho \cdot R \cdot V^2 \left(\pi \sqrt{\frac{1}{6}\frac{R}{V t'}} - \sqrt[4]{\frac{8}{3}\frac{V}{R}t'} \cdot \operatorname{atanh} \sqrt{1 - \frac{V}{R}t' \sqrt{6\frac{V}{R}t'}} \right)$$

for

$$\frac{3}{32}\frac{R}{V} \leq t' \leq \frac{12}{32}\frac{R}{V} \qquad t' = t - \frac{1}{32}\frac{R}{V}$$

where ηb is the crest elevation with respect to the still water level, λ is the curling factor equal to 0.46 (Wienke & Oumeraci, 2005), ρ is the water mass density, R is the average radius of the of the lighthouse in the zone of impact and V is the water velocity. The resulting load curve is shown in Figure 4 and demonstrates the very short duration of the initial impact loading. The azimuthal horizontal distribution of the pressures was chosen according to Wienke & Oumeraci (2005) and the vertical distribution according to Tanimoto et al. (1986).

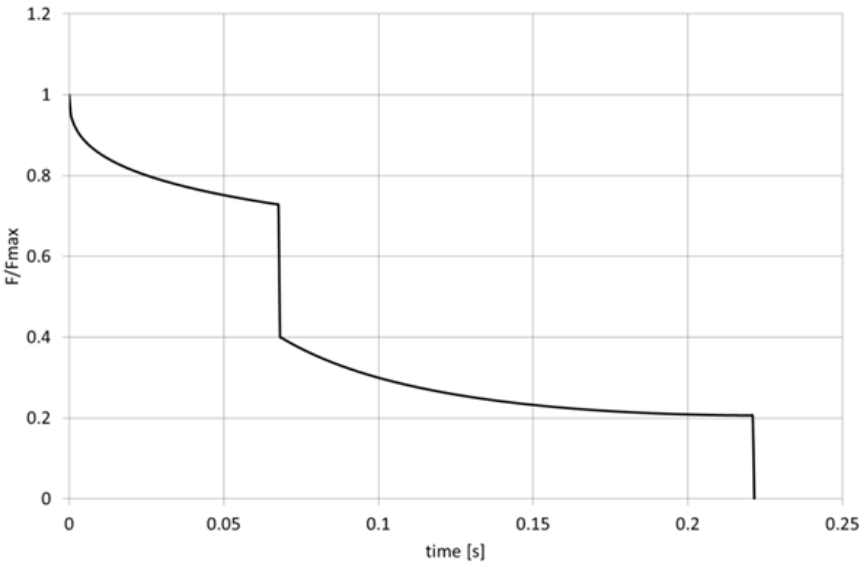

Figure 4. Dynamic element of impact load curve based upon Wienke & Oumeraci (2005).

Based on this wave loading, the stability of the Eddystone lighthouse to material failure, overturning and sliding was assessed. Regarding material failure the results showed that the most stressed point was well inside the Mohr failure domain i.e. the structure is not expected to suffer from material failure. Also, the structure is safe from overturning and sliding with factors of safety greater than 5 for both failure modes.

CONCLUSION

The pilot project has shown that despite constraints to conventional monitoring, it is possible to obtain useful information from battery-operated/remote-controlled equipment. Analysis of data has shown that the interpretation of the wave runup information and geophone response data is complicated by a variety of issues including the complex 3D bathymetry. Furthermore, modelling the lighthouse as a monolith has produced good agreement with the field data, though the model has not reproduced one of the oscillation modes. Finally, according to the FE model the structure appears to be safe according to typical failure modes. The project is on-going and will comprise laboratory modelling, improved photogrammetry to better assess wave runup and the monitoring of more exposed lighthouses in the British Isles.

ACKNOWLEDGEMENTS

The authors would like to acknowledge the support of the General Lighthouse Authorities, particularly Martin Bransby and Ron Blakeley (ex-Trinity House) and their lighthouse engineers who assisted with deployments on station; Peter Ganderton and Tony Tapp of Plymouth University who designed much of the installed equipment; the School of Marine Science and Engineering who funded Davide Banfi's studentship; Quang Trinh who conducted the FEA; Professors Bernardino Chiaia and Mauro Corrado from Politecnico di Torino who co-supervised Quang Trinh's MSc dissertation; and Mr Gwyn Jones who organised the Eddystone reef survey, supervising Paul McAuley's MSc dissertation at Plymouth University.

REFERENCES

Bullock, G., Obhrai, C., Müller, G., Wolters, G., Peregrine, D. H., and Bredmose, H. (2003). "Field and laboratory measurements of wave impacts." *In Proceedings of the 3rd Coastal Structures Conference*, ASCE.

Chan, E., Cheong, H., and Tan, B. (1995). "Laboratory study of plunging wave impacts on vertical cylinders." *Coastal Engineering,* 25, 87-107.

Douglass, W.T. (1883). "The new Eddystone Lighthouse." Paper 1960, *Proceedings, Institution of Civil Engineers,* UK. Vol. 75, Part 1, 1884, 20-60.

Raby, A., Bullock, G.N., Banfi, D., Rafiq, Y., and Cali, F. (2015). "Wave loading on rock lighthouses." Accepted for publication in *Maritime Engineering*.

Stagonas, D., Muller, G., Ramachandran, K., Schimmels, S., and Dane, A. (2012). "Distribution of impact induced pressures at the face of uniformly sloped sea dikes: preliminary 2D experimental results." *Proceedings of 33rd International Conference on Coastal Engineering,* Santander.

Tanimoto, K., Takahashi, S., Kaneko, T., and Shiota, K. (1986). "Impulsive breaking wave forces on an inclined pile exerted by random waves." *Coastal Engineering,* 2288-2302.

Trinh, Q. (2015). "Structural analysis of the Eddystone Lighthouse through the realisation of a Finite Element Model." MSc Civil Engineering dissertation, *Plymouth University* and *Politecnico di Torino*.

Wienke, J., and Oumeraci, H. (2005). "Breaking wave impact force on a vertical and inclined slender pile – theoretical and large-scale model investigations. " *Coastal Engineering,* 52(5), 435-462.

Wave loading on rock lighthouses

A. Raby, G. Bullock, D. Banfi, Y. Rafiq and F. Cali

Electronic version of an article published in Proceedings of the Institution of Civil Engineers-Maritime Engineering. Thomas Telford Ltd, 2015. p. 15-28.

This paper may be found at
https://www.icevirtuallibrary.com/doi/10.1680/jmaen.15.00002

Maritime Engineering
Volume 169 Issue MA1
Wave loading on rock lighthouses
Raby, Bullock, Banfi, Rafiq and Cali

ice | proceedings

Proceedings of the Institution of Civil Engineers
Maritime Engineering 169 March 2016 Issue MA1
Pages 15–28 http://dx.doi.org/10.1680/jmaen.15.00002
Paper 2015-2
Received 06/02/2015 Accepted 06/08/2015
Published online 25/11/2015
Keywords: field testing and monitoring/maritime engineering/mathematical modelling

ice Institution of Civil Engineers
publishing

Wave loading on rock lighthouses

1 **Alison Raby** BSc, PhD, DPhil
Reader, School of Marine Science and Engineering, Plymouth University, Plymouth, UK

2 **Geoffrey N. Bullock** BSc, PhD, CEng, MICE (Retd.)
Emeritus Professor, School of Marine Science and Engineering, Plymouth University, Plymouth, UK

3 **Davide Banfi** Ing
PhD Student, School of Marine Science and Engineering, Plymouth University, Plymouth, UK

4 **Yaqub Rafiq** BSc, MSc, PhD, CEng, MIstructE, MASCE, FHEA
Senior Lecturer, School of Marine Science and Engineering, Plymouth University, Plymouth, UK

5 **Federico Cali** Ing
Former MSc Student, School of Marine Science and Engineering, Plymouth University, Plymouth, UK





Historical and contemporary observations of wave-impact loading on rock lighthouses during storms are presented. With climate change potentially causing sea level rise and more energetic wave climates, the longevity of these heritage structures cannot be taken for granted. To obtain a better understanding of the wave–structure interaction, Plymouth University has been working with the General Lighthouse Authorities to develop monitoring and modelling techniques suitable for these isolated masonry structures. Details of the field campaign, in which 2978 impact events were recorded during the winter storms of 2013/2014, are presented together with an initial analysis that begins to shed light on the dynamic response of these iconic structures. The results indicate that the response can be sensitive to the type of wave impact and that the overall motion of the Eddystone tower was less than might have been expected. A finite-element model of the tower was able to reproduce accurately the frequencies of the first and third modes of vibration but, unlike the field data, failed to show response at a frequency near the second mode. Preliminary attempts to apply wave loads estimated on the basis of ISO 21650 show reasonable agreement between the model displacements and those measured.

Notation

H_{max}	maximum wave height
H_s	significant wave height
T_p	period associated with the peak of wave energy spectrum

1. Introduction

There are about 20 masonry lighthouses around the UK that are exposed to wave action. The locations of three of the most exposed (Wolf Rock, Longships and Eddystone) are shown in Figure 1.

The perilous Eddystone reef, some 14 miles (22·53 km) off Plymouth, gained its first lighthouse in 1698. This stone-clad wooden structure was swept away by the great storm of 1703. Three further lighthouses have stood at that location, each larger and more sturdy than its predecessor. The structure designed by Smeaton represented a major advance in the art of civil engineering and is featured in the Institution of Civil Engineers' coat of arms. It was replaced by the present lighthouse, the Douglass tower, in 1882 (Figure 2).

Although mariners are making ever greater use of satellite-based navigation technologies, the General Lighthouse Authorities (the umbrella organisation of Trinity House, the Northern Lighthouse Board and the Commissioners for Irish Lights) recognises the need to retain rock lighthouses as physical aids to navigation. However, there is concern about how well they would withstand the additional wave loading associated with predicted sea level rises and increased

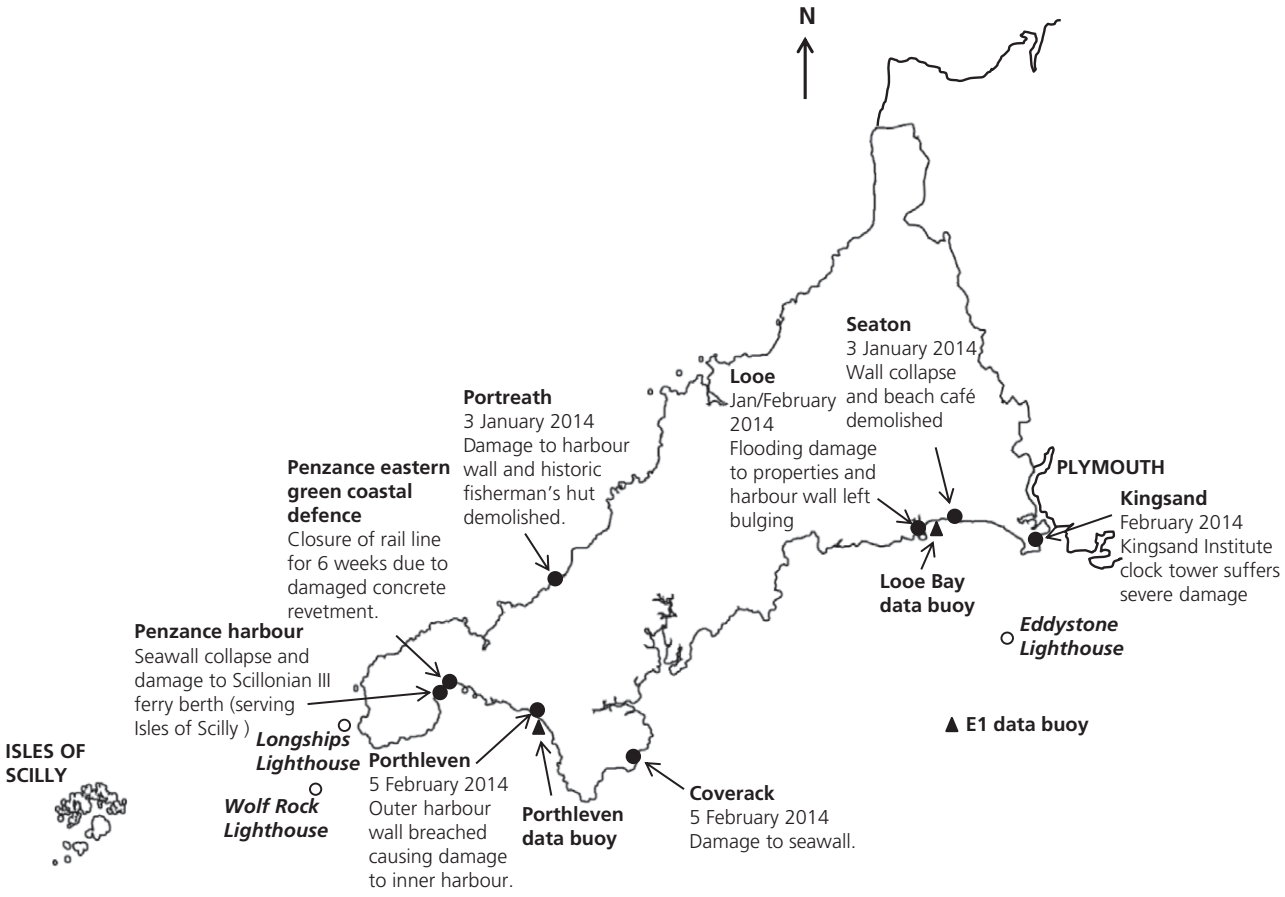

Figure 1. Locations of storm damage, lighthouses and wave buoys in Cornwall

storminess. The UK planning policy statement 25 (Planning Portal, 2010), produced by the Department for Communities and Local Government includes isostatic subsidence in its predictions and has recommended contingency allowances for sea level rise in the southwest of 3·5 mm/year from 1990 to 2025, 8·0 mm/year from 2025 to 2055, 11·5 mm/year from 2055 to 2085 and 14·5 mm/year from 2085 to 2115. This gives a net sea level rise from 2009 levels of 0·786 m by 2095. The UK planning policy statement 25 (Planning Portal, 2010) also provides national precautionary sensitivity ranges for extreme wave heights, suggesting that a factor of +5% is applied from 1990 to 2055, increasing to +10% for 2055 to 2115.

Victorian engineers expended considerable effort on trying to assess the wave loading on their maritime structures, and constructed lighthouses so durable that little thought had to be given to their behaviour under extreme conditions until now. Section 2 of this paper contrasts what the Victorians knew about the wave environment with what is now known. Section 3 describes the instrumentation that was installed on the Eddystone Lighthouse to record both the waves that reached the structure and its response. Section 4 outlines details of a finite-element (FE) model of the Eddystone Lighthouse. Section 5 presents the data acquired during the winter storms of 2013/2014 that had such a devastating effect in the southwest of England, as outlined in Figure 1. Section 6 provides concluding remarks.

2. Wave loading on exposed maritime structures

2.1 Historical approach

Much of the early work on understanding wave loading was undertaken by the Stevensons, the family of lighthouse builders responsible for building all the rock lighthouses around the coast of Scotland over four generations (Bathhurst, 2005). Robert Stevenson (grandfather of the author Robert Louis Stevenson) provides a descriptive view of the waves interacting with the Bell Rock Lighthouse in Scotland. He describes how

Figure 2. Eddystone lighthouses: (a) photograph of the construction of the Douglass tower in the foreground and the Smeaton tower in the background, taken *c.* 1880–1881, reproduced by kind permission of ICE; (b) the Douglass tower in 2013 with the stump of the Smeaton tower to the right, reproduced by kind permission of M. Docker; and (c) outline of the Eddystone Lighthouse showing the masonry courses, internal spaces and the locations of the deployed instruments

in some circumstances the door could be left open without fear of water ingress despite big seas

> … the waves separate below, and are sent round the building with such force, that their collision upon the lee-side produces … a downy spray, white as snow, rises at some distance from the house, to the height of 20 or 30 feet above the medium surface of the sea, and comes in minute particles upon those within the entrance-door, producing a sensation as if dust were falling upon them. (Stevenson, 1824)

At the Eddystone the wave climate is affected by the complex three-fingered reef and a tidal range that can exceed 5 m. During construction of the lighthouses there were constant delays due to the inability to land on the reef even during calm summer weather. Winstanley (1699), who built the first tower, is quoted (Majdalany, 1959) as saying that

> … though the weather should seem to be most calm in other places, yet here it would mount and fly more than two hundred foot …

Smeaton, who designed the third lighthouse, made the observation that 'on a perfectly calm day, with the water for half a mile around seemingly as smooth as glass, a scarcely perceptible ground swell could send an unexpected wave billowing over the rock, even though its peak was at the time nine feet above water level' (Majdalany, 1959). Smeaton made further interesting observations that during periods of 'comparatively innocuous swell' waves could be sent up to a height of around 10 m or so as they broke at low tide on the western end of the reef, although at high tide the same was not witnessed even though the swell was much greater (Majdalany, 1959).

In their search for knowledge, the Victorian pioneers were quite prepared to draw on the experience of others. Thus, a circular letter was sent to lighthouse keepers asking them to find out from the 'oldest and most intelligent fishermen' which wind directions caused the 'heaviest seas' and to complement this with their own views. One recorded observation concerning the height of the spray at the Bell Rock states that it reached between 60 and 80 ft (18–24 m) during February 1845 (Stevenson, 1848).

Quantitative estimations of wave height were attempted at Skerryvore in Scotland by fixing a graduated pole to a nearby submerged rock. Unsurprisingly it was found that 'observances were not of so satisfactory a nature' due to the fact that 'the poles soon worked loose from their attachments, and disappeared' (Stevenson, 1848).

2.1.1 The marine dynamometer

Frustration at the paucity of wave loading knowledge is reflected in the comments of Alan Stevenson (1848)

> We have little more than conjecture to guide us … to estimate the power or intensity to which Sea Towers are subject … The only

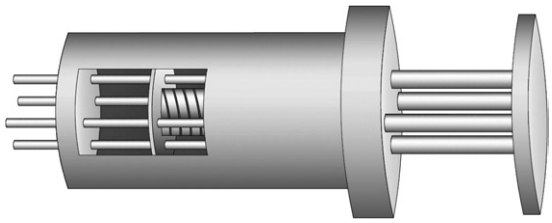

Figure 3. Thomas Stevenson's marine dynamometer based on a sketch in Stevenson (1848)

> experiments … are those of Mr Thomas Stevenson, Civil-Engineer, who had long entertained the idea of registering the force of the impulse of the waves, and lately contrived an instrument for the purpose, which he has applied at various parts of the coast.

The marine dynamometer, as it was called, was an ingenious device designed to measure the maximum wave-impact pressure at a particular location. It was constructed from cast iron and securely bolted to the reef so that the plate shown to the right in Figure 3 faced the approaching waves. Each wave impact on the plate then pushed rods through the cylindrical body of the device against the resistance of the set of springs housed inside it. Small leather rings on the rods indicated the maximum displacement, which, together with knowledge of the springs' stiffness, enabled the pressure on the plate to be estimated. Some redundancy in the number of guide rods gave confidence that the leather rings had kept their maximum positions. Individual pressure readings at a specific location would therefore be available from a storm, once conditions permitted the lighthouse keeper to access the instrument.

Extensive experimentation in the placement and design of the dynamometer was undertaken. In some situations the size of the plate had to be reduced and/or the stiffness of the springs increased because the impact pressures were too large. As a quality check two devices were placed side by side and maximum pressures were found to be within 1% of each other. The effect of placing devices at different elevations was also explored. Over a period of some 23 months, Thomas Stevenson used three of his dynamometers to obtain the world's first set of systematic measurements of wave-impact pressures. Given the importance of estimating forces, he recognised that his methodology should not be restricted to lighthouses, but was also applicable to other 'seaworks' such as breakwaters.

The first four columns of data in Table 1 have been taken directly from Stevenson (1848), where instrument I was placed 'several feet lower' and 'about 40 foot seaward' of instrument II, which was closest to the lighthouse. Evident from Table 1 is that the device placed closest to the tower and

Date	Remarks	No. of instrument	Pressure: kN/m^2	Pressure: kN/m^2
Jan. 7	Heavy sea	I	1714	82
		II	4182	200
Jan. 12	Very heavy swell	I	2856	137
		II	5032	241
Jan. 16	Heavy ground swell	I	2856	137
		II	4752	228
Jan. 22	A good deal of sea	I	2856	137
		II	5323	255
Jan. 28	Heavy ground swell	I	2627	126
		II	4562	218
Feb. 5	Fresh gales	I	856	41
		II	3042	146
Feb. 21		I	1827	87
		II	3422	164
Feb. 24	Fresh breezes	I	1256	60
		II	3802	182

Table 1. Pressure readings from Skerryvore Lighthouse in 1848 (Stevenson, 1848)

at the elevated level recorded higher pressures. This may be related to a comment that Stevenson makes on how the state of the tide affects the reading, with low tides reducing the water that makes it over the reef.

2.1.2 Structural response observations

Attempts to estimate wave loads were enhanced by observations of how lighthouses behaved during violent storms. In respect of the Bell Rock Lighthouse, Robert Stevenson (Stevenson, 1824) reports that the keepers were startled by one particular wave impact while they were in the kitchen, fairly low down the tower. This impact was accompanied by a noise similar to that of a gun discharging and caused the doors to rattle. The keepers' first thought was that the tower must have been struck by a vessel, but this was quickly ruled out. Reflecting on these observations, Stevenson suggests that they may have been caused by a 'disturbance in the equilibrium of the air' resulting from the wave rushing up the outside of the tower. He further likens tremors experienced higher up the tower as not being dissimilar to the effect of a normal house door being slammed or a carriage of the time 'making a rattling noise in passing along the street'. On another occasion at Bell Rock, Professor John Robison, a renowned professor of natural philosophy (physics) at the University of Edinburgh, was sitting in one of the rooms in the lighthouse when the structure was hit by a violent wave. The impact caused a vibratory motion following which Robison assured others that the vibration was 'the strongest proof of the unity and connection of the fabric in all its parts' (Stevenson, 1824).

Majdalany (1959) recounts many tales concerning the behaviour of the early Eddystone lighthouses. For example, Winstanley's structure was said to rock so much that crockery could be shaken from the table and the lighthouse keepers made seasick. Rudyard's tower, the second on the Eddystone reef, was also said to vibrate enough not only to shake utensils off surfaces but also to rock men out of their bunks. The principal keeper's log indicates that even Smeaton's tower could have a noticeable response to wave impacts. The report for a particularly violent storm states that it caused 'considerable motion of the cylinder glasses fixed in the lamps' and describes how the tower appeared to 'jump as if resting on an elastic body'.

Smeaton's lighthouse was replaced mainly because the gneiss rock on which it stood had been eroded. James Douglass (Douglass, 1878) also drew attention to the fact that storm waves could rise up the tower 'considerably above the summit of the lantern, thus frequently eclipsing the light and altering its distinctive character'; an impressive feat given that the focal plane of the light was 72 ft (~23 m) above high water level. Furthermore, when the upward jet of water hit the projecting cornice just below the lantern (see Figure 2(a)) it 'lifted the portion of the building above this level'; a problem that was eventually solved by reducing the projection by 5 in (~130 mm) and adding bolts to the wrought-iron ties that had already been installed in an attempt to stop the joints in the masonry near the top of the tower from opening.

William Douglass (1883) explained how his father, now Sir James, reduced the height of wave uprush on his lighthouse by founding it on a 22 ft (~6·7 m) high by 44 ft (~13·4 m) dia. cylindrical base. This, together with the tower it supported, was constructed from 2171 granite blocks that were dovetailed together both horizontally and vertically. The resultant structure increased the elevation of the focal plane of the upper of two lights to 133 ft (~40·5 m) above high water. Trinity House (2015) gives the height of the current light as 41 m above mean high water.

2.2 A brief review of current measuring techniques and knowledge

Equipment is now available for measuring the height of ocean waves from below, at or above the air–water interface. Accelerometer buoys are well suited for taking measurements at remote deep-water locations and one was moored near the Eddystone for extended periods between 1973 and 1981 (Draper, 1991). Thanks to the prevailing southwesterly winds and the long fetch of the English Channel, the maximum winter wave heights were found to exceed 3 m for 10% of the time with a 1:50 year maximum wave height greater than 20 m. The E1 data buoy is of particular relevance to the present investigation as it provided the data presented in Figure 6 and Figure 8. This Western Channel Observatory autonomous buoy, operated by Plymouth Marine Laboratory, is located as shown in Figure 1.

Various pressure and force transducers can be adapted to measure wave loading in the field. The pressure aeration units developed by Bird *et al.* (1998) also enabled the level of aeration to be estimated. Bagnold (1939) was the first to provide scientific evidence of the importance of air when he found that waves breaking against a vertical wall in a laboratory channel tended to generate the highest impact pressures when they trapped a small pocket of air against the wall. It has subsequently been demonstrated that entrained air tends to reduce wave-impact pressures (Bullock *et al.*, 2001). Despite this, pressures up to 775 kN/m^2 have been recorded in the field (Bullock and Bredmose, 2010) and over 1 MN/m^2 in large-scale laboratory tests (Bullock *et al.*, 2007).

Even in well-controlled laboratory tests (e.g. Bagnold, 1939; Bullock *et al.*, 2007) wave-impact pressures are highly sensitive to small differences in the breaking wave's profile. This makes detailed analysis of results obtained from physical tests extremely difficult. Numerical models provide a means of gaining insight into the physics, and it has been shown that the pressure waves emanating from the impact zone can become shock waves in the most extreme cases (Bredmose *et al.*, 2009). Entrained air has also been shown to play a pivotal role in reducing impact pressures (Bredmose *et al.*, 2015), and it is fortunate that entrained air tends to persist in full-scale waves for longer than suggested by small-scale model tests (Blenkinsopp and Chaplin, 2011).

Because wave-impact pressures tend to be both spatially and temporally localised (Bullock *et al.*, 2001, 2007), it was sometimes thought that the resultant impulses were of too short a duration to displace large structures. However, since Oumeraci (1994) attributed a number of breakwater failures to breaking waves, it has become common practice in Japan to assess the expected sliding distance of breakwaters (Goda, 2010).

The installation of offshore wind turbines on monopoles has led to renewed interest in the loading and run-up of breaking waves on cylindrical structures (Bredmose *et al.*, 2006). Other findings, including those arising from interest in oil platforms, included confirmation of the variability of impacts (Chan *et al.*, 1995; Lykke Andersen *et al.*, 2011), the importance of breaking wave type to the resulting impact (Chan *et al.*, 1995; Wienke and Oumeraci, 2005) and their spatially localised nature (De Vos *et al.*, 2007; Kyte and Tørum, 1996). Also of great relevance to rock lighthouses has been the work to investigate the role of bathymetry, specifically reefs, into the wave transformation and subsequent impact (e.g. Mase *et al.*, 2001). However, the authors are not aware of any modern research, at

either model or full scale, into the wave loading on tapered structures such as lighthouses.

3. Instrumentation of the Eddystone Lighthouse

As a precursor to a more detailed investigation into the relationship between wave loading and the structural response of more vulnerable masonry lighthouses, equipment was installed on the Douglass tower to understand better the magnitude and direction of incoming waves and to see if it would be possible to record the subsequent motion of the tower. The choice of equipment was constrained by a number of factors including

- power availability limited to 300 W for 1 h periods and a maximum total energy of about 260 kWh over a year, due to all power being generated by photovoltaic panels with diesel generator back-up
- the inability to access instrumentation between the two or three short annual maintenance visits by helicopter of Trinity House staff
- the difficulty of attaching anything to the outside of the masonry structure
- the hostile wave climate at the reef.

These factors effectively rule out a conventional wave loading field campaign that would measure surface elevations within close proximity of the structure using bottom-mounted pressure transducers or wave buoys, and would obtain localised impact pressures using ruggedised pressure transducers. Given the highly localised nature of the wave impacts mentioned previously, it would also be impractical to install enough transducers to get a clear indication of the overall pressure distribution.

Instead, both to satisfy the constraints and facilitate regular monitoring, it was decided to use remote-controlled, DC-powered video cameras to record the wave conditions around the structure, together with two RDL//Vibe geophone systems to measure any structural response. The use of two geophone systems provided data quality checks and some redundancy. The equipment was installed in the arrangement shown schematically in Figure 4, during a 48 h visit to the lighthouse by two members of staff from Plymouth University in the summer of 2013.

3.1 Camera system

Four cameras were attached to the helideck structure at the intermediate platform level as indicated in Figure 2(c). One of the cameras was angled towards the 'far field' to provide information about wave transformation across the reef, while the others looked down at the waves reaching the lighthouse from the three directions listed in Table 2. All the cameras were linked to a digital video recorder controlled by an internet protocol switch accessed by way of a line of sight wireless bridge to the Plymouth University campus.

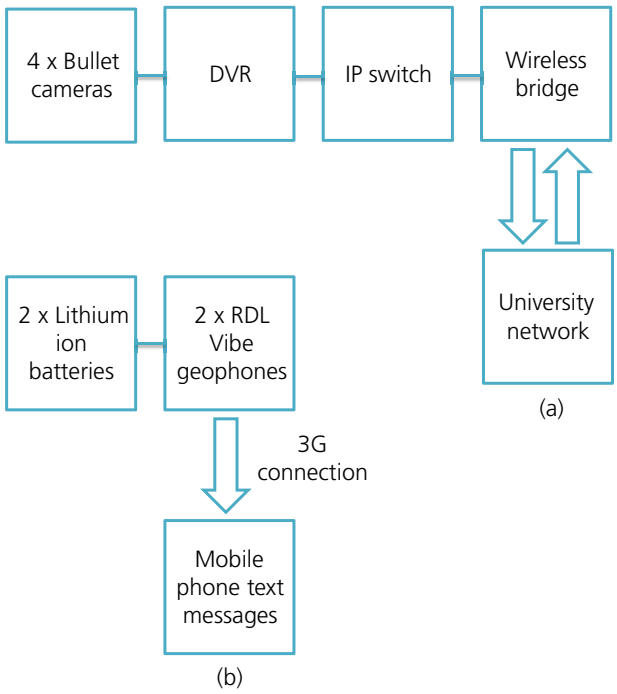

Figure 4. Schematic diagram showing installed equipment and connectivity: (a) camera system and (b) geophone system

Camera no.	Direction	Near or far-field
1	SW (225°)	Far
2	NNW (337·5°)	Near
3	ESE (112·5°)	Near
4	SW (225°)	Near

Table 2. Orientation of cameras

To avoid wasting power and data storage, the camera system was set to be off between the hours of 22:00 GMT and 04:00 GMT and was not switched on during calm conditions. It was only switched on after an alert based on data from the Channel Coastal Observatory (CCO) indicated that the significant wave height at the Porthleven, Looe Bay (see Figure 1) or the (South Devon) Start Bay wave buoy exceeded 1·5 m. Because impacts were rarely, if ever, recorded at that wave height threshold, the cameras were not automatically switched on, but the alert was taken as a forewarning of potential activity.

When on, the cameras would normally capture video images at a rate of 1 frame/s. A region at the base of the tower in each near-field image was also monitored for activity typical of a wave running up the structure. When this happened the cameras acquired data at 5 frames/s for a period of at least 30 s and continued at this higher recording rate while evidence of run-up in that region persisted.

Although the system was designed to enable remote downloading of the data, this was rarely undertaken as it took approximately 1 min to download 1 s of video image. Consequently, most of the data were analysed after swapping the digital video recorder hard drives during visits to the lighthouse. This further constrained the time that the cameras could be on as the hard drives could only store 1862 GB of data, which corresponds to about 994 h of recording at the higher rate.

Assessment of the wave loading on the lighthouse was based on the statistical wave parameters obtained from the E1 buoy and the heights of individual wave run-up events estimated from the distorted images captured by the video cameras. To improve the accuracy of the estimates, a geo-referenced grid was established for images of the tower by holding targets at known elevations out of windows. With appropriate processing, the elevations of the masonry courses could then be determined and a correcting grid produced. However, nothing could be done to reduce the errors introduced by poor light and white water.

3.2 Geophone system

Geophone systems are normally used to acquire the velocity time history of seismic disturbances, and are activated when a disturbance exceeds a set threshold level. The data can then be integrated or differentiated to obtain displacements and accelerations, respectively.

The two systems used to monitor the vibration of the tower were installed in the subsidiary light room on level LXX between the kitchen and bedroom levels, as shown in Figure 2(c). They communicated by way of the global system for mobile communications so that alerts could be received and data remotely downloaded. Data-acquisition features such as the threshold level and acquisition rate could also be changed without visiting the lighthouse.

4. Finite-element modelling of the Eddystone Lighthouse

In parallel with the field campaign, a structural model of the Eddystone Lighthouse was developed using an FE model (LUSAS v.15). Only the masonry portion of the lighthouse was modelled, fully fixed at its base, and the initial validation comprised comparisons with theory in increasing degrees of complexity: first an axisymmetric cylinder subjected to self-weight compared with theory by Timoshenko and Goodier (1951); then a hollow cantilever beam displacement subjected to a uniformly distributed load (Capurso, 1971), and a single degree of freedom triangular impulsive load on a hollow cantilever beam (Clough and Penzien, 1993). Historic drawings of the lighthouse permitted a full representation of the tower as shown in Figure 5, with a solid core up to 4 m above the cylindrical plinth and then a hollow core with a tapering wall thickness of about 3·2 m reducing to about 0·7 m. The FE model also included window openings. Mesh convergence tests determined the elements and order of interpolation and resulted in a model comprising hexahedral elements with a quadratic interpolation order and 15 188 nodes.

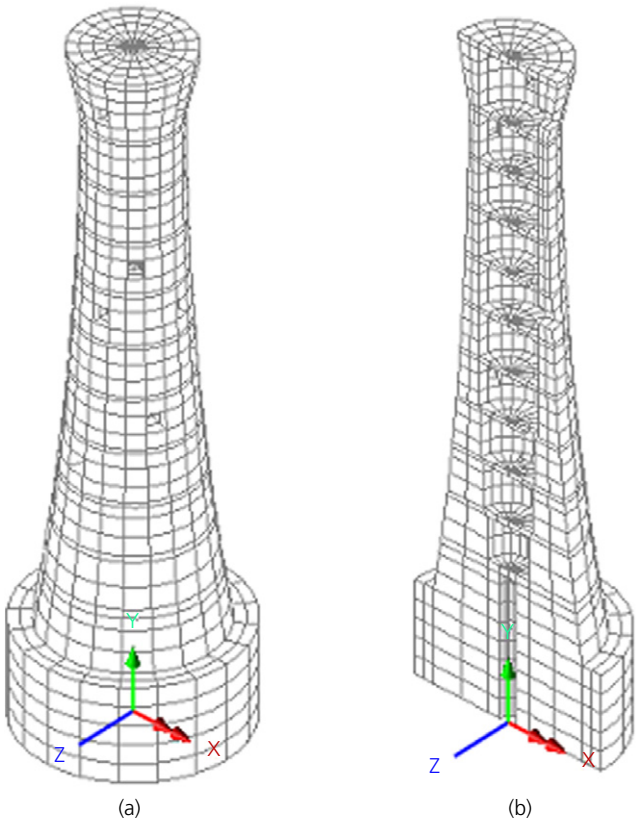

Figure 5. Finite-element model of the Eddystone Lighthouse: (a) full model and (b) symmetrical half model

According to Majdalany (1959), the lighthouse was built with granite from the quarries of De Lank in Cornwall and Dalbeattie in Scotland. Young's modulus values for those quarries was obtained as 32 GPa and 40 GPa, respectively, and without further information on which of the blocks was used where, a mean value of 36 GPa was used. Finally, the mass density of the blocks was assumed to be 2640 kg/m^3, the elastic tangent modulus 15 GPa and the Poisson ratio 0·2.

The full model of the tower provided vibration mode information. Deflections were also obtained by applying load curves to the nodes, as described in Section 5.3.

5. Results

Beginning a few days before Christmas 2013, the southwest of England experienced a sequence of 12 discrete storms resulting in the stormiest weather for 52 years (Owens, 2014). Key storm dates going back to October 2013 are shown in Figure 6 with further information in Figure 1. On 5 February 2014 the CCO wave buoy at Penzance (CCO, 2014) recorded a 21 m wave in the range of the 1 in 50 year wave given by Draper (1991). However, this was later identified as a data spike sometimes observed in high, steep seas when waves are breaking onto the buoy. Figure 6, which presents H_s data from the E1 data buoy, gives a maximum H_s value of about 6·5 m for 5 February.

5.1 Observations by lighthouse personnel

Automation of lighthouses began in the 1980s and all lighthouses are now unmanned (Trinity House, 2014). However, Trinity House engineers happened to be carrying out maintenance on both the Bishop and Wolf Rock Lighthouses on 5 February 2014. Following the tradition of the early lighthouse keepers, their observations provide useful anecdotal evidence on the structural behaviour of the towers.

On Bishop Rock, the project engineer recounted that he and his colleagues were all awoken at about 3.00 a.m. by a severe wave impact. Several more notable impacts followed through the night. The largest impact was accompanied by a loud booming noise. Then an oscillation of the tower similar to a minor earthquake was experienced – perhaps three or four cycles with a period of a few (perhaps 3 to 4) seconds.

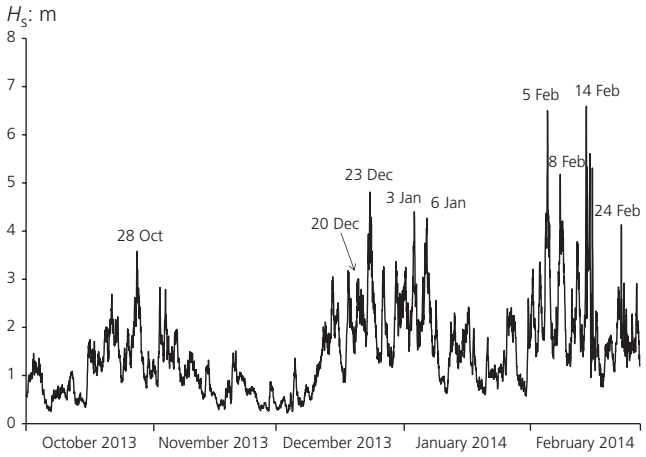

Figure 6. Hourly significant wave height from E1 data buoy with significant storms and dates indicated

A groaning noise accompanied the oscillations together with a rattling that may have been due to movement of fittings within the tower. During less extreme impacts, when the personnel were up and about, chinking of glasses in cupboards was heard and when seated the motion felt like a gentle rocking.

A lighthouse technician on Wolf Rock also awoke at 3.00 a.m. with the noise of crockery rattling on surfaces. He estimated the vibrations to have a period of around 10–15 s, although these may have been confused with the interval between successive wave impacts. The noise of the wave impacts sounded like a car being crushed – a deep rolling rumbling noise with vibrations following. A sloshing motion was set up in the 250 l water tanks situated at the top of the tower, on the level under the lantern gallery. He noted the wind speed, as measured on an anemometer, recorded gusts of more than 100 mph (160·93 km/h), although it was typically 70–88 mph (112·65–141·62 km/h). Finally, he commented that it was the worst storm he had experienced in 25 years of working on lighthouses.

5.2 Video and geophone data

Although the Met Office (2013) placed the St Jude storm of 28 October 2013 within the ten most severe autumn storms in southern England during the last 40 years, with wind gusting up to 99 mph (159·33 km/h) at the Needles on the Isle of Wight, the geophones on the Eddystone Lighthouse failed to register any structural response. However, any doubts about the ability of the geophones to detect structural motions evaporated on 20 December 2013 when further storms came in from the Atlantic providing data for 2978 individual vibration events between then and 14 March 2014. Looking back at Figure 6, it is evident that the significant wave height on 28 October only reached about 2·5 m. The fact that the storm was a fast-moving depression that passed through during low tide probably explains the discrepancy between the strength of the wind and the size of the waves and hence the lack of registered impacts on the lighthouse. This is confirmed by the impact data, which suggest that impacts occur when the significant wave height exceeds 2 m for more than 6–12 h and particularly when large waves coincide with high tide.

Figure 7 shows a histogram of the maximum velocities measured by the geophone during each of the 2978 events. A broken vertical axis is used due to the fact that events are very heavily weighted to smaller events in the first bins. In fact only 14 events caused the maximum velocity to exceed 4 mm/s (eight at 4–5 mm/s; four at 5–6 mm/s and two greater than 6 mm/s) with the two largest occurring overnight when no video information was available. Even when video information was available, there was no way of using it to determine accurately the characteristics of the wave that caused each event. Consequently, the significant wave height and direction in the

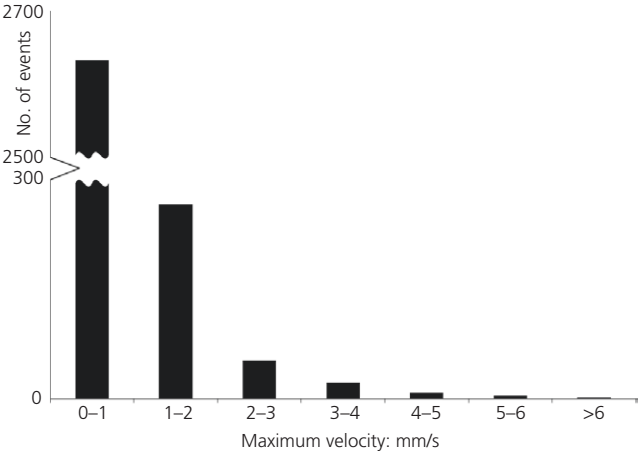

Figure 7. Histogram of the maximum velocity values measured by the geophone

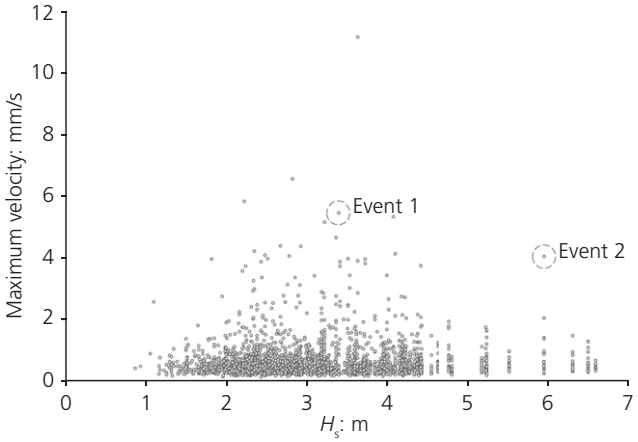

Figure 8. The relationship between maximum velocity and significant wave height

vicinity of the Eddystone reef were assumed to be the same as the hourly estimates available from the E1 buoy and these values were used for most of the subsequent analysis.

The relationship between velocity and significant wave height shown in Figure 8 indicates that there was no clear correlation between these variables. To explain this it is necessary to consider the influence of factors such as the surrounding bathymetry, the local depth of water, the direction of wave approach and characteristics of the waves that ultimately reached the tower.

The local bathymetry was determined by means of a multibeam sonar survey in the summer of 2013 (McAuley, 2013). This confirmed the irregular structure of the reef that climbs steeply from a depth of about 50 m, with some submerged slopes as steep as 1:3 along the southwesterly transect. The water level around the Eddystone reef also varies widely due to the influence of tides, the atmospheric conditions and the presence of swell. In this environment, the size and nature of the waves that reach the lighthouse are determined by a complex interaction of processes such as shoaling, refraction, reflection and breaking. All of the waves that both caused a vibration event and were recorded clearly on video had already broken to some extent before their impact on the tower. Given that the sooner a wave breaks the longer it has to dissipate energy and momentum, it was not surprising to find that the maximum velocities recorded by the geophone tended to increase with the estimated depth of water at the base of the tower, the greater depth tending to delay breaking. Conversely, increasing height and steepness cause waves to break earlier. The bathymetry also had a strong influence on the ability of waves from a particular direction to reach the tower, with analysis showing that the largest tower responses were due to waves approaching from bearings between 220° and 244°, as measured at the E1 buoy.

	Event 1	Event 2
Date	6 January 2014	5 February 2014
Significant wave height, H_s	3·38 m	5·95 m
Maximum wave height, H_{max}	9·02 m	15·14 m
Peak period, T_p	11·8 s	13·3 s
Water depth at base of structure	4·52 m	6·04 m
Wave direction	240°	233°

Table 3. Wave and depth parameters for events 1 and 2

To shed more light on the wave impacts and structural response, two particular events for which video data exist will now be analysed in more detail. The events are identified in Figure 8 and the prevailing sea conditions are listed in Table 3.

In event 1 an impact was registered even though the wave was of relatively modest size and celerity. Lack of height enabled the wave to break very close to the tower, which it hit fairly low down and with considerable intensity. As can be seen from Figure 9(a), the impact created a great deal of white water at the base of the tower but very little run-up. In fact, were it not for the large structural response measured it would not appear to be a significant impact.

In event 2 a much larger wave with a greater estimated celerity broke about 30 m from the tower, thereby creating a much more dispersed impact zone. Figure 9(b) shows the dramatic way in which water rises quickly up the tower to the level of the photovoltaic panels some 40 m above the structure's cylindrical base. The velocity of the run-up can be estimated by use of the grid described in Section 3.1 to estimate the run-up levels in sequential video frames (not all shown in Figure 9 (b)). This gives a maximum of about 50 m/s at 16 m above the cylindrical base (10 m above the impact zone), reducing to 35 m/s at an elevation of about 23 m above the base. Above this level the camera's view was obscured by the photovoltaic panels, but the rapid deceleration of the jet between the two locations suggests that it would probably have travelled only a little further. At the time of this event, the water near the tower was about 6 m deep which, on the basis of shallow water wave theory, suggests that the wave celerity prior to impact was around 7·7 m/s. Use of the latter value together with the guidance in Eurotop (Pullen *et al.*, 2007) enables the vertical velocity of the jet produced when an impulsive wave hits a vertical wall to be estimated. The resultant range of 39–54 m/s is compatible with the experimental estimate of 50 m/s.

Figure 10 shows the temporal variation in the velocity of motion along the principal axis of vibration for events 1 and 2, as recorded by one of the geophones (the other produced virtually identical data). The maximum velocities are about 5·5 mm/s and 4 mm/s, respectively. The response for event 1, although it was initially the larger of the two, dies down within one data capture window, whereas the response for event 2 was still sufficiently large at the end of the data capture window to trigger further signal acquisition. The reason for this is evident when the displacements are considered, as seen in Figure 11. The displacement time histories clearly show that event 2 is responsible for a significantly larger displacement of 0·069 mm when compared with 0·033 mm for event 1, so its vibration

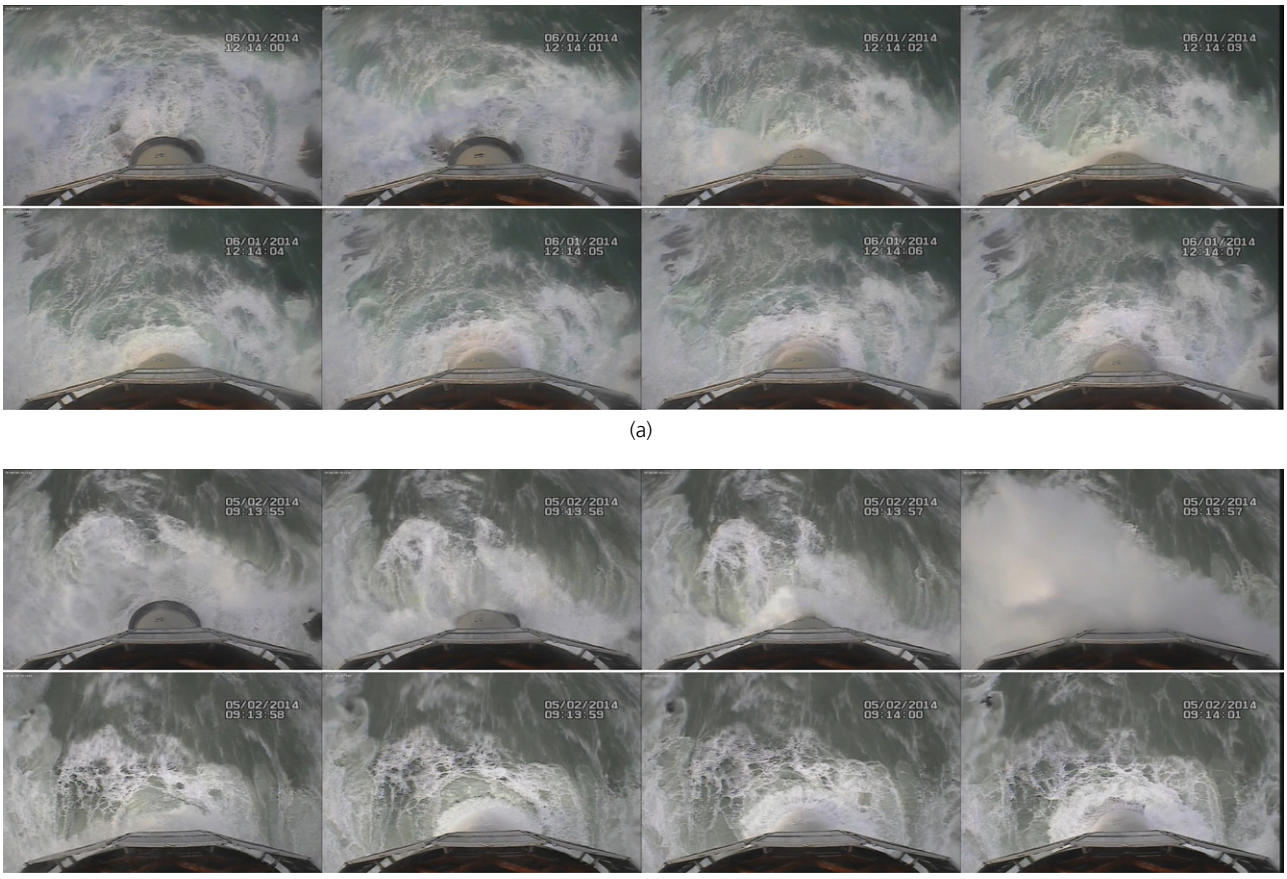

Figure 9. Time sequence of impacts: (a) event 1 against the base of the tower and (b) event 2 impact and subsequent run-up on the tower

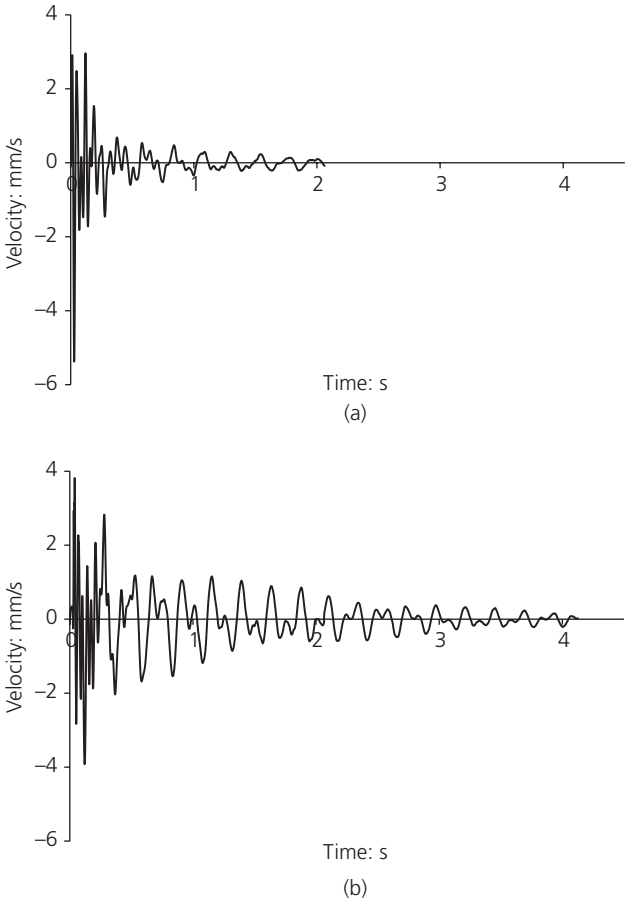

Figure 10. Geophone sensor no. 1 principal axis velocity time history for: (a) event 1 and (b) event 2

motion would indeed be expected to persist for longer assuming that structural damping is similar along the two principal axes.

Linking the angle of vibration to the direction of wave approach as measured at the E1 buoy, data obtained from the principal axis analysis indicate that for event 1 the impact had a bearing of 239°, which is in close agreement with the 240° obtained for the wave direction from the E1 buoy. In event 2, the bearing of the impact is almost due southwest at 223°, which is a little further from the buoy wave data angle of 233°. This difference is likely to be due to refraction effects around the reef.

Further information can be obtained from the amplitude spectra of the displacements. Figure 12 indicates that there are clear peaks in the spectra corresponding to vibration modes of the structure at 4·4 Hz, 8·2 Hz and 15·3 Hz. Event 2 was the more energetic, which is consistent with the motion persisting for longer. However, the vibration at around 15 Hz was more significant in event 1 than in event 2, possibly due to the magnitude and elevation of the impact exciting this mode.

Finally, the event 1 wave delivered a much cleaner impact to the structure than the event 2 wave. Most of the event 1 impulse seems to have occurred within the first ~0·1 s, whereas the event 2 impulse was probably significant for at least twice as long. The different vibration signatures due to these breaking and broken wave examples are entirely consistent with findings from large-scale (1:4) laboratory tests (Bullock *et al.*, 2007), in which broken waves were demonstrated to cause much longer duration impacts than those of breaking waves, and their spatial extent was also much greater.

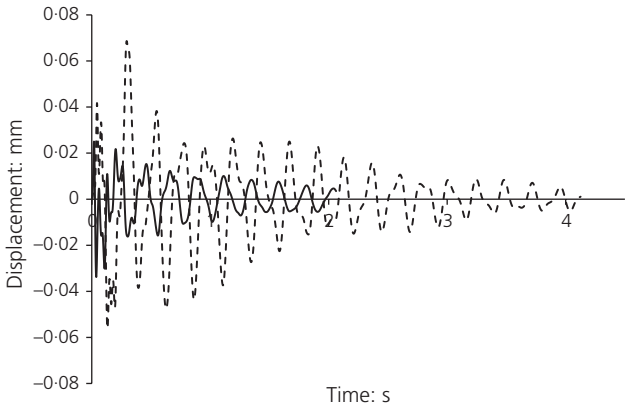

Figure 11. Displacements along the respective principal axes for event 1 (—) and event 2 (- -)

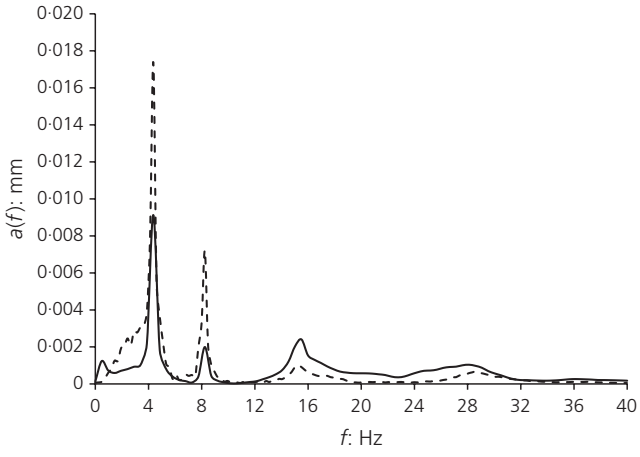

Figure 12. Amplitude spectra of the geophone displacement for event 1 (—) and event 2 (- -)

5.3 Finite-element model results

A modal analysis was undertaken using the FE model with the first mode of the tower initially predicted to be 4·7 Hz, 0·3 Hz higher than the value shown in Figure 12. Agreement between the FE model and the field data was achieved by decreasing the Young's modulus from the initial mean estimate of 36 GPa to 34 GPa. Subsequently, it was discovered that Douglass (1883) made mention of the fact that the Dalbeattie blocks were used to complete the solid portion of the tower, while De Lank blocks were used for the whole of the remainder of the tower, providing further justification for choosing a Young's modulus closer to 32 GPa than 40 GPa. The FE model did not exhibit any response near 8·2 Hz, although there was a strong response at 15·2 Hz, which is in good agreement with the field value of 15·5 Hz. The reason for the absence of any response at 8 Hz is currently being investigated, but it may be due to the fact that the lighthouse was modelled as a monolithic structure rather than one comprising mortared blocks. It might also be the case that the geophones are picking up vibrational responses of the complex reef–structure interaction or helideck not considered in the FE analysis.

The effect of wave loading on the tower was investigated by simulating the loading in two phases. The initial phase concerned the impact and was based on the work of Wienke and Oumeraci (2005), which has been incorporated in the international standard 'Actions from wave and currents on coastal structures' (ISO/CD 21650 (ISO, 2007)). This was followed by the application of drag and inertia forces for a wave interacting with a cylinder as described by the Morison equation (Morison *et al*., 1950). The spatial distribution of loads in the azimuthal direction was described by Wienke and Oumeraci (2005) and a qualitative vertical distribution was based on the work of Kyte and Tørum (1996). Wave parameters used in the formulae were based on the buoy data and typical wave breaking characteristics. Initial tests (Cali, 2014) produced deflections several times greater than those measured in the field, not unsurprising given the difficulty in specifying the characteristics of a particular breaking wave. The most recent results, using a finer mesh with more precise wave loading locations, are showing very good agreement with the geophone results: the maximum displacement is still over-estimated (by about two) but the subsequent oscillations closely match the field data.

An initial stability analysis has also been undertaken with the FE model, based on material failure and overturning collapse. As would be expected, the results indicated that the design of this tower was well within safe limits for that particular wave.

6. Conclusions and further work

Occupants of exposed lighthouses during a severe storm report the experience in much the same way now as their forbears did. Similarly, investigators seeking data from these hostile environments still face challenges, although the issues are now ones of data storage and transmission rather than the hazards faced by a lighthouse keeper clambering over rocks to recover each maximum pressure reading. However, despite the lack of electronics, Stevenson's archived data from the marine dynamometer list values that are comparable to some recent field values (Bullock *et al*., 2007). Significant advances have been made and modern instrumentation enables subjective impressions of structural motion to be complemented by detailed measurements.

Even for the largest wave impacts measured during the 2013/2014 storms, the geophone readings taken in the Eddystone Lighthouse indicate that the motion of the tower was smaller than might have been expected after reading the reports mentioned in Sections 2.1.2 and 5.1. Possibly, the current Eddystone Lighthouse responds less than the others. Conversely, while the cylindrical base of the lighthouse may reduce the wave run-up (Douglass, 1883), video data show that it does not prevent water from jetting up to around the level of the photovoltaic panels (where the cameras become submerged) and possibly even obscuring the light. The speed of the highest run-up recorded was well described by recent impulsive jet velocity guidance (Pullen *et al*., 2007).

Field data have shown the structural response of the lighthouse to be sensitive to the precise nature of the wave loading. An FE model of the tower has been developed and successfully tuned to the first and third modes of vibration measured in the full-scale structure, although the second mode is missing, possibly due to the model being represented as a monolithic structure or because the geophones are picking up the vibrations of the reef or helideck. Attempts to reproduce an example of the full-scale response to wave loading, by the application of empirical formulae adopted in the relevant international standards, have resulted in a slight over-prediction of the displacement. Revised loads based on both physical model tests in the Coastal, Ocean and Sediment Transport laboratory at Plymouth University and a computational study using OpenFoam are currently being determined. The FE model also confirmed the stability of the tower to the wave tested. The stability is further corroborated by the lack of any visible impairment of the structure over the passage of time.

Other ongoing work includes fitting lenses with a smaller field of view to the cameras on the Eddystone to improve the resolution of the waves against the tower; the addition of two further geophones systems at different elevations giving more detailed information on the vibration modes, and the placement of a lower frequency geophone on the more exposed Longships Lighthouse to compare with the Eddystone responses. This multifaceted approach will give further insight

into event-based structural response and be the next step towards providing a means to identify structures at risk.

Acknowledgements

The authors would like to acknowledge the support of the General Lighthouse Authorities, particularly Martin Bransby and Ron Blakeley (ex-Trinity House) and their lighthouse engineers who assisted with deployments on station; Peter Ganderton and Tony Tapp of Plymouth University who designed much of the installed equipment; the School of Marine Science and Engineering who funded Davide Banfi's studentship; Professors Bernardino Chiaia and Mauro Corrado from Politecnico di Torino who co-supervised Federico Cali's MSc dissertation; and Mr Gwyn Jones who organised the Eddystone reef survey, supervising Paul McAuley's MSc dissertation at Plymouth University.

REFERENCES

Bagnold RA (1939) Interim report on wave-pressure research. *Journal of the Institution of Civil Engineers* **12(7)**: 202–226.

Bathhurst B (2005) *The Lighthouse Stevensons*. Harper Perennial, London, UK.

Bird PAD, Crawford AR, Hewson PJ and Bullock GN (1998) An instrument for field measurement of wave impact pressures and seawater aeration. *Coastal Engineering* **35(1–2)**: 103–122.

Blenkinsopp CE and Chaplin JR (2011) Void fraction measurements and scale effects in breaking waves in freshwater and seawater. *Coastal Engineering* **58(5)**: 417–428.

Bredmose H, Skourup J, Hansen EA *et al.* (2006) Numerical reproduction of extreme wave loads on a gravity wind turbine foundation. In *25th International Conference on Offshore Mechanics and Arctic Engineering (OMAE2006). Volume 1: Offshore Technology; Offshore Wind Energy; Ocean Research Technology; LNG Specialty Symposium*. American Society of Mechanical Engineers (ASME), New York, NY, USA, pp. 279–287.

Bredmose H, Peregrine DH and Bullock GN (2009) Violent breaking wave impacts. Part 2: modelling the effect of air. *Journal of Fluid Mechanics* **641**: 389–430.

Bredmose H, Bullock GN and Hogg AJ (2015) Violent breaking wave impacts. Part 3. Effects of scale and aeration. *Journal of Fluid Mechanics* **765**: 82–113.

Bullock G and Bredmose H (2010) Breaking wave impacts on coastal structures. *Proceedings of the 5th Annual Conference on Advances in Computing and Technology*, University of East London, London, UK, pp. 17–26.

Bullock GN, Crawford AR, Hewson PJ, Walkden MJA and Bird PAD (2001) The influence of air and scale on wave impact pressures. *Coastal Engineering* **42(4)**: 291–312.

Bullock GN, Obhrai C, Peregrine DH and Bredmose H (2007) Violent breaking wave impacts. Part 1: results from large-scale regular wave tests on vertical and sloping walls. *Coastal Engineering* **54(8)**: 602–614.

Cali F (2014) *Finite Element Model of the Eddystone Lighthouse*. MSc dissertation, Plymouth University, Plymouth, UK.

Capurso M (1971) *Lezioni di Scienza delle Costruzioni*. Pitagora, Bologna, Italy, pp. 402–417 (in Italian).

CCO (Channel Coastal Observatory) (2014) *Regional Coastal Monitoring Programmes*. CCO, Penzance, UK. See http://www.channelcoast.org/data_management/real_time_data/charts/?chart=75 (accessed 11/07/2014).

Chan E, Cheong H and Tan B (1995) Laboratory study of plunging wave impacts on vertical cylinders. *Coastal Engineering* **25(1–2)**: 87–107.

Clough RW and Penzien J (1993) *Dynamics of Structures*, 2nd edn. McGraw-Hill, Inc, New York, NY, USA.

De Vos L, Frigaard P and De Rouck J (2007) Wave run-up on cylindrical and cone shaped foundations for offshore wind turbines. *Coastal Engineering* **54(1)**: 17–29.

Douglass JN (1878) Note on the Eddystone Lighthouse. *Minutes of the Proceedings of the Institution of Civil Engineers* **53(Part 3)**: 247–248.

Douglass WT (1883) The new Eddystone Lighthouse. *Minutes of the Proceedings of the Institution of Civil Engineers* **75(Part 1)**: 20–60.

Draper L (1991) *Wave Climate Atlas of the British Isles*. HMSO, London, UK.

Goda Y (2010) *Random Seas and the Design of Maritime Structures*, 3rd edn. World Scientific, London, UK.

ISO (2007) ISO 21650:2007: Actions from waves and currents on coastal structures. International Organization for Standardization, Geneva, Switzerland.

Kyte A and Tørum A (1996) Wave forces on vertical cylinders upon shoals. *Coastal Engineering* **27(3–4)**: 263–286.

Lykke Andersen T, Frigaard P, Damsgaard ML and De Vos L (2011) Wave run up on slender piles in design conditions – model tests and design rules for offshore wind. *Coastal Engineering* **58(4)**: 281–289.

Majdalany F (1959) *The Red Rocks of Eddystone*. Longmans, London, UK.

Mase H, Kosho K and Nagahashi S (2001) Wave runup of random waves on a small circular pier on a sloping seabed. *Journal of Waterway, Port, Coastal and Ocean Engineering* **127(4)**: 192–199.

McAuley P (2013) *Investigation into the Bathymetry of the Eddystone Reef for Use in Modelling Wave Loading at the Base of the Lighthouse*. MSc dissertation, Plymouth University, Plymouth, UK.

Met Office (2013) *Autumn Storm, October 2013*. Met Office, Exeter, UK. See http://www.metoffice.gov.uk/climate/uk/interesting/2013-octwind (accessed 17/07/2014).

Morison JR, O'Brien MP, Johnson JW and Schaaf SA (1950) The force exerted by surface waves on piles. *Petroleum Transactions (American Institute of Mining Engineers)* **189**: 149–154, http://dx.doi.org/10.2118/950149-G.

Oumeraci H (1994) Review and analysis of vertical breakwater failures – lessons learned. *Coastal Engineering* **22(1–2)**: 3–29.

Owens D (2014) Cornwall winter events 2013/14. *ICE South West: Coastal Defences Meeting the Challenge. New Continental Hotel, Plymouth*, 4 April.

Planning Portal (2010) *PPS25: Planning Policy Statement 25: Development and Flood Risk*. See http://www.planningportal.gov.uk/planning/planningpolicyandlegislation/previousenglishpolicy/ppgpps/pps25 (accessed 15/09/2015).

Pullen T, Allsop NWH, Bruce T *et al.* (2007) *EurOtop: Wave Overtopping of Sea Defences and Related Structures: Assessment Manual*. HR Wallingford, Wallingford, UK. See http://www.overtopping-manual.com (accessed 15/09/2015).

Stevenson A (1848) *Account of the Skerryvore Lighthouse with Notes on the Illumination of Lighthouses*. Adam and Charles Black, Edinburgh, UK.

Stevenson R (1824) *An Account of the Bell Rock Light-House Including the Erection and Peculiar Structure of that Edifice*. Archibald Constable & Co, Edinburgh, UK.

Timoshenko SP and Goodier JN (1951) *Theory of Elasticity*, 2nd edn. MacGraw Hill Inc, Tokyo, Japan.

Trinity House (2014) *Lighthouses*. Trinity House, London, UK. See http://www.trinityhouse.co.uk/mariner_info/aids_to_navigation/lighthouses.html (accessed 09/01/2015).

Trinity House (2015) *Eddystone*. Trinity House, London, UK. See http://www.trinityhouse.co.uk/lighthouses/lighthouse_list/eddystone.html (accessed 27/05/2015).

Wienke J and Oumeraci H (2005) Breaking wave impact force on a vertical and inclined slender pile – theoretical and large scale model investigations. *Coastal Engineering* **52(1)**: 435–462.

Winstanley H (1699) *Eddystone Lighthouse, Narrative of the Building*. HM Treasury, London, UK, Calendar of Treasury Papers, 1702–7.

Modelling the Eddystone Lighthouse response to wave loading

Q. Trinh, A. Raby, D. Banfi, M. Corrado, B. Chiaia, Y. Rafiq and F. Cali

Electronic version of an article published in Engineering Structures, 2016, V.125: p.566-578.

Engineering Structures 125 (2016) 566–578

Contents lists available at ScienceDirect

Engineering Structures

journal homepage: www.elsevier.com/locate/engstruct

Modelling the Eddystone Lighthouse response to wave loading

Quang Trinh [a,1], Alison Raby [a,*], Davide Banfi [a], Mauro Corrado [b,2], Bernardino Chiaia [b], Yaqub Rafiq [a], Federico Cali [a,1]

[a] School of Marine Science and Engineering, Plymouth University, Plymouth PL4 8AA, Devon, UK
[b] Politecnico di Torino, Corso Duca degli Abruzzi 24, 10129 Torino, Italy

ARTICLE INFO

Article history:
Received 21 December 2015
Revised 13 May 2016
Accepted 20 June 2016
Available online 4 August 2016

Keywords:
Finite element analysis
Structural response
Wave loading

ABSTRACT

The Eddystone Lighthouse is an imposing granite structure that has guided mariners through the treacherous waters off the Plymouth coast for nearly 150 years. The General Lighthouse Authorities (GLAs) of the UK and Ireland, recognising the continuing importance of rock-mounted lighthouses as physical aids for navigation, funded a pilot project, commissioning Plymouth University to monitor the tower. The present study aims to provide more information on the structural behaviour of the Eddystone Lighthouse under the impacts from wave loading, through the utilisation of a 3D finite element model. Data from geophones, an offshore wave buoy and video cameras installed on the tower have been used to calibrate and validate the model; in particular, the wave that caused the maximum displacement during the winter 2013/2014 storms has been considered. The point of application of the wave load is important in the tower's structural response; the lighthouse being especially vulnerable to larger displacements when the wave acts above its cylindrical base. Finite element analysis suggests that the lighthouse is stable with regard to material failure, and for failure mechanisms of overturning and sliding there are factors of safety of 6.3 and 8.0 respectively. A hypothetical unbroken wave of 17.5 m height would be required to overturn the lighthouse, and one of height 17 m would cause cracking at the base, but in such a location these waves would not be possible.

1. Introduction

The magnificent granite Eddystone Lighthouse is a structure of incalculable cultural importance. Taking its name from the Eddystone Rocks on which it was built, a gneiss reef some 22.5 km south south-west of Plymouth in the UK, the current lighthouse is an engineering masterpiece designed by James Nicholas Douglass. The so-called Douglass Tower has withstood the forces of the Atlantic Ocean since 1882, marking the presence of these treacherous rocks. Fig. 1(a) shows the lighthouse in benign conditions alongside the stump of the preceding Smeaton's tower, the upper courses of which now stand on Plymouth Hoe. The construction of these rock lighthouses is well-described (see e.g. [1–4]) but limited observations of structural response have been provided in archive literature. The most notable accounts are by Robert Stevenson on Bell Rock lighthouse [4,5] and as reported on a number of previous Eddystone lighthouses [1,5]. While fascinating to read, at best they provide a patchy understanding of how wave impacts are related to tower motions.

Despite modern navigation technologies, such as the Global Positioning System, the UK General Lighthouse Authorities (GLAs) are committed to maintain their rock lighthouses as physical aids to navigation, because satellite systems are by no means failsafe. However, the anticipated increase induced by climate change in sea level, general storminess and in particular individual extreme wave heights could undermine the stability of these structures. In this regard, the GLAs have funded a pilot project commissioning Plymouth University to monitor the Eddystone Lighthouse; four video cameras and two geophone systems have been installed on the tower, in order to better understand its long term stability against impacting waves [5].

This paper presents the structural behaviour of the Eddystone Lighthouse through the utilisation of a Finite Element (FE) model. Other aspects of the project reported elsewhere include anecdotal observations of wave loading and structural response [5], comprehensive details of the wave hydrodynamics and a description of the wave characteristics that influence the tower motions (in preparation). To properly model the behaviour of the tower, historical

* Corresponding author.
E-mail address: alison.raby@plymouth.ac.uk (A. Raby).
[1] Former Erasmus exchange student from Politecnico di Torino, Italy.
[2] Currently based at Civil Engineering Institute, Materials Science and Engineering Institute, Ecole Polytechnique Fédérale de Lausanne (EPFL), Station 18, CH-1015 Lausanne, Switzerland.

http://dx.doi.org/10.1016/j.engstruct.2016.06.027
0141-0296/

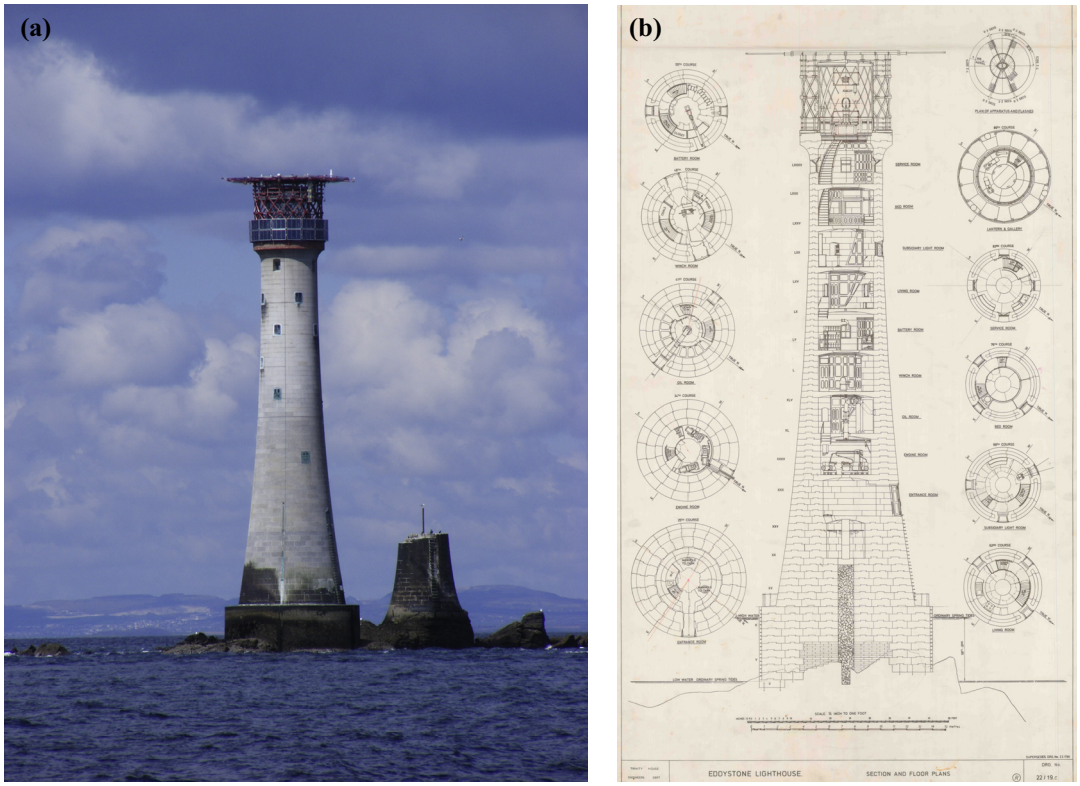

Fig. 1. Douglass Tower, the current Eddystone Lighthouse: (a) photograph alongside stump of previous Smeaton's Lighthouse (reproduced with kind permission of Helen Nance); (b) sections and floor plans (reproduced with kind permission of Trinity House).

archive drawings of the tower have been used to accurately represent its complex geometry, while data from video cameras, geophones and an offshore wave buoy were utilised to calibrate the material properties and define the wave load. The event considered is the wave that induced the highest displacement in the tower during the winter storms of 2013/2014; for England and Wales, this season saw one of the most exceptional periods of winter rainfall in at least 248 years and the stormiest weather for 52 years [6].

The steps followed in the creation of the FE model were: construction of the geometry, assignment of an adequate mesh and material properties, and the definition of boundary conditions and wave load.

2. Structure geometry

The lighthouse consists of two parts: a solid cylindrical base, 13.4 m in diameter and 6.7 m high, and a tapered tower with a maximum and minimum diameter of 10.7 m and 7.2 m respectively (Fig. 1). The 2171 blocks of granite constituting the structure were laid in less than four years, from 1878 to 1882, under the supervision of Douglass. Each block was dovetailed to the next (Fig. 2) and a liquefied mortar of cement Portland was poured to fill the remaining voids in the grooves. The blocks fitted so closely together that it is said the tower, in total tall 41.5 m and weighing 4743 tonnes, could have been built without the need for mortar [2].

Excluding a water tank built into the solid base section, the interior of the tower comprises nine different levels, with the thickness of the walls varying from 2.6 m at the bottom to 0.7 m at the top. Above these comes the lantern room, converted in 1959 to electricity formerly having used Argand burners, then paraffin lamps to provide the warning light. A helideck on top of the lantern was built in 1980, supported on a latticework of steel attached to the top courses of masonry [2].

3. Monitoring instrumentation and results

In order to monitor and better understand the structural behaviour of the Eddystone Lighthouse, Plymouth University installed the following instrumentation on the tower:

(1) Four remote-controlled, DC-powered video cameras, to record the wave conditions around the structure [5]. These were attached to the helideck structure, with the recording controlled remotely via an internet connection. Three cameras were downwards-pointing in the directions SW, NNW, ESE, while the remaining camera was angled toward the 'far-field' in the SW direction, to provide information about wave transformation across the reef. Video images were captured at a rate of 1 or 5 frames per second depending on whether wave activity was detected over the base of the tower.
(2) Two geophone systems (RDL//Vibe) to measure the structural response of the tower in the form of velocity time histories [5]. Displacements and accelerations were then obtained from the velocities through integration or differentiation respectively. The acquisition rate was either 100 Hz (around 10 s of acquisition) or 500 Hz (around 2 s of acquisition), limited by a maximum number of data points from any event.

As previously mentioned, the wave that in winter 2013/2014 caused the largest displacement of the Eddystone Lighthouse was considered; video images (Fig. 3) have been used to evaluate the distance between wave breaking and the tower and its resulting

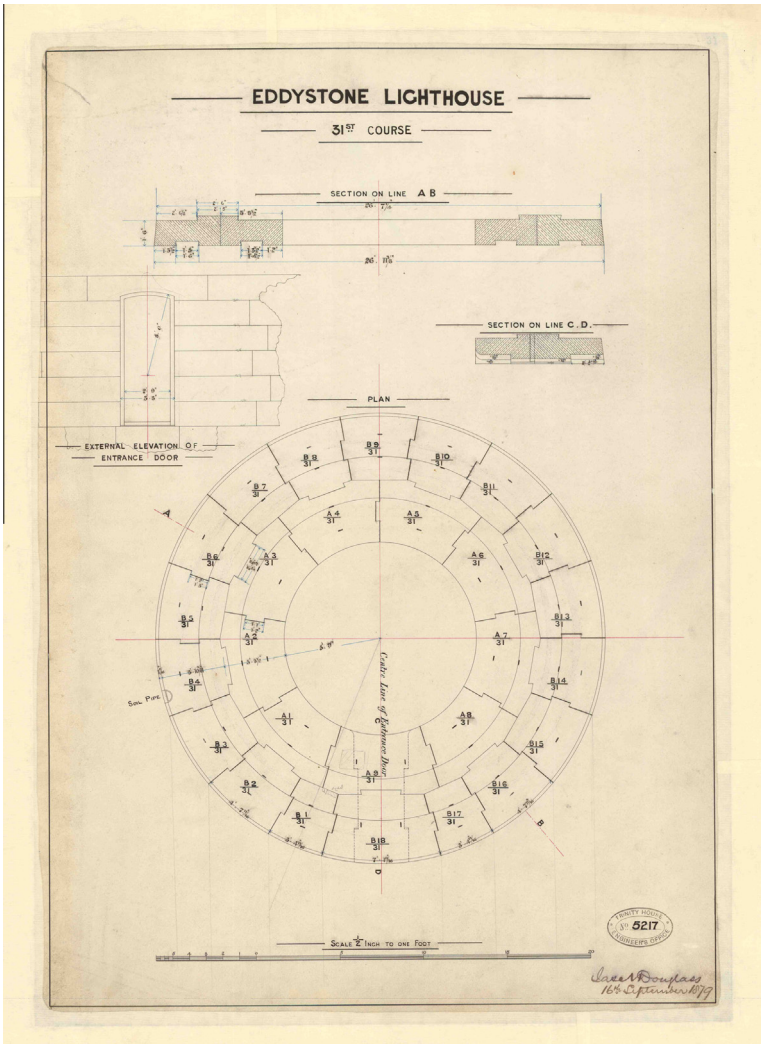

Fig. 2. Archive drawing signed by Douglass, showing plans and sections through the top of the entrance level of the Eddystone Lighthouse. Note the horizontal and vertical dovetail joints (reproduced by kind permission of Trinity House).

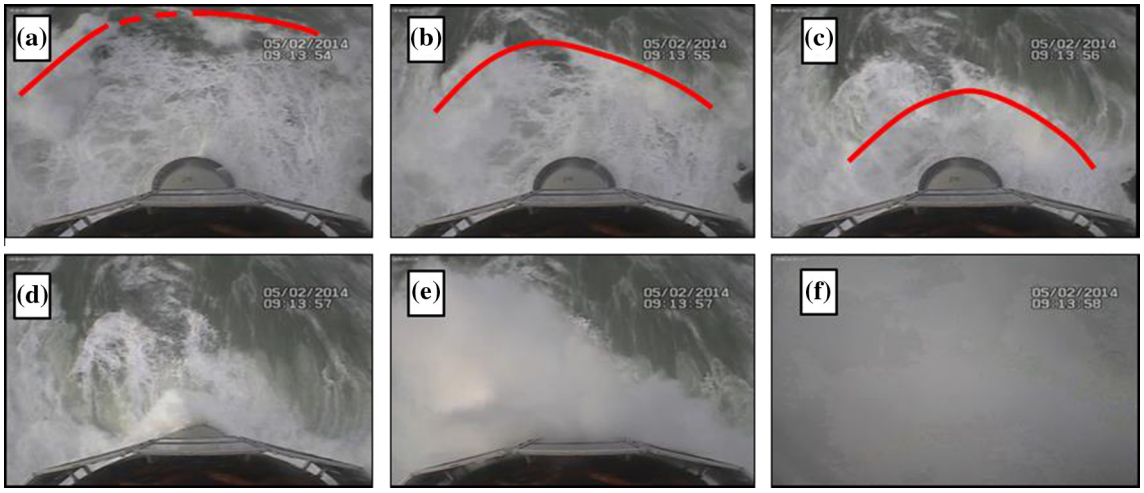

Fig. 3. Time sequence of impact at approximately 1 s intervals: (a to c) show the effect of wave refraction on the incoming wave, causing the wavefront (indicated by a red line) to become increasingly concave (and broken) as it heads into shallower water, (d) is close to the moment of impact, (e) shows the resulting wave runup the tower and spray and at (f) the spray obliterates the cameras some 41.6 m above the top of the cylindrical base. (For interpretation of the references to color in this figure legend, the reader is referred to the web version of this article.)

impact area, while the geophone displacement signals and amplitude spectra were utilised to calibrate the FE model. To this end, only the dynamic component of the displacement was considered, obtained from the total geophone signal by eliminating the quasi-static contribution through a high-pass filter with a cut-off frequency of 0.5 Hz. This operation was carried out because the quasi-static load has little influence on the overall response of the structure. The largest displacement at the geophone location (positioned at 26 m from the top of the cylindrical base) was 0.0745 mm (see Fig. 4); this low value gives an idea of the colossal stature of the tower.

Alongside video images, statistical information of the wave environment was obtained from the E1 data buoy, a Western Channel Observatory buoy operated by Plymouth Marine Laboratory, situated around 15 miles (24 km) SW of the Eddystone reef.

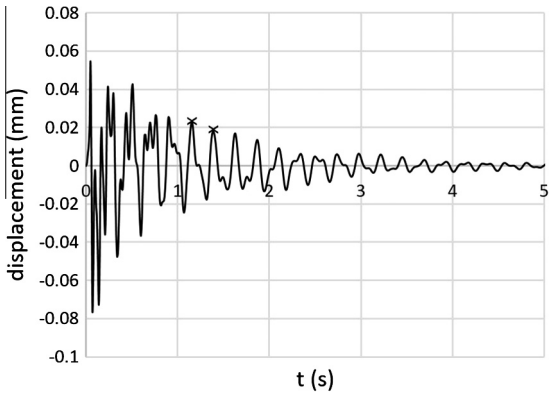

Fig. 4. Geophone displacement signal: first 5 s, with two adjacent peaks indicated by crosses to determine the damping ratio (see Section 4.3).

4. Structural model

4.1. Modelling approach

Prior to the development of an FE model, the relevant information about the structure must be gathered. This includes, for example, historical information about the materials and geometry as described by Pena et al. (2010) [7]. Information on the dynamic response of the structure can be gained from monitoring or vibration tests with accelerometers. In recent years, the recording of ambient vibration has become the conventional testing method, since no excitation equipment is needed, hence there is minimal interference with the normal use of the structure [8]. The natural frequencies of the structure can then be estimated by analysing the power spectral response obtained from the accelerometer signals [9] (or geophones as used in this study), while the modal shapes could be determined if more accelerometers/geophones are present on the structure; for example, a dominant bending mode is identifiable when all the sensors show the same harmonic [10].

Once all the necessary information has been acquired, the construction and calibration of the FE model can be carried out. There are several proprietary finite element analysis (FEA) software packages that could be used to model a structure, such as SAP2000, DIANA and LUSAS. The LUSAS package [11] has been used here since it was readily available for this pilot project. When modelling slender masonry towers, solid elements are usually implemented for the walls, while solid or shell elements can be used to model the floors [12]. With regard to the calibration of the FE model, it was limited to the definition of a fictitious roof simulating the mass of the helipad structure (since it was too onerous to model the fine details) and the assessment of the damping coefficients (see Section 4.3). For the material properties, the adopted values for the granite were based on literature that described the construction [5,14]. This was done because the origin of the construction materials was well-known and their mechanical properties are well-defined. Also, there is no evidence of damage along the structure that justifies the variation of the mechanical properties with respect to the nominal values. However, in case more uncertainties are associated with the material properties, more complex numerical techniques could be used to tune them and minimise the difference between the computational and the experimental behaviour [7–10,12]. In masonry structures, for instance, the distributions of the elastic modulus, E, and the density, ρ, are usually non-uniform, and the calibration process could require the subdivision of the structure in different zones, each characterised by a different value of E and ρ; in this case, the calibration is usually implemented with numerical strategies, such as the Inverse Eigen-Sensitivity and the Douglas-Reid (DR) methods [12,8].

4.2. Mesh assignment

In order to minimise the computational time necessary to solve the transient dynamic problem, the decision was made not to model individual dovetailed blocks, but instead to represent the Eddystone Lighthouse as a monolithic structure. Creation of the geometry was achieved by referring to the historic drawings of the tower with a slight modification of the cylindrical base from a height of 6.7 m to 5.6 m since the first 2 courses in the Eddystone Lighthouse are incomplete due to uneven bedrock levels and have therefore not been modelled. After this it was necessary to construct an appropriate mesh. The hexahedral element type was selected for this study, since the complex geometry of the tower, comprising window openings and chambers through its height, can be appropriately modelled with this choice. Moreover, the hexahedral element usually gives better results than the tetrahedral and pentahedral element types [13].

Different mesh refinements, obtained by changing the number of elements and interpolation order (linear or quadratic), were tested and compared, both in quasi-static and dynamic analyses. Then, the mesh giving the best compromise between required running time and precision was selected (Fig. 5). This mesh, formed of 1558 hexahedral elements with quadratic interpolation functions, with a total of 9944 nodes (29,832 degrees of freedom), was more refined in the zone where the impact wave was likely to act, namely between the 13th and 26th courses; this allowed the application of a more accurate wave load.

As far as the boundary conditions were concerned, the bottom surface of the lighthouse was considered as fully fixed. With reference to the original structure, this would certainly be the most obvious condition since all the blocks of granite in the lowest course were not only cemented and dovetailed to the reef, but also bolted with heavy iron bolts [2]. In today's situation, we can conservatively assume that the connection given by the bolts is no longer effective due to a deterioration of the bolts and, therefore, the shear load is transferred only by friction. In this regard, the analyses presented in Section 7 show how the base is always in compression and friction alone is able to globally resist the critical wave load. These results support the choice of a perfect bond between the base of the tower and the reef.

4.3. Model calibration through modal analysis

The Eddystone Lighthouse comprises granite from two different locations: the quarries of De Lank (Cornwall) and Dalbeattie (Scotland) [1]. The Dalbeattie blocks were used to complete the solid portion of the tower, while the De Lank blocks were used for the

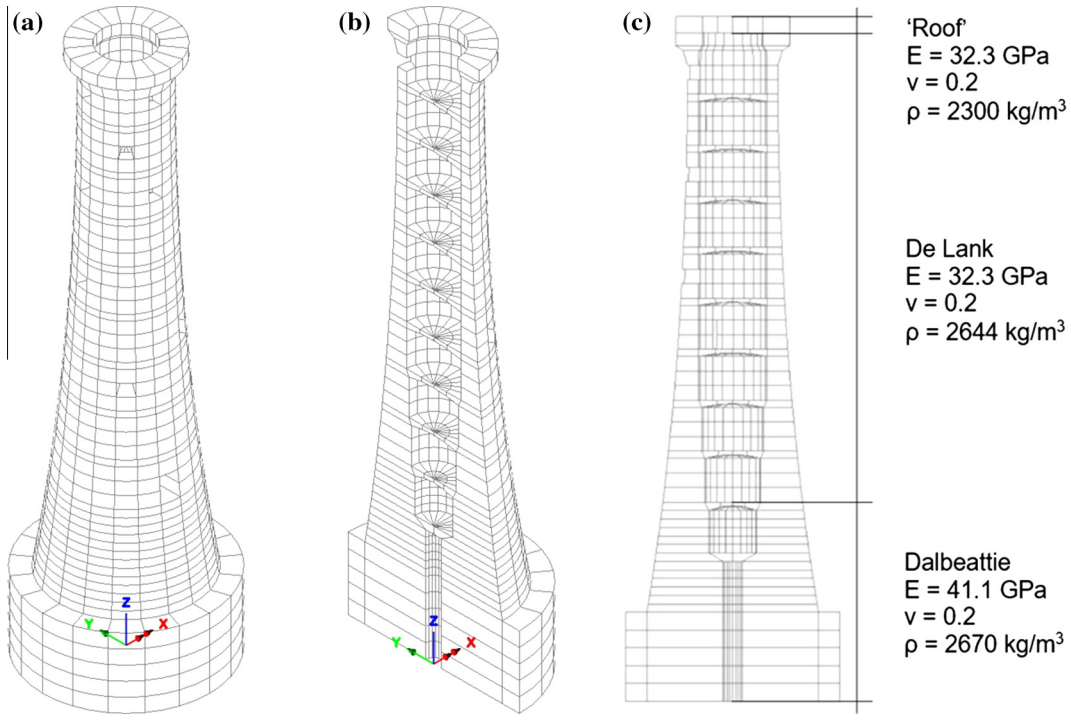

Fig. 5. Eddystone Lighthouse model: (a and b) original model and mesh (c) modified model with fictitious roof and calibrated material properties, indicating the De Lank and Dalbeattie quarry sources.

remaining part of the tower [14] as shown in Fig. 5. Their mechanical properties were obtained from Bell (1983) [15] and from the De Lank Quarry Limited (St. Breward, Nr Bodmin, Cornwall) respectively (Table 1). As these values were fixed, the calibration of the model required modelling and tuning of a fictitious roof, simulating the lantern and helipad structure (as discussed next).

From the displacement spectrum obtained from the geophones signal, the fundamental frequency of the lighthouse was determined to be 4.36 Hz. To attain a fundamental frequency similar to the one recorded by the geophones, the fictitious roof with an arbitrary thickness of 1 m was modelled upon the last course (Fig. 5), and its material properties calibrated. Given that the 'roof structure' presents numerous elements (e.g. the light and its lenses; the lantern including its roof and walkway; the helipad and its support structure; the PV panels and their support structure) there were great uncertainties in the values of the Young's modulus and density to be used. However, since the stiffness of the roof has a small influence on the overall behaviour of the tower, a value of 32.3 GPa was chosen for the Young's modulus, in continuity with the value assigned to the granite on which the roof is attached. A mass density of 2300 kg/m^3 for the roof gave an FE fundamental frequency equal to the one obtained from the geophones (i.e. 4.36 Hz). Fig. 5c shows the material properties distribution in the FE model, while Table 2 presents the first 10 modes of vibration obtained using LUSAS.

To analyse the response of the lighthouse to the wave impacts, the damping characteristics of the model had to be first determined. If the damping is assumed to be proportional (Rayleigh damping), the damping matrix, C, can be expressed as a linear combination of the mass matrix, M, and the stiffness matrix, K [16]:

$$[C] = a_0[M] + a_1[K]. \tag{1}$$

The damping ratio for the nth mode is expressed as a function of frequency, ω_n, as:

Table 1
Mechanical properties of the De Lank and Dalbeattie granites.

	De Lank granite	Dalbeattie granite
Young's modulus (E)	32.3 GPa	41.1 GPa
Density (ρ)	2644 kg/m^3	2670 kg/m^3
Compressive strength (σ_c)	219 MPa	147.8 MPa

Table 2
First 10 natural modes of vibration obtained with the LUSAS model modified with the fictitious roof.

Mode	Natural frequency, f (Hz)	Period, T (s)	Mode shape description
1	4.36	0.229	First bending Y-axis
2	4.39	0.228	First bending X-axis
3	15.17	0.066	Second bending X-axis
4	15.30	0.065	Second bending Y-axis
5	20.73	0.048	First torsional
6	29.18	0.034	First axial
7	30.66	0.033	Third bending X-axis
8	30.86	0.032	Third bending Y-axis
9	43.27	0.023	Second torsional
10	48.64	0.021	Fourth bending Y-axis

$$\zeta_n = \frac{a_0}{2}\frac{1}{\omega_n} + \frac{a_1}{2}\omega_n \tag{2}$$

where the coefficients a_0 and a_1, the mass and stiffness Rayleigh damping constants, can be determined from specific damping ratios ζ_i and ζ_j for the ith and jth modes respectively. Expressing Eq. (2) in matrix form for these two modes gives:

$$\frac{1}{2}\begin{bmatrix} 1/\omega_i & \omega_i \\ 1/\omega_j & \omega_j \end{bmatrix}\begin{pmatrix} a_0 \\ a_1 \end{pmatrix} = \begin{pmatrix} \zeta_0 \\ \zeta_1 \end{pmatrix}. \tag{3}$$

If both modes are assumed to have the same damping ratio ζ, which is reasonable based on experimental data [16], then:

$$a_0 = \zeta \frac{2\omega_i \omega_j}{\omega_i + \omega_j} \tag{4}$$

$$a_1 = \zeta \frac{2}{\omega_i + \omega_j} \tag{5}$$

and the damping matrix can be determined using Eq. (1).

The modes i and j, with specified damping ratios, should be chosen to ensure reasonable values for the damping ratios in all the modes contributing significantly to the response. In fact, the definition of ζ_n given by Eq. (2) ensures that the damping ratio of all of the modes included between modes i and j will be slightly smaller than the selected value ζ. Instead, the damping ratio of higher modes will increase monotonically with frequency, and the corresponding modal responses will be essentially eliminated from the global response of the structure.

In the absence of experimental tests, the value of the damping ratio ζ can be estimated considering the decay of the geophone displacement signal (Fig. 4). This signal represents only the dynamic component, obtained from the total by eliminating the static contribution. Considering the two adjacent peaks indicated in Fig. 4, the damping ratio can be calculated using Eq. (6) [16]:

$$\zeta = \frac{1}{\sqrt{1 + \left(\frac{2\pi}{\ln(x_0/x_1)}\right)^2}}. \tag{6}$$

With values of x_0 = 0.0215 mm and x_1 = 0.0183 mm, ζ is equal to 2.56%.

In our study, the modes that contributed significantly to the response were deemed to be modes 1–6, because the lowest peak that could be seen in the geophones' amplitude spectra corresponded to a frequency of approximately 28.5 Hz; this value is close to the sixth natural frequency of 29.18 Hz (axial mode) found from the FE analysis.

Using Eqs. (4) and (5), with $\omega_i = \omega_1 = (2\pi)/T_1 = 27.4$ rad/s and $\omega_j = \omega_6 = (2\pi)/T_6 = 183.32$ rad/s, the Rayleigh damping constants have then been estimated to be equal to $a_0 = 1.22$ rad/s and $a_1 = 2.44 \times 10^{-4}$ 1/(rad/s).

5. Wave load

5.1. Wave loading descriptions

A literature review for the present study has revealed a paucity of rock lighthouse wave loading research, though numerous laboratory studies have been conducted on cylindrical structures situated in deep water and intermediate depth, such as wind turbines and oil platforms. The presence of reefs around rock lighthouses causes incoming waves to become more nonlinear and ultimately break due to the shallow water. Also, unlike wind turbines and oil platforms, lighthouses are generally constructed above mean water. Furthermore, their geometries are almost exclusively tapered, like that of a tree trunk. However, with no other guidance available, wave loading on surface-piercing cylinders had to serve as a proxy.

The total wave load acting on a cylinder is usually expressed as the sum of a dynamic component, which acts for a very short time and can be seen as an impact load, and a quasi-static component, which varies in time in accordance with the water surface elevation associated with the wave cycle [17]. Given the complexity of the wave loading phenomena, several contrasting formulations for wave loading on cylinders have been published. For example, Goda et al. (1966) [18] and Wienke & Oumeraci (2005) [17] provide different expressions for the dynamic component, while the quasi-static component can be estimated using the methods of Morison et al. (1950) [19] or Irschik et al. (2004) [20].

In the present study, the dynamic component of the load was estimated using the theory of Wienke & Oumeraci (2005) [17] since it forms the basis of ISO 21650 'Actions from wave and currents on coastal structures' [21]. The quasi-static component was neglected, since the maximum displacement was reached approximately 0.1 s after the wave impact and hence was not influenced by the quasi-static load.

5.2. Application of wave load

The load was based on the best estimations of the wave that yielded the largest displacement as measured by the geophones. It was applied in the SW direction, corresponding to the negative y-axis of Fig. 5. The force time history of an impacting wave is represented mathematically by Eqs. (7) and (8) as two discontinuous phases, as proposed by Wienke & Oumeraci (2005) [17]:

$$F(t) = \lambda \eta_b \rho_w R V^2 \left(2\pi - 2\sqrt{\frac{V}{R}t}\ \operatorname{atanh}\sqrt{1 - \frac{1}{4}\frac{V}{R}t}\right) \quad \text{for} \quad 0 \leqslant t \leqslant \frac{1}{8}\frac{R}{V}. \tag{7}$$

$$F(t) = \lambda \eta_b \rho_w R V^2 \left(\pi\sqrt{\frac{1}{6}\frac{R}{Vt'}} - \sqrt[4]{\frac{8}{3}\frac{V}{R}t'}\ \operatorname{atanh}\sqrt{1 - \frac{V}{R}t'\sqrt{6\frac{V}{R}t'}}\right) \quad \text{for} \quad \frac{3}{32}\frac{R}{V} \leqslant t' \leqslant \frac{12}{32}\frac{R}{V} \quad \text{where } t' = t - \frac{1}{32}\frac{R}{V}. \tag{8}$$

where λ is the curling factor equal to 0.46 [9], η_b is the crest elevation with respect to the still water level, ρ_w is the water mass density, R is the average radius of the lighthouse in the impact zone, V is the water velocity, t is time within the first phase and t′ the time within the second phase.

For a typical plunging wave, V is assumed equal to the wave celerity (C). Also, recalling the typical wave breaking limit ($H_b/h_b \approx 1$, where H_b and h_b are the wave height and water depth at breaking point, respectively), Eq. (9) is obtained:

$$V = C_b = \sqrt{gh_b} \approx \sqrt{gH_b}. \tag{9}$$

The wave height at the breaking point H_b was estimated using the following method. From the E1 offshore wave buoy the significant wave height at that location $H_{S,0}$ had a value of 3.3 m and the peak wave period T_p was 16.7 s. From this information it is possible to calculate the wave steepness S_0 through Eq. (10), in which L is the wavelength and g the gravitational acceleration:

$$S_0 = \frac{H_{S,0}}{L} = \frac{H_{S,0}}{\frac{gT_p^2}{2\pi}} = 0.008. \tag{10}$$

Assuming a sea bed slope of 1/10 (realistic for that location from a bathymetry survey) and rounding up the wave steepness to $S_0 \cong 0.01$, Goda's wave height ratio to relative water depth graph (Goda, 2000 [22]) (Fig. 6) can be used to determine the maximum wave height at breaking point $H_{b,max}$. From Fig. 6, it can be estimated that $H_{b,max} = 2.45 \times H_{S,0} = 8$ m.

Table 3 lists the values used in Eqs. (7) and (8) to calculate the impact load curve for the Eddystone Lighthouse.

Then according to Eqs. (7) and (8), the total duration of the impact is $T = \frac{12}{32}\frac{R}{V} = 0.22$ s, and the maximum impact force, at t = 0, is 7007 kN. The resulting normalised load curve is shown in Fig. 7.

However, this wave load corresponds to the most critical situation, in which the wave breaks against the lighthouse [17]. This is not the case for the Eddystone Lighthouse, where video images

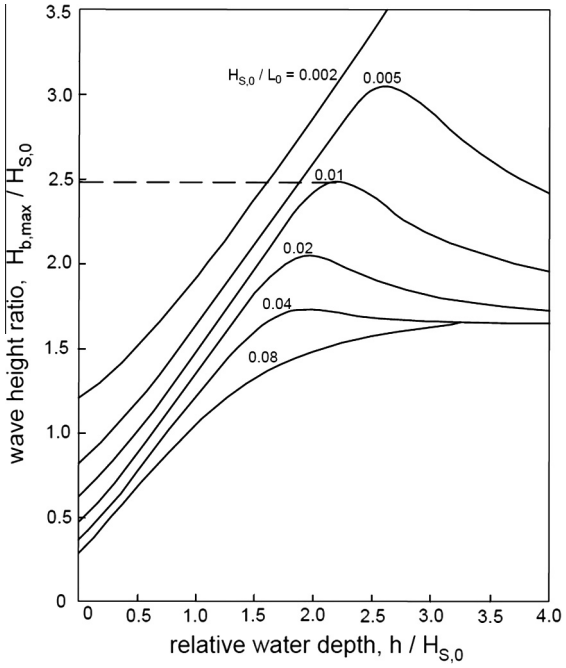

Fig. 6. Graph correlating $H_{S,0}$ with $H_{b,max}$ for Sea Bottom Slope = 1/10 (based upon Goda (2000) [22]).

Table 3
Values used to calculate the impact time history according to Wienke & Oumeraci (2005) [17].

Symbol	Definition	Value	Units
λ	Curling factor	0.46	[–]
$\eta_b = 0.78\ H_{b,max}$	Crest elevation	6.24	[m]
ρ	Water density	1025	[kg/m^3]
R	Average radius	4.83	[m]
V	Water velocity	8.86	[m/s]

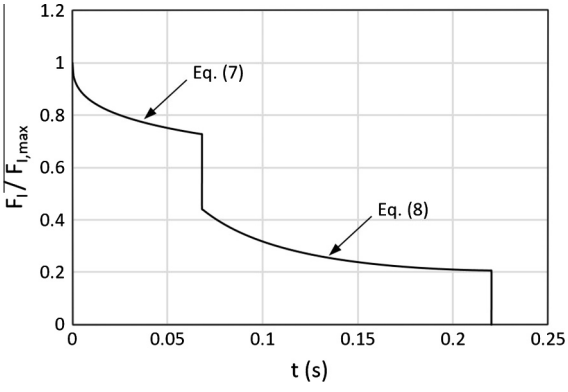

Fig. 7. Normalised load curve for the dynamic force calculated according to Wienke & Oumeraci (2005) [17].

show that for severe loads the wave breaking is roughly estimated to occur at least 20 m from the tower (Fig. 8). Irschik (2012) [23] provides experimental results that correlate the load intensity with the breaking distance of the wave from a cylinder, for a particular maximum wave height of 1.55 m (Fig. 9). The horizontal axis can be made dimensionless by dividing breaking distance, x, by H_{max} = 1.55 m. Knowing that the dimensionless breaking distance, d, for the Eddystone Lighthouse is equal to $d = x/H_{b,max}$ = 25/8 = 3.13 (−3.13 in Fig. 9 due to the axis orientation), a load

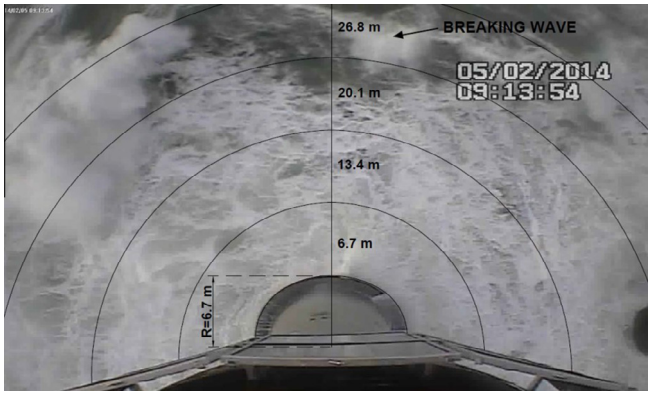

Fig. 8. Video camera image with grid showing instant of wave breaking (note that concentric circles are used for simplicity for the grid, incorrectly assuming there is no camera image distortion).

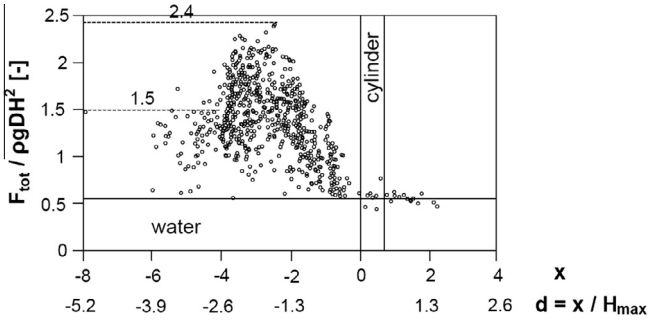

Fig. 9. Experimental results correlating wave load with breaking distance (based upon Irschik (2012) [23]).

reduction factor of 2.4/1.5 = 1.6, was assumed. This allowed a more realistic loading case to be applied, with a maximum impact force equal to 4379 kN (= 7007/1.6 kN).

The impact zone was estimated from video camera images, while the assumed load spatial distributions follow those proposed by Tanimoto et al. (1986) [24] (triangular vertical distribution) and Wienke & Oumeraci (2005) [17] (azimuthal horizontal distribution), as shown in Fig. 10. In Fig. 10, f is the impact line force (kN/m), representing the distribution of the impact force F (kN) along the height of the impact area.

Dynamic analysis has been carried out through a time step analysis, with an implicit integration time method, considering a lumped mass matrix and the damping characteristics estimated in Section 4.3. Given the impulsivity of the impact (the impact total duration is T = 0.22 s) and the fact that the peak occured in the first 0.1 s, a small time step of 0.002 s was utilised to obtain an accurate solution.

The displacement history obtained from the FE model for the point corresponding to the position of the geophone is shown in Fig. 11, where it is compared with the real displacements, obtained by integrating the velocities captured by the geophone. The comparison shows relatively poor agreement in the first 0.15 s with an FE peak amplitude in the direction of the wave impact of 0.0998 mm, 30% higher than the value derived from the geophone data (0.0745 mm). *N.B.* The wave impact is directed toward the negative y-axis. However, beyond 0.15 s the FE signal matches the geophone signal quite well in terms of amplitude and frequency, with only a modest phase shift. This gives confidence that the construction and calibration of the FE model have been performed to an acceptable degree and that the model is able to reasonably reproduce the dynamic behaviour of the actual structure.

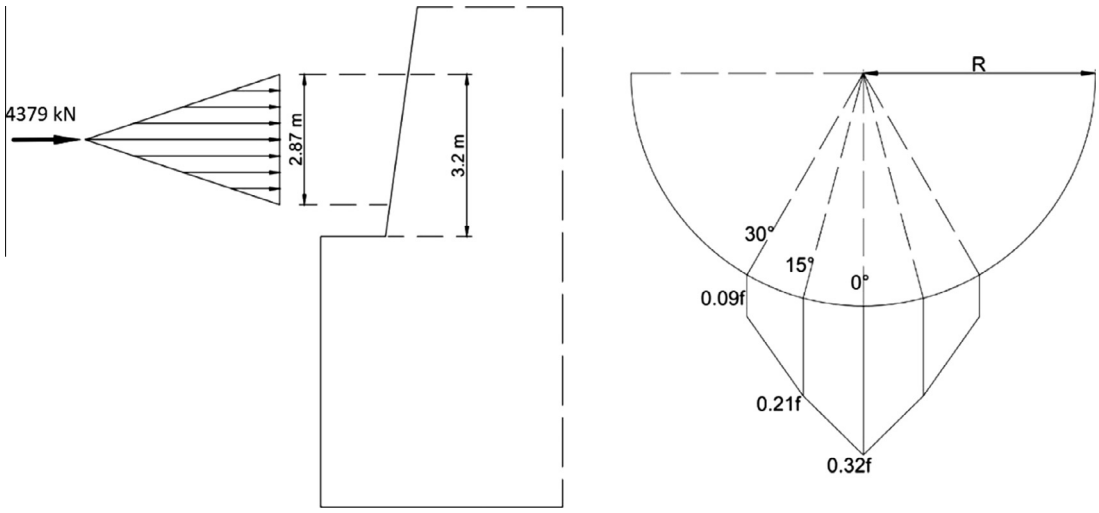

Fig. 10. Theoretical load spatial distribution: vertical distribution (left) and azimuthal distribution (right).

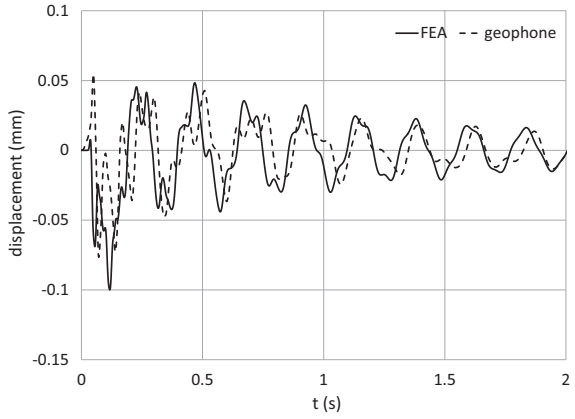

Fig. 11. Comparison between displacement histories: FEA signal (continuous) and filtered geophone signal (dashed).

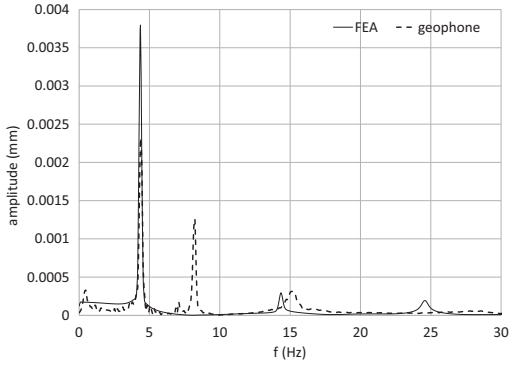

Fig. 12. Amplitude spectra of FEA (continuous) and geophone (dashed) displacements.

Fig. 12 shows the corresponding displacement amplitude spectra obtained from the FE signal and the geophone. The FE model is able to capture the natural frequencies of approximately 4 Hz, 15 Hz and 28 Hz, even though it is slightly more flexible than the actual structure, since the frequencies of the numerical analysis are lower than those obtained from the geophone. A significant difference between the two spectra is that the 8 Hz frequency is not evident from the FE analysis. There are a number of possible reasons for the absence of this vibration mode. The most likely cause is the simplistic representation of the combined helideck structure and lantern room at the top of the structure. Detailed drawings exist for these elements but their representation in this pilot study was deemed unnecessary. Another potential factor is that the reef on which the lighthouse stands was not included in the model. Certainly wave impacts on the reef will influence the lighthouse vibrations: the earlier Smeaton lighthouse was removed from the Eddystone reef because of a 'dangerous abscess' in the rock [1] with associated vibrations of the tower. The effect of the absence of mortar and the connections between the base and the reef are likely to be limited to slight changes in modal frequencies.

As a further remark, we acknowledge that the effects of temperature were not considered in the evaluation of the natural frequencies from the geophone data, since this parameter was not monitored. The natural frequencies were obtained by analysing the geophone data referred to different storm events, all of them taking place in the winter season, and then averaged without considering the temperature effect. According to the work carried out by Saisi et al. [25], the natural frequencies of a masonry structure slightly increase with temperature. Variations between 5 and 11% were evidenced for temperatures varying from −2 to 45 °C, due to the closure of superficial cracks, minor masonry discontinuities or mortar gaps induced by the thermal expansion of materials. However, compared to a masonry structure the present tower is more monolithic and less sensitive to the behaviour of the mortar joints due to the presence of the dovetail connections. Therefore, the effects of the temperature should be less relevant.

6. Wave load parametric study

The dynamic wave load defined in Section 5 was next applied to impact areas below and above the location previously considered, but with the same wave load characteristics and the same vertical and azimuthal distributions. This was carried out to better understand how the structural response of the lighthouse is influenced by the height of the impact area.

Fig. 13 shows how the maximum displacement grows with the height of the upper limit of the impact area, the height being defined relative to the bottom of the cylindrical base. When the impact load acts completely (or partly) on the base, the maximum displacement grows linearly with impact height. However a much steeper linear trend is evident beyond an elevation of 8 m, where the impact load acts completely above the base; in this case, with

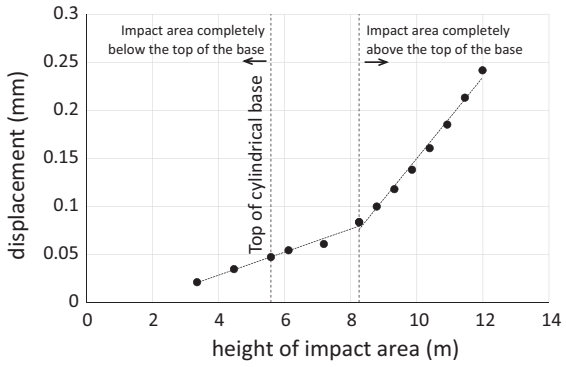

Fig. 13. Relationship between maximum displacement and height of the impact area.

an increase in the impact area height of 0.5334 m (equivalent to the height of one course of blocks) the average increment of the maximum displacement is 16%. This increased displacement is due to the fact that the base has a larger radius and can be considered to be a massive structure, which absorbs most of the impact, while the upper part is more slender and comprises openings (windows and a door) and cavities (rooms), making the tower more flexible.

This investigation shows that the structural response is highly influenced by the height at which the wave acts, which in turn depends on the tide level, on the breaking distance and on the maximum wave height $H_{b,max}$ at the breaking point.

7. Stability analysis

The stability of the lighthouse was analysed with respect to three possible failure mechanisms: material failure, overturning and sliding. The material failure was evaluated assuming that the Eddystone Lighthouse is a monolithic granite structure, while the failures due to overturning and sliding were considered with the conservative hypothesis that the original iron rods securing the base to the reef were no longer effective.

7.1. Material failure

Material failure occurs when the stress state at a point of the structure, as defined by the principal tensions, is tangential to the assumed failure domain. To obtain the stress distribution in the lighthouse, the stress due to self-weight is added to that caused by the wave impact.

The vertical normal stress distribution due to self-weight only is shown in Fig. 14; the materials remain in the elastic field, since the level of stress is everywhere smaller than the intrinsic strength. The total weight obtained from LUSAS is 51,340 kN, equal to a mass of 5233 tonnes. Removing the fictitious roof this gives a weight of 5140 tonnes, only 8% higher than the value of 4743 tonnes obtained from Nicholson (1983) [2] for the granite parts of the structure.

Applying the wave, the point subjected to the maximum vertical stress was at the base, on the same side as the impact (point A in Fig. 15), and the maximum stresses induced by the wave occur at 0.012 s from the beginning of the impact. While it should be borne in mind that the agreement in the FE and geophone time signals was fairly poor before 0.15 s, the LUSAS model over-predicts the maximum displacement and hence any findings can be regarded as conservative. Fig. 15 shows the combined vertical stress distribution in the lighthouse at 0.012 s, while Fig. 16 indicates how the application of the wave changes the vertical stress along the bottom of the base, at 0.012 s. It can be seen that all of the base remains compressed. The stress distribution concentrations at the ends are due to the fixed constraints assumed for the bottom surface of the tower. This distribution is in accordance with the analytical solution provided by Tarn et al. (2009) [26] for the case of a circular elastic cylinder under its own weight; their study showed that the 'end effect' is more pronounced when the bottom plane is perfectly bonded, in contrast to the situation in which the base is simply supported.

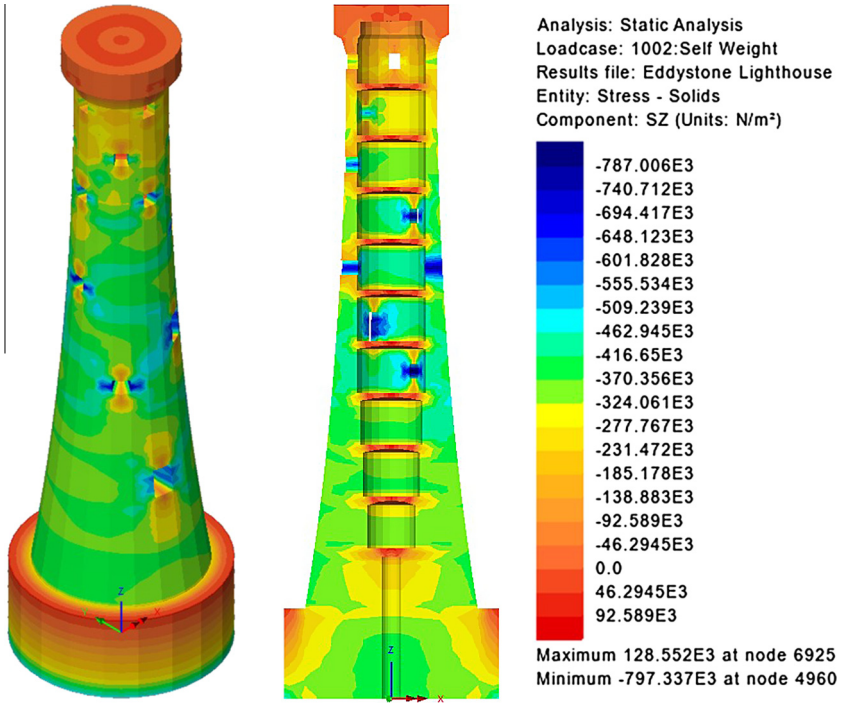

Fig. 14. Vertical normal stress distribution due to self-weight: axonometric view (left) and vertical cross section (right).

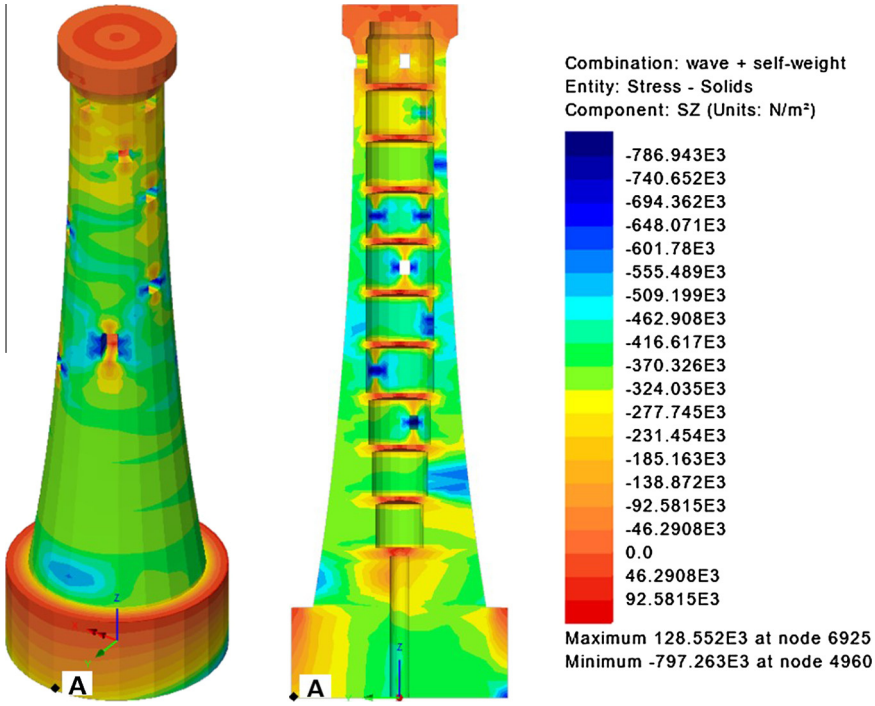

Fig. 15. Vertical stress distribution caused by combined self-weight and wave impact at 0.012 s: axonometric view (left) and vertical cross section (right).

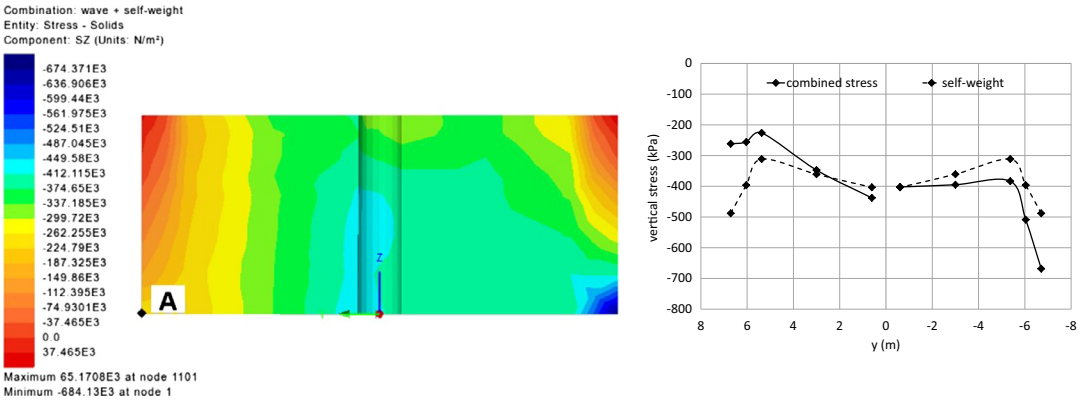

Fig. 16. Vertical stress distribution in the base caused by self-weight and wave impact at 0.012 s.

The Mohr-Coulomb failure criterion was considered in order to evaluate the material failure, since it is suitable for describing the failure of materials in which the compressive strength far exceeds the tensile strength [27]. In the Mohr diagram this criteria is represented by Eq. (11):

$$\tau = \tau_c + \sigma \tan \varnothing \tag{11}$$

where τ is the shear strength, τ_c is the shear strength in the absence of vertical compression, $\varnothing$ (°) is the angle of internal friction and σ is the vertical compression. For granites, tan $\varnothing$ is assumed to be 0.7, with $\varnothing = 35°$ [28,29]. The base of the lighthouse comprises blocks of the Dalbeattie granite with a compressive strength, $\sigma_c = 147.8$ MPa. The tensile strength can be assumed to be 40 times smaller than the compressive strength [30], therefore a value of $\sigma_t = 3.7$ MPa was considered. The shear strength, in the absence of compression, can be fixed at $\tau_c = 31$ MPa [29]. Considering these values, the failure domain was obtained by plotting Eq. (11) with the two vertical cut-offs corresponding to the tensile and compressive strengths (Fig. 17). In Fig. 17, the stress state in point A at 0.012 s is also plotted ($\sigma_1 = -281.69$ kPa, $\sigma_2 = -38.08$ kPa, $\tau_{max} = 121.8$ kPa).

It can be seen that the stress state of the point subjected to the maximum (with sign) vertical stress (point A at 0.012 s) is well inside the failure domain. The structure therefore remains in the elastic region, and the stability against material failure for the monolithic model under this particular applied load is guaranteed.

7.2. Overturning

Failure due to overturning occurs if the destabilising moment due to the wave impact is higher than the stabilising moment provided by the self-weight. The moments were calculated around the extreme point at the base, on the opposite side with respect to the impact.

The horizontal force due to the wave impact, R_{wave}, is equal to the force previously calculated using the approach of Wienke & Oumeraci (2005) [17] i.e. $F_{W\&O,reduced} = 4379$ kN, multiplied by an amplification factor taking into account the fact that the load is applied dynamically [31]. The static equivalent wave force can be assumed to be equal to the maximum reaction at the base of the lighthouse when the impact load curve is applied. From the FE

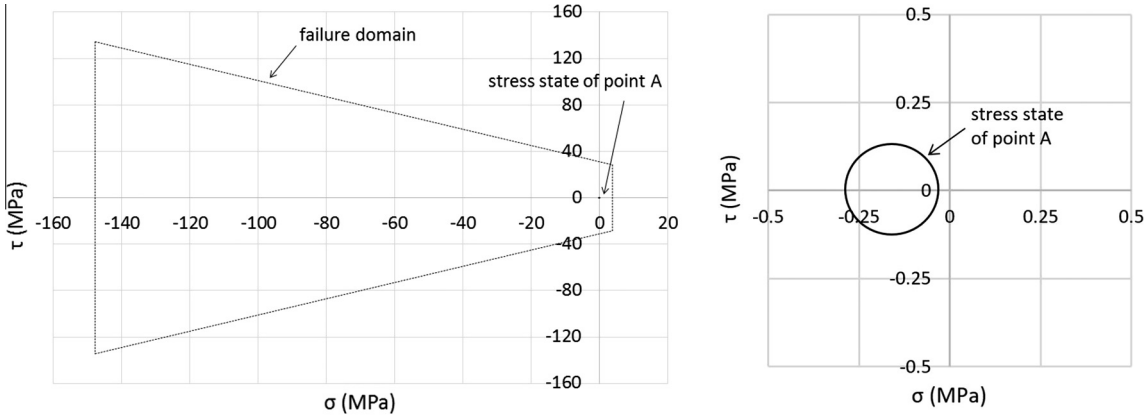

Fig. 17. Mohr-Coulomb failure criteria and stress state of point A in the Mohr diagram: full diagram (left) and zoom around the stress state of point A (right).

Fig. 18. Cracking limit: combined vertical stress in point A as a function of wave height.

simulation, a value of R_{wave} = 5674 kN was found, therefore giving a dynamic amplification factor of 5674/4379 = 1.3. The resulting force due to the self-weight, R_{weight}, was obtained from the FE model and is equal to 51,340 kN.

The moment arm of R_{wave} is equal to the height of the barycenter of the impact area with respect to the base of the lighthouse, i.e. 7.45 m, whereas the moment arm of R_{weight} is half the diameter of the base, i.e. 6.71 m. It follows that the destabilizing moment is $M_{destab} = 42.3 \times 10^3$ kN m whereas the stabilizing one is $M_{stab} = 344.5 \times 10^3$ kN m. The stability of the lighthouse against overturning under these conditions is therefore guaranteed ($M_{destab} < M_{stab}$), with a safety factor of M_{stab}/M_{destab} = 8.14.

7.3. Sliding

Sliding failure occurs when the horizontal force induced by the wave is higher than the frictional force present at the interface between the base of the lighthouse and the reef. The frictional resistant force is calculated as $R_{friction} = \mu R_N$, where μ is the friction coefficient and R_N the total normal force acting on the potential sliding surface. The friction coefficient μ was assumed to be equal to 0.7 (since the reef is composed of gneiss with similar properties to granites), while the normal force was equivalent to the resultant force due to self-weight, i.e. $R_N = R_{weight}$ = 51,340 kN.

It follows that the frictional resistance force is $R_{friction}$ = 35,938 kN, while the horizontal force induced by the wave is R_{wave} = 5674 kN, as previously calculated. The stability of the lighthouse against sliding under these conditions is therefore guaranteed ($R_{wave} < R_{friction}$), with a safety factor of $R_{friction}/R_{wave}$ = 6.33.

7.4. Critical waves

Considering the previous analyses, two critical waves can be estimated for the lighthouse: one which produces cracking (i.e. tensile forces at one extremity of the base of the lighthouse) and one that destabilizes the lighthouse (for overturning or sliding).

The cracking limit does not determine the opening of the joints between the granite blocks since they are linked together with dovetail connections. However, it may be critical for the joint between the tower base and the reef, especially in the hypothesis of full degradation of the iron bolts. The opening of this joint would permit the infiltration of water, with a consequent acceleration of

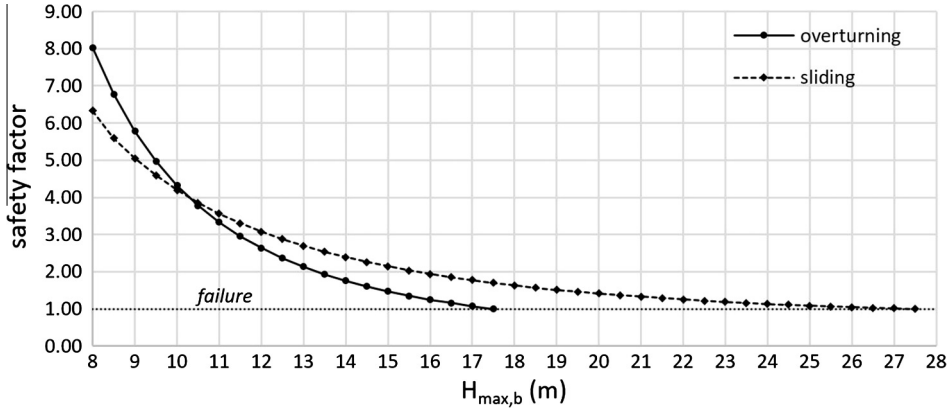

Fig. 19. Overturning and sliding: safety factor as a function of wave height.

the material deterioration. The wave that induces cracking has been estimated assuming a linear relationship between impact wave heights and induced vertical stresses (see Fig. 18, which shows the vertical stresses in point A); this assumption is reasonable, given that a linear trend was also found for induced displacements (Fig. 13). From Fig. 18, it can be deduced that the critical wave that induces tensile stresses in point A has a height of approximately 17 m.

The second, and more severe critical wave, namely the one that undermines the stability of the Eddystone Lighthouse, has been estimated using the load distributions of Wienke & Oumeraci (2005) [17], assuming the same load reduction factor estimated in Section 5.2 (i.e. 1.6). Fig. 19 shows how the safety factors for overturning and sliding decrease with increasing $H_{b,max}$. The safety factor for overturning drops faster than the one of sliding, since, with each increase in wave height, both the wave load and the moment arm increase. Overturning failure occurs for a wave height at the breaking point of 17.5 m, corresponding to an impact force of 21,141 kN and a moment arm of 16 m.

However, it must be remembered that the load reduction factor used (i.e. 1.6) has been estimated for a particular wave height of 8 m (see Section 5.2). Higher waves would break further from the lighthouse (due to depth-limited breaking as the water depth decreases dramatically around the tower) and higher load reduction factors should therefore be used. Hence, the results obtained are conservative.

8. Conclusions and further work

The aim of this study was to investigate the structural response of the Eddystone Lighthouse under wave loading, through the development of a 3D FE model. The geometry was defined from historic drawings of the tower, while the calibration required the modelling and tuning of a fictitious roof, simulating the lantern and helipad structure. The wave that caused the largest displacements in the tower in winter 2013/2014 was then applied, allowing the verification of the correct construction and calibration of the FE model. It was found that both the displacement signal and the amplitude spectra obtained from the FE model were generally similar to the ones extracted from the geophones.

On the basis of this agreement, the model has been used to evaluate the stability of the lighthouse. Considering the self-weight and the most severe wave for the loads, the tower remained comfortably safe against the three failure mechanisms analysed - material failure, overturning and sliding. A parametric study was also conducted, and the results demonstrated that the structural response of the lighthouse is highly influenced by the height at which the impact occurs. This in turn depends on the tide level, on the wave breaking distance and on the maximum wave height. Finally, it was possible to estimate that a wave of 17 m would induce cracking at the base of the lighthouse, while failure of the tower would occur for overturning with a wave of 17.5 m. However, these results, obtained with a load reduction factor of 1.6, are conservative; since the maximum water depth at the toe of the tower is 6.67 m (as deduced from a bathymetric survey), high waves break far from the structure, and higher load reduction factors should be used.

While the close similarity between the displacement signals obtained with the FE model and the geophones gives confidence in the model, as well as the correct definition of the impact wave, several improvements could be made: a more refined mesh, a more realistic distribution of the material properties, a more accurate modelling of the lantern and helipad structures, and a more precise definition of the boundary conditions and wave loads. Among these aspects, the most critical is represented by the wave load definition; the theory of Wienke & Oumeraci (2005) [17] was implemented in this study, though it was developed for cylinders and for waves breaking against the structure. The pilot study has led to a wider project research, STORMLAMP, funded by the UK Engineering and Physical Sciences Research Council. This project will assess a number of rock lighthouses using field data analysis, combined with structural and physical modelling. The fieldwork will use forced and ambient vibration testing, and will develop long-term monitoring instrumentation for the most vulnerable lighthouse. The structural modelling will use field, hydrodynamic laboratory and computational fluid dynamics data to provide better estimations of wave loading and to validate sophisticated FE models. This approach will lead to structural health monitoring methods for rock lighthouses worldwide and to other masonry structures under severe wave loading.

Acknowledgements

The authors would like to acknowledge the support of the General Lighthouse Authorities, particularly Martin Bransby and Ron Blakeley (ex-Trinity House) and their lighthouse engineers who assisted with deployments on station; Peter Ganderton and Tony Tapp of Plymouth University who designed much of the installed equipment; and the School of Marine Science and Engineering at Plymouth University who funded Davide Banfi's studentship. We also acknowledge the helpful comments of the anonymous reviewers.

References

[1] Majdalany F. Red rocks of Eddystone. London: White Lion Publishers Ltd; 1959.
[2] Nicholson C. Rock Lighthouses of Britain. Cambridge: Patrick Stephens; 1983.
[3] Bathurst B. The Lighthouse Stevensons. London, UK: Harper Perennial; 2005.
[4] Stevenson R. An account of the Bell Rock Light-House including the erection and peculiar structure of that edifice. Edinburgh, UK: Archibald Constable & Co; 1824.
[5] Raby A, Bullock GN, Banfi D, Rafiq Y, Cali F. Wave loading on rock lighthouses. Marit Eng 2016;169(1):15–28. http://dx.doi.org/10.1680/jmaen.15.00002.
[6] Slingo J. The recent storms and floods in the UK. Met Office and Centre for Ecology & Hydrology; 2014.
[7] Pena F, Lourenco P, Mendes N, Oliveira D. Numerical models for the seismic assessment of an old masonry tower. Eng Struct 2010;32:1466–78.
[8] Foti D, Diaferio M, Giannoccaro N, Mongelli M. Ambient vibration testing, dynamic identification and model updating of a historic tower. NDT&E Int 2012;47:88–95.
[9] Ivorra S, Pallares F. Dynamic investigations on a masonry bell tower. Eng Struct 2006;28:660–7.
[10] Ivorra S, Pallares F, Adam J. Dynamic behaviour of a modern bell tower – a case study. Eng Struct 2009;31:1085–92.
[11] LUSAS. LUSAS Finite Element Analysis; 2016. <http://www.lusas.com/>.
[12] Gentile C, Saisi A. Ambient vibration testing of historic masonry towers for structural identification and damage assessment. Constr Build Mater 2007;21:1311–21.
[13] LUSAS. A Brief Guide to Meshing; 2013. Retrieved from <www.2.lusas.com: http://www.2.lusas.com/protected/documentation/1025_Brief%20Guide%20to%20Meshing.pdf>.
[14] Douglass W. The new Eddystone Lighthouse. London: Institution of Civil Engineers; 1883. PRO MT 10/495.
[15] Bell F. Fundamentals of engineering geology. Frome and London: Butterworth & Co. (Publishers) Ltd.; 1983.
[16] Chopra A. Dynamics of structures. theory and applications of earthquake engineering. Englewood Cliffs, New Jersey: Prentice Hall; 1995.
[17] Wienke J, Oumeraci H. Breaking wave impact force on a vertical and inclined slender pile - theoretical and large-scale model investigations. Coast Eng 2005;52:435–62.
[18] Goda Y, Haranaka S, Kitahata M. Study on impulsive breaking wave forces on piles. Rep Port Harbour Tech Res Inst 1966;6(5):1–30.
[19] Morison J, O'Brien M, Johnson J, Schaaf S. The forces exerted by surface waves on piles. J Petrol Technol Petrol Trans AIME 1950;189:149–54.
[20] Irschik K, Sparboom U, Oumeraci H. Breaking wave loads on a slender pile in shallow water. In: Proc. 29th Int. Conf. Coastal Eng. Lisbon: ASCE; 2004.
[21] ISO. ISO 21650:2007: actions from waves and currents on coastal structures. Geneva, Switzerland: International Organization for Standardization; 2007.
[22] Goda Y. Random seas and design of maritime structures. Yokohama: World Scientific; 2000.

[23] Irschik K. Belastung schlanker zylindrischer Pfahlbauwerke durch nicht brechende und brechende Wellen: großmaßstäbliche Laborversuche und theoretische Untersuchungen [Doctoral dissertation], 2012.
[24] Tanimoto K, Takahashi S, Kaneko T, Shiota K. Impulsive breaking wave forces on an inclined pile exerted by random waves. Coast Eng 1986:2288–302.
[25] Saisi A, Gentile C, Guidobaldi M. Post-earthquake continuous dynamic monitoring of the Gabbia Tower in Mantua, Italy. Constr Build Mater 2015;81:110–2.
[26] Tarn J, Tseng W, Chang H. A circular elastic cylinder under its own weight. Int J Solids Struct 2009;46:2886–96.
[27] Carpinteri A. Structural mechanics. A unified approach. London: E & FN Spon; 1997.
[28] Wyllie D, Mah C. Rock slope engineering – civil and mining. Bury St Edmunds, Suffolk: St Edmundsbury Press; 2004.
[29] Schellart W. Shear test results for cohesion and friction coefficients for different granular materials: scaling implications for their usage in analogue modelling. Tectonophysics 2000;324:1–16.
[30] EN 12372. Natural stone test methods. Determination of flexural strength under concentrated load. BSI; 2007.
[31] Clough R, Penzien J. Dynamics of structures. McGraw-Hill Education; 1993.

Characterisation of breaking waves on the Eddystone lighthouse: a laboratory investigation on wave pressure

D. Banfi, A. Raby and D. Simmonds

Electronic version of an article published in
Coastal Engineering Proceedings, 2017, 1.35: 15.

This paper may be found at https://doi.org/10.9753/icce.v35.structures.15

CHARACTERISATION OF BREAKING WAVES ON THE EDDYSTONE LIGHTHOUSE: A LABORATORY INVESTIGATION ON WAVE PRESSURE

D. Banfi[1], A. Raby[1] and D. Simmonds[1]

Commonly, rock lighthouses are erected on the top of steep reefs and in limited water depths. The effect of these environmental conditions on wave loading requires deeper understanding. This paper investigates wave loading at small scale for a particular case study: the Eddystone lighthouse (UK). Load characteristics due to breaking waves are obtained by the use of pressure transducers and the test program is designed to generate a comprehensive data set covering a broader range of wave conditions. Although the magnitude of wave pressures is rather random from wave to wave of the same train of regular waves, the pressure impulsivity tends to decrease with increasing relative breaking distance. Four breaker types are described and particular attention is given to time histories of the line of action of horizontal force and vertical spatial distributions. Estimation of overall forces, obtained by pressure integration, indicates that the wave loading is strongly affected by the limited water depth condition. In fact, only small plunging waves are able to break at the structure; thus, they cause small forces despite the small breaking distances. Finally, the occurrence of the breakers is investigated on a dimensionless plane given by the combination of the Iribarren number and momentum flux of Hughes.

Keywords: Eddystone lighthouse; limited water depth; breaking waves; wave load; spatial load distributions; breaking map

INTRODUCTION

Wave loads are usually categorised as non-breaking or breaking waves. While wave loading due to non-breaking waves is well understood, the wave-structure interaction due to breaking waves further adds to the difficulty in predicting the underlying processes. This is essentially given by the intrinsic random nature of wave pressure due to the unknown mixture of water-air involved during the breaking process (Bullock et al. 2001). So far, multiple laboratory tests have been carried out in order to investigate the effects of breaking waves on load characteristics i.e. load peak, impact duration and spatial distribution. While many of these investigations have been focused on vertical or near vertical walls (Oumeraci et al. 1993; Hattori et al. 1994; Hull and Muller 2002; Bullock et al. 2007), very few studies have been conducted on structures as rock lighthouses (Kyte and Tørum 1996). Commonly, rock lighthouses are erected on the top of steep reefs and in limited water depths. Relatively little is known about the effects of these environmental conditions on wave loading. The objective of the present paper is to investigate, at small scale, the load characteristics due to breaking wave for a particular case of study: the Eddystone lighthouse (UK). Geophones and cameras were installed on this structure, which is located on a perilous group of rocks some 21 km offshore from Plymouth. The field monitoring showed that the lighthouse can be exposed to different types of breaking waves (Raby et al. 2015).

LITERATURE REVIEW

Breaking waves and load characteristics

Bagnold (1939) was one of the first to perceive that wave loading is affected by the amount of aeration involved during the breaking process. Thus, the coastal literature has provided several breaker classifications on the basis of the breaking shape/breaking distance (Oumeraci et al. 1993; Hattori et al. 1994; Hull and Muller 2002) or the amount of air measured under controlled conditions (Bullock et al. 2007). Although it is not possible to identify the breaker that causes the highest pressure, severe loads are usually associated with plunging impacts that break at the structure, i.e. characterised by small breaking distances or low aeration levels. In addition, it is generally accepted that the impulsivity tends to decrease with the increase in the breaking distance and the aeration effect results in a cushioning effect (visible with a pressure oscillation), which tends to damp the pressure peak and to increase the impact duration (Oumeraci et al. 1993; Hattori et al. 1994; Hull and Muller 2002; Bredmose et al. 2009; Cuomo et al. 2011). Typically, broken waves exhibit much smaller pressures than plunging impacts. However, the latest considerations concerning the highest load peaks were not found for High Mound Composite Breakwaters (HMCBs), which are characterised by large and steep mounds that cause a limited water depth at the toe of the vertical superstructure. As a consequence, only small waves

[1] Faculty of Marine and Science Engineering, Plymouth University, Drake Circus, Plymouth, Devon, PL4 8AA, UK

are able to break at the superstructure, thereby causing lower loads despite the small breaking distance (Muttray et al. 1998).

For design purposes, a full characterisation of wave loads requires the identification of spatial distributions in order to determine the line of action of the force. Especially for rock lighthouses, which can have a tapered geometrical configuration, the spatial distribution can play a fundamental role in terms of structural deflections. In particular, for the Eddystone lighthouse, numerical simulations have been carried out with a view to analyse the structural response of the tower. The investigation indicates that the structural deflection of the Eddystone lighthouse is highly influenced by the height at which the impacts occur. In particular, maximum displacements show a steep linear trend with impact height (Trinh et al. 2016). Concerning vertical walls, distinct pictures have been given in the literature about the location of maximum pressure since the spatial distribution tend to be random for breaking waves, even for regular waves that were supposedly identical. Large scale experiments of Bullock et al. (2007) show a sharp triangular distribution of maximum peaks (non-instantaneous) slightly above the still water level (SWL) for low aeration level. For high aeration levels, the triangular distribution tends both to enlarge and to centralise more close to the SWL; while broken impacts result in smoother and extended distributions with extreme pressures around or just below the SWL (Bullock et al. 2007).

Laboratory tests and wave parameters

Most of the aforementioned breaker classifications were obtained in 2D situations and with trains of regular waves. Small-scale tests introduce laboratory effects that are difficult to quantify (Bullock et al. 2003; Cuomo et al. 2010; Blenkinsopp and Chaplin 2011; Bredmose et al. 2015). However, one of the advantages of laboratory tests is the control over wave characteristics so as to understand the influence of various wave parameters on the wave loading during the process of breaking. Usually, the hydraulic variables (wave height H, wave period T and water depth h) are combined to form dimensionless wave parameters, which helps to reduce the number of independent variables. Two of the most used coastal parameters are the Iribarren number and the momentum flux of Hughes (2005).

Iribarren number

The Iribarren number, also known as the surf similarity parameter (Battjes 1974), has been identified as a good predictor parameter in several design applications. It was initially developed to describe the occurrence of regular wave breaking on slopes as follows:

$$\xi_o = \frac{\tan\alpha}{\sqrt{H_o / L_o}} \tag{1}$$

where α is the slope of the seabed, H_o the offshore wave height and L_o is the offshore wave length, which is equal to $gT^2/2\pi$ (where g is the gravity acceleration). Therefore, the Iribarren number relates the offshore wave steepness H_o/L_o to the slope. This parameter is an index of the breaker violence through the well-known classification proposed by Galvin (1968), in which four categories of breaker are defined (spilling, plunging, collapsing and surging).

Momentum flux of Hughes

Hughes (2005) suggests that the Iribarren number may be not the best parameter to describe flow kinematics because local water depth h is not included. Thus, while different combinations of H/h (relative wave height) and h/L (relative water depth) can yield the same value of deepwater wave steepness, the wave kinematics will be different. Consequently, Hughes (2005) considers the following dimensionless momentum flux (based on wave linear theory of Airy) as a better parameter to analyse wave-structure interactions:

$$M_{\mathrm{f}} = \frac{1}{2}\frac{H}{h}\frac{\tanh kh}{kh} + \frac{1}{8}\left(\frac{H}{h}\right)^2\left[1 + \frac{2kh}{\sinh 2kh}\right] \tag{2}$$

where $k=2\pi/L$ is the wave number and L is the local wave length, which can be determined with the linear dispersion relationship (Eq. A-1 in Appendix). Eq. 2 indicates that M_{f} increases with the increasing of H and/or T and with the decreasing of h.

EXPERIMENTAL SETUP

Regular wave tests were carried out in the 35 m long x 0.6 m wide x 1.2 m deep sediment wave flume of the COAST Laboratory at Plymouth University. The experiments were conducted at 1:70 length scale (Froude scaling) compared to the prototype and the bathymetry was modelled with two slopes: 1:20 and 1:8, as shown in Fig. 1. The water depths at the paddle and at the toe of the lighthouse model were h_p=0.63 m and h_t=0.095 m, respectively, in agreement with the depths in the prototype at highest astronomical tide (i.e. 44 m and 6.65 m).

The lighthouse model, which was screwed down to an uppermost horizontal plane located at the end of the 1:20 slope (Fig. 1), comprised two circular cylinders (one above the other) having different diameters. The cylindrical base had a height of 0.10 m and a diameter of 0.20 m, the upper cylinder a height of 0.55 m and a diameter of 0.155 m. The lighthouse model could be disassembled into two rigid parts, as shown in Fig. 2a, so that pressure transducers could be installed in nine 10 mm diameter threaded holes. The two parts were connected using eight screws and a perfect watertight was ensured by locating absorbing paper and petroleum jelly between them. The thickness of the cylinder walls was 10 mm and they were manufactured in Plexiglas in order to be simultaneously waterproof and rigid.

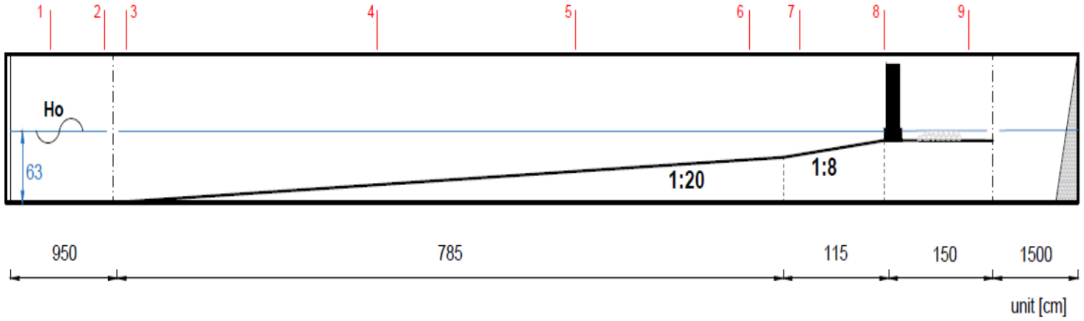

Figure 1. Setup of the experiments

Three of the threaded holes were under the SWL (on the cylindrical base) and six were above the SWL (on the upper cylinder); in order to provide the most detailed spatial resolution, two consecutive holes were spaced at intervals of 15 mm (Fig. 2b). Pressure signals were measured by six dynamic piezoelectric pressure sensors of type XP1102, which had a range of up to 1 bar and a resonant frequency of 50 kHz. Data was acquired at a sampling rate of 1.8 kHz. The six transducers were fixed as illustrated in Fig. 2b. Pressure transducer cables were inserted through another hole of 40 mm diameter on the leeside of the upper section model.

Finally, nine resistance wave gauges and three cameras completed the setup of the experiments. One of the three cameras was both high speed and high definition (3600 fps at 1024x1024 resolution).

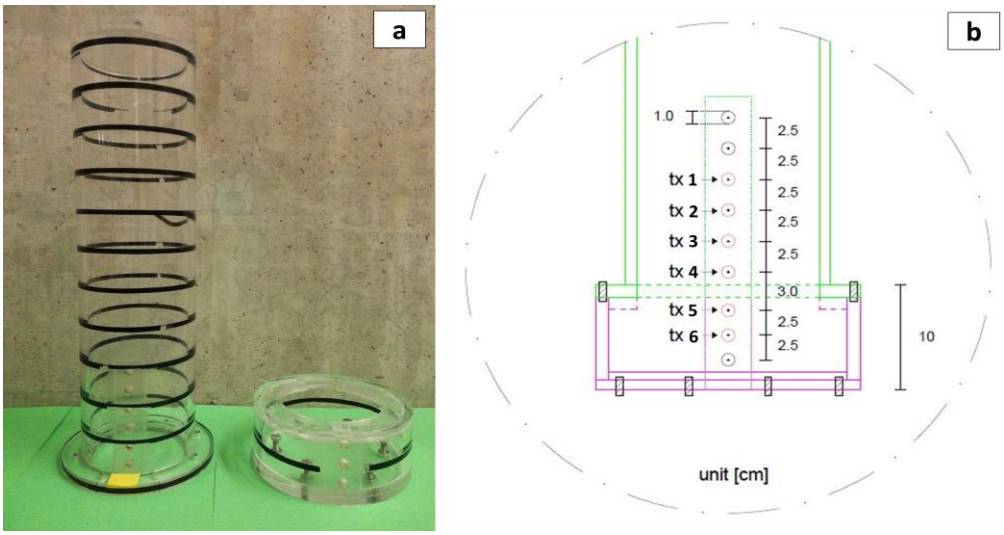

Figure 2. (a) Photo of the dissembled lighthouse model; (b) sketch of the pressure transducers locations

TEST PROGRAM AND THEORETICAL CONSIDERATIONS

Experimental tests included 128 runs of regular waves (with target values of H_o and T covering 0.02-0.25 m and 0.6-3.0 s, respectively). These ranges of target values were identified thanks to a sort of breaking map, which was obtained in a dimensionless plane of momentum flux of Hughes versus Iribarren number, as shown in Fig. 3. On the horizontal axis, the Iribarren number (Eq. 1) was determined according to the uppermost slope (α=1/8=0.125) and the offshore wave steepness (H_o/L_o). On the vertical axis, the momentum flux was determined according to Eq. 2 and setting $H=H_o$. As may be observed from Fig. 3, the test program is enclosed by three limiting conditions: the two breaking limits for wave steepness (H/L) and wave height (H/h), and the shallow water limit (h/L). For determining the three limits, it was firstly necessary to identify the section at which the momentum flux is calculated, i.e. the value of the water depth h that must be inserted into Eq. 2. It was decided to select the depth section at a distance from the model of approximately 5 times the maximum offshore wave height (H_o=0.25 m); above this value the wave tends to dissipate most of the energy (Goda 1974). Thereby, the location was identified at a distance of 1.2 m from the model, where the water depth is h^*=0.24 m and the slope is 1:20 (Fig. 1). As a consequence, the three limiting conditions were identified at h^* according to the linear wave theory (Airy). Below are described the procedures used for their identification.

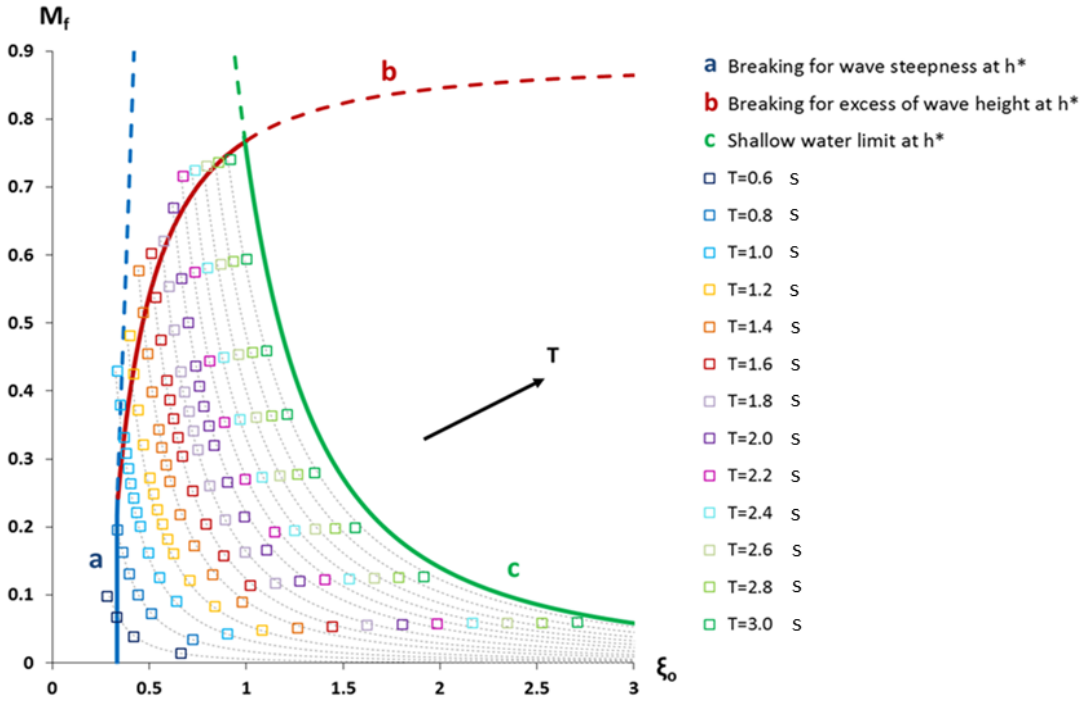

Figure 3. Test program plotted on the breaking map given by the combination of ξ_o and M_f

Breaking limit according to wave steepness

The wave steepness limit (H/L=0.14) was estimated by setting the breaking water depth h_b at h^*=0.24 m (note: subscripts "b" indicate wave characteristics at breaking point). A reduction coefficient of 0.91 was introduced to take into account the maximum possible decrease of the offshore wave height H_o for shoaling (Fig. A-1 in Appendix). On this basis, the limit was determined as follows.

1. Define the wave steepness limit at h_b equal to $0.91H_o/L_b$=0.14.
2. Select a value for T, e.g. T=0.1 s.
3. Calculate L_o and L_b at h_b using the linear dispersion relationship (Eq. A-1 in Appendix).
4. Determine H_o from step 1 above.
5. Repeat steps 2-4 by defining different values of T (with an interval ΔT=0.1 s).

Finally, the blue curve (a), shown in Figure 3, was drawn according to $\xi_o = f(H_o, L_o)$ and $M_f = f(H_o, T \text{ and } h^*)$.

Breaking limit according to wave height

The breaking wave height H_b, on the 1:20 slope at $h_b = h^* = 0.24$ m, was estimated as follows.

1. Define the breaking relationship between H_b/h_b and H_b/gT^2 according to the Eq. A-2 (in Appendix) obtained from the diagram of Weggel (1972) (Fig. A-2 in Appendix).
2. Select the first value of relative wave height, $H_b/h_b = 0.01$, with its relative value of H_b/gT^2 (from step 1).
3. Since $h_b = 0.24$ m, define H_b and, then, the associated T (from step 2).
4. Determine both L_o and L_b at h_b using the linear dispersion relationship (Eq. A-1).

Once these local variables were determined at the breaking location, it was necessary to calculate their relative offshore values, as explained below.

5. Known h/L (i.e. h_b/L_b from step 4), identify the ratio $H_{(h)}/H_o$ from the shoaling curve (Fig. A-1).
6. Determine the value of H_o from step 5, where $H_{(h)} \equiv H_b$.
7. Repeat steps 2-6 by varying the values of H_b/h_b (with an interval $\Delta = 0.01$).

Finally, the red curve (b), shown in Fig. 3, was drawn according to $\xi_o = f(H_o, L_o)$ and $M_f = f(H_o, T \text{ and } h^*)$.

Shallow water limit

The wave period T, which implies the shallow water limit at $h^* = 0.24$ m, was calculated according to $h^*/L_{(h^*)} = 0.05$, where the wavelength $L_{(h^*)}$ was determined using Eq. A-1.

Therefore, the blue limit (c), shown in Fig. 3, represents the curve at constant period ($T = 3.2$ s) that causes the shallow water limit at $h^* = 0.24$ m.

DATA PROCESSING

Vertical spatial distribution and time history of the line of action of the force

Vertical spatial distributions have been determined applying a linear interpolation between the measured pressures. As shown in Fig. 4a, the spatial distribution was vertically extrapolated below the lowest transducer to the bottom and it was not extrapolated above the upper sensor. The spatial distribution was truncated on the top in order to avoid an unrealistic extrapolation above the measured run up on the model. Elevations of the application force point have been obtained by determining barycenter time histories of the vertical spatial distributions.

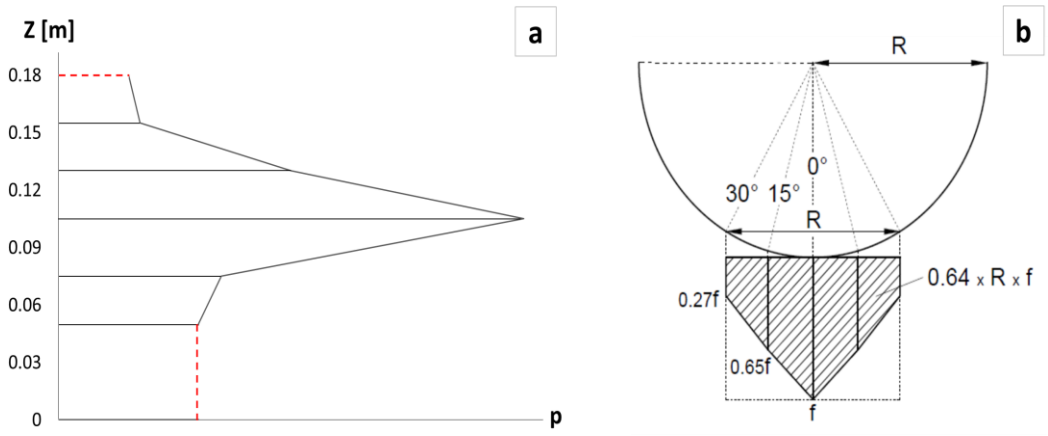

Figure 4. (a) Integration method to calculate the vertical spatial distribution and related force in line f; (b) azimuthal distribution for the estimation of the overall force F

Azimuthal distribution and estimation of the overall force

The spatial integration of the pressure measurements gives the force in line (f) with the central section of the cylindrical model (Fig. 4a). An estimation of the overall force (F) has been obtained

according to the azimuthal distribution derived from pressure measures shown in Wienke and Oumeraci (2005). They measured pressures around a vertical cylinder and they found that the pressures at ±15° and ±30° were 0.65 and 0.27 times lower than the pressure in line with the wave direction (i.e. at 0°). As a consequence, their azimuthal integration results 0.64 times smaller with respect to a force line equally distributed along a horizontal extension equal to the radius of the cylinder (Fig. 4b). Note that the distance between +30° and -30° coincides with the radius of the cylinder (R) and for the present analysis it was fixed equal to 0.10 m (i.e. equivalent to the radius of the cylindrical base).

RESULTS AND DISCUSSION

Classification and description of breaker types

The test program, previously described, generates non-breaking and breaking waves. The first three waves in each wave train were omitted from the analysis, as they had not reached the required amplitude; instead the subsequent 15-20 waves were analysed. The magnitude of wave pressures tends to be rather random from wave to wave of the same test, despite the repeatability of the breaking point. However, the nature of the load characteristics tends gradually to vary from test to test on the basis of the breaking distance (x) with respect to the lighthouse model. In particular, the load impulsivity increases as the relative breaking distance decreases ($d=x/H_b$).

Except for non-breaking/slightly breaking and spilling waves, which cause lower wave loadings, the load characteristics have been classified into four main breakers types on the basis of the relative breaking distance as follows:

- weak impact (x/H_b = 0.1-0.5);
- violent impact (x/H_b = 0.5-1.5);
- large air pocket (x/Hb = 1.5-3.5);
- broken (x/H_b > 3.5).

Fig. 5 shows video images of four examples that are used to describe the typical load characteristics of the four breaker types. The subsequent paragraphs provide data from these particular experiments.

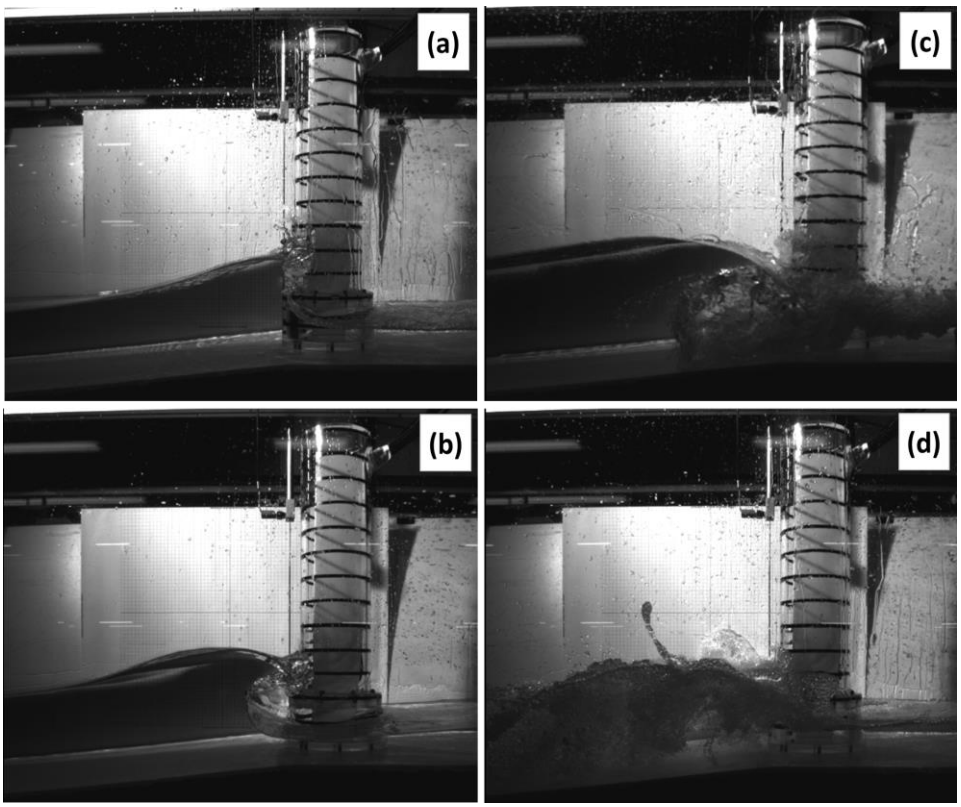

Figure 5. (a) weak impact (H_o=0.11m, T=1.4s); (b) violent impact (H_o=0.13m, T=1.8s); (c) large air pocket (H_o=0.17m, T=2.2s); (d) broken (H_o=0.22m, T=2.4s).

Weak impact

This is a small plunging impact that breaks approximately at the model with the wave front almost vertical (Fig. 5a). Impulsive pressure time histories are highly localised in space and they tend to occur in the proximity of transducer 3 (above SWL). Here, the impinging jet causes a rapid pressure spike, followed by the quasi-static component of the wave surface (Fig. 6a). Usually, the other pressure transducers (under and above the area hit by the small plunging jet) do not exhibit the occurrence of a pressure spike. The maximum measurements, related to the pressure transducers under SWL, occur first, followed by quasi-static loads measured above the impact area from the subsequent run up. Very often, the pressure records show high frequency oscillations at the location just below the occurrence of the impulsive peak. These oscillations, which occur later than the impulsive peak, suggest the presence of a small amount of air (transducer 4 in Fig. 6a).

The integrated force (F) exhibits a sharper peak highly localised in time (Fig. 6b). The instant of the maximum force is coincident with the instant of the maximum peak in the barycentre time history (dimensionless with respect to the water depth at the toe of the lighthouse, i.e. h_t=0.095 m) (Fig. 6c). At this instant, the spatial distribution tends to be a sharp triangle with the peak above SWL (Fig. 6d).

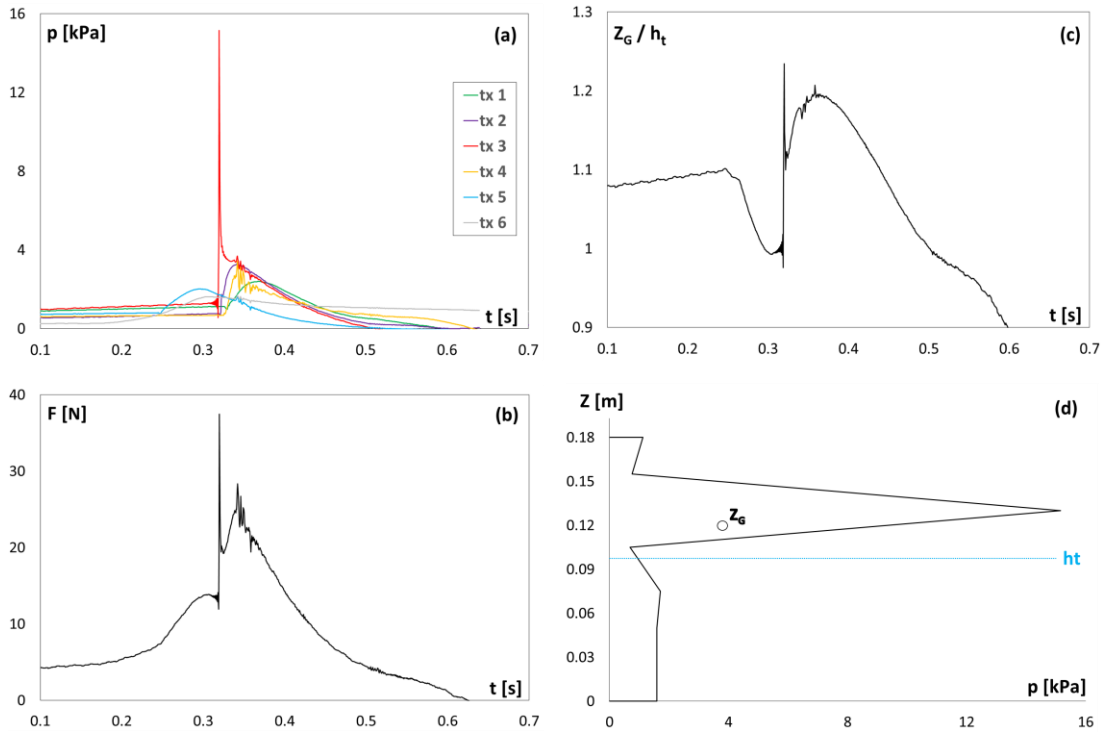

Figure 6. Weak impact (Ho=0.11m, T=1.4s): (a) pressure time histories; (b) overall force time history; (c) dimensionless barycentre time history; (d) vertical spatial distribution at the maximum force peak.

Violent impact

With respect to the previous breaker, this is a larger plunging impact that breaks relatively close to the model (Fig. 5b). Impulsive pressures tend to occur over all the pressure transducers, also for those under the SWL (Fig. 7a). All the pressure time histories tend to have a well-defined triangular shape and, frequently, extreme spikes are visible on the top of the triangular peaks (Fig. 7a). The maximum pressure peak, highly localised in the time, occurs randomly between the four pressure transducers above SWL (i.e. tx1, tx2, tx3 and tx4) depending on the direction of the forward jet. High frequency oscillations after maximum peaks indicate the presence of air, as confirmed by video images (Fig. 5b).

The integrated force (F) results in a triangle with a sharp spike on the top (Fig. 7b). Often, the first pressure spike, which occurs for the highest pressure transducers (i.e. tx1 and tx2), is so localised (in both time and space) that it loses its effects when the pressures are integrated over the whole interface of the lighthouse model (Fig. 7b). As a consequence, the maximum peaks in the barycentre (Z_G/h_t) and force time (F) histories do not occur at the same instant (Fig. 7b-c). However, spatial distributions, at

the instant of the maximum peak force (F), tend to be triangular; but the shape tends to be wider than that of the weak impact and with the peak just slightly above the SWL (Fig. 7d).

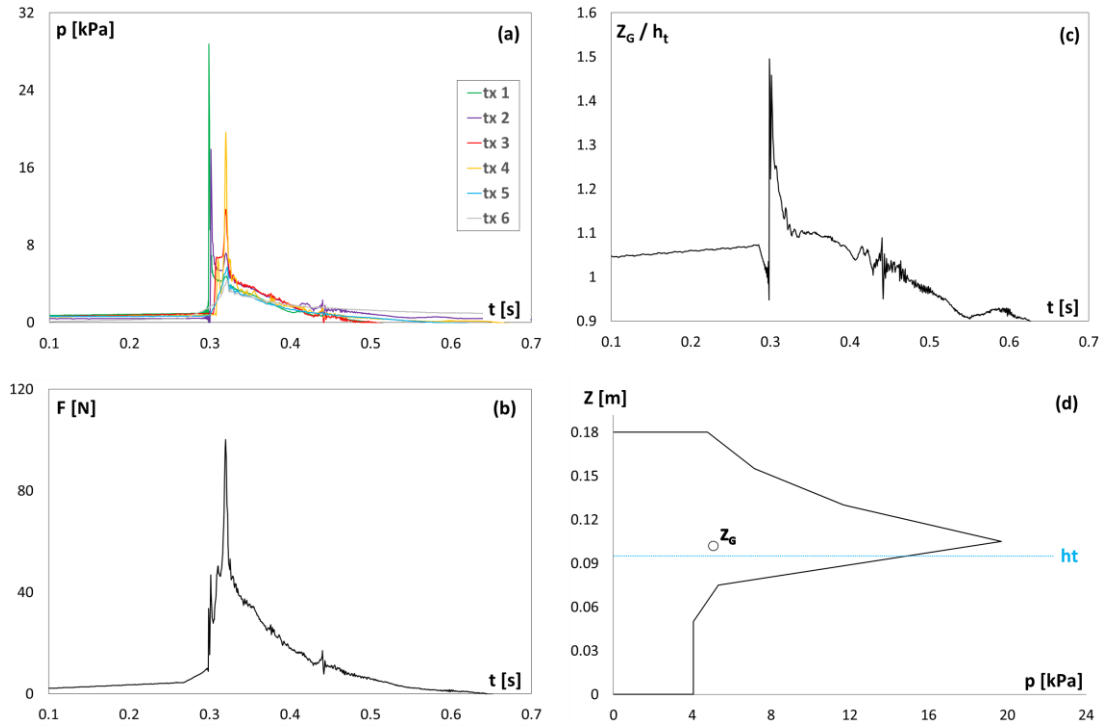

Figure 7. Violent impact (Ho=0.13m, T=1.8s): (a) pressure time histories; (b) overall force time history; (c) dimensionless barycentre time history; (d) vertical spatial distribution at the maximum force peak.

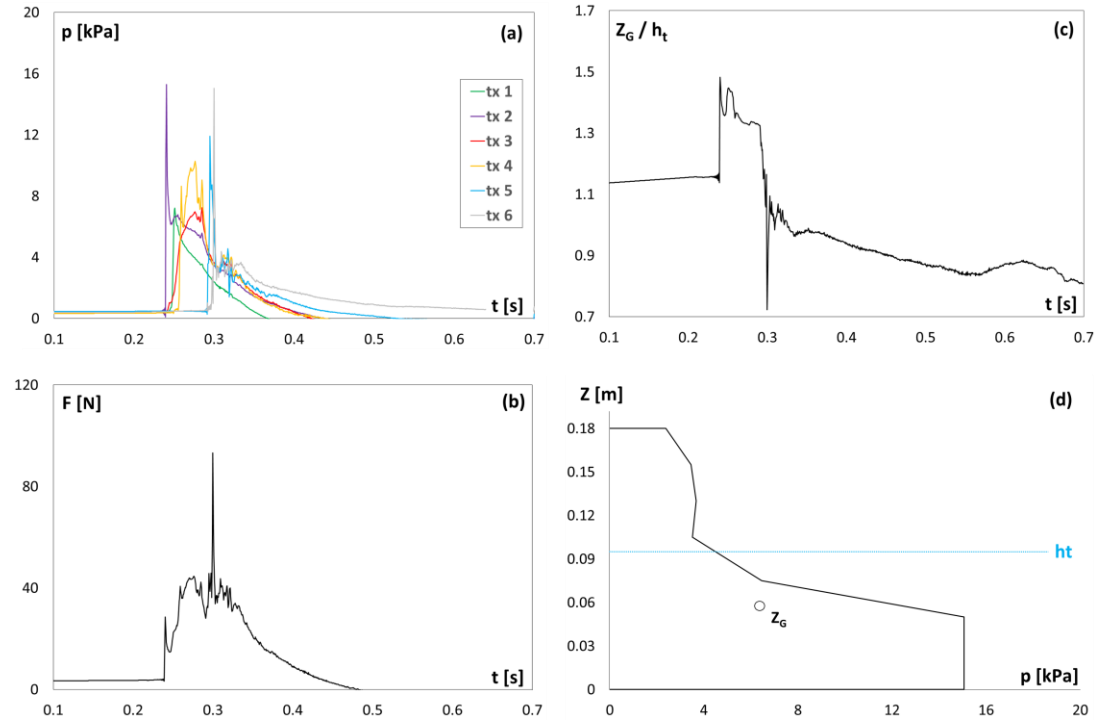

Figure 8. Large air pocket (Ho=0.17m, T=2.2s): (a) pressure time histories; (b) overall force time history; (c) dimensionless barycentre time history; (d) vertical spatial distribution at the maximum force peak.

Large air pocket

This is a large plunging wave that breaks farther from the lighthouse model due to the limited water depth condition. The wave crest, which overturns and hits the model as it falls down, can entrap a large air pocket (Fig. 5c). Maximum run up, approximately 4 times the water depth h_t, occurred for this breaker type. However, this value is lower with respect to the maximum run up observed in the 3D situation of the field during the UK winter storms of 2013/2014 (Raby et al. 2015).

This breaker exhibits two distinct temporal phases. The first phase is caused by the falling-down jet, which generates impulsive pressures above the SWL; the second phase is caused by the incoming wave that generates impulsive pressures under the SWL (Fig. 8a). Although the maximum pressure peak can occur in both the phases, it tends to be smaller and wider when compared to those recorded for violent impact type. In addition, the effects of the entrapped air generate irregular oscillations, recorded under SWL, after the secondary peaks (Fig. 8a).

As consequence of the distinct phases, the force time history (F) shows several peaks and its shape is less triangular than that of the violent impact type (Fig. 8b).

The barycentre time history (Z_G/h_t) shows the line of action moves from above to under SWL (Fig. 8c). Despite the repeatability of the barycentre time histories, two different spatial distributions can be associated with this breaker depending on whether the maximum peak force occurs in the first or in the second phase. When the maximum force peak is related to the falling-down jet, the spatial distribution has a triangular shape similar to that of the violent impact type (Fig. 7d). Alternatively, when the maximum force peak is caused by the incoming wave, the spatial distribution is characterised by a wide area under the SWL (Fig. 8d).

Broken

The wave crest strikes the water and the cylinder is subsequently hit by a turbulent mass of water with high residual velocities (Fig. 5d). This breaker tends to cause lower run up, even if these wave impacts tend to persist for longer durations.

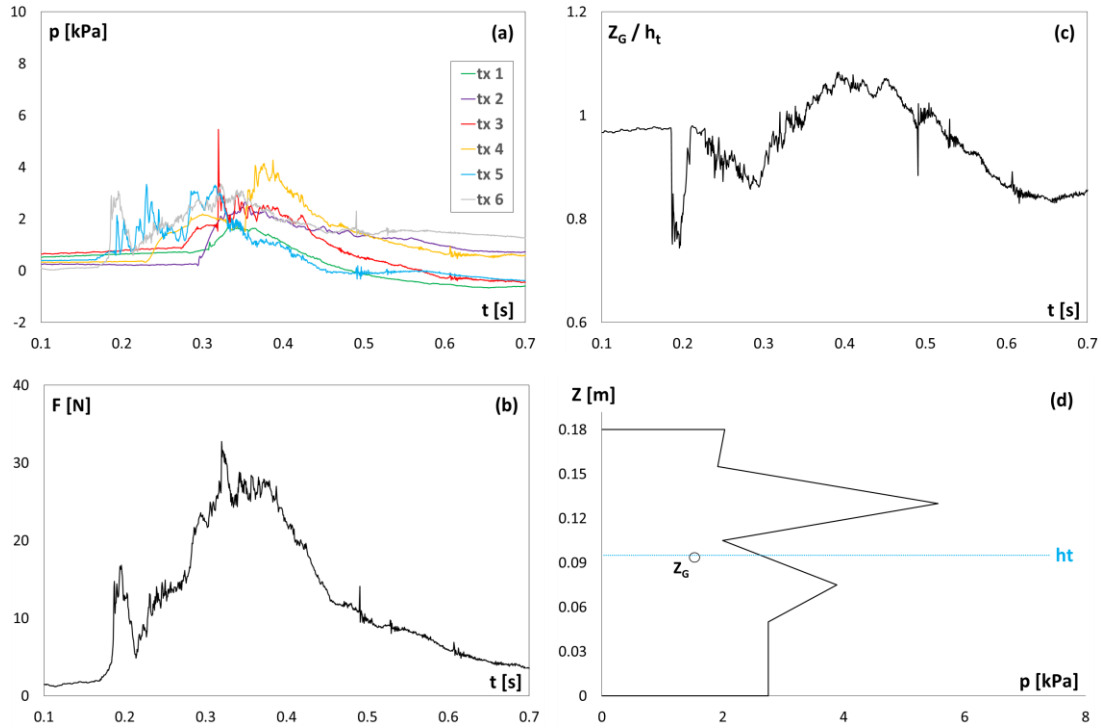

Figure 9. Broken (Ho=0.22m, T=2.4s): (a) pressure time histories; (b) overall force time history; (c) dimensionless barycentre time history; (d) vertical spatial distribution at the maximum force peak.

All the pressure transducers tend to show a highly variable signal characterised by random peaks due to the impact of the air-water mixture (spray) and secondary small jets (Fig. 9a). The pressure

measurements are not in phase with each other and the pressure event moves gradually from tx6 (lower transducer) to tx1 (upper transducer) due to the turbulent bore that runs up the model (Fig. 9a).

The integrated force (F) shows a quasi-static noisy signal (Fig. 9b); usually, two peaks can be observed because pressures are not simultaneous.

The barycentre of the spatial distributions moves from under to above SWL (Fig. 9c). Due to the fact that pressure magnitudes from tx3, tx4 and tx5 tend to be similar, the maximum spatial distributions can occur slightly under or above SWL. Although they tend to be characterised by a more uniform distribution over the whole impact extent, the shape is completely random (Fig. 9d).

Load characteristics and wave parameters

The magnitude of wave pressures tends to be rather random from wave to wave for the same test, despite the repeatability of the breaking point. Fig. 10 shows dimensional and dimensionless pressure peaks against Iribarren number and momentum flux. The peaks are the maximum values recorded for each test by each pressure transducer (six in total). The dimensional values are in kPa, while the dimensionless values (usually used as an indicator of the impulsivity) are obtained by dividing the pressure by the specific weight of the water γ and the offshore wave height H_o i.e. measured before the wave transformation that occurs on the 1:20 slope.

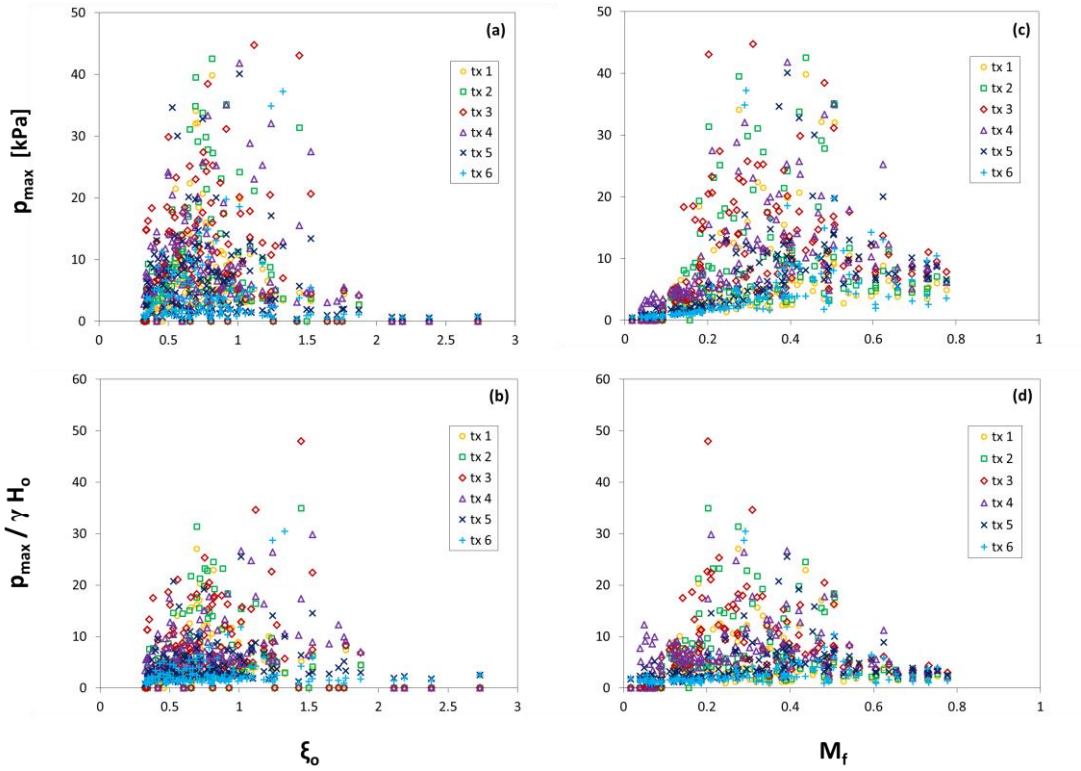

Figure 10. Dimensional (upper) and dimensionless (bottom) pressures vs ξ_o (left) and M_f (right)

As may be observed from Fig. 10a-b, pressure peaks are quite random when plotted against ξ_o. Also, similar maximum values (dimensional and dimensionless) can occur over a large range ($0.4<\xi_o<1.5$). However, the pressures are much smaller when $\xi_o>1.5$. This is due to the fact that plunging waves can occur if $\xi_o<1.5$, instead only non-breaking/slightly breaking wave occur when $\xi_o>1.5$. When $1.0<\xi_o<1.5$, dimensionless values tend to show a larger scatter because they are characterised by stronger wave transformation. When plotted against M_f, most of the highest dimensional pressure peaks occur over the range 0.2-0.6 (Fig. 10c). This is given by the fact that non-breaking/slightly breaking waves occur only if $M_f<0.2$, while only broken waves occur when $M_f>0.6$. Except for the lower values in the first part ($M_f<0.2$), where waves are non-breaking/slightly breaking, the dimensionless pressure shows a tendency to decrease with the increase in the momentum flux.

Fig. 11 shows dimensional and dimensionless maximum force peaks against Iribarren number and momentum flux. The dimensionless values are obtained by dividing the force line (f) by the specific weight of the water γ, the offshore wave height H_o and the water depth at the toe of the cylinder h_t. As for the dimensional and dimensionless pressures, most of the highest force peaks tend to occur for $\xi_o<1.5$ and $0.2<M_f<0.6$ (Fig. 11).

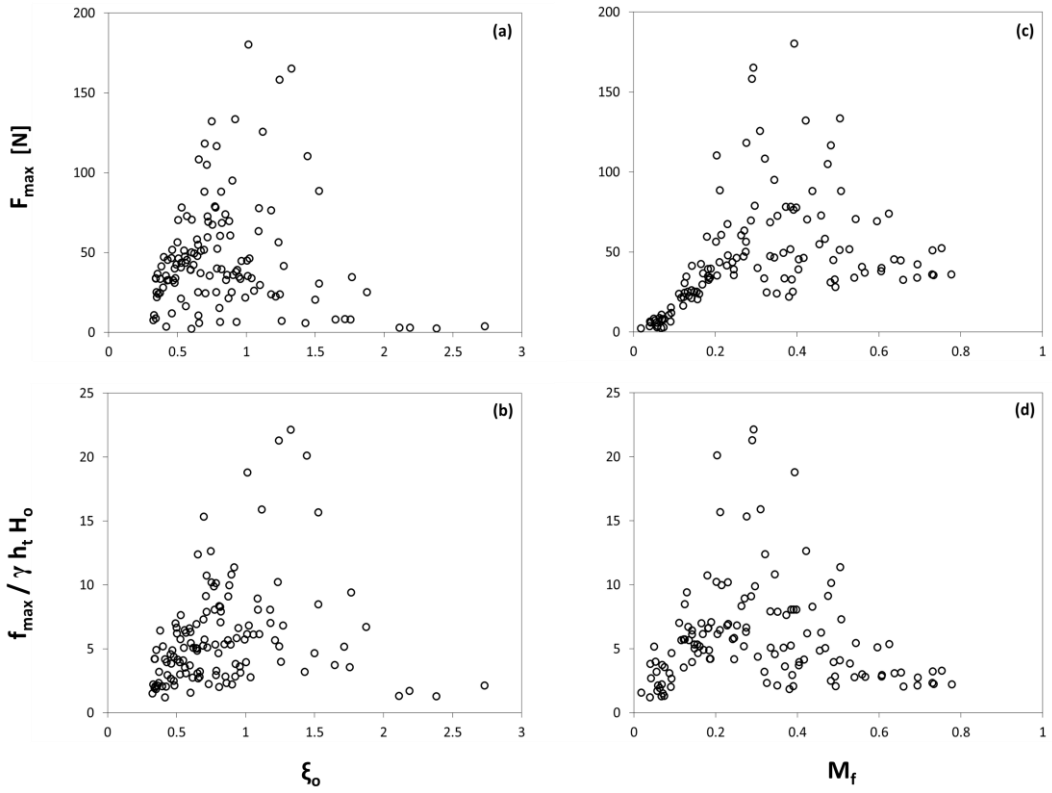

Figure 11. Dimensional (upper) and dimensionless (bottom) force vs ξ_o (left) and M_f (right)

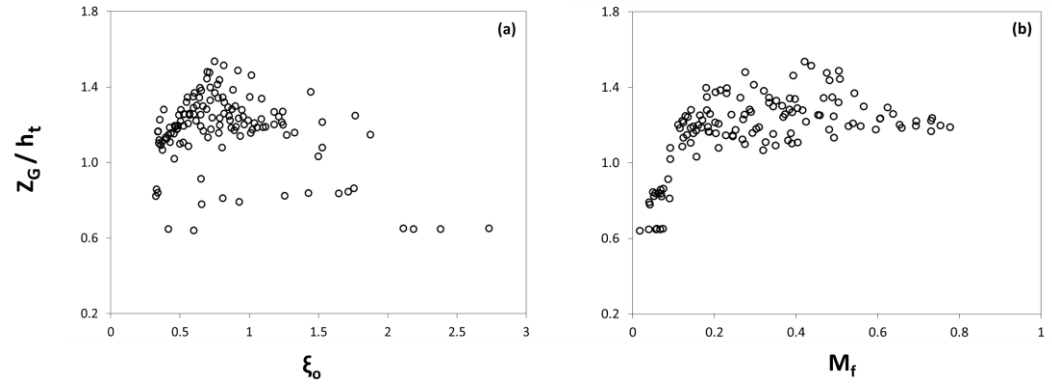

Figure 12. Maximum dimensionless barycenter peaks vs ξ_o (left) and M_f (right)

As may be observed by comparing Fig. 11c and 11d, momentum flux below 0.2 show a scatter moving from dimensional to dimensionless value. This portion of data includes slightly-breaking waves, which are characterised by small offshore wave heights that become steeper in the proximity of the model. As a result, they cause small impulsive load peaks with respect to the offshore wave heights. However, the dimensional forces are rather small because these waves are so small that the two upper transducers did not record the pressure event. Moreover, events with $M_f>0.6$ generate larger forces

(dimensional values) with respect to those with M_f<0.2, even if the latest exhibit stronger impulsivity (i.e. larger dimensionless values).

In the previous section spatial distributions that occur at the instant of the maximum force were described. Figure 12 shows the maximum peaks of the barycentre time history. These peaks are plotted against the Iribarren number and momentum flux. As may be observed, the Iribarren number does not show a clear tendency (Fig.12a). Instead, when plotted against the momentum flux, the lowest barycentre peaks occur for M_f <0.2, then the highest values (approximately 1.5) occur over the range 0.2-0.6 and they tend to 1.2 when M_f>0.6 (Fig.12b).

Occurrence of breaker types on the ξ_o - M_f plane

As may be observed from Fig. 13, the breaker types tend to cover certain areas of the plane ξ_o-M_f, where data are plotted according to the measured offshore wave height H_o. In particular, the breaker types tend to gradually vary with the momentum flux, moving from non-breaking to broken wave. As a consequence, the relative breaking distance tends to increase with the increasing of M_f. Only small waves (weak impact, slightly breaking and non-breaking) occur when ξ_o>1.5. Spilling breakers tend to occur according to wave steepness limit (curve a). Similarly, waves break for excess of wave height in the proximity of the depth section h^*=0.24 m, in agreement with the wave height limit (curve b).

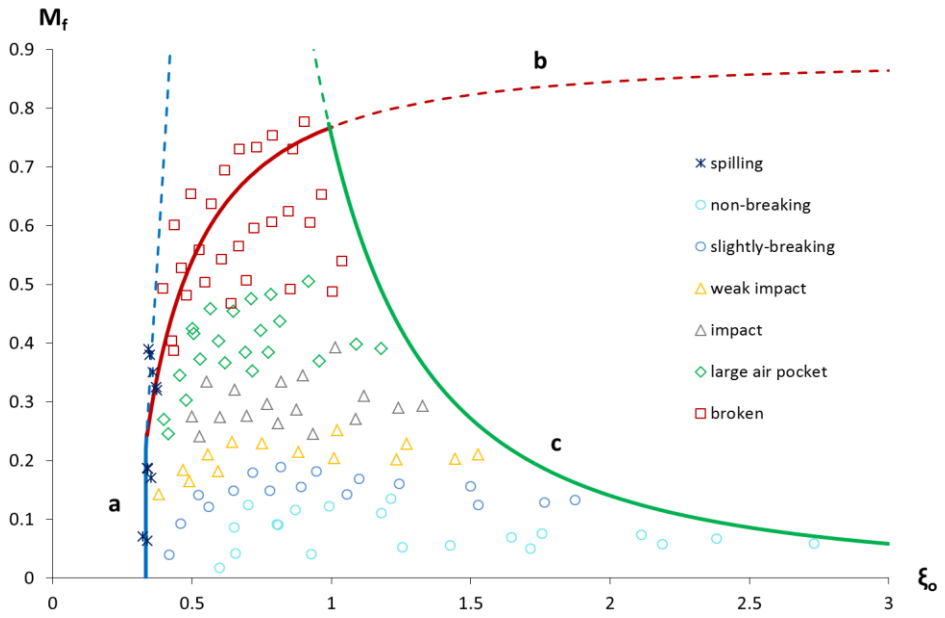

Figure 13. Breaker types occurrence on the dimensionless plane ξ_o - M_f

Fig. 14 shows histograms of the maximum peaks (pressure and overall force) recorded for the four breaker types previously described. The peaks are shown for both dimensional and dimensionless values. As may be observed, the dimensionless pressures decrease from weak impact to broken. Consequently, the impulsivity of the pressure signals tends to decrease with the increasing of the relative breaking distance. In contrast, weak impact, violent impact and large air pocket are able to generate similar dimensional pressures (Fig. 14). This means that smaller waves (weak impact), characterised by smaller masses, can generate pressures similar to those generated by larger wave heights. Thus, due to the fact that pressure transducers provide spatially localised measurements, the pressures may be more affected by the acceleration of the water than by the amount of the water mass.

In contrast with pressure, dimensional forces exhibit larger scatter among the four breaker types, and maximum values (both dimensional and dimensionless) are given by violent impact type (Fig. 14). This result is caused by the fact that a couple of vertical spikes tend to be almost simultaneous over two pressure transducers for the violent impact type. As a consequence, the integrated force (f) tends to show a strong vertical spike highly localised in time. Although the weak impact types arises from a plunging wave that breaks at the structure with the wave front almost vertical, it causes lower forces when compared to breaker characterised by larger breaking distances. This is explained by the fact that

the lighthouse model is in depth limited conditions and only small plunging waves are able to break at the structure. Thus, even if larger plunging waves break farther from the lighthouse, they are characterised by larger wave heights and periods that generate larger forces.

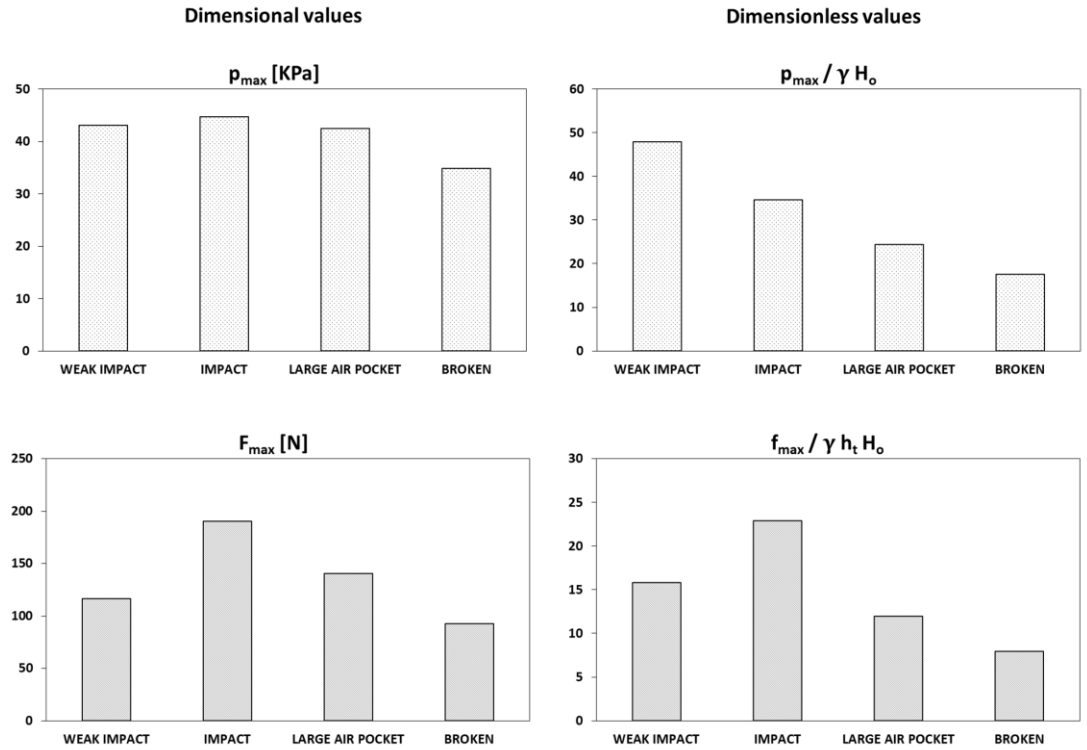

Figure 14. Histograms of the maximum load peaks recorded for the four breaker types. At the top are pressures and on the bottom forces; at the left dimensional values and on the right dimensionless values.

CONCLUSIONS

Four main groups of load characteristics have been identified and classified in four breaker types on the basis of the relative breaking distance. Although the repeatability of the breaking point for the same wave regular test is consistent, the magnitude of pressures is rather random wave by wave. However, the pressure impulsivity increases as the relative breaking distance decreases.

Vertical spatial distributions and barycentre time histories of the force have been also investigated. Weak impact and impact are characterised by triangular vertical distributions with the barycentre above SWL. The barycentre time history shows that the line of action moves from above to under SWL for large air pocket. Thus, depending on the instant of the maximum force peak, two different spatial distributions can occur: triangular, with the barycentre above SWL, or trapezoidal, with the barycentre under SWL. For broken waves the barycentre moves from under to above SWL, but the shape of the spatial distribution is random and the barycentre can occur slightly under or slightly above SWL.

Due to the limited depth condition at the toe of the lighthouse, only small plunging waves are able to break at the structure. As a consequence, larger overall forces (from integrated pressures) are caused by larger waves, even if they break farther from the lighthouse.

In addition, the occurrence of breaker types has been investigated in a sort of dimensionless breaking map given by the combination of the Iribarren number and momentum flux of Hughes.

Within this experimental campaign, overall force measurements were also obtained by using load cells and results will be presented in future works.

ACKNOWLEDGMENTS

The authors would like to acknowledge Alastair Reynolds and Peter Arber for the assistance provided during the laboratory test and the School of Marine Science and Engineering who funded the PhD project of D. Banfi. The authors are also grateful to Professor G. Bullock for his stimulating thoughts and for the valuable suggestions provided during the aforementioned PhD project.

APPENDIX

Waves are affected by transformations when they propagate from deep (h/L>0.5) to shallow waters (h/L<0.05). The decrease of the depth implies the decrease of the wave length and the variation of the offshore wave height H_o for shoaling (Fig. A-1).

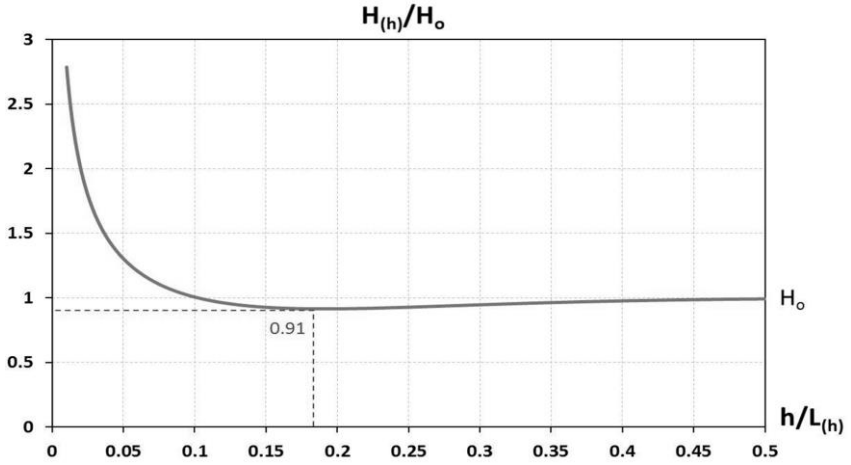

Figure A-1. Shoaling curve: wave height $H_{(h)}$ variation that occurs during the wave propagation.

The local wave length $L_{(h)}$ at the generic water depth h is calculated according to the linear dispersion relationship (Eq. A-1).

$$L_{(h)} = L_o \tanh kh = \frac{gT^2}{2\pi} \tanh kh \qquad \text{(A-1)}$$

In the surf zone the wave height can reach a limiting value. Above this value, the wave breaks for excess of wave height with respect to the water depth. The breaking limit is calculated according to the relative wave height H_b/h_b and it depends on both slope (α) and offshore wave steepness (H/L). Figure A-2 shows the breaking limits proposed by Weggel (1972) for regular waves and Eq. A-2 the breaking limit related to the slope 1:20.

$$\frac{H_b}{h_b} = 1.13 - 26.5 \frac{H_b}{gT^2} \qquad \text{(A-2)}$$

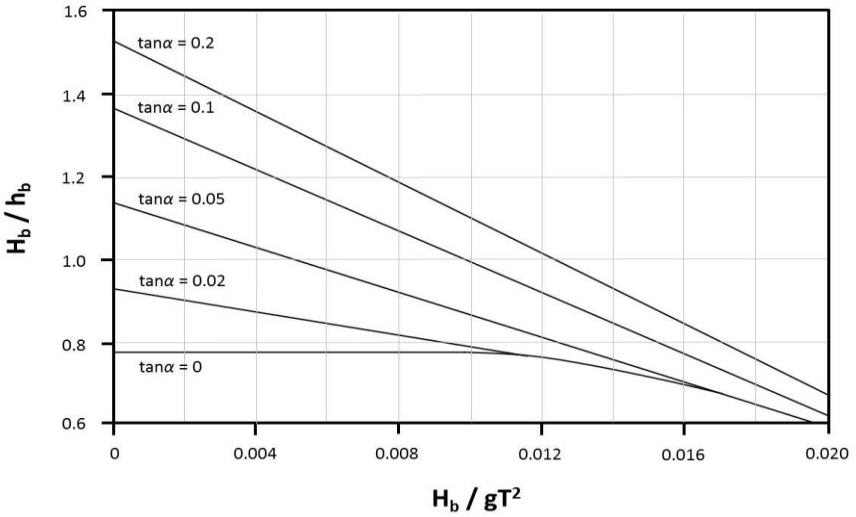

Figure A-2. Breaker depth index (for regular wave) as a function of wave steepness H_b/gT^2 (Weggel 1972)

REFERENCES

Bagnold, M.R.A. 1939. Interim report on wave-pressure research. *Proc. Inst. Civ. Engrs*, 12, 201–226.

Battjes, J.A. 1974. Surf similarity. *Proceedings 14th Coastal Engineering Conference*. ASCE, New York, N.Y., 466-480.

Blenkinsopp, C. E., and J. R. Chaplin. 2011. Void fraction measurements and scale effects in breaking waves in fresh water and sea water. *Coastal Engineering,* 58(5), 417-428.

Bredmose, H., D.H. Peregrine, and G.N Bullock. 2009. Violent breaking wave impacts. Part 2: modelling the effect of air. *Journal of Fluid Mechanics*, 641, 389-430.

Bredmose, H., G.N. Bullock, and A.J. Hogg. 2015. Violent breaking wave impacts. Part 3. Effects of scale and aeration. *Journal of Fluid Mechanics*, *765*, 82-113.

Bullock, G.N., A.R. Crawford, P.J. Hewson, M.J.A. Walkden, and P.A.D. Bird. 2001. The influence of air and scale on wave impact pressures. *Coastal Engineering*, 42(4), 291-312.

Bullock, G., C. Obhrai, G. Müller, G.Wolters, H. Peregrine, and H. Bredmose. 2003. Field and laboratory measurements of wave impacts. *In Proc. Coastal Structures* (pp. 343-355).

Bullock, G.N., C. Obhrai, D.H. Peregrine, and H. Bredmose. 2007. Violent breaking wave impacts. Part 1: Results from large-scale regular wave tests on vertical and sloping walls. *Coastal Engineering*, 54(8), 602-617.

Cuomo, G., W. Allsop, and S. Takahashi. 2010. Scaling wave impact pressures on vertical walls. *Coastal Engineering*, *57*(6), 604-609.

Cuomo, G., R. Piscopia, and W. Allsop. 2011. Evaluation of wave impact loads on caisson breakwaters based on joint probability of impact maxima and rise times. *Coastal Engineering*, *58*(1), 9-27.

Galvin, C. J. 1968. Breaker type classification on three laboratory beaches. *Journal of geophysical research*, 73(12), 3651-3659.

Goda, Y. 1974. New wave pressure formulae for composite breakwaters. *Proc. 14th International Conference on Coastal Engineering,* pp 1702-1720, Copenhagen, publn. ASCE, New York.

Hattori, M., A. Arami, and T. Yui. 1994. Wave impact pressure on vertical walls under breaking waves of various types. *Coastal Engineering*, 22(1), 79-114.

Hughes, S. A. 2005. Wave momentum flux parameter: a descriptor for nearshore waves. *Coastal Engineering*, 51(11), 1067-1084.

Hull, P., and G. Müller. 2002. An investigation of breaker heights, shapes and pressures. *Ocean Engineering*, 29(1), 59-79.

Kyte, A., and A. Tørum. 1996. Wave forces on vertical cylinders upon shoals. *Coastal engineering*, 27(3), 263-286.

Muttray, M., H. Oumeraci, K. Shimosako, and S. Takahashi. (1998). Hydraulic performance of a high mound composite breakwater. *Coastal Engineering Proceedings*, 1(26).

Oumeraci, H., P. Klammer, H.W. Partenscky. 1993. Classification of breaking wave impact loads on vertical structures. ASCE, *J. Waterway, Port, Coastal and Ocean Eng*., 119(4), 381-397.

Raby, A., G. Bullock, D. Banfi, Y. Rafiq, and F. Cali. 2015. Wave loading on rock lighthouses. *In Proceedings of the Institution of Civil Engineers-Maritime Engineering,* Vol. 169, No. 1, pp. 15-28. Thomas Telford Ltd.

Trinh, Q., A. Raby, D. Banfi, M. Corrado, B. Chiaia, Y. Rafiq, and F. Cali. 2016. Modelling the Eddystone Lighthouse response to wave loading. *Engineering Structures*, 125, 566-578.

Weggel, J. R. 1972. Maximum breaker height for design. *Coastal Engineering Proceedings*, 1(13).

Wienke, J., and H. Oumeraci. 2005. Breaking wave impact force on a vertical and inclined slender pile – theoretical and large-scale model investigations. *Coastal Engineering*, 52(5), 435-462.

Wave impacts on the Eddystone lighthouse: a field and laboratory investigation

D. Banfi, A. Raby, D. Simmonds, Y. Rafiq and G. Bullock

Electronic version of an article published in Proceedings of ICE Coasts, Marine Structures and Breakwaters Conference, September 2017, Liverpool, UK.

Wave impacts on the Eddystone lighthouse: a field and laboratory investigation

Davide Banfi*, PhD student
Alison Raby*, Associate Professor
David Simmonds*, Associate Professor
Yaqub Rafiq*, Associate Professor
Geoffrey Bullock*, Emeritus Professor

* School of Engineering, Plymouth University, Plymouth, UK

Abstract
Because little was known about how the masonry lighthouses constructed during the 19th century at exposed locations around the British Isles were responding to wave action, the dynamic response of the Eddystone lighthouse is investigated both in the field and by means of a small-scale model mounted in a laboratory wave channel. Like other so called 'rock lighthouses', the Eddystone lighthouse was built on top of a steep reef at a site that is fully submerged at most states of the tide. Consequently, the structure is exposed to loading by unbroken, breaking and broken waves. Field data obtained by the use of geophones, cameras and a wave buoy are presented together with information on the force time histories measured with load cells during the laboratory tests.
The geophone signals, which provide the structural response in terms of velocity data, are differentiated and integrated in order to obtain accelerations and displacements respectively. The results show that the higher velocities and accelerations are usually associated with the more impulsive loads caused by waves that break on or just in front of the structure. However, such loads do not necessarily lead to the largest displacements. In the current data broken waves were found to generate the largest structural deflections. The laboratory tests demonstrate how the limited water depth strongly affects the wave loading. In particular, only small plunging waves are able to break on or near the structure and larger waves that break further away can impose a greater overall impulse due to the longer duration of the load.

Introduction
Climate change is increasing the general concern about effects of sea level rise on reliability of coastal structures. However, while coastal defence structures have been the subject of many investigations, little work has been done concerning structures such as rock lighthouses (Kyte and Tørum, 1996; Raby *et al*., 2015; Banfi *et al*., 2017). Commonly, rock lighthouses are erected on the top of a steep reef and in limited water depths. As a consequence of these environmental conditions, waves are strongly affected by surf-zone transformations and breaking waves can occur. While wave loading due to non-breaking waves is well understood, the wave-structure interaction due to breaking waves further adds to the difficulty in predicting the underlying processes. This is essentially given by the intrinsic random nature of wave pressure due to the unknown mixture of water-air involved during the breaking process (Bullock *et al.*, 2001). Experimental studies on breaking waves are based on either field observations or laboratory measurements. Due to the random nature of wave field and the highly localised nature of pressure in space and time (Blackmore *et al.*, 1984; Bullock *et al.*, 2003), wave loads are rather difficult to analyse in the field. Although small-scale tests introduce laboratory effects that are difficult to quantify (Bullock *et al.,* 2003; Cuomo *et al.,* 2010; Blenkinsopp & Chaplin, 2011; Bredmose *et al.,* 2015), the major advantage of laboratory experiments on breaking waves over field measurements is the control over wave characteristics in order to estimate the effects of waves on the structure during the process of breaking.

The present paper investigates wave impacts for a particular case of study: the Eddystone lighthouse (Figure 1a). This is a masonry structure that consists of two parts: a solid cylindrical base with a tapered tower on top of it. The Eddystone lighthouse marks a perilous reef of the same name that lies in the English Channel some 21 km offshore from Plymouth, UK (Figure 1b). At low tides, the structure is virtually protected by surface-piercing rocks, with exception of a small sector, centred approximately in the SW direction (Figure 1a). Within this sector are the longest fetches from the Atlantic Ocean and the seabed rises from the toe of the reef (approximately at a depth of 44 m at highest astronomical tide) with increasing steepness towards the tower: moving from an average slope of 1:20 to 1:8.
This investigation includes field data and laboratory tests. Geophones have been installed on the Eddystone lighthouse in order to analyse the dynamic response of the structure, while small-scale tests have been carried out in order to obtain information concerning the wave loading.

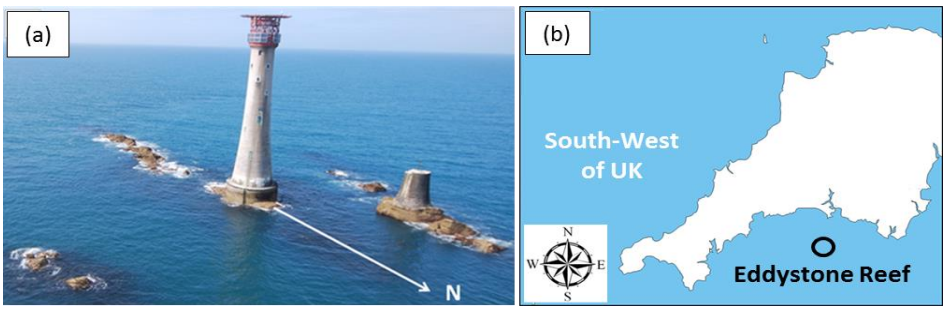

Figure 1: (a) Eddystone lighthouse and rock outcrops; (b) location of the reef.

Literature review

Breaking shape and impulsivity of wave loading

Several investigations on rigid structures have already demonstrated that the impulsivity of wave loading depends on the breaking shape and tends to decrease with increasing breaking distance. This was found for both plane surface (Chan and Melville, 1989; Oumeraci *et al*., 1993) and cylindrical structures (Chan and Melville, 1989; Zouh *et al*., 1991; Wienke and Oumeraci, 2005; Banfi *et al*., 2017). Plunging impacts are characterised by a sharp peak in the pressure time history (Oumeraci *et al*., 1993; Hattori *et al*., 1994; Hull and Muller, 2002). They are usually called small air pocket impacts when the wave breaks at the plane wall and the crest front is almost vertical at the instant of impact; in contrast they are called large air pocket impacts when the wave overturns and strikes the structure trapping a large air pocket. Both types generate impulsive (high frequency) loads and thus, a dynamic analysis is required in order to evaluate their effects on the structure (Allsop *et al*., 1996; Kortenhaus & Oumeraci, 1997). With a further increase in the breaking distance, the plunging wave is completely developed and a turbulent air-water mixture collides with the structure. This wave, which is called broken, tends to dissipate most of the energy and the impact is usually considered as a quasi-static load (Allsop *et al*., 1996; Kortenhaus & Oumeraci, 1997).

Highest pressure peak, impact duration and spatial distribution

Typically, plunging impacts exhibit much higher pressures than broken waves, as found in investigations on rigid structures, such as plane walls (Goda, 1974; Oumeraci *et al*., 1993; Bullock *et al*., 2007) and slender cylinders (Chan and Melville, 1989; Zouh *et al*., 1991). Among plunging impacts on plane walls, both small and large air pocket have been found to be responsible for the highest pressure peaks. However, although both plunging breakers can generate the highest peak pressures, it is generally accepted that the increase in size of the air pocket results in a cushioning effect with a pressure oscillation, which tends to increase the impact duration (Oumeraci *et al*., 1993; Hattori *et al*., 1994; Hull and Muller, 2002; Bullock *et al*., 2007). As a consequence of the effect of aeration, the pressure impulse may increase due to the fact that the load can act for longer on the structure and over a larger extent, even if the peak pressure may decrease (Bredmose *et al*., 2009).
Previous considerations concerning the highest load peaks were not found for High Mound Composite Breakwaters (HMCBs), which are characterised by large and steep mounds that cause a limited water depth at the toe of the vertical superstructure. If the mound is wide enough, only small waves are able

to break at the superstructure, thereby causing lower loads despite the small breaking distance (Muttray *et al*., 1998).
Both plunging breakers on plane walls tend to be characterised by triangular vertical distributions but for small air pockets the peak occurs above SWL whereas for large air pockets the peak occurs closer to the SWL (Hull and Muller, 2002). For broken waves the spatial distribution is more uniformly distributed over the structure with the maximum peak that can occur around or slightly under the SWL (Bullock *et al*., 2007). Banfi *et al.* (2017) investigated wave pressure distributions on a small-scale model of the Eddystone lighthouse mounted in a laboratory wave channel. This investigation indicates that the highest spatial distributions occur for plunging impacts.

Structural response

Very few studies have considered the dynamic response of structures under breaking waves. This might be undertaken with accelerometers, which provide acceleration data, or with geophones, which provide velocity data. Such a structural response depends on both the characteristics of the structure (natural frequencies and geometrical configuration) and the external wave load (temporal and spatial variation of the force). In this regard, Kirkgöz (1990) found that the longer-lasting low impact forces are more effective in producing the larger wall deflections. Manjula *et al*. (2013) used accelerometers in their laboratory tests in order to investigate the effect of breaking waves on the dynamic response of a slender cylinder. They found that maximum structural deflections were not related to the extreme force events, suggesting that the impulse should have more importance than the violence of the impact. For their part, Loraux (2013) combined numerical modelling and geophones data obtained from the Jument lighthouse (France). This numerical investigation indicated that the structural response is strongly affected by the nature of the impulse. As shown in Loraux (2013), equivalent instantaneous forces (maximum value) cause different responses depending on the extent of the load duration. In particular, he demonstrated that impulses characterised by shorter impact durations resulted in higher structural acceleration but lower deflections when compared to those caused by longer impact durations. Also, the presence of higher frequencies was found to increase for more rapid impulses (Loraux, 2013).

Methodology

Field instrumentation

Two geophones and four video cameras were installed on the Eddystone lighthouse. Both the geophones were installed on the bottom of the 7^{th} level (subsidiary light room), which is approximately 25 m from the base of the tapered tower. The geophones provided the structural motions of the lighthouse in the form of velocity time histories. They were automatically activated when the vibration measurement exceeded a threshold value, set to 0.32 mm/s. Almost all the events were recorded at 500 Hz for a time duration of about 2 seconds, constrained by a maximum number of data points in a vibration record. Velocity signals can be integrated and differentiated to obtain displacements and acceleration, respectively. They were integrated using Simpson's rule (3 point-formula) and were differentiated using 2^{nd} order central method. Dominant frequencies of the signals were determined with peak spectra analysis i.e. the magnitude of the spectra is measured in terms of peak amplitudes.
The four DC-powered video cameras, controlled remotely by internet, were installed on the top part of the Eddystone lighthouse. Impact responses have been analysed by considering offshore wave data from the nearby Western Channel Observatory E1 buoy (some 15 km south-west of the lighthouse) in conjunction with video images for a qualitative description of the wave climate. Water level data along the coast at Plymouth have been obtained from the British Oceanographic Data Centre. Further details about the field instrumentation are described in Raby *et al*. (2015).

Laboratory tests

Because the structural response events recorded in the field could not be accurately linked to the characteristics of the individual waves that caused them, regular wave tests were conducted to gain a better understanding under well-controlled conditions of how breaker shape and limited water depth affect wave loading. The regular wave tests were carried out in the 35 m long x 0.6 m wide x 1.2 m deep sediment wave flume of the COAST Laboratory at Plymouth University. The experiments were conducted at 1:70 length scale (Froude scaling) compared to the prototype and the bathymetry was modelled according to the SW direction with two average slopes, 1:20 and 1:8, as shown in Figure 2. The water depths at the paddle and at the toe of the model were 0.63 m and 0.095 m, respectively, in agreement with the depths in the prototype at highest astronomical tide (i.e. 44 m and 6.65 m).

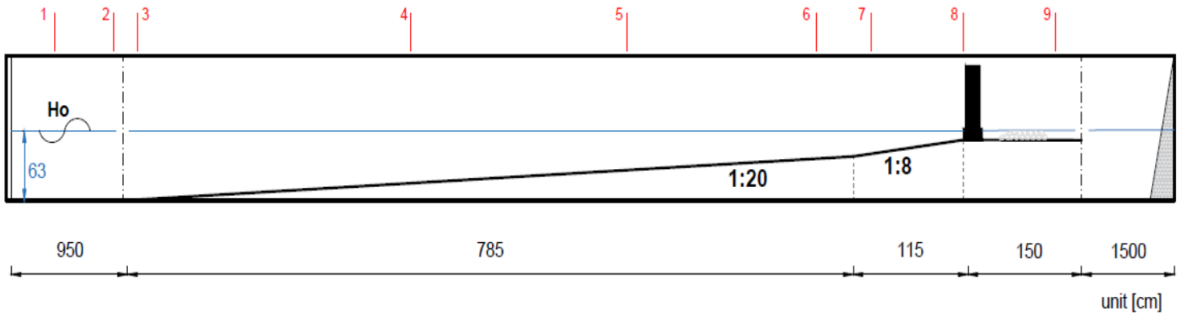

Figure 2: Setup of the experiment with locations of wave gauges indicated.

Regular wave tests were carried out to obtain the horizontal component of the force in-line with the wave direction. To this end, two unidirectional load cells (FSLB) were used. The FSLB is a stainless steel platform load cell (beam type), sealed at a waterproof level of IP67, with a nominal capacity of 890 N and an accuracy of 0.02% of the maximum capacity. Force signals were acquired at 1.8 kHz.
The model comprised two circular cylinders (one above the other) having different diameters. The cylindrical base had a height of 0.10 m and the upper cylinder was 0.55 m high, their diameters were 0.20 m and 0.155 m, respectively. The thickness of the cylinder walls was 0.01 m and they were manufactured in Plexiglas in order to be simultaneously waterproof, rigid and light (Figure 3a).
The model was connected with two axial ball joints to the two load cells and was supported at the top by a sliding-pivot (in line with the wave direction). This support consisted of two sliding rails (circular section of low friction) and two pivots (spherical pillow blocks). The support hence avoided the weight of the model acting on the load cells. It also prevented lateral vibration due to impulsive impacts of the model whilst still allowing deflections in line with the load cell axes. Both the sliding-pivot and the load cells were attached to a framework rigidly connected to the top of the wave flume.
The frequency response of the system was empirically determined from the free oscillation of the model. It was measured both in air and with the lighthouse model slightly submerged (i.e. test condition). Results showed three dominant peaks at 25, 140 and 180 Hz.
The load cells gave, instant by instant, the force applied to the application load point of the devices, and solving the static scheme in Figure 3b, it was possible to obtain the time history of the horizontal component of the wave force. The load cell system has the advantage of providing more accurate measurements of the overall force acting on the model than would be possible by spatially-integrated pressures, which are highly localised in both space and time.
Finally, nine resistance wave gauges (locations indicated in Figure 2) and three cameras completed the setup of the experiments. One camera, which was located in line with the lighthouse model (lateral side), was both high speed and high definition (3600 fps at 1024x1024 resolution). The other two cameras were located in different positions in order to obtain a large view, from the side and from the top, of the approaching wave.

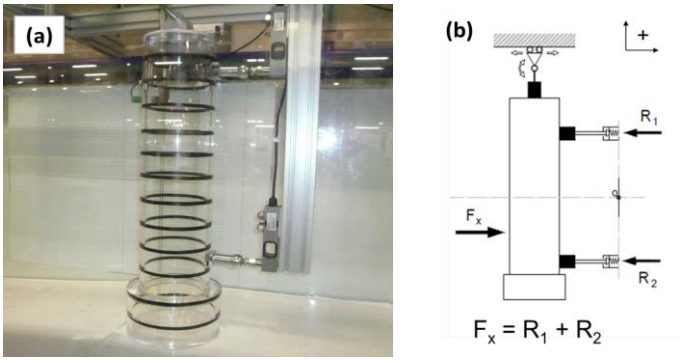

Figure 3: (a) Physical model; (b) static scheme of the load cell system.

Results and discussion

The oscillation of the Eddystone lighthouse, in terms of accelerations and displacements, were obtained from the velocity signals recorded by the geophones. These signals may be considered as

three outputs generated by an input, i.e. the impulse of the wave ($I = \int F\,dt$). This way, the structure may be imagined as a 'filter' that transforms the input signal (Figure 4). The small-scale experiments were carried out in order to obtain information concerning the impulse generated by different breaker shapes.

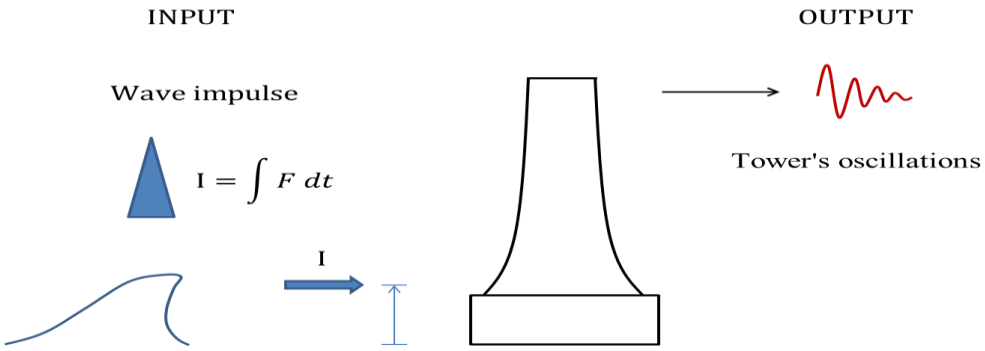

Figure 4: Wave impulse (input) and tower oscillations (output).

Structural responses measured in the field

The UK winter storms of 2013-2014 caused more than 3000 geophone-registered events on the Eddystone lighthouse (see Raby *et al.*, 2015). The structural responses show a variety of different behaviours but higher frequency contents tend to occur with a clear sharp peak in the velocity time history.

Figures 5 and 6 show video frames of two impacts that caused typical structural responses. In order to compare the different events, each subsequent frame has the same time step (1 s). In addition, the wave front is highlighted with a red line, which is solid when the wave front is stable and dashed when the wave is broken. Details of the events with their respective date/time and wave data (significant offshore wave height $H_{s,o}$, peak period T_p, water level CD and offshore wave direction β) are given in Table 1. As may be observed in Figure 5, Event 1 is characterised by a clear wave front that advances towards the lighthouse. Then, the wave height suddenly increases and it breaks in the proximity of the structure. However, in Event 2 the plunging jet is completely developed and the breaking distance is so large that the impact is caused by a large amount of turbulent and aerated water, which seems to act on the structure for a long time (Figure 6).

Figure 7 shows the velocity time history and associated amplitude spectra of the two events. Event 1 is characterised by a predominant sharp peak at the beginning of the time history (Figure 7a). This maximum velocity peak (1.3 mm/s) is, in absolute terms, 2.6 times the second one (0.5 mm/s). Conversely, for Event 2 the highest peaks tend to reach the same amplitude. In particular, the two maximum peaks, reached at 0.18 and 0.24 s, are approximately 1.0 and 1.25 mm/s, respectively (Figure 7c).

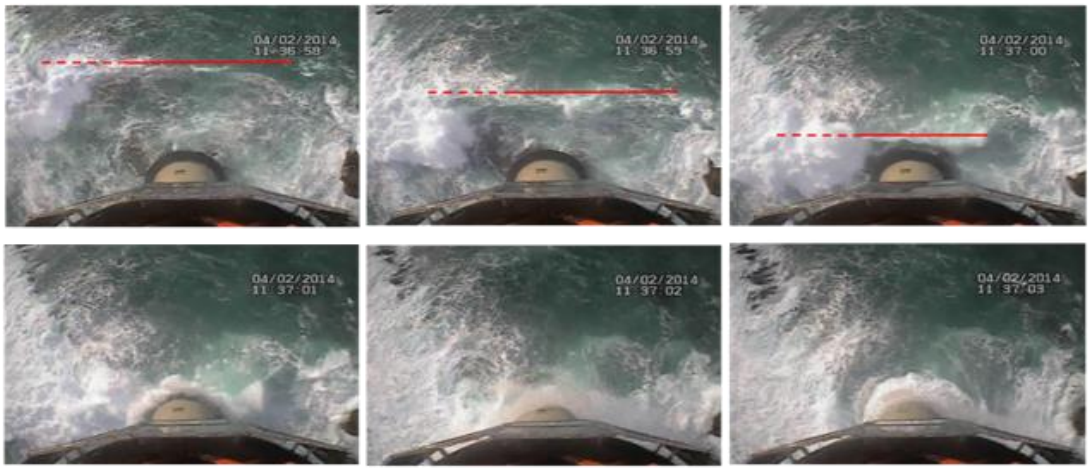

Figure 5: Video images of Event 1 (time step 1 s).

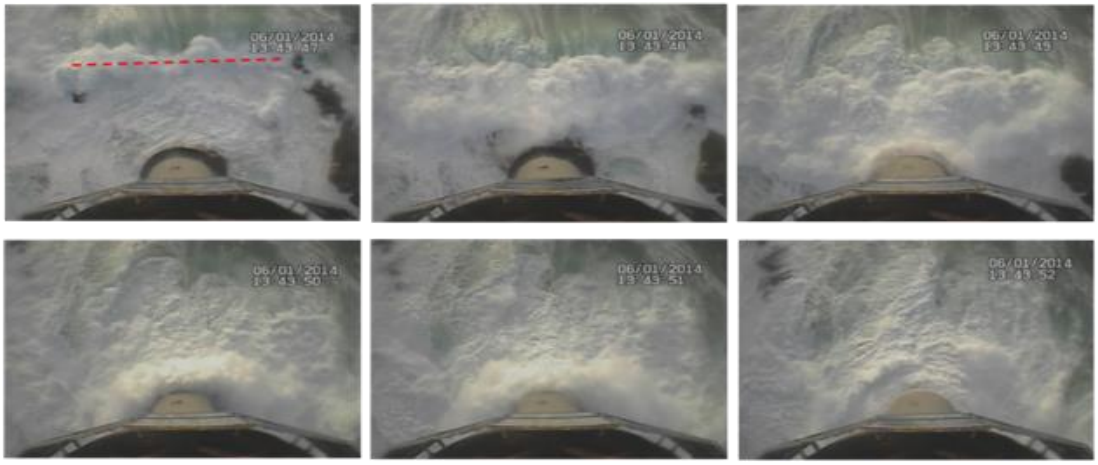

Figure 6: Video images of Event 2 (time step 1 s).

Table 1: Hydraulic details of the two structural events.

	Data/time	$H_{s,o}$ [m]	T_p [s]	CD [m]	β [° to true north]
Event 1	4/2/14 - 11:36	1.81	11.9	4.74	220
Event 2	6/1/14 - 13:34	3.11	18.2	2.87	237

As may be observed from Figures 7b and 7d, the velocity signal of Event 1 is characterised by higher frequency contents when compared to Event 2; thus, Event 1 shows a more impulsive nature because it has a higher peak and shorter oscillation periods. As a consequence of the different frequency contents, Event 2 results in a higher maximum displacement with respect to Event 1; even if its maximum velocity is slightly lower. In fact, Event 1 has a maximum displacement of 0.016 mm at 0.03 s (Figure 8a), whereas Event 2 has a maximum displacement of 0.028 mm at 0.44 s (Figure 8b).
From a physical point of view, this means that the oscillations of the lighthouse are affected by the different impulsivity of the two velocity signals. In particular, Event 1 causes a smaller displacement peak, but with a higher velocity with respect to Event 2. Figures 8b and 8d indicate that the displacement peak spectrum of Event 1 is characterised by higher frequencies with respect to Event 2. Video frames shown in Figures 5 and 6 suggest that the nature of the structural responses depends on the different ways that the waves approach the structure. In particular, Event 1 is simultaneously characterised by a more impulsive velocity signal and a shorter breaking distance. On the other hand, it is generally accepted that for rigid structures the impulsivity of wave loading, which depends on the breaking shape, increases as the breaking distance decreases.
Although video images indicate that the nature of the structural responses (clear sharp peak and frequency content) may be affected by the type of breaking, it is reasonable to presume that the magnitude of the structural deflection is affected by both wave characteristics and application point of the wave load. Alongside the field data monitoring, a numerical structural model of the Eddystone lighthouse was developed and results are presented in Trinh *et al*. (2016). Some of the numerical simulations aimed to investigate the effects of the variation of the load application point on the structural deflection of the lighthouse. The same external impulse was applied but varying the elevation of the impact area on the structure. Results show that the structural deflection of the Eddystone lighthouse is highly influenced by the height at which the impacts occur. In particular, maximum displacements show a steep linear trend with impact height (Trinh *et al*., 2016). The increase in displacements is explained by the fact that the cylindrical base, which has a larger diameter, can be considered a massive structure that is more rigid; while, the upper part of the lighthouse tends to be more slender and, so, less rigid. However, Event 2 is a broken wave that occurs during a lower water level condition with respect to the plunging impact of Event 1 (Table 1). Therefore, a higher elevation of the impact area could not justify the larger structural deflection measured for Event 2. Indeed, several reasons may explain the different displacements of the two events despite their similar velocities, among which are: value of the maximum instantaneous wave force, duration of the impact and extension of the load area. Figure 9 shows acceleration time histories and amplitude spectra of Event 1 and 2. As may be observed, Event 1 results in a higher acceleration peak (180 mm/s^2) when compared to the one of Event 2 (80 mm/s^2). Thus, while Event 1 results in a

more impulsive event, Event 2 generates a larger deflection. According to Loraux (2013), this result indicates that the impact duration of the event may play a fundamental role in terms of displacements generated.

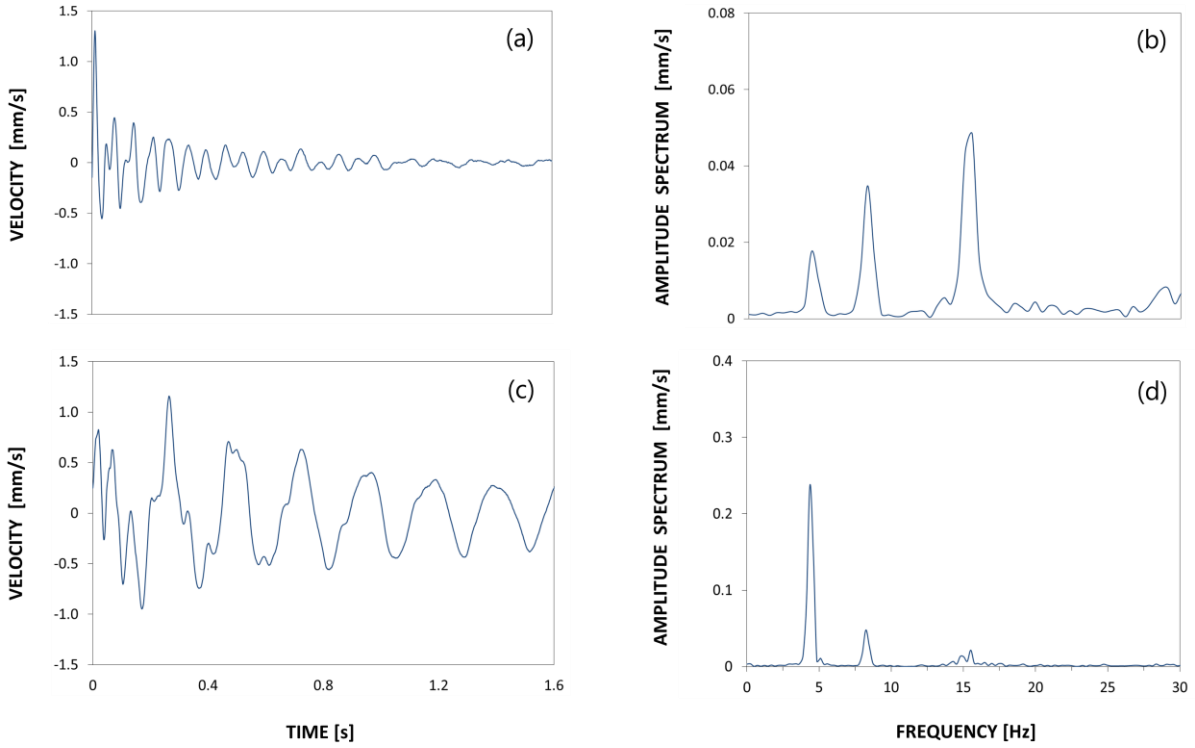

Figure 7: Structural responses (velocity time history and spectrum) of Event 1 (top) and Event 2 (bottom). Note the use of different vertical scales in Figs 7b and 7d.

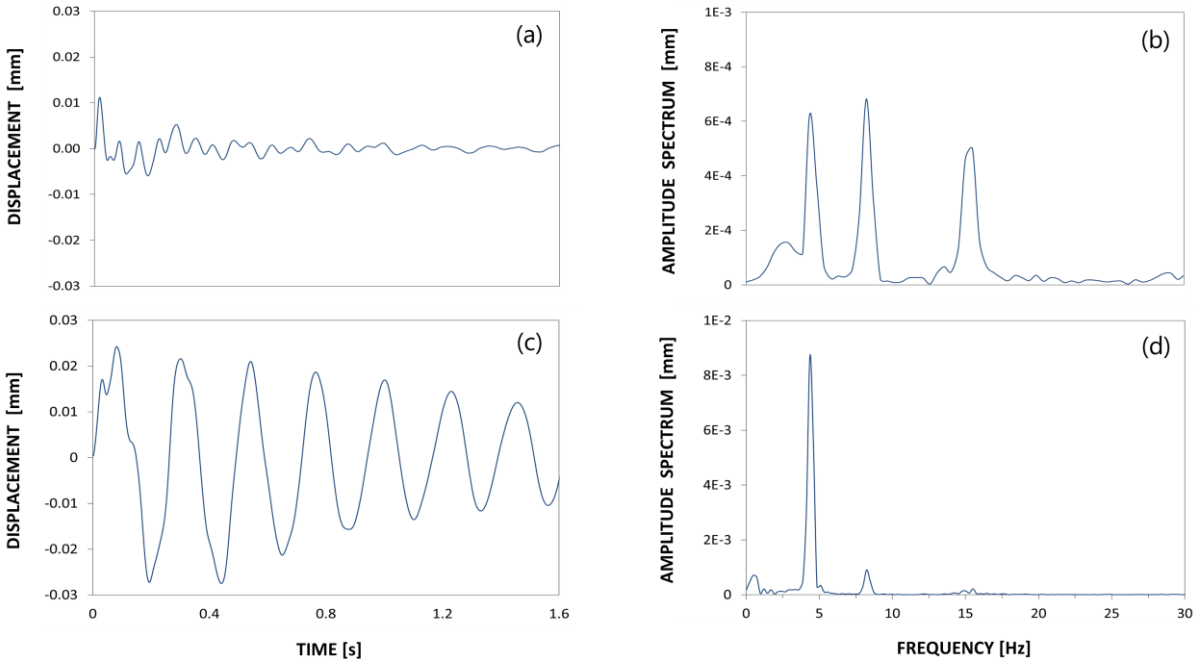

Figure 8: Structural responses (displacement time history and spectrum) of Event 1 (top) and Event 2 (bottom). Note the use of different vertical scales in Figs 8b and 8d.

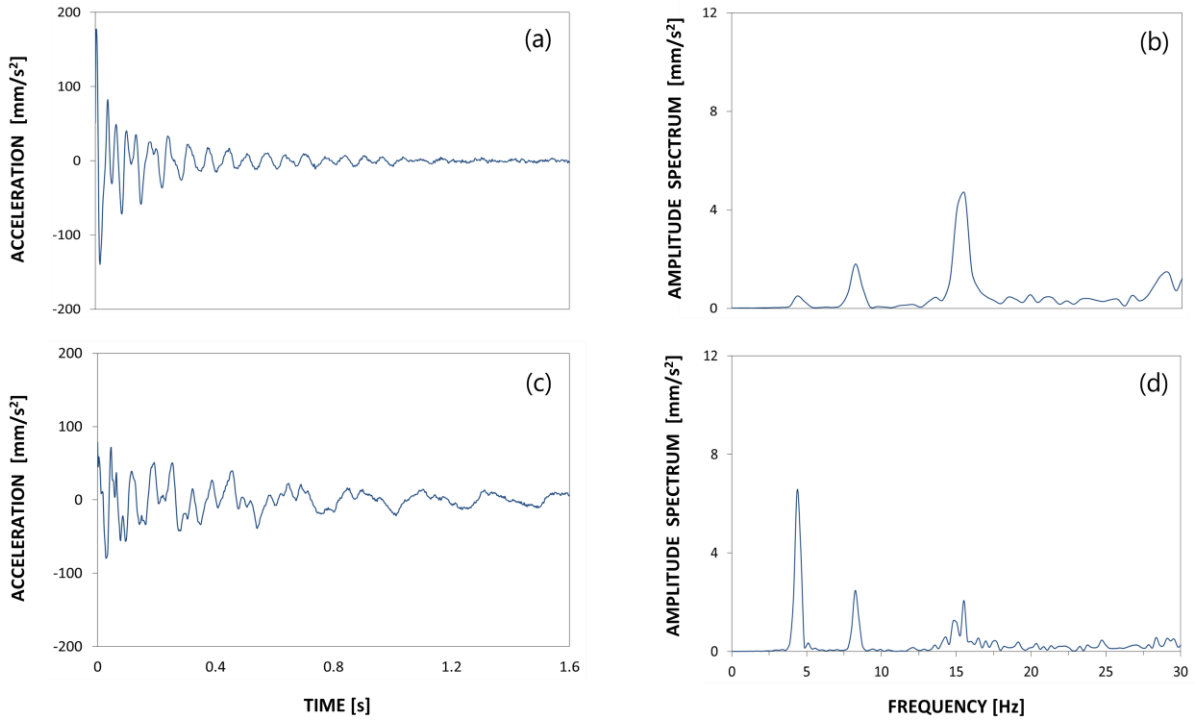

Figure 9: Structural responses (acceleration time history and amplitude spectra) of Event 1 (top) and Event 2 (bottom).

Finally, it should be noted that the natural frequencies of the lighthouse are approximately at 4, 8, 15 and 28 Hz.

Wave loading at small-scale

Regular wave tests were conducted at 1:70 scale for both plunging and broken wave impacts as illustrated by the video images included in Figure 10. In Test 1 a plunging wave breaks at the structure with the wave front almost vertical and minimal quantities of air are trapped, whereas in Test 2 the wave has broken before it reaches the structure and the impact is caused by a turbulent air water mixture. Thus, the conditions are broadly similar but not directly related to those previously considered in Events 1 and 2 respectively of the field data. The offshore heights and periods of the regular waves are listed together with the maximum forces measured in Table 2. Both model and prototype values are given, with the latter calculated on the basis of the Froude Law.

Although the load cells system recorded a similar maximum value (approximately 45 N) for both the tests, the time histories are rather different (Figure 10). However, it should be noted that the natural frequency of the system (25 Hz) did not enable the force-time history of the highly impulsive part of each impact event to be accurately recorded. As a consequence, Test 1 is characterised by high frequency oscillation that occurs after the maximum peak (Figure 10). This oscillation is the response of the load cell and not the instantaneous wave-induced force. The maximum peak of Test 2 exhibits a longer rise time when compared to Test 1. Then the signal tends gradually to decrease and a second quasi-static peak can be detected (Figure 10).

Table 2: Model and prototype values of Test 1 and Test 2.

	MODEL			PROTOTYPE		
	H_o [m]	T [s]	F_{max} [N]	H_o [m]	T [s]	F_{max} [MN]
TEST 1	0.11	1.4	45	7.7	11.7	15.4
TEST 2	0.22	2.4	42	15.4	20.0	14.4

The similar load peaks are explained by the fact that the water depth at the toe of the model is limited in the present investigation. Thus, the broken wave (Test 2) is characterised by a larger breaking distance that increases the dissipation of energy, but at the same time by a larger period (T) and

offshore wave height (H_o) with respect to the plunging impact (Test 1). The longer rise time of the broken wave is in well agreement with the coastal literature, in which the impact duration increases with the increasing of the breaking distance or amount of air.

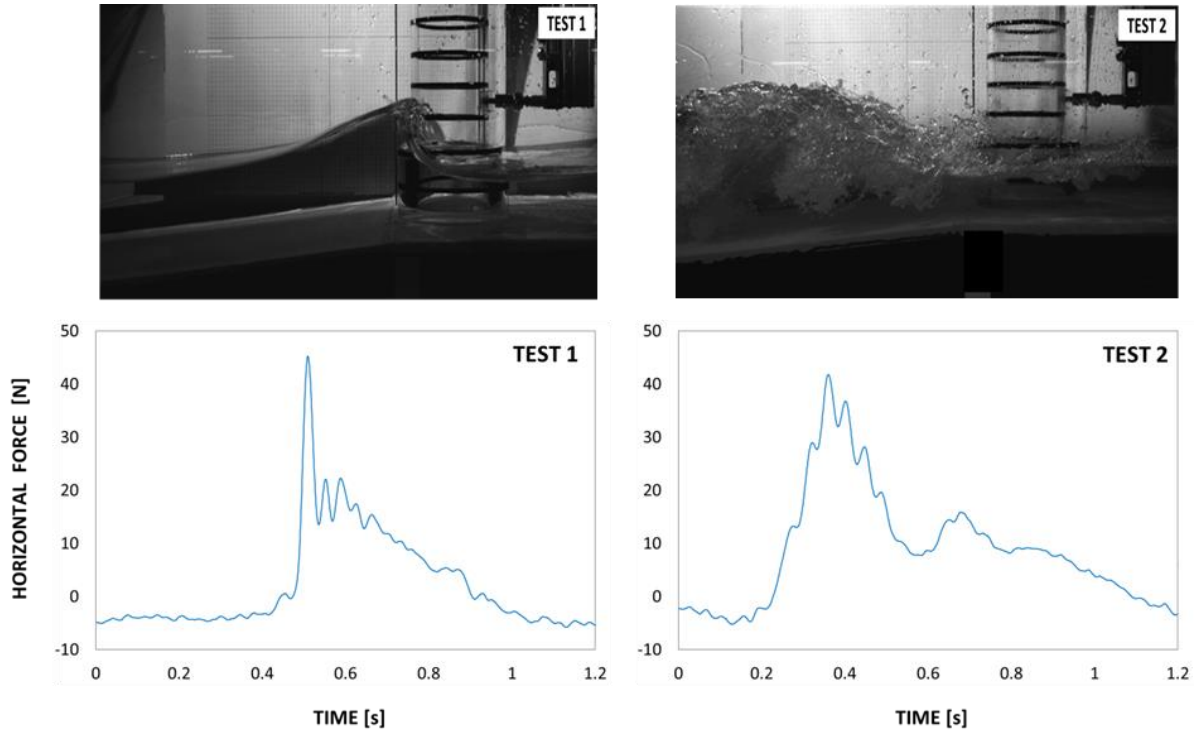

Figure 10: High definition video images and force time histories for Test 1 and Test 2.

Conclusions

This investigation suggests that the nature of the structural response of the Eddystone lighthouse is strongly affected by the way in which the waves approach the tower. Impulsive responses, characterised by higher frequencies and sharper peaks in the velocity time histories, are generated by waves that break on or just in front of the structure. However, these breaking waves can generate smaller displacements when compared to those generated by broken waves, despite the former show structural responses that are characterised by higher velocities and accelerations. Several parameters could justify the larger deflection produced by broken waves, e.g. load peak, impact duration, spatial distribution and load application point. According to the small-scale experiments, the wave loading is strongly affected by the depth limited conditions of the Eddystone lighthouse. In fact, only small plunging impacts are able to break on or near the structure. Although they show more impulsive loads with higher force peaks when compared to broken waves, the latest can impose a greater overall impulse due to the longer duration of the load.

Acknowledgments

The authors would like to acknowledge the support of the General Lighthouse Authorities, particularly Martin Bransby and Ron Blakeley (ex-Trinity House) and their lighthouse engineers who assisted with deployments on station; Peter Ganderton and Tony Tapp of Plymouth University who designed much of the installed equipment; Alastair Reynolds and Peter Arber for the assistance provided during the laboratory test and the School of Marine Science and Engineering who funded Davide Banfi's studentship.

References

Allsop NWH., Vicinanza D., & McKenna JE. (1996) *Wave forces on vertical and composite breakwaters,* Strategic Research Report SR 443, pp 1-94, HR Wallingford, March 1996, Wallingford.

Banfi D., Raby A., & Simmonds D. (2017) *Characterisation of breaking waves on the Eddystone lighthouse: a laboratory investigation on wave pressure,* Coastal Engineering Proceedings, 1(35), 15.

Blackmore P. A. & Hewson P. J. (1984) *Experiments on full-scale wave impact pressures,* Coastal Engineering, 8(4), 331-346.
Blenkinsopp C. E. & Chaplin J. R. (2011) *Void fraction measurements and scale effects in breaking waves in fresh water and sea water,* Coast. Engng 58 (5), 417–428.
Bredmose H., Peregrine D. H., & Bullock G. N. (2009) *Violent breaking wave impacts. Part 2: modelling the effect of air,* Journal of Fluid Mechanics, 641, 389-430.
Bredmose H., Bullock G., & Hogg A.J. (2015) *Violent breaking wave impacts. Part 3. Effects of scale and aeration*, Journal of Fluid Mechanics, 765, 82-113.
Bullock G.N., Crawford A.R., Hewson P.J., Walkden M.J.A., & Bird P.A.D. (2001) *The influence of air and scale on wave impact pressure,* Coastal Engineering, 42(4), 291-312.
Bullock G., Obhrai C., Müller G., Wolters G., Peregrine H., & Bredmose H. (2003) *Field and laboratory measurements of wave impacts,* In Proc. Coastal Structures (pp. 343-355).
Bullock G.N., Obhrai C., Peregrine D.H., & Bredmose H. (2007) *Violent breaking wave impacts. Part 1: Results from large-scale regular wave tests on vertical and sloping walls,* Coastal Engineering, 54(8), 602-617.
Chan E. S. & Melville W. K. (1989) *Plunging wave forces on surface-piercing structures*, Journal of Offshore Mechanics and Arctic Engineering, 111(2), 92-100.
Cuomo G., Allsop NWH., & Takahashi S. (2010) *Scaling wave impact pressures on vertical walls,* Coastal Engineering, 57(6), 604-609.
Goda Y. (1974) *New wave pressure formulae for composite breakwaters*, Proc. 14th International Conference on Coastal Engineering, pp 1702-1720, Copenhagen, publn. ASCE, New York.
Hattori M., Arami A., & Yui T. (1994) *Wave impact pressure on vertical walls under breaking waves of various types,* Coastal Engineering, 22(1), 79-114.
Hull P. & Müller G. (2002) *An investigation of breaker heights, shapes and pressures,* Ocean Engineering, 29(1), 59-79.
Kirkgöz M. S. (1990) *An experimental investigation of a vertical wall response to breaking wave impact,* Ocean Engineering, 17(4), 379-391.
Kortenhaus A. & Oumeraci H. (1998) *Classification of wave loading on monolithic coastal structures*, Proc. 26th International Conference on Coastal Engineering, pp. 867 880, Copenhagen, publn. ASCE, New York.
Kyte A., & A. Tørum (1996) *Wave forces on vertical cylinders upon shoals*, Coastal engineering, 27(3), 263-286.
Loraux C. (2013) *Comportement structural des phares en mer – Étude historique sur le phare de la Jument et propositions d'interventions,* École Polytechnique Fédérale De Lausanne, Institut D'Ingénierie Civile.
Manjula R., Sannasiraj S. A., & Palanichamy K. (2014) *Experimental Investigations of acceleration on slender cylindrical member under breaking waves,* The International Journal of Ocean and Climate Systems, 5(3), 117-125.
Muttray M., Oumeraci H., Shimosako K., & Takahashi S. (1998) *Hydraulic performance of a high mound composite breakwater,* Coastal Engineering Proceedings, 1(26).
Oumeraci H., Klammer P., Partenscky H.W. (1993) *Classification of breaking wave impact loads on vertical structures*, ASCE, J. Waterway, Port, Coastal and Ocean Eng., 119(4), 381-397.
Raby A., Bullock G., Banfi D., Rafiq Y., & Cali F. (2015) *Wave loading on rock lighthouses,* Proceedings of the Institution of Civil Engineers-Maritime Engineering, Vol. 169, No. 1, pp. 15-28, Thomas Telford Ltd.
Trinh Q., Raby A., Banfi D., Corrado M., Chiaia B., Rafiq Y., & Cali F. (2016) *Modelling the Eddystone Lighthouse response to wave loading,* Engineering Structures, 125, 566-578.
Wienke J. & Oumeraci H. (2005) *Breaking wave impact force on a vertical and inclined slender pile – theoretical and large-scale model investigations,* Coastal Engineering, 52(5), 435-462.
Zhou D., Chan E.S., & Melville W.K. (1991) *Wave impact pressures on vertical cylinders,* J. Appl. Ocean Res., 13(5): 22&234.